ELECTROCHEMISTRY FOR MATERIALS SCIENCE: IN MEMORY OF KEN NOBE AND MORTON SCHWARTZ

EDITED BY: Nosang Vincent Myung, Bongyoung Yoo, Peter Pintauro,
Syed Mubeen Jawahar Hussaini and Jae-Hong Lim
PUBLISHED IN: Frontiers in Chemistry

frontiers Research Topics

Frontiers eBook Copyright Statement

ISSN 1664-8714
ISBN 978-2-88976-520-1
DOI 10.3389/978-2-88976-520-1

About Frontiers

Frontiers is more than just an open-access publisher of scholarly articles: it is a pioneering approach to the world of academia, radically improving the way scholarly research is managed. The grand vision of Frontiers is a world where all people have an equal opportunity to seek, share and generate knowledge. Frontiers provides immediate and permanent online open access to all its publications, but this alone is not enough to realize our grand goals.

Frontiers Journal Series

The Frontiers Journal Series is a multi-tier and interdisciplinary set of open-access, online journals, promising a paradigm shift from the current review, selection and dissemination processes in academic publishing. All Frontiers journals are driven by researchers for researchers; therefore, they constitute a service to the scholarly community. At the same time, the Frontiers Journal Series operates on a revolutionary invention, the tiered publishing system, initially addressing specific communities of scholars, and gradually climbing up to broader public understanding, thus serving the interests of the lay society, too.

Dedication to Quality

Each Frontiers article is a landmark of the highest quality, thanks to genuinely collaborative interactions between authors and review editors, who include some of the world's best academicians. Research must be certified by peers before entering a stream of knowledge that may eventually reach the public - and shape society; therefore, Frontiers only applies the most rigorous and unbiased reviews.
Frontiers revolutionizes research publishing by freely delivering the most outstanding research, evaluated with no bias from both the academic and social point of view. By applying the most advanced information technologies, Frontiers is catapulting scholarly publishing into a new generation.

What are Frontiers Research Topics?

Frontiers Research Topics are very popular trademarks of the Frontiers Journals Series: they are collections of at least ten articles, all centered on a particular subject. With their unique mix of varied contributions from Original Research to Review Articles, Frontiers Research Topics unify the most influential researchers, the latest key findings and historical advances in a hot research area! Find out more on how to host your own Frontiers Research Topic or contribute to one as an author by contacting the Frontiers Editorial Office: frontiersin.org/about/contact

ELECTROCHEMISTRY FOR MATERIALS SCIENCE: IN MEMORY OF KEN NOBE AND MORTON SCHWARTZ

Topic Editors:
Nosang Vincent Myung, University of Notre Dame, United States
Bongyoung Yoo, Hanyang University, South Korea
Peter Pintauro, Vanderbilt University, United States
Syed Mubeen Jawahar Hussaini, The University of Iowa, United States
Jae-Hong Lim, Gachon University, South Korea

Citation: Myung, N. V., Yoo, B., Pintauro, P., Hussaini, S. M. J., Lim, J.-H., eds. (2022). Electrochemistry for Materials Science: In Memory of Ken Nobe and Morton Schwartz. Lausanne: Frontiers Media SA.
doi: 10.3389/978-2-88976-520-1

Table of Contents

frontiers
in Chemistry

ORIGINAL RESEARCH
published: 28 May 2021
doi: 10.3389/fchem.2021.681313

Humidity-Insensitive NO_2 Sensors Based on SnO_2/rGO Composites

Yingyi Wang[1,2], Lin Liu[2], Fuqin Sun[2,3], Tie Li[2,3], Ting Zhang[2,3]* and Sujie Qin[1]**

[1]Department of Health and Environmental Sciences, Xi'an Jiaotong-Liverpool University, Suzhou, China, [2]I-Lab, Key Laboratory of Multifunctional Nanomaterials and Smart Systems, Suzhou Institute of Nano-Tech and Nano-Bionics (SINANO), Chinese Academy of Sciences (CAS), Suzhou, China, [3]School of Nano-Tech and Nano-Bionics, University of Science and Technology of China, Hefei, China

This study reported a novel humidity-insensitive nitrogen dioxide (NO_2) gas sensor based on tin dioxide (SnO_2)/reduced graphene oxide (rGO) composites through the sol-gel method. The sensor demonstrated ppb-level NO_2 detection in p-type sensing behaviors (13.6% response to 750 ppb). Because of the synergistic effect on SnO_2/rGO p-n heterojunction, the sensing performance was greatly enhanced compared to that of bare rGO. The limit of detection of sensors was as low as 6.7 ppb under dry air. Moreover, benefited from the formed superhydrophobic structure of the SnO_2/rGO composites (contact angle: 149.0°), the humidity showed a negligible influence on the dynamic response (S_g) of the sensor to different concentration of NO_2 when increasing the relative humidity (RH) from 0 to 70% at 116°C. The relative conductivity of the sensor to 83% relative humidity was 0.11%. In addition, the response ratio (S_g/S_{RH}) between 750 ppb NO_2 and 83% RH was 649.0, indicating the negligible impaction of high-level ambient humidity on the sensor. The as-fabricated humidity-insensitive gas sensor can promise NO_2 detection in real-world applications such as safety alarm, chemical engineering, and so on.

Keywords: gas sensor, SnO_2/rGO composites, humidity-insensitive, low temperature, nitrogen dioxide (NO_2)

Edited by:
Jae-Hong Lim,
Gachon University, South Korea

Reviewed by:
Xingxing Gu,
Chongqing Technology and Business University, China
Yong-Ho Choa,
Hanyang University, South Korea

****Correspondence:***
Tie Li
Tli2014@sinano.ac.cn
Ting Zhang
Tzhang2009@sinano.ac.cn
Sujie Qin
Sujie.Qin@xjtlu.edu.cn

Specialty section:
This article was submitted to Nanoscience,
a section of the journal Frontiers in Chemistry

Received: *16 March 2021*
Accepted: *10 May 2021*
Published: *28 May 2021*

Citation:
Wang Y, Liu L, Sun F, Li T, Zhang T and Qin S (2021) Humidity-Insensitive NO_2 Sensors Based on SnO_2/rGO Composites.
Front. Chem. 9:681313.
doi: 10.3389/fchem.2021.681313

INTRODUCTION

Air pollution has become a pressing global issue facing the development of industry and technology. Nitrogen dioxide (NO_2), as one of the most toxic air pollutants, is generated from industries and vehicle emissions, which can cause some serious environmental issues such as haze, photochemical smog, and acid rain (Mallik and Lal, 2014). United Statess Occupational Safety and Health Administration (OSHA) reported that when the concentration of NO_2 is over 1 ppm, inhalation of NO_2 for 15 min will cause some respiratory diseases such as asthma (Cheng, et al., 2019; Yuvaraja, et al., 2020). In the urban atmosphere, the concentration of NO_2 commonly measured in the range from 20 to 100 ppb (Brunet, et al., 2008). Therefore, a NO_2 sensor, which is sensitive enough to detect at least 20 ppb or ultralow concentration of NO_2 (ppb level), is urgently demanded.

Up to now, metal oxide semiconductors-based NO_2 sensors have been used in many applications owing to high chemical stability and low cost of sensing materials such as CuO (Bo, et al., 2020; Wang Y, et al., 2020), ZnO (Wang J, et al., 2019; Choi, et al., 2020), WO_3 (Liu, et al., 2020; Wang M, et al., 2020), NiO (Wei, et al., 2019; Wilson, et al., 2020), and SnO_2 (Kamble, et al., 2017; Zhong, et al., 2019). Among them, SnO_2 is a typical n-type wide bandgap semiconductor (3.6 eV) that has been regarded as one of the most promising industrialized candidates for NO_2 sensing due to its attractive characteristics, including controlled size, low limits of detection, and facile large-scale fabrication (Maeng, et al., 2014; Lee, et al., 2015). However, there are several shortcomings of pure SnO_2-based sensors that limit their practical applications. Firstly, aggregation occurs when the size is too small during the material synthesis and the sensor fabrication processes, which decreases the surface-specific area, reduces the sensitivity of gas sensors and influences the long-term stability of the as-fabricated sensor (Li, et al., 2015; Wu, et al., 2020). Meanwhile, the SnO_2-based gas sensor generally needs a high operation temperature (>200°C) to achieve high sensitivity, which causes high power consumption (Van Hieu, 2010; Guo J, et al., 2016). Nowadays, combining SnO_2 with low-dimensional materials (e.g., MoS_2 (Qiao, et al., 2018), carbon nanotube (Minh Nguyet, et al., 2017), metal oxide (Park, et al., 2020), graphene (Hu, et al., 2020), etc.) to form p-n heterojunction has been regarded as the prospective strategies to overcome the shortcomings of pure SnO_2-based gas sensors (Yin, et al., 2014; Gui, et al., 2018). Among low-dimensional materials, owing to the low-cost, ultrahigh specific surface area, controllable bandgap and various oxygen-containing functional group (e.g., C-O, O-C=O, and O-C(O)-O), rGO is an ideal material to obtain high-performance gas sensor by decorating with metal oxides (Guo, et al., 2019; Yin, et al., 2020). Hence, constructing p-n heterojunction between rGO and SnO_2 is a potential approach to enhance the sensing performance of sensors through modulating the carrier transportation due to different working functions (Neri, et al., 2013; Choi, et al., 2014; Kim, et al., 2018). For example, Zhu, et al. (2017) reported a NO_2 gas sensor based on rGO/SnO_2 nanocomposites, and the sensing response of sensors increased three times compared with that of sensors based on pure rGO. Meanwhile, Kim, et al. (2017) fabricated graphene-SnO_2 nanocomposites (SnO_2-G)-based sensors, and the sensing response of SnO_2-G-based sensors toward 1 ppm NO_2 is 24.7, which is around two folds higher than that of SnO_2-based sensors. Similarly, Lin, et al. (2020) prepared Co_3O_4/N-doped rGO (N-rGO) nanocomposites-based ethanol sensors. The sensing response value of Co_3O_4/N-rGO-based sensors to 100 ppm ethanol at 200°C is around 20 folds higher than that of N-rGO-based sensors.

Although heterojunction enhances the gas sensing performance, the high-level nonconstant humidity will severely impact the sensing performances of these reported NO_2 sensors, which is difficult to distinguish the target gas from ambient humidity and hinder the applications in the real world. For example, Wang, et al. (2018) fabricated Pd-SnO_2-RGO-based NO_2 sensors and showed 76% sensing response to 1 ppm NO_2 gas. However, when the sensor exposed to NO_2 gas with 80% RH, the sensing response declined by 20%. The limit of detection of Pd-SnO_2-RGO-based NO_2 sensors is 50 ppb under dry air. Similarly, Guo, et al. (2019) reported Bi@rGO/SnO_2-based benzene sensors. The sensing response to 5 ppm benzene with 60% RH is three times lower than that without humidity. Degler, et al. (2018) found that the gas sensing response cannot be controlled by doping different noble metal content (Pt) on SnO_2. To date, there are some strategies have been developed to address this issue, including the construction of gas preconcentration techniques and dehumidification techniques (Groves and Zellers, 2001; Peng, et al., 2008). However, these methods are costly, complex, and sacrifice the sensor's sensitivity (Konvalina and Haick, 2012).

To solve these problems, we proposed the humidity-insensitive NO_2 sensors based on SnO_2/rGO p-n heterojunction, which was used to detect NO_2 at low temperatures (as low as 116°C). The sensing performance of SnO_2/rGO composite-based NO_2 sensors was studied, and the LOD was found to be as low as 6.7 ppb, which is below the standard of United States OSHA and NO_2 pollutant concentration in the urban atmosphere. Notably, the NO_2 sensor showed a reliable sensing response under increasing relative humidity conditions (3–70% RH), and the resistance of the sensor almost kept constant under 83% RH, promising real-world applications.

MATERIALS AND METHODS

Materials and Synthesis of Composites

Natural graphite flake (325 meshes, 99.8%) was purchased from Sigma Aldrich; H_2SO_4 (AR) and $KMnO_4$ (AR) was purchased from Shanghai Hushi Laboratorial Equipment Co., Ltd.; $SnCl_4.5H_2O$ (AR) was purchased from Macklin; Epichlorohydrin (PPD) (Analytical reagent) and N, N-Dimethylformamide (DMF) (97%) were purchased from Aladdin. These reagents were used without any further purification. The micro-hotplates were purchased from Leanstar-Tech Co., Ltd. The SnO_2/rGO composite was prepared through a sol-gel method. Briefly, the GO was synthesized from nature graphite powder based on modified Hummer's method. Secondly, the $SnCl_4{\cdot}5H_2O$ and epichlorohydrin (PPD) were slowly added into the GO/DMF solution and stirred for a short time. The SnO_2/rGO composite was formed after three days of solution exchange and dried by supercritical CO_2 to carbonize at 600°C for 2 h under the Ar atmosphere. The synthesized sensing material was suspended in a dimethylformamide solution (DMF) solution. The SnO_2/rGO composite was drop-coated onto the micro-hotplate to fabricate gas sensors. After that, sensors were annealed at 200°C for 20 min under Ar atmosphere protection to reduce the contacting barrier.

Characterization of Composites and Microstructures

The morphology and crystal structure of SnO_2/rGO composites were analyzed by scanning electron microscopy (SEM, Hitachi-s4800), transmission electron microscopy (TEM, Tecnai G2 F20 S-Twin). The chemical composite of materials was carried out by energy dispersive spectrometry (EDS, FEI, Quanta FEG 250). The crystal lattice was analyzed by X-ray Diffraction (XRD, Bruker AXS, D8 Advance). The degree of reduction of rGO was characterized by Raman spectroscopy (Raman, Horriba-JY, LABRAM HR).

Measurements Sensing Performance of NO_2 Sensors

The gas sensing performance under dry air (~3% RH) was investigated by a designed testing system based on previous work (Liu, et al., 2019). In general, firstly, the sensor chip was

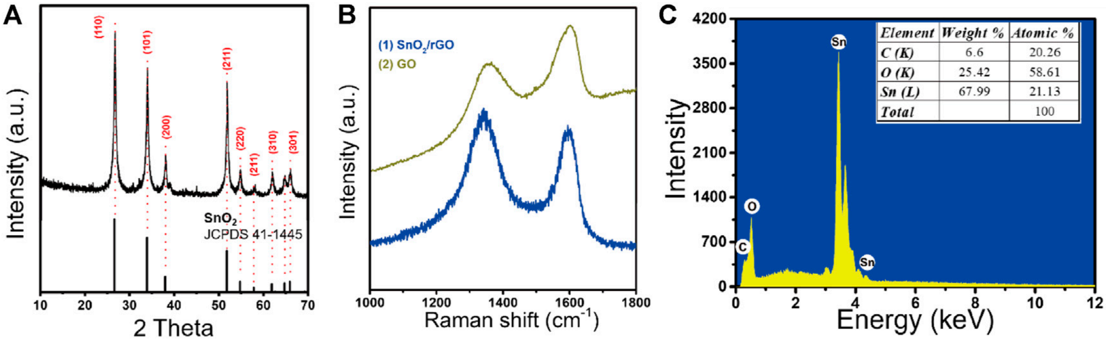

Element	*Weight %*	*Atomic %*
C (K)	6.6	20.26
O (K)	25.42	58.61
Sn (L)	67.99	21.13
Total		100

FIGURE 1 | (A) The XRD patterns of SnO_2/rGO composites; **(B)** the Raman spectra of SnO_2/rGO composites and GO; **(C)** the EDS analysis of SnO_2/rGO composites.

connected in series with a loaded resistor, which was selected to close to sensor resistance to optimize the resolution obtained from measurements. Secondly, the specific concentration of NO_2, which was implemented by dry air (80% N_2 and 20% O_2) and controlled by mass flow controllers (MFCs, Sevenstar CS200, China), goes through a quartz chamber (volume: 1 cm^3, 200 sccm). Finally, sensor resistance was determined by the Fieldpoint analog input and output modules by continuously controlling and monitoring the voltage of the circuit (National Instruments, Austin, TX). The loaded resistor calculated by Ohm's law was recorded in a custom LabView computer program (**Supplementary Figure S1**).

Measurements Sensing Performance of NO_2 Sensors Under Humidity

Dynamic conductivity response to high humidity conditions (83% RH) was tested by the KNO_3 saturated saline solution, added to a humidity controller (**Supplementary Figure S1**). Saturated saline solutions produce various saturated vapor pressures and form different relative humidity (Greenspan, 1977). One commercial high-precision temperature/humidity sensor (Sensirion Company, SHT75) was used as the reference sensor to detect real-time humidity. The static relative response to various concentrations of NO_2 under 70% RH was tested in the homemade testing chamber (20 L) (**Supplementary Figure S2**). The specific high concentration of NO_2 gas was injected into the testing chamber and diluted by the air in the testing chamber. The air humidity (~70% RH) of the day is recorded as the ambient humidity.

RESULTS AND DISCUSSION

Material Characterizations

The crystal structure of SnO_2/rGO composites was examined by XRD, as shown in **Figure 1A**. The positions of characteristic peaks are located at $2\theta = 26.61°$, 33.89°, 37.95°, 51.78°, 54.76°, 64.72°, and 65.94°, which are, respectively, collaborated with (110), (101), (200), (211), (220), (310), and (301) planes of tetragonal rutile SnO_2 (JCPDS. 41–1,445). Compared with the reported XRD patterns of pristine rGO at $2\theta = 24.7°$ and 42.8° (Wang Z, et al., 2019), SnO_2/rGO composites do not show a peak assigned to rGO. The high density of SnO_2 nanoparticles is uniformly decorated on the surface of the rGO, which can prevent the reassembled behavior of SnO_2 and cover its XRD pattern information (Zhang, et al., 2014). Moreover, the Raman spectroscopy was employed to further study the reduced structure of the rGO in SnO_2/rGO composites (**Figure 1B**). The peaks located at around 1,341 and 1,594 cm^{-1} are assigned to the typical D band and G band of rGO, respectively, (Guo D, et al., 2016). The intensity ratio of D peak to G peak (I_D/I_G) of SnO_2/rGO (1.12) is higher than that of GO (0.81), which indicates that the oxygen functional groups (e.g., C-O, O-C=O, and O-C(O)-O) have been removed and induced defects during the synthesis process (Tuan, et al., 2018; Hu, et al., 2017; Xu, et al., 2019). The EDS analysis (**Figure 1C**) shows that the product contained C, O, Sn elements. The atomic ratios of Sn, O, and C are 21.13, 58.61, and 20.26%, respectively. These results indicate that no other impurities and crystals were mixed in the reaction product.

The morphology of SnO_2/rGO composites was characterized via the SEM and TEM techniques and displayed in **Figure 2**. It can be seen from **Figure 2A,B** that the SnO_2 nanoparticles (NPs) are uniformly and densely anchored on the surfaces of the rGO nanosheets without any agglomeration. The low-resolution TEM images in **Figure 2C** show the size distribution of the SnO_2 NPs in the composites, around 5.5 nm with normal distribution from 4.5 to 6.5 nm (**Figure 2C**, inset). Moreover, the high-resolution TEM (HRTEM) image of SnO_2/rGO in **Figure 2D** shows that the SnO_2 NPs are highly crystallized with a crystalline interplanar spacing of ~0.335 nm, which is attributed to the (110) crystal plane.

Gas Sensing Performances

The gas sensing performance of the SnO_2/rGO composite-based sensors was tested. The relative responses of the sensors were defined as the relative changes of resistance in the air and those in target gases: $S_g = (|R_g-R_a|/R_a)*100\%$ for oxidizing gas or $S_g = (|R_a-R_g|/R_a)*100\%$ for reducing gas (where R_a is the sensor resistance in air and R_g is the sensor resistance in target gas). **Figure 3A** shows the response of these sensors to 1.5 ppm of

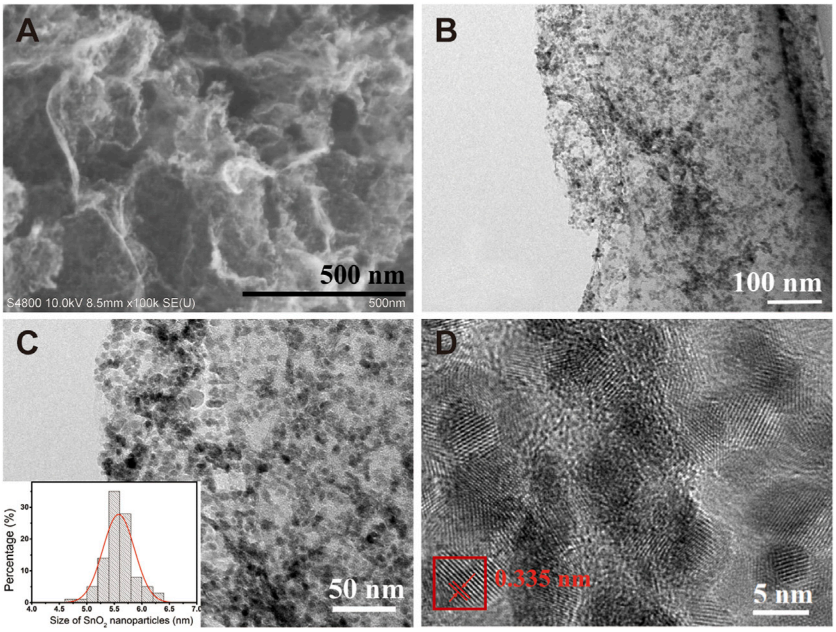

FIGURE 2 | (A) Typical SEM images of SnO_2/rGO composites; **(B, C)** Low magnification TEM images of SnO_2/rGO composites, (c, inset) SnO_2 NPs size distribution histogram; **(D)** the HRTEM image and corresponding crystalline interplanar of SnO_2/rGO composites.

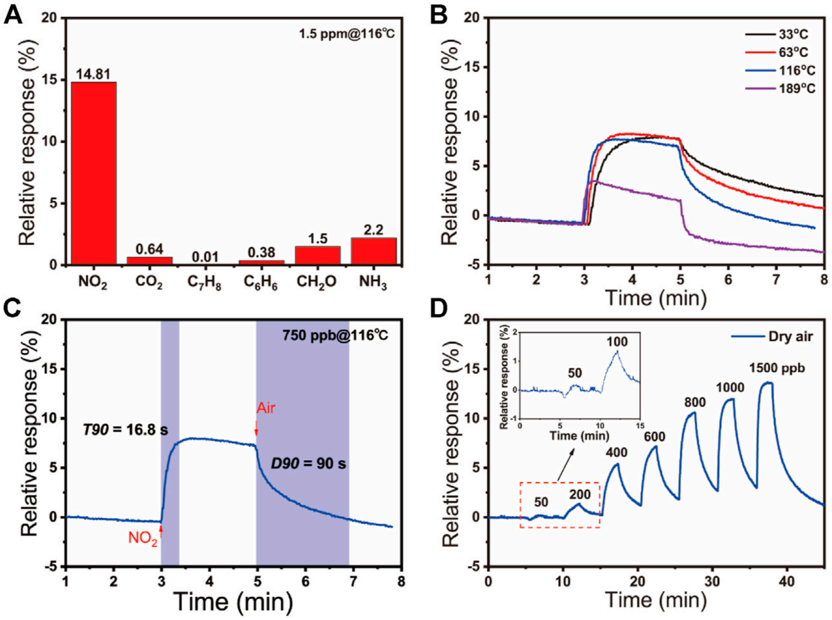

FIGURE 3 | (A) The relative responses of SnO_2/rGO composite-based sensors to different gases (NO_2, CO_2, C_7H_8, C_6H_6, CH_2O, and NH_3) at 116°C; **(B)** The response curves to 750 ppb NO_2 at the increasing operating temperature of 33, 63, 116, 189°C; **(C)** The response curve to 750 ppb NO_2 of sensors based on SnO_2/rGO composites at 116°C; **(D)** The relative responses to different concentrations of NO_2 (50–1500 ppb) under dry air.

various gases at 116°C, including ammonia (NH_3), methanal (CH_2O), benzene (C_6H_6), toluene (C_7H_8), carbon dioxide (CO_2), and NO_2. The result reveals that the as-prepared SnO_2/rGO composite has high selectivity to NO_2 compared with other gases. It attributed to the relatively high adsorption energy of NO_2 on sensing materials among these gases (Huang, et al., 2008; Schröder, 2013; Lazar, et al., 2013; Chakradhar, et al., 2016; Zhu, et al., 2021), indicating its high selectivity to NO_2 (**Supplementary Table S1**). To determine the optimized operating temperature, **Figure 3B** and **Supplementary Table S1**

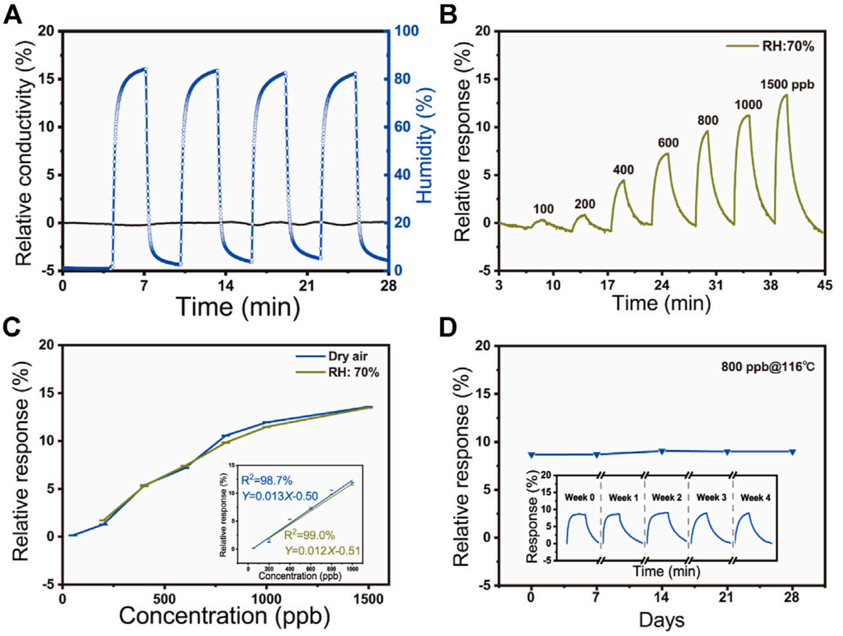

FIGURE 4 | (A) The relative response of sensors in high humidity in four cycles (83% RH); **(B)** The relative response to different concentrations of NO_2 (50–1500 ppb) under 70% RH environment at 116°C; **(C)** The relative response of the various NO_2 concentration to ambient humidity at 116°C; (c. inset) The linear fit between the concentration of NO_2 and dynamic response under dry air (blue) and 70% RH (green) at 116°C; **(D)** Long time stability of SnO_2/rGO composite-based sensors to 800 ppb NO_2 at room temperature for about 28 days; (d. inset) The repeatability of sensors to 800 ppb NO_2 during the five testing cycles at 116°C.

show the response plots of SnO_2/rGO composite-based NO_2 sensors toward 750 ppb NO_2 at the serial operation temperature from 33 to 189°C. The relative response of sensors at low temperature (e.g., 33, 63, and 116°C) have slight difference (7.80% at 33°C, 8.29% at 63°C, and 7.57% at 116°C) and then it dramatically decreased by further increasing the operation temperature (3.51% at 189°C). However, the response time (T90) and recovery time (D90) dramatically decrease along with the operating temperature increase. The T90 and D90 are, respectively, defined as the time required for a sensor to reach 90% of the stable resistance value when the test gas is turned on and off. As **Figure 3C** shows, the fast T90 (7 s) and D90 (31 s) of NO_2 sensors to 750 ppb NO_2 are obtained when the operating temperature was elevating to 189°C. Decreasing the operating temperature to 116°C, the T90 and D90 of NO_2 sensors increase to 17 and 90 s, respectively, (**Figure 3C**; **Supplementary Figure S3**). When the devices worked at 63 and 33°C, the T90 and D90 have been further increased (**Supplementary Figure S4**; **Supplementary Table S2**). Because of the similar and relatively high response value at 33, 63, and 116°C, SnO_2/rGO composite-based sensors are regarded as the candidate to work at room temperature. The temperature can affect the adsorption/desorption process on the sensing materials and sensor surface. The rate of adsorption/desorption increases as the temperature rose, resulting in a shorter T90 and D90 (Walker, et al., 2019). However, when the temperature arrives too high, the quantity and properties of active sites on the surface of sensing materials have been changed (Neri, et al., 2013), which causes the adsorbed oxygen species and NO_2 cannot remain on the surface of sensing materials to undergo a reaction (Jinkawa, et al., 2000), resulting in a low sensing response and the drifting of baseline were observed correspondently. Therefore, taking the T90, D90, and the relative response of NO_2 sensors into consideration, the optimal operating temperature was chosen to be 116°C. **Figure 3D** demonstrates the dynamic response of sensors to various NO_2 concentrations at dry air from 50 to 1,500 ppb, indicating a broad response range. Contrastively, the sensing performances of pure rGO to 4 ppm were dramatically declined (**Supplementary Figure S5**), which attracted the electrons from rGO to SnO_2 and enhanced sensing performance by SnO_2/rGO composite-based NO_2 sensors.

The dynamic responses of SnO_2/rGO composite-based NO_2 sensors toward high humidity (around 83% RH) have been measured (**Figure 4A**). It can be seen that the relative conductivity of NO_2 sensors shows extremely weak fluctuation (~0.11%). Compared with other works and the commercial bare NO_2 sensor (MEMS NO_2 sensor, GM-102B, Zhenzhou Winsen Electronics Technology Co., Ltd.) summarized in **Supplementary Table S3**, as-fabricated SnO_2/rGO composite-based NO_2 sensors showed an extremely high response ratio (S_g/S_{RH} = 649.0) between 750 ppb NO_2 and 83% RH, which indicates that the high-level ambient humidity shows negligible impaction on the NO_2 sensor. Moreover, the static sensing performance of the sensor to different concentrations of NO_2 (from 200 to 1,500 ppb) under the real-world environment (70% RH) was estimated (**Figure 4B**). Compared with the above-obtained results under dry air, as **Figure 4C** showed, the two curves have similar trends and the effect of humidity on the sensor can be neglected. The

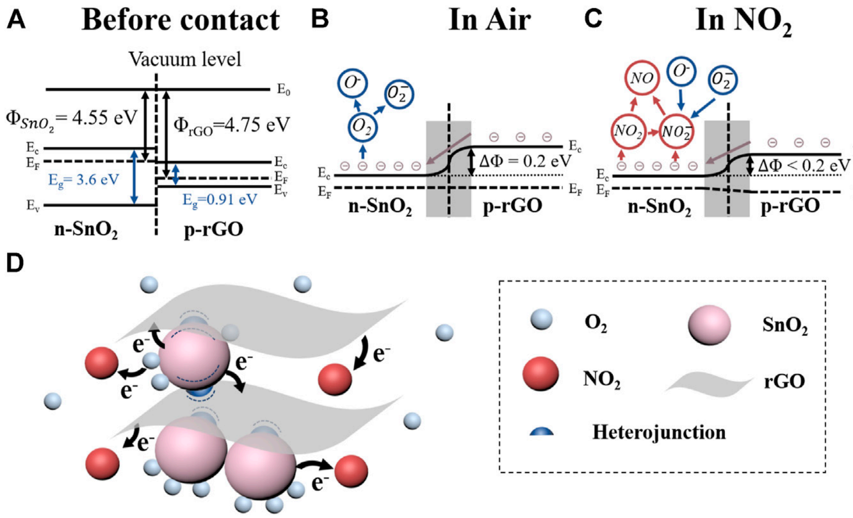

FIGURE 5 | (A) Schematic bandgap structure of n-type SnO_2 and p-type rGO; **(B)** Schematic bandgap structure of SnO_2/rGO heterojunction in air and **(C)** in NO_2; **(D)** Schematic of sensing mechanisms of SnO_2/rGO composite-based sensors with exposure to NO_2.

humidity-insensitive property of high-performance NO_2 sensors attributes to the formed superhydrophobic structure of SnO_2/rGO composites, which the exhibited contact angle is 149.0° (**Supplementary Figure S6**). Two main factors determine the superhydrophobicity of a material surface: surface roughness and surface energy. In general, a rough surface with low surface energy leads to a hydrophobic surface (Lin, et al., 2011; Chen and Dong, 2013). The as-fabricated SnO_2/rGO composites by this sol-gel method have high porosity and high surface roughness (Lin, et al., 2011). Meanwhile, the high anneal temperature (600°C) during carbonized process vastly decreases the hydrophilic oxygen-containing function groups on the rGO surface (e.g., C-O, O-C=O, and O-C(O)-O), which can decrease the surface energy of SnO_2/rGO composites and form a superhydrophobic surface (Wu, et al., 2018; Xu, et al., 2019; Cao, et al., 2019). The performance of humidity insensitivity of the NO_2 sensor may be weakened by working temperature (116°C) in some extent. However, the superhydrophobic structure of nanocomposites plays a vital role in the humidity insensitivity of the NO_2 sensor (Phan and Chung, 2015; Wu, et al., 2018).

The relative response of the sensor increased along with the increase of the concentration of the NO_2 whatever under humid air or not (50–1,500 ppb under dry air and 200–1,500 ppb under 70% RH) (**Figure 4C**). Meanwhile, it can be observed that the relative response exhibits a rapidly increasing linear trend under the low concentration of 1,000 ppb, indicating that SnO_2/rGO composite-based sensors have an excellent sensing performance for the detection of low-concentration NO_2. The observed slope differences between the low concentration (below 1,000 ppb) and the high concentration (1,500 ppb) could be attributed to the degradation of electron transfer and saturation phenomenon of the SnO_2/rGO composites under high NO_2 concentration. The linear fit of the gas response of the sensor to the various concentration of NO_2 can be represented by relative response = b Concentration + a. The inset of **Figure 4C** indicates that the SnO_2/rGO composite-based NO_2 sensors have a linear correlation (R^2 > 98%). According to linear fit results, the theoretical limit of detection (LOD) of NO_2 under 0 and 70% RH are calculated as 6.7 and 25 ppb based on **Eq. 1**, respectively, (Mateos, et al., 2019; Song, et al., 2016). Both LODs are below the threshold concentration for causing diseases and the NO_2 pollutant concentration in the urban atmosphere.

$$LOD = 3 \times \frac{RMS_{noise}}{Slope} \tag{1}$$

RMS_{noise} is the standard deviation of the noise level. Under dry air, the RMS_{noise} (0.029) was obtained from 150 baseline data points before exposure to NO_2 from **Figure 3D**. Thus, according to **Figure 5A** (inset), the LOD was around 6.7 ppb. Under 70% RH, the RMS_{noise} (0.10) was obtained from 150 data. And the calculated LOD was about 25 ppb. **Figure 4D** illustrated the long-time stability of SnO_2/rGO composite-based sensors to 800 ppb NO_2 at room temperature for 28 days. The response is maintained between 8 and 9% and the standard deviation of NO_2 sensors is 0.19, which indicated its good stability of sensitivity. However, the T90 and D10 varies as a function of deterioration of time which implies the sensor (**Figure 4D** inset).

Sensing Mechanism

The sensing performance of SnO_2/rGO composite-based sensors to NO_2 shows a p-type sensing behavior indicating that the rGO dominates the conduction channel of NO_2 sensors. In the vacuum state, the working functions of SnO_2 ($\Phi_{(SnO2)}$) and rGO ($\Phi_{(rGO)}$) are 4.55 and 4.75 eV, respectively, (Kim, et al., 2016) (**Figure 5A**). As **Figure 5B** showed, after connection, the electrons will be transferred from SnO_2 to rGO at the hetero-interface to balance the Fermi level (E_f). Because of the charge transfer, it will form a depletion layer and heterojunction potential barrier ($\Delta\Phi_{hetero}$ = 0.2 eV). In the air, oxygen molecules will adsorb on the surface of SnO_2/rGO composites and withdraw electrons from SnO_2 to form O_2^- and O^-. Since the diameter of SnO_2 nanoparticles is comparable or less than two times the Debye length (λ_D ~6 nm) of the SnO_2 in the air, the SnO_2 nanoparticles will almost fully deplete after adsorption of oxygen molecules (Xu, et al., 1991) (**Figure 5B**). Once exposed to NO_2, owing to the high electron affinity of NO_2 molecules, the NO_2 molecules will further withdraw the electrons from oxygen ions and SnO_2/rGO composites, as shown in **Eqs. 2–5** and **Figure 5C**.

$$NO_2 + e^- \rightarrow NO_2^- \quad (2)$$

$$NO_2 + e^- \rightarrow NO + O^- \quad (3)$$

$$2NO_2 + O_2^- + e^- \rightarrow 2NO_2^- + O_2 \quad (4)$$

$$NO_2^- + O^- + 2e^- \rightarrow NO + 2O^{2-} \quad (5)$$

The Fermi level of SnO_2 will shift far away from the conduction band leading to the reduction of the $\Delta\Phi_{hetero}$. Meanwhile, the hole accumulation layer will form at the surface of rGO in the air and forma homojunction potential barrier ($\Delta\Phi_{homo}$). When exposing to NO_2, the NO_2 molecules can directly adsorb on the surface of rGO and withdraw the electrons from rGO, which leads to an increasing in the hole concentration and reduction of the $\Delta\Phi_{homo}$ (Miller, et al., 2014). As the resistance of sensors based on heterogeneous materials is exponential with the changing of the effective potential barrier ($\Delta\Phi$, including $\Delta\Phi_{hetero}$ and $\Delta\Phi_{homo}$, according to **Eq. 6** (Feng, et al., 2017; Hua, et al., 2017). Thus, due to the synergistic effect of the $\Delta\Phi_{hetero}$ and $\Delta\Phi_{homo}$, the sensing performance of SnO_2/rGO composites is greatly improved compared with bare rGO (**Supplementary Figure S3**).

$$R = R_0 \exp\left(\frac{\Delta\Phi}{k_b T}\right) \quad (6)$$

where R_0 is constant, k_b is Boltzmann's constant, T is the absolute temperature, and $\Delta\Phi$ is the effective potential barrier (including homojunction barrier and heterojunction barrier).

CONCLUSION

In summary, this work demonstrated the simple sol-gel method to decorate rGO nanosheet with SnO_2 NPs to improve NO_2 detection. Due to the synergistic effect of SnO_2/rGO p-n heterojunction and rGO/rGO homojunction, the sensing performance of SnO_2/rGO composites was greatly enhanced compared with that of bare rGO. A low LOD of 6.7 ppb was obtained at 116°C under dry air. Compared with the reported humidity-insensitive NO_2 sensors, the designed SnO_2/rGO composite-based NO_2 sensor showed an extremely high response ratio (649.0) between 750 ppb NO_2 and 83% RH. The superhydrophobic property of the fabricated SnO_2/rGO composites contributes to the humidity insensitivity. The superhydrophobic property is caused by the high roughness and low surface energy of the SnO_2/rGO composites. It is promised to use the SnO_2/rGO composite-based NO_2 sensors in real-world applications.

DATA AVAILABILITY STATEMENT

The original contributions presented in the study are included in the article/**Supplementary Material**, further inquiries can be directed to the corresponding authors.

AUTHOR CONTRIBUTIONS

YW and LL contributed equally to this work.

All authors listed have made a substantial, direct, and intellectual contribution to the work and approved it for publication.

FUNDING

The authors acknowledge the funding support from the National Key R&D Program of China (2017YFA0701101, 2020YFB2008501), the National Natural Science Foundation of China (51702354, 62071462), the Youth Promotion Association of Chinese Academy of Sciences (2020320), the Foundation Research Project of Jiangsu Province (BK20201195), and the Suzhou Key Industrial Technology Innovation Project (SYG202029).

SUPPLEMENTARY MATERIAL

The Supplementary Material for this article can be found online at: https://www.frontiersin.org/articles/10.3389/fchem.2021.681313/full#supplementary-material

REFERENCES

Bo, Z., Wei, X., Guo, X., Yang, H., Mao, S., Yan, J., et al. (2020). SnO_2 Nanoparticles Incorporated CuO Nanopetals on Graphene for High-Performance Room-Temperature NO_2 Sensor. *Chemical Physics Letters*. 750, 137485. doi:10.1016/j.cplett.2020.137485

Brunet, J., Garcia, V. P., Pauly, A., Varenne, C., and Lauron, B. (2008). An Optimised Gas Sensor Microsystem for Accurate and Real-Time Measurement of Nitrogen Dioxide at Ppb Level. *Sensors Actuators B: Chem.* 134, 632–639. doi:10.1016/j.snb.2008.06.010

Cao, Y., Zhao, Y., Wang, Y., Zhang, Y., Wen, J., Zhao, Z., et al. (2019). Reduction Degree Regulated Room-Temperature Terahertz Direct Detection Based on Fully Suspended and Low-Temperature Thermally Reduced Graphene Oxides. *Carbon* 144, 193–201. doi:10.1016/j.carbon.2018.12.023

Chakradhar, A., Sivapragasam, N., Nayakasinghe, M. T., and Burghaus, U. (2016). Adsorption Kinetics of Benzene on Graphene: An Ultrahigh Vacuum Study. *J. Vacuum Sci. Techn. A: Vacuum, Surf. Films.* 34, 021402. doi:10.1116/1.4936337

Chen, Z., Dong, L., Yang, D., and Lu, H. (2013). Yang D and Lu HSuperhydrophobic Graphene-Based Materials: Surface Construction and Functional Applications. *Adv. Mater.* 25, 5352–5359. doi:10.1002/adma.201302804

Cheng, M., Wu, Z., Liu, G., Zhao, L., Gao, Y., Zhang, B., et al. (2019). Highly Sensitive Sensors Based on quasi-2D rGO/SnS2 Hybrid for Rapid Detection of NO2 Gas. *Sensors Actuators B: Chem.* 291, 216–225. doi:10.1016/j.snb.2019.04.074

Choi, H., Kwon, S., Lee, W., Im, K., Kim, T., Noh, B., et al. (2020). Ultraviolet Photoactivated Room Temperature NO_2 Gas Sensor of ZnO Hemitubes and Nanotubes Covered with TiO_2 Nanoparticles. *Nanomater.* 10, 462. doi:10.3390/nano10030462

Choi, S.-W., Katoch, A., Kim, J.-H., and Kim, S. S. (2014). Prominent Reducing Gas-Sensing Performances of N-SnO2 Nanowires by Local Creation of P-N Heterojunctions by Functionalization with P-Cr2O3 Nanoparticles. *ACS Appl. Mater. Inter.* 6, 17723–17729. doi:10.1021/am504164j

Degler, D., Müller, S. A., Doronkin, D. E., Wang, D., Grunwaldt, J.-D., Weimar, U., et al. (2018). Platinum Loaded Tin Dioxide: A Model System for Unravelling the Interplay between Heterogeneous Catalysis and Gas Sensing. *J. Mater. Chem. A.* 6, 2034–2046. doi:10.1039/C7TA08781K

Feng, Q., Li, X., and Wang, J. (2017). Percolation Effect of Reduced Graphene Oxide (rGO) on Ammonia Sensing of rGO-SnO2 Composite Based Sensor. *Sensors Actuators B: Chem.* 243, 1115–1126. doi:10.1016/j.snb.2016.12.075

Greenspan, L. (1977). Humidity Fixed Points of Binary Saturated Aqueous Solutions. *J. Res. Natl. Bur. Stan. Sect. A.* 81A, 89. doi:10.6028/jres.081A.011

Groves, W., and Zellers, E. (2001). Analysis of Solvent Vapors in Breath and Ambient Air with a Surface Acoustic Wave Sensor Array. *Ann. Occup. Hyg.* 45, 609–623. doi:10.1093/annhyg/45.8.60910.1016/s0003-4878(01)00020-5

Gui, Y.-h., Wang, H.-y., Tian, K., Yang, L.-l., Guo, H.-s., Zhang, H.-z., et al. (2018). Enhanced Gas Sensing Properties to NO2 of SnO2/rGO Nanocomposites Synthesized by Microwave-Assisted Gas-Liquid Interfacial Method. *Ceramics Int.* 44, 4900–4907. doi:10.1016/j.ceramint.2017.12.080

Guo, D., Cai, P., Sun, J., He, W., Wu, X., Zhang, T., et al. (2016). Reduced-graphene-oxide/metal-oxide P-N Heterojunction Aerogels as Efficient 3d Sensing Frameworks for Phenol Detection. *Carbon* 99, 571–578. doi:10.1016/j.carbon.2015.12.074

Guo, J., Zhang, J., Gong, H., Ju, D., and Cao, B. (2016). Au Nanoparticle-Functionalized 3D SnO2 Microstructures for High Performance Gas Sensor. *Sensors Actuators B: Chem.* 226, 266–272. doi:10.1016/j.snb.2015.11.140

Guo, W., Zhou, Q., Zhang, J., Fu, M., Radacsi, N., and Li, Y. (2019). Hydrothermal Synthesis of Bi-doped SnO2/rGO Nanocomposites and the Enhanced Gas Sensing Performance to Benzene. *Sensors Actuators B: Chem.* 299, 126959. doi:10.1016/j.snb.2019.126959

Hu, J., Chen, M., Rong, Q., Zhang, Y., Wang, H., Zhang, D., et al. (2020). Formaldehyde Sensing Performance of Reduced Graphene Oxide-Wrapped Hollow SnO2 Nanospheres Composites. *Sensors Actuators B: Chem.* 307, 127584. doi:10.1016/j.snb.2019.127584

Hu, R., Zhao, J., and Zheng, J. (2017). Synthesis of SnO 2/rGO Hybrid Materials by Sol-Gel/thermal Reduction Method and its Application in Electrochemical Capacitors. *Mater. Lett.* 197, 59–62. doi:10.1016/j.matlet.2017.03.082

Hua, Z., Qiu, Z., Li, Y., Zeng, Y., Wu, Y., Tian, X., et al. (2017). A Theoretical Investigation of the Power-Law Response of Metal Oxide Semiconductor Gas Sensors II: Size and Shape Effects. Sensors & Actuators B:. *Chemical* 255, 3541–3549. doi:10.1016/j.snb.2017.09.189

Huang, B., Li, Z., Liu, Z., Zhou, G., Hao, S., Wu, J., et al. (2008). Adsorption of Gas Molecules on Graphene Nanoribbons and its Implication for Nanoscale Molecule Sensor. *J. Phys. Chem. C* 112, 13442–13446. doi:10.1021/jp8021024

Jinkawa, T., Sakai, G., Tamaki, J., Miura, N., and Yamazoe, N. (2000). Relationship between Ethanol Gas Sensitivity and Surface Catalytic Property of Tin Oxide Sensors Modified with Acidic or Basic Oxides. *J. Mol. Catal. A: Chem.* 155, 193–200. doi:10.1016/S1381-1169(99)00334-9

Kamble, D. L., Harale, N. S., Patil, V. L., Patil, P. S., and Kadam, L. D. (2017). Characterization and NO2 Gas Sensing Properties of spray Pyrolyzed SnO2 Thin Films. *J. Anal. Appl. Pyrolysis* 127, 38–46. doi:10.1016/j.jaap.2017.09.004

Kim, H. W., Na, H. G., Kwon, Y. J., Kang, S. Y., Choi, M. S., Bang, J. H., et al. (2017). Microwave-Assisted Synthesis of Graphene-SnO2 Nanocomposites and Their Applications in Gas Sensors. *ACS Appl. Mater. Inter.* 9, 31667–31682. doi:10.1021/acsami.7b02533

Kim, J.-H., Lee, J.-H., Mirzaei, A., Kim, H. W., and Kim, S. S. (2018). SnO2 (N)-NiO (P) Composite Nanowebs: Gas Sensing Properties and Sensing Mechanisms. *Sensors Actuators B: Chem.* 258, 204–214. doi:10.1016/j.snb.2017.11.063

Kim, J. H., Katoch, A., Kim, H. W., and Sang, S. K. (2016). Realization of ppm-level co detection with an exceptionally high sensitivity using reduced graphene oxide-loaded SnO_2 nanofibers with the au functionalization. *Chem Commun.* 52, 3832. doi:10.1039/C5CC10482C

Konvalina, G., and Haick, H. (2012). Effect of Humidity on Nanoparticle-Based Chemiresistors: A Comparison between Synthetic and Real-World Samples. *ACS Appl. Mater. Inter.* 4, 317–325. doi:10.1021/am2013695

Lazar, P., Karlický, F., Jurečka, P., Kocman, M., Otyepková, E., Šafářová, K., et al. (2013). Adsorption of Small Organic Molecules on Graphene. *J. Am. Chem. Soc.* 135, 6372–6377. doi:10.1021/ja403162r

Lee, J.-H., Katoch, A., Choi, S.-W., Kim, J.-H., Kim, H. W., and Kim, S. S. (2015). Extraordinary Improvement of Gas-Sensing Performances in SnO2 Nanofibers Due to Creation of Local P-N Heterojunctions by Loading Reduced Graphene Oxide Nanosheets. *ACS Appl. Mater. Inter.* 7, 3101–3109. doi:10.1021/am5071656

Li, L., He, S., Liu, M., Zhang, C., and Chen, W. (2015). Three-Dimensional Mesoporous Graphene Aerogel-Supported SnO2 Nanocrystals for High-Performance NO2 Gas Sensing at Low Temperature. *Anal. Chem.* 87, 1638–1645. doi:10.1021/ac503234e

Lin, G., Wang, H., Lai, X., Yang, R., Zou, Y., Wan, J., et al. (2020). Co3O4/N-Doped RGO Nanocomposites Derived from MOFs and Their Highly Enhanced Gas Sensing Performance. *Sensors Actuators B: Chem.* 303, 127219. doi:10.1016/j.snb.2019.127219

Lin, Y., Ehlert, G. J., Bukowsky, C., and Sodano, H. A. (2011). Superhydrophobic Functionalized Graphene Aerogels. *ACS Appl. Mater. Inter.* 3, 2200–2203. doi:10.1021/am200527j

Liu, H., Xu, Y., Zhang, X., Zhao, W., Ming, A., and Wei, F. (2020). Enhanced NO2 Sensing Properties of Pt/WO3 Films Grown by Glancing Angle Deposition. *Ceramics Int.* 46, 21388–21394. doi:10.1016/j.ceramint.2020.05.236

Liu, L., Wang, Y., Dai, Y., Li, G., Wang, S., Li, T., et al. (2019). *In Situ* Growth of NiO@SnO2 Hierarchical Nanostructures for High Performance H2S Sensing. *ACS Appl. Mater. Inter.* 11, 44829–44836. doi:10.1021/acsami.9b13001

Maeng, S., Kim, S.-W., Lee, D.-H., Moon, S.-E., Kim, K.-C., and Maiti, A. (2014). SnO2 Nanoslab as NO2 Sensor: Identification of the NO2 Sensing Mechanism on a SnO2 Surface. *ACS Appl. Mater. Inter.* 6, 357–363. doi:10.1021/am404397f

Mallik, C., and Lal, S. (2014). Seasonal Characteristics of SO2, NO2, and CO Emissions in and Around the Indo-Gangetic Plain. *Environ. Monit. Assess.* 186, 1295–1310. doi:10.1007/s10661-013-3458-y

Mateos, M., Tchangaï, M.-D., Meunier-Prest, R., Heintz, O., Herbst, F., Suisse, J.-M., et al. (2019). Low Conductive Electrodeposited Poly(2,5-Dimethoxyaniline) as a Key Material in a Double Lateral Heterojunction, for Sub-ppm Ammonia Sensing in Humid Atmosphere. *ACS Sens.* 4, 740–747. doi:10.1021/acssensors.9b00109

Miller, D. R., Akbar, S. A., and Morris, P. A. (2014). Nanoscale Metal Oxide-Based Heterojunctions for Gas Sensing: A Review. *Sensors Actuators B: Chem.* 204, 250–272. doi:10.1016/j.snb.2014.07.074

Minh Nguyet, Q. T., Van Duy, N., Phuong, N. T., Trung, N. N., Hung, C. M., Hoa, N. D., et al. (2017). Superior Enhancement of NO2 Gas Response Using N-P-N Transition of Carbon nanotubes/SnO2 Nanowires Heterojunctions. *Sensors Actuators B: Chem.* 238, 1120–1127. doi:10.1016/j.snb.2016.07.143

Neri, G., Leonardi, S. G., Latino, M., Donato, N., Baek, S., Conte, D. E., et al. (2013). Sensing Behavior of SnO2/reduced Graphene Oxide Nanocomposites toward NO2. *Sensors Actuators B: Chem.* 179, 61–68. doi:10.1016/j.snb.2012.10.031

Park, K.-R., Cho, H.-B., Lee, J., Song, Y., Kim, W.-B., and Choa, Y.-H. (2020). Design of Highly Porous SnO2-CuO Nanotubes for Enhancing H2S Gas Sensor Performance. *Sensors Actuators B: Chem.* 302, 127179. doi:10.1016/j.snb.2019.127179

Peng, G., Trock, E., and Haick, H. (2008). Detecting Simulated Patterns of Lung Cancer Biomarkers by Random Network of Single-Walled Carbon Nanotubes Coated with Nonpolymeric Organic Materials. *Nano Lett.* 8, 3631–3635. doi:10.1021/nl801577u

Phan, D.-T., and Chung, G.-S. (2015). Effects of Rapid thermal Annealing on Humidity Sensor Based on Graphene Oxide Thin Films. *Sensors Actuators B: Chem.* 220, 1050–1055. doi:10.1016/j.snb.2015.06.055

Qiao, X.-Q., Zhang, Z.-W., Hou, D.-F., Li, D.-S., Liu, Y., Lan, Y.-Q., et al. (2018). Tunable MoS2/SnO2 P-N Heterojunctions for an Efficient Trimethylamine Gas Sensor and 4-Nitrophenol Reduction Catalyst. *ACS Sustainable Chem. Eng.* 6, 12375–12384. doi:10.1021/acssuschemeng.8b02842

Schröder, E. (2013). Methanol Adsorption on Graphene. *J. Nanomater.* 2013, 1–6. doi:10.1155/2013/871706

Song, Z., Wei, Z., Wang, B., Luo, Z., Xu, S., Zhang, W., et al. (2016). Sensitive Room-Temperature H2S Gas Sensors Employing SnO2 Quantum Wire/ Reduced Graphene Oxide Nanocomposites. *Chem. Mater.* 28, 1205–1212. doi:10.1021/acs.chemmater.5b04850

Tuan, P. V., Hieu, L. T., Ngoc, T. K., Hoang, C., Hoa, N. D., Hoa, T. T. Q., et al. (2018). Hydrothermal Synthesis, Structure, and Photocatalytic Properties of SnO_2/rgo Nanocomposites with Different Go Concentrations. *Materials Research Express* 5, 095506. doi:10.1088/2053-1591/aad6ca

Van Hieu, N. (2010). Comparative Study of Gas Sensor Performance of SnO_2 Nanowires and Their Hierarchical Nanostructures. Sensors and Actuators B: *Chemical* 150, 112–119. doi:10.1016/j.snb.2010.07.033

Walker, J. M., Akbar, S. A., and Morris, P. A. (2019). Synergistic Effects in Gas Sensing Semiconducting Oxide Nano-Heterostructures: A Review. *Sensors Actuators B: Chem.* 286, 624–640. doi:10.1016/j.snb.2019.01.049

Wang, J., Shen, Y., Li, X., Xia, Y., and Yang, C. (2019). Synergistic Effects of UV Activation and Surface Oxygen Vacancies on the Room-Temperature NO2 Gas Sensing Performance of ZnO Nanowires. *Sensors Actuators B: Chem.* 298, 126858. doi:10.1016/j.snb.2019.126858

Wang, Z., Jia, Z., Li, Q., Zhang, X., Sun, W., Sun, J., et al. (2019). The Enhanced NO2 Sensing Properties of SnO2 Nanoparticles/reduced Graphene Oxide Composite. *J. Colloid Interf. Sci.* 537, 228–237. doi:10.1016/j.jcis.2018.11.009

Wang, M., Wang, Y., Li, X., Ge, C., Hussain, S., Liu, G., et al. (2020). WO3 Porous Nanosheet Arrays with Enhanced Low Temperature NO2 Gas Sensing Performance. *Sensors Actuators B: Chem.* 316, 128050. doi:10.1016/j.snb.2020.128050

Wang, Y., Xue, J., Zhang, X., Si, J., Liu, Y., Ma, L., et al. (2020). Novel Intercalated CuO/black Phosphorus Nanocomposites: Fabrication, Characterization and NO_2 Gas Sensing at Room Temperature. *Mater. Sci. Semiconductor Process.* 110, 104961. doi:10.1016/j.mssp.2020.104961

Wang, Z., Han, T., Fei, T., Liu, S., and Zhang, T. (2018). Investigation of Microstructure Effect on NO2 Sensors Based on SnO2 Nanoparticles/ Reduced Graphene Oxide Hybrids. *ACS Appl. Mater. Inter.* 10, 41773–41783. doi:10.1021/acsami.8b15284

Wei, Z., Zhou, Q., Wang, J., Lu, Z., Xu, L., and Zeng, W. (2019). Hydrothermal Synthesis of SnO2 Nanoneedle-Anchored NiO Microsphere and its Gas Sensing Performances. *Nanomaterials* 9, 1015. doi:10.3390/nano9071015

Wilson, R. L., Simion, C. E., Stanoiu, A., Taylor, A., Guldin, S., Covington, J. A., et al. (2020). Humidity-tolerant Ultrathin Nio Gas-Sensing Films. *ACS Sens.* 5, 1389–1397. doi:10.1021/acssensors.0c00172

Wu, J., Li, Z., Xie, X., Tao, K., Liu, C., Khor, K. A., et al. (2018). 3D Superhydrophobic Reduced Graphene Oxide for Activated NO2 Sensing with Enhanced Immunity to Humidity. *J. Mater. Chem. A.* 6, 478–488. doi:10.1039/c7ta08775f

Wu, J., Wu, Z., Ding, H., Wei, Y., Huang, W., Yang, X., et al. (2020). Three-Dimensional Graphene Hydrogel Decorated with SnO2 for High-Performance NO2 Sensing with Enhanced Immunity to Humidity. *ACS Appl. Mater. Inter.* 12, 2634–2643. doi:10.1021/acsami.9b18098

Xu, C., Tamaki, J., Miura, N., and Yamazoe, N. (1991). Grain Size Effects on Gas Sensitivity of Porous SnO2-Based Elements. *Sensors Actuators B: Chem.* 3, 147–155. doi:10.1016/0925-4005(91)80207-z

Xu, D., Liu, J., Chen, P., Yu, Q., Wang, J., Yang, S., et al. (2019). *In Situ* growth and Pyrolysis Synthesis of Super-hydrophobic Graphene Aerogels Embedded with Ultrafine β-Co Nanocrystals for Microwave Absorption. *J. Mater. Chem. C* 7, 3869–3880. doi:10.1039/C9TC00294D

Yin, F., Li, Y., Yue, W., Gao, S., Zhang, C., and Chen, Z. (2020). Sn3O4/rGO Heterostructure as a Material for Formaldehyde Gas Sensor with a Wide Detecting Range and Low Operating Temperature. *Sensors Actuators B: Chem.* 312, 127954. doi:10.1016/j.snb.2020.127954

Yin, L., Chen, D., Cui, X., Ge, L., Yang, J., Yu, L., et al. (2014). Normal-pressure Microwave Rapid Synthesis of Hierarchical SnO2@rGO Nanostructures with Superhigh Surface Areas as High-Quality Gas-Sensing and Electrochemical Active Materials. *Nanoscale* 6, 13690–13700. doi:10.1039/C4NR04374J

Yuvaraja, S., Surya, S. G., Chernikova, V., Vijjapu, M. T., Shekhah, O., Bhatt, P. M., et al. (2020). Realization of an Ultrasensitive and Highly Selective OFET NO2 Sensor: The Synergistic Combination of PDVT-10 Polymer and Porphyrin-MOF. *ACS Appl. Mater. Inter.* 12, 18748–18760. doi:10.1021/acsami.0c00803

Zhang, H., Feng, J., Fei, T., Liu, S., and Zhang, T. (2014). SnO2 Nanoparticles-Reduced Graphene Oxide Nanocomposites for NO2 Sensing at Low Operating Temperature. *Sensors Actuators B: Chem.* 190, 472–478. doi:10.1016/j.snb.2013.08.067

Zhong, Y., Li, W., Zhao, X., Jiang, X., Lin, S., Zhen, Z., et al. (2019). High-Response Room-Temperature NO2 Sensor and Ultrafast Humidity Sensor Based on SnO2 with Rich Oxygen Vacancy. *ACS Appl. Mater. Inter.* 11, 13441–13449. doi:10.1021/acsami.9b01737

Zhu, X., Guo, Y., Ren, H., Gao, C., and Zhou, Y. (2017). Enhancing the NO2 Gas Sensing Properties of rGO/SnO2 Nanocomposite Films by Using Microporous Substrates. *Sensors Actuators B: Chem.* 248, 560–570. doi:10.1016/j.snb.2017.04.030

Zhu, X., Xu, Y., Cheng, Z., Wang, Y., Lu, Z., and Zhang, G. (2021). First Principles Study of Atmospheric Pollutants Adsorption on Non-defect and Monatomic Defect Graphene. *Diamond Relat. Mater.* 112, 108252. doi:10.1016/j.diamond.2021.108252

Conflict of Interest: The authors declare that the research was conducted in the absence of any commercial or financial relationships that could be construed as a potential conflict of interest.

frontiers in Chemistry

ORIGINAL RESEARCH
published: 21 July 2021
doi: 10.3389/fchem.2021.699231

Highly Water-Dispersible Graphene Nanosheets From Electrochemical Exfoliation of Graphite

Si-Woo Park[1,2†], Byungkwon Jang[1†], Han Kim[1], Jimin Lee[1], Ji Young Park[1], Sung-Oong Kang[2] and Yong-Ho Choa[1]**

[1]Department of Materials Science & Chemical Engineering, Hanyang University, Ansan, South Korea, [2]MExplorer Co., Ltd., Ansan, South Korea

The electrochemical exfoliation of graphite has been considered to be an effective approach for the mass production of high-quality graphene due to its easy, simple, and eco-friendly synthetic features. However, water dispersion of graphene produced in the electrochemical exfoliation method has also been a challenging issue because of the hydrophobic properties of the resulting graphene. In this study, we report the electrochemical exfoliation method of producing water-dispersible graphene that importantly contains the relatively low oxygen content of <10% without any assistant dispersing agents. Through the mild *in situ* sulfate functionalization of graphite under alkaline electrochemical conditions using a pH buffer, the highly water-dispersible graphene could be produced without any additional separation processes of sedimentation and/or centrifugation. We found the resulting graphene sheets to have high crystalline basal planes, lateral sizes of several μm, and a thickness of <5 nm. Furthermore, the high aqueous dispersion stability of as-prepared graphene could be demonstrated using a multi-light scattering technique, showing very little change in the optical transmittance and the terbiscan stability index over time.

Keywords: graphene, water dispersion, sulfate functionalization, electrochemical exfoliation, edge functionalization

Edited by:
Syed Mubeen Jawahar Hussaini,
The University of Iowa, United States

Reviewed by:
Yao Yang,
Shanghai Jiao Tong University, China
Yunpei Zhu,
King Abdullah University of Science and Technology, Saudi Arabia

Correspondence:
Sung-Oong Kang
kso3710@gmail.com
Yong-Ho Choa
choa15@hanyang.ac.kr

†These authors have contributed equally to this work and share first authorship

Specialty section:
This article was submitted to Electrochemistry, a section of the journal Frontiers in Chemistry

Received: *23 April 2021*
Accepted: *21 June 2021*
Published: *21 July 2021*

Citation:
Park S-W, Jang B, Kim H, Lee J, Park JY, Kang S-O and Choa Y-H (2021) Highly Water-Dispersible Graphene Nanosheets From Electrochemical Exfoliation of Graphite. Front. Chem. 9:699231. doi: 10.3389/fchem.2021.699231

INTRODUCTION

Graphene, atomically thin carbon layers exfoliated from graphite in which multiple layers of sp^2-bonded carbon atoms are arranged in a hexagonal lattice, has been standing at the center of materials due to its great potential applications in next-generation electronic devices (Kwon et al., 2020; Alonso et al., 2018), energy conversion and storage devices (Jang et al., 2021; Tanguy et al., 2020), catalysis (Hwang et al., 2019; Lu et al., 2016), and other functional composites (Ryu et al., 2020; Wu et al., 2017) owing to its unique electrical, mechanical, optical, and chemical properties (Kwon et al., 2017; Dong et al., 2017; Kim et al., 2019). While the preparation methods of graphene such as Scotch Tape exfoliation (Novoselov et al., 2004), epitaxial growth (Yang et al., 2013), and chemical vapor deposition using gaseous precursors (Plutnar et al., 2018) could yield high-quality graphene, its commercialization has been hindered owing to the lack of cost-effective industrial-scale production methods.

Among the alternatives, wet chemical approaches that operate *via* chemical reduction of graphene oxide (GO) and mechanical liquid-phase exfoliation of graphite such as ultrasonication or shear mixing have opened pathways to the mass production of graphene (Chuaa et al., 2014; Paton et al., 2014). In particular, the classical and well-known wet chemical route, oxidation of graphite into GO and its concurrent reduction of GO to reduced GO (rGO), has suffered from generating a large amount of hazardous wastes and poisonous gases while leaving inevitable structural defects within the as-reduced GO (Chuaa et al., 2014). In addition, the liquid-phase mechanical exfoliation of graphite into graphene has also presented the limits of small size and low yield of thin graphene nanosheets with respect to the use of solvent- or surfactant-assisted exfoliation using expanded graphite or graphite intercalation compounds (GICs) (Lee et al., 2009; Paton et al., 2014).

Recently, the electrochemical exfoliation of graphite has drawn attention as an easy, simple, and eco-friendly method to produce high-quality graphene (Parvez et al., 2014). When a voltage is applied to a graphite electrode, few-layer graphene sheets are exfoliated from the graphite layers over successive reaction steps, including the formation of GICs, expansion of the graphite layer through gas-evolving electrolysis, and exfoliation of graphite layers in various electrolytes (Parvez et al., 2014). The electrochemical exfoliation of graphite has been performed by changing the electrolyte type to control the characteristics of the resulting graphene sheets, such as their lateral size, thickness, and electronic and chemical properties (Yang et al., 2016). For the easy applications of graphene in industrial fields, water-dispersible graphene is believed to be economically and technologically useful. The generation of a large amount of oxygen functional groups (hydroxyl and carboxyl groups) on graphene led to the water dispersion of graphene; however, such over-oxidation of graphene should involve a trade-off of losing the inherent structural, electrical, and physical properties (Wang et al., 2018; Hashimoto et al., 2019). Therefore, an effective electrochemical approach is highly required to cut across such a trade-off between the high water dispersion and the over-oxidation of graphene in the electrochemical exfoliation methods.

According to the Derjaguin–Landau–Verwey–Overbeek (DLVO) theory, the aggregation of the aqueous dispersion is related to the combination of electrostatic repulsion and van der Waals attraction between particle and particle. In order to obtain a stable water dispersion of graphene, electrostatic repulsion should dominate over van der Waals attraction (Hierrezuelo et al., 2010). With the approach of introducing functional groups that can effectively offer surface charge to graphene sheets despite the small amount of functional groups, it is possible to increase the water dispersion stability without disturbing the inherent properties of graphene sheets.

In this work, we report the preparation of highly water-dispersible graphene through the mild *in situ* sulfate functionalization of graphite manipulated by controlling the reaction of persulfate ($S_2O_8^{2-}$) ions to graft sulfate ($R–OSO_3^-$) groups onto the graphene sheets during the electrochemical reactions. The as-functionalized sulfate groups on graphene are believed to induce the stable water dispersion of graphene rather than the conventional oxygen functional groups such as carboxyl and hydroxyl groups; the strongly acidic sulfate groups are expected to be fully dissociated and induce strong negative charges under all relevant solution conditions, but the carboxyl or hydroxyl groups offer negative charges at a relatively higher pH value (Behrens et al., 2001). In our electrochemical regime of mild *in situ* sulfate functionalization, the highly water-dispersible graphene could be prepared with a relatively lower oxygen content of <10% compared with the inevitable over-oxidization of graphene in the conventional electrochemical exfoliation process. As a consequence, the as-derived strong negative charge of sulfate-functionalized graphene could generate the water dispersion without the generally additional separation processes of sedimentation and/or centrifugation. Here, we expect that the results regarding water-dispersible graphene produced in this study may significantly contribute to providing a high-quality graphene product to the practical industrial fields.

MATERIALS AND METHODS

Materials

Ammonium persulfate (>98%), potassium hydroxide (>97%), and ammonium acetate (>97%) were purchased from Sigma-Aldrich. Graphite foil (99.8%) was purchased from Alfa-Aesar. All chemicals were used as received without any further purification.

Electrochemical Exfoliation of Graphite Foil

In a typical procedure, graphite foil was used as the anode for the electrochemical exfoliation of graphite, with Pt foil being used as the cathode. As the electrolytes for the electrochemical reaction, ammonium persulfate (as an oxidant) and ammonium acetate (as pH buffer) were dissolved in deionized water using a mechanical stirrer to obtain 0.35 and 0.5 M solutions, respectively. The pH of the solution was adjusted by adding potassium hydroxide (KOH) to prevent the solution from becoming acidic (below pH 7) during the electrochemical reaction. The electrochemical exfoliation reaction was carried out by applying a constant voltage (10 V) to the graphite-foil electrode at 25°C for 1 h. The reaction product was collected by vacuum filtration and washed several times with deionized water. The resulting wet black powder was ultrasonicated in deionized water for 30 min, and a stable graphene nanosheet dispersion was obtained without any additional sedimentation and/or centrifugation processes. The dispersion stability of the graphene nanosheet could be controlled by changing the initial pH of the electrolyte.

Measurement and Characterization

Electrochemical exfoliation was conducted by using a ZIVE MP1 electrochemical workstation (WonATech). Transmission electron microscopy (TEM) and high-resolution transmission electron microscopy (HRTEM) images of the graphene samples were acquired using a JEOL JEM-2010 microscope at an accelerating voltage of 200 kV. Atomic force microscopy (AFM) images were obtained using an XE-100 (Park Systems) instrument. X-ray photoelectron spectroscopy (XPS) results were obtained using a Kratos AXIS Ultra DLD with an Al Kα radiation source (1,486.8 eV) in an ultrahigh vacuum chamber (7×10^{-9} Torr). The Raman spectrum of the graphene sample was measured using a UniRAM Raman microscope (Uninanotech) at room temperature and an excitation wavelength of 532 nm. The attenuated total reflection Fourier transform infrared (ATR-FTIR) spectrum of the graphene was collected using a Nicolet

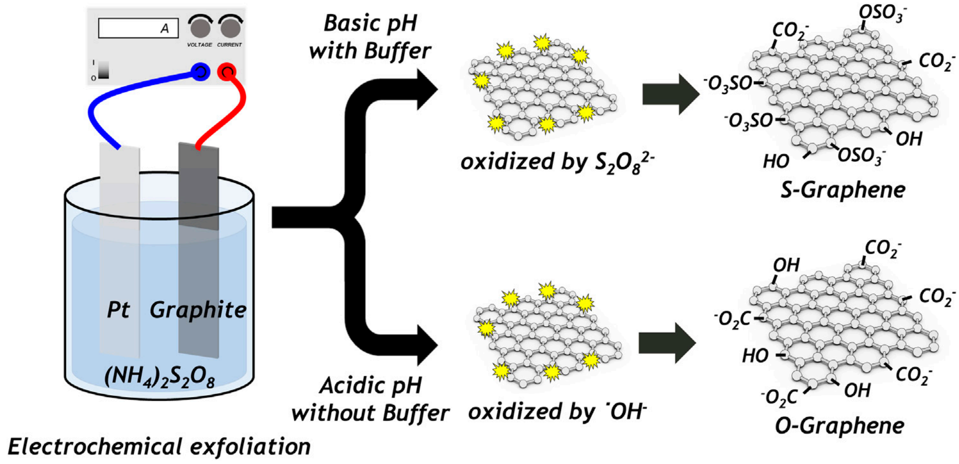

FIGURE 1 | Schematic of the electrochemical exfoliation of graphite with and without pH buffer.

iS10 FT-IR spectrometer (Thermo Scientific). The sample dispersion stability was characterized using a Leanontech Turbiscan Lab Expert instrument with a near-infrared (NIR) light source (880 nm). The zeta potential was obtained by using an ELSZ-1000 (Otsuka Electronics).

RESULTS AND DISCUSSION

The persulfate anion ($S_2O_8^{2-}$), a strong oxidant ($E^0 = 2.01$ V) (Yuan et al., 2014), undergoes chemical or thermal dissociation to become an intermediate of sulfate free radicals (SO_4^{-}), which can be readily converted to hydroxyl free radicals (·OH) in aqueous solution *via* a radical interconversion reaction. In particular, under acidic conditions, the breakdown of $S_2O_8^{2-}$ can be further acid-catalyzed; as a result, most of the $S_2O_8^{2-}$ converts into ·OH (Liang et al., 2007). For this reason, the electrochemical exfoliation of graphite in a persulfate electrolyte affords only oxygen functional groups (i.e., carboxyl and hydroxyl groups) grafted on graphene, which is specifically formed by ·OH despite the use of sulfur atom–containing oxidizing reagents. To anchor sulfate functional groups onto the graphene in the electrochemical exfoliation step, it is necessary to prevent the dissociation of persulfate ions into radical species, which can be achieved by maintaining the basicity of the solution during the electrochemical reaction. Therefore, the pH of the electrolyte employed in our study was carefully kept at a value of higher than seven during the whole electrochemical reaction. By using potassium hydroxide and a pH buffer reagent, the basic condition of the electrochemical reaction (pH value > 7) was maintained until the electrochemical reactions terminate. As a result, the highly water-dispersible graphene functionalized with the sulfate groups could be obtained in our electrochemical scheme (**Figure 1**).

In the specific two-electrode system with the use of graphite foil as the anode and Pt foil as the cathode, the electrolyte solutions were first prepared by dissolving ammonium persulfate in deionized water to obtain a 0.35 M aqueous solution, and the pH value was adjusted using potassium hydroxide with ammonium acetate buffer solution (pH 11). Subsequently, a constant voltage of 10 V was applied to the graphite-foil electrode at a temperature of 25°C to prevent the thermal decomposition of persulfate ions (Liang et al., 2007). For 10 min from the beginning of applying the voltage, the current was gradually increased due to decreasing interfacial resistance between the electrode and the electrolyte by increasing the surface area of the graphite electrode, which resulted from the gas-evolved expansion of graphite. After that, as the expanded graphite electrode was eroded and exfoliated into flakes, the current was gradually decreased. The exfoliation process was almost completed with a slight change in the current at 50 min, and the reaction was terminated at 1 h (**Figure 2**). The as-exfoliated graphite separated in the form of a black powder was collected by vacuum filtration and repeatedly washed with deionized water to remove any residual impurities and salts. The

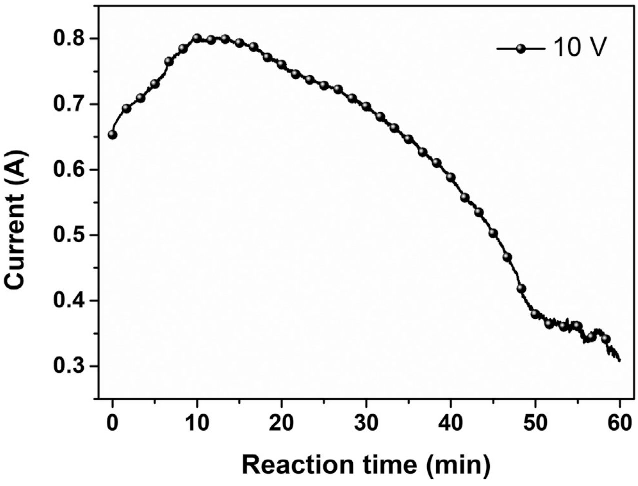

FIGURE 2 | Current–time plot during the electrochemical exfoliation of graphite applying 10 V.

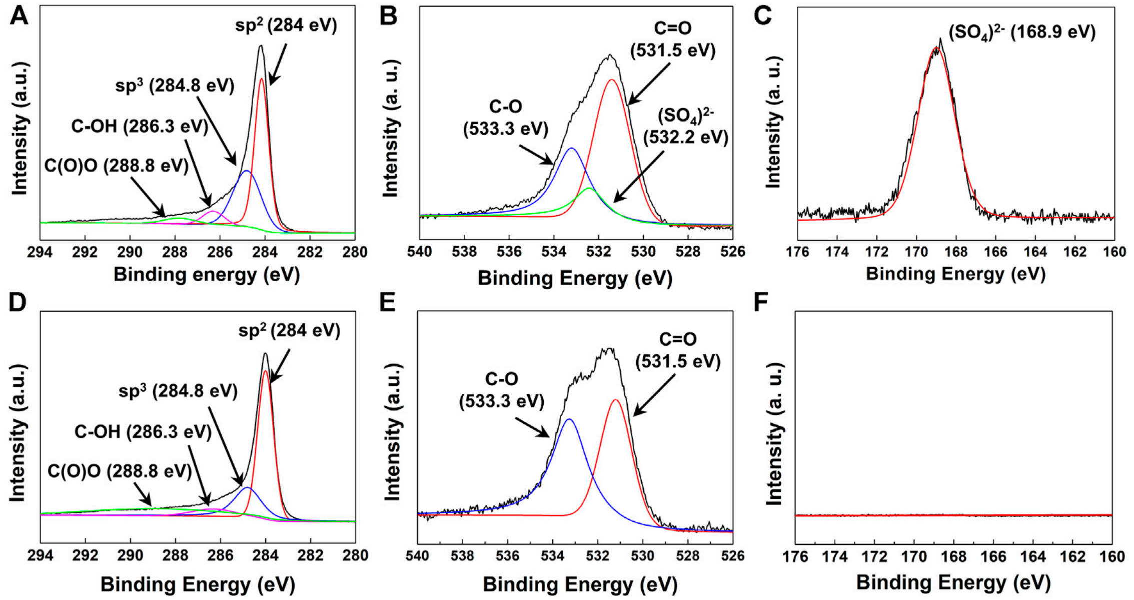

FIGURE 3 | (A) C 1s, **(B)** O 1s, and **(C)** S 2p XPS spectra of electrochemically exfoliated graphene with pH buffer. **(D)** C 1s, **(E)** O 1s, and **(F)** S 2p spectra of electrochemically exfoliated graphene without pH buffer.

as-collected black powder was ultrasonicated to obtain a highly concentrated aqueous graphene dispersion with a concentration of 15 mg/ml, importantly without any additional separation processes of sedimentation and/or centrifugation. It is also noted that the simple ultrasonication step could completely exfoliate the as-expanded graphite into individual graphene sheets without any dots of un-exfoliated graphite powder.

The chemical structure and bonds of water-dispersible graphene were investigated by X-ray photoelectron spectroscopy (XPS), which depicts the detailed chemical composition in the form of the peak binding energies of C 1s, O 1s, and S 2p. The sulfate-functionalized graphene could be identified as mostly consisting of sp^2-type carbon as per the peak at 284.0 eV with a small amount of sp^3-type, hydroxyl-type, and carboxyl-type carbon, corresponding to peaks at 284.8, 286.3, and 288.8 eV, respectively (**Figure 3A**) (Parvez et al., 2014). As the peak of the C–S bond (285.2 eV) (Ye et al., 2015) could not be observed, we notice that the sulfonate group ($R–SO_3^-$) has not been grafted on the surface of graphene. Instead, we could observe the chemical bonds between carbon and oxygen (533.3 eV for C–O and 531.5 eV for C=O) and between sulfur and oxygen (SO_4^{2-}, 532.2 eV) (**Figure 3B**) (Kwan et al., 2015; Singh et al., 2018) from the O 1s peaks. Moreover, the peak corresponding to the sulfate bond (SO_4^{2-}, 168.9 eV) is found in the S 2p spectra, without other peaks corresponding to the sulfonate (SO_3^{2-}, 167.5 eV) bond (**Figure 3C**) (Massonnet et al., 2015). Based on the results of XPS analysis, the water-dispersible graphene nanosheets are signified to be sulfate-functionalized where sulfur atom–containing functional groups were introduced in the form of sulfate ($R–OSO_3^-$) instead of sulfonate ($R–SO_3^-$). Furthermore, the FT-IR spectrum of graphene collected in the ATR mode also revealed that water-dispersible graphene has various types of functional groups in the structure (**Supplementary Figure S1**). The distinctive peak was observed at 1,170 cm^{-1} and 1,060 cm^{-1}, corresponding to the stretching vibration of the sulfate group (Guo et al., 2019), while the vibrational bands at 3,400 cm^{-1} and 1720 cm^{-1} correlate with hydroxyl and carboxyl, respectively (Aunkor et al., 2016).

The key role of the mild *in situ* sulfate functionalization of graphene employed in our study for the production of water-dispersible graphene could be confirmed in comparison to the hydrophobic graphene produced without maintaining the basic pH of the electrolyte during the electrochemical reaction. Different from the specific electrochemical reaction of water-dispersible graphene, we conducted the same electrochemical reaction without using the buffer reagent. In detail, we carried out the electrochemical reaction in the solution with the concentration of 0.35 M, adjusting the pH of the electrolyte to 11, applying the constant voltage of 10 V at a temperature of 25°C, continuing the reaction for 1 h, and only without using the buffer reagent of ammonium acetate. Without using the buffer reagent, the pH value of the electrolyte changes from 6.5–7 to 2 during the electrochemical reaction because the persulfate ions dissociate into sulfuric acid as the reaction proceeds (Liang et al., 2007). As a result, the comparison reaction condition yielded only the hydrophobic graphene sheets that could only be dispersed in organic solvents (e.g., dimethylformamide and N-methylpyrrolidone) instead of water. From the hydrophobic graphene prepared without the buffer solution, the peak C 1s positions are similar to those of the sulfated graphene sheets at 284.0, 284.8, 286.3, and 288.8 eV, corresponding to sp^2-, sp^3-, hydroxyl-, and carboxyl-type carbon, respectively (**Figure 3D**).

TABLE 1 | Elemental percentage, atomic ratio, and surface zeta potential of graphene sheets with different initial pH values during electrochemical exfoliation.

	pH 8	pH 9	pH 10	pH 11	pH 12
C (%)	90.17	89.83	89.28	88.38	89.12
O (%)	9.11	9.27	9.56	10.21	9.28
S (%)	0.72	0.90	1.16	1.41	1.60
S/C	0.008	0.010	0.013	0.016	0.018
ζ (mV)	−25.40	−28.73	−30.91	−33.34	−34.68

The peaks at 533.3 and 531.5 eV correspond to C–O and C=O binding about O 1s, respectively (**Figure 3E**). However, no peaks are observed at 532.2 eV in the O 1s spectra and at 168.9 eV in the S 2p spectra, which, importantly, indicates the absence of sulfur-containing functional groups on the graphene sheet without the buffer solution (**Figure 3F**).

To confirm the effect of pH on the sulfate functionality and surface charges of graphene sheets generated during the electrochemical exfoliation process, we used XPS to analyze the sulfate-functionalized graphene obtained by changing the initial pH value to determine the degree of sulfation, according to the atomic concentration of carbon and sulfur from the peak areas of C 1s and S 2p, respectively. The zeta-potential analyzer was used to measure the surface zeta potential (ζ) in neutral deionized water (**Table 1**). It is noticed in **Table 1** that as the initial pH value increases from 8 to 12, the carbon atomic concentration decreases from 90.17 to 89.12% and the sulfur atomic concentration increases from 0.72 to 1.60%, with the relatively low oxygen contents of <10%, respectively. In other words, as the initial pH value of the solution in the electrochemical exfoliation reaction increases, the S/C ratio increases from 0.008 to 0.018, indicating the stronger sulfate functionalization of graphene under the strong basic conditions. Moreover, the surface zeta potential increases from −25.40 mV to −34.68 mV in accordance with the increase in the initial pH value. Based on the relationship between the atomic ratios and the initial pH values of electrolytes, we may draw a conclusion that the strong sulfate functionalization of graphene corresponds to the graphene sheet with the higher surface zeta potential.

The microstructures of water-dispersible graphene were observed by high-resolution transmission electron microscopy (HRTEM), as shown in **Figure 4**. The water-dispersible graphene sheet is few-layered graphene with a lateral size of several micrometers. In addition, the selected area electron diffraction (SAED) pattern represents the high crystallinity in the basal plane of the graphene sheet, where carbon atoms array in a hexagonal lattice structure (the inset), as generally observed in the electrochemically exfoliated graphene. Such high crystallinity of water-dispersible graphene is further confirmed by observing hexagonal SAED patterns at various points on the basal plane of a single graphene sheet (**Supplementary Figure S2**). The typical atomic force microscopy (AFM) images shown in **Figure 5** exhibit the graphene sheets with the lateral sizes ranging approximately from 1 to 5 µm (**Figures 5A,B**) and the thickness measurement results for 100 graphene sheets, with the average thickness of graphene sheets being <5 nm (**Figure 5C**).

The compositional characteristics of water-dispersible graphene were investigated by Raman spectroscopy, which is an important tool to characterize graphene materials. The Raman spectrum provides information about the surface disorder and the graphitic composition of graphene materials together with the number of the graphene layers, which was expressed in the D band, the G band, and a weak 2D band, respectively (Kudin et al., 2008). The water-dispersible graphene showed the D band at 1,340 cm^{-1}, the G band at 1,570 cm^{-1}, and the weak 2D band at 2,680 cm^{-1} (**Figure 6**). The intensity ratio of bands D and G (I_D/I_G) is used to investigate the degree of disorders in graphene. Contrary to the TEM analysis result, it shows a high I_D/I_G value of 1.03, similar to rGO (Aunkor et al., 2016), which is a result of numerous edge defects originating from nanocrystalline domains of water-dispersible graphene. From the Knights empirical equation expressed by $L_a = 4.35(I_D/I_G)^{-1}$, the size of the sp^2 carbon domains (L_a) in the water-dispersible graphene was found to be 4.23 nm (Tai et al., 2010).

The dispersion stability of water-dispersible graphene in aqueous solutions (0.01 wt%) over 3 days was quantitatively analyzed using a multi-light scattering technique (**Figure 7A**),

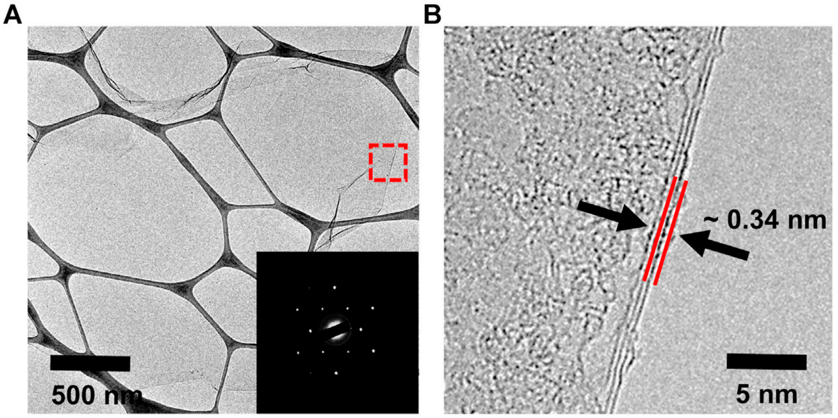

FIGURE 4 | (A) TEM image and SAED pattern (inset) and **(B)** HRTEM image of the graphene sheet prepared with pH buffer at an initial pH value of 11.

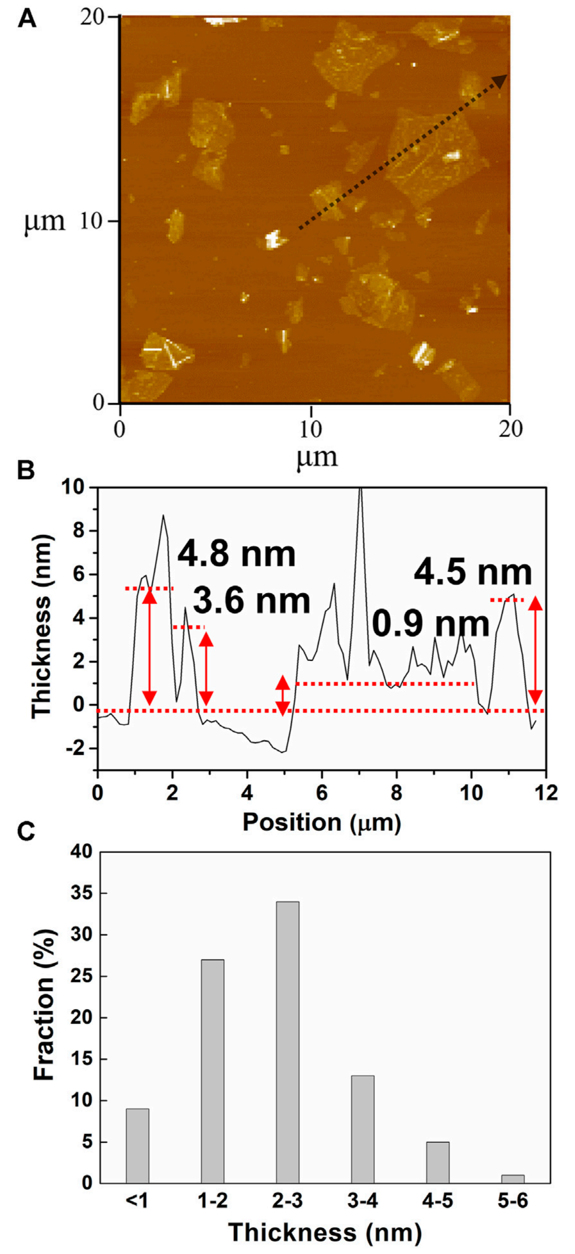

FIGURE 5 | (A) AFM image of the graphene sheets prepared with pH buffer at an initial pH value of 11. **(B)** Height profile of a line scan about the black arrow in **Figure 5A**. **(C)** Histogram of thickness measurements of 100 graphene sheets.

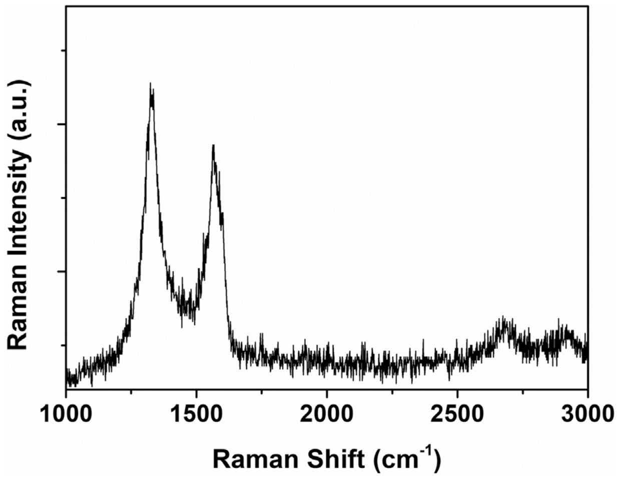

FIGURE 6 | Raman spectrum of the graphene sheets prepared with pH buffer at an initial pH value of 11.

in which the dispersion stability is confirmed by studying the variations in transmittance across the entire height of the sample solution (Terayama et al., 2003). As recognized from the results, the highly stable dispersion presents the constant transmittance regardless of the solution height, and there is very little change in the transmittance over time. From **Figure 7A**, it is noted that the transmittance of the water dispersion of graphene ranges from 17.5 to 18.5% across the entire height of the sample; moreover, the transmittance remains in the range of 18.1–19.2% even after 12 weeks. A slight increase in the transmittance over time is also observed owing to the minimized flocculation and/or coalescence of graphene. To better understand the water dispersion stability of graphene, we numerically calculated the turbiscan stability index (TSI) from the mean kinetics value of the transmittance over time. The value of the TSI was found to slightly increase from 0 to 0.4%, indicating the high water dispersion stability of graphene (**Figure 7B**).

CONCLUSION

In summary, we report the preparation of highly water-dispersible graphene using electrochemical exfoliation of graphite *via* mild *in situ* sulfate functionalization by controlling the reaction of $S_2O_8^{2-}$ ions. Under the basic pH conditions (>pH 7) during the electrochemical exfoliation of graphite, the sulfate functionalization of graphene could be effectively induced, and as a result, the water-dispersible graphene could be prepared with high crystallinity and a relatively low oxygen content of <10% compared with graphene obtained from conventional electrochemical exfoliation. The aqueous dispersion of sulfated graphene was highly stable over a long time without any additional separation processes of sedimentation and/or centrifugation, exhibiting constant transmittance regardless of the solution height and very little change in the transmittance and the TSI. This result indicates that the sulfate functional group attached to the graphene sheet effectively stabilizes the dispersion from electrostatic repulsive forces by increasing the surface charge even when only a small amount of sulfate functional groups is present. More importantly, our study shows that a comprehensive understanding of the persulfate reaction can provide a tool to introduce sulfate functional groups in various materials and

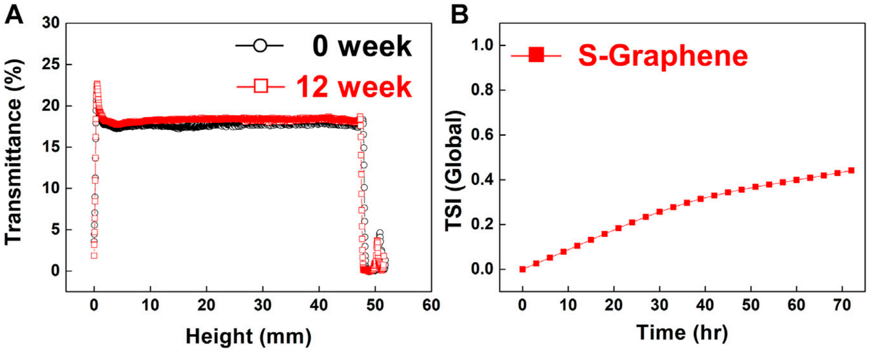

FIGURE 7 | (A) Transmittance of aqueous dispersion of water-dispersible graphene sheets as a function of the solution height at 0 and 12 weeks. **(B)** TSI of the dispersion over time.

increase dispersion stability without inhibiting their original characteristics.

DATA AVAILABILITY STATEMENT

The original contributions presented in the study are included in the article/**Supplementary Material**; further inquiries can be directed to the corresponding authors.

AUTHOR CONTRIBUTIONS

S-WP and BJ conducted the experiments and wrote the manuscript. HK, JL, and JYP characterized the samples. S-OK and Y-HC revised the manuscript and are the corresponding authors. All authors contributed to the manuscript and approved the submitted version.

FUNDING

This research was supported by the Nano Material Technology Development Program through the National Research Foundation of Korea (NRF) funded by the Ministry of Science, ICT and Future Planning (No. 2016M3A7B4900044) and by a National Research Foundation of Korea (NRF) grant funded by the Korean government (MSIT) (No. 2015R1A5A1037548). This research was also supported by the Future Materials Discovery Program through the National Research Foundation of Korea (NRF) funded by the Ministry of Science, ICT and Future Planning (NRF-2019M3D1A2104158).

SUPPLEMENTARY MATERIAL

The Supplementary Material for this article can be found online at: https://www.frontiersin.org/articles/10.3389/fchem.2021.699231/full#supplementary-material

REFERENCES

Alonso, E. T., Rodrigues, D. P., Khetani, M., Shin, D. W., Sanctis, A. D., Joulie, H., et al. (2018). Graphene Electronic Fibres with Touch-Sensing and Light-Emitting Functionalities for Smart Textiles. *npj Flexible Electron.* 2, 25. doi:10.1038/s41528-018-0040-2

Aunkor, M. T. H., Mahbubul, I. M., Saidur, R., and Metselaar, H. S. C. (2016). The green Reduction of Graphene Oxide. *RSC Adv.* 6, 27807–27828. doi:10.1039/c6ra03189g

Behrens, S. H., and Grier, D. G. (2001). The Charge of Glass and Silica Surfaces. *J. Chem. Phys.* 115, 6716–6721. doi:10.1063/1.1404988

Chua, C. K., and Pumera, M. (2014). Chemical Reduction of Graphene Oxide: a Synthetic Chemistry Viewpoint. *Chem. Soc. Rev.* 43, 291–312. doi:10.1039/C3CS60303B

Dong, P., Jiang, B.-P., Liang, W.-Q., Huang, Y., Shi, Z., and Shen, X.-C. (2017). Synthesis of white-light-emitting Graphene Quantum Dots via a One-step Reduction and Their Interfacial Characteristics-dependent Luminescence Properties. *Inorg. Chem. Front.* 4, 712–718. doi:10.1039/C6QI00587J

Guo, Y., Wang, C., Dun, J., Du, L., Hawley, M., and Sun, C. C. (2019). Mechanism for the Reduced Dissolution of Ritonavir Tablets by Sodium Lauryl Sulfate. *J. Pharm. Sci.* 108, 516–524. doi:10.1016/j.xphs.2018.10.047

Hashimoto, H., Muramatsu, Y., Nishina, Y., and Asoh, H. (2019). Bipolar Anodic Electrochemical Exfoliation of Graphite Powders. *Electrochemistry Commun.* 104, 106475. doi:10.1016/j.elecom.2019.06.001

Hierrezuelo, J., Sadeghpour, A., Szilagyi, I., Vaccaro, A., and Borkovec, M. (2010). Electrostatic Stabilization of Charged Colloidal Particles with Adsorbed Polyelectrolytes of Opposite Charge. *Langmuir* 26, 15109–15111. doi:10.1021/la102912u

Hwang, T.-Y., Go, G.-M., Park, S., Lee, J., Song, Y., Kim, S., et al. (2019). Pt/graphene Catalyst and Tellurium Nanowire-Based Thermochemical Hydrogen (TCH) Sensor Operating at Room Temperature in Wet Air. *ACS Appl. Mater. Inter.* 11, 47015–47024. doi:10.1021/acsami.9b12604

Jang, B., Kim, H., Park, S.-W., Lim, M., Lee, J., Go, G.-M., et al. (2021). *In Situ* exfoliation and Modification of Graphite Foil in Supercapacitor Devices: a Facile Strategy to Fabricate High-Performance Supercapacitors. *RSC Adv.* 11, 4006–4010. doi:10.1039/D0RA10533C

Kim, H., Lee, H., Lim, H.-R., Cho, H.-B., and Choa, Y.-H. (2019). Electrically Conductive and Anti-corrosive Coating on Copper Foil Assisted by Polymer-Nanocomposites Embedded with Graphene. *Appl. Surf. Sci.* 476, 123–127. doi:10.1016/j.apsusc.2019.01.066

Kudin, K. N., Ozbas, B., Schniepp, H. C., Prud'Homme, R. K., Aksay, I. A., and Car, R. (2008). Raman Spectra of Graphite Oxide and Functionalized Graphene Sheets. *Nano Lett.* 8, 36–41. doi:10.1021/nl071822y

Kwan, Y. C. G., Ng, G. M., and Huan, C. H. A. (2015). Identification of Functional Groups and Determination of Carboxyl Formation Temperature in Graphene Oxide Using the XPS O 1s Spectrum. *Thin Solid Films* 590, 40–48. doi:10.1016/j.tsf.2015.07.051

Kwon, Y.-T., Kang, S.-O., Cheon, J.-A., Song, Y., Lee, J.-J., and Choa, Y.-H. (2017). Fabrication of a Graphene/ZnO Based P-N junction Device and its Ultraviolet Photoresponse Properties. *Appl. Surf. Sci.* 415, 2–7. doi:10.1016/j.apsusc.2016.10.159

Kwon, Y.-T., Kim, Y.-S., Kwon, S., Mahmood, M., Lim, H.-R., Park, S.-W., et al. (2020). All-printed Nanomembrane Wireless Bioelectronics Using a Biocompatible Solderable Graphene for Multimodal Human-Machine Interfaces. *Nat. Commun.* 11, 3450. doi:10.1038/s41467-020-17288-0

Lee, J. H., Shin, D. W., Makotchenko, V. G., Nazarov, A. S., Fedorov, V. E., Kim, Y. H., et al. (2009). One-Step Exfoliation Synthesis of Easily Soluble Graphite and Transparent Conducting Graphene Sheets. *Adv. Mater.* 21, 4383–4387. doi:10.1002/adma.200900726

Liang, C., Wang, Z.-S., and Bruell, C. J. (2007). Influence of pH on Persulfate Oxidation of TCE at Ambient Temperatures. *Chemosphere* 66, 106–113. doi:10.1016/j.chemosphere.2006.05.026

Lu, J., Li, Y., Li, S., and Jiang, S. P. (2016). Self-assembled Platinum Nanoparticles on Sulfonic Acid-Grafted Graphene as Effective Electrocatalysts for Methanol Oxidation in Direct Methanol Fuel Cells. *Sci. Rep.* 6, 21530. doi:10.1038/srep21530

Massonnet, N., Carella, A., de Geyer, A., Faure-Vincent, J., and Simonato, J.-P. (2015). Metallic Behaviour of Acid Doped Highly Conductive Polymers. *Chem. Sci.* 6, 412–417. doi:10.1039/C4SC02463J

Novoselov, K. S., Geim, A. K., Morozov, S. V., Jiang, D., Zhang, Y., Dubonos, S. V., et al. (2004). Electric Field Effect in Atomically Thin Carbon Films. *Science* 306, 666–669. doi:10.1126/science.1102896

Parvez, K., Wu, Z.-S., Li, R., Liu, X., Graf, R., Feng, X., et al. (2014). Exfoliation of Graphite into Graphene in Aqueous Solutions of Inorganic Salts. *J. Am. Chem. Soc.* 136, 6083–6091. doi:10.1021/ja5017156

Paton, K. R., Varrla, E., Backes, C., Smith, R. J., Khan, U., O'Neill, A., et al. (2014). Scalable Production of Large Quantities of Defect-free Few-Layer Graphene by Shear Exfoliation in Liquids. *Nat. Mater* 13, 624–630. doi:10.1038/nmat3944

Plutnar, J., Pumera, M., and Sofer, Z. (2018). The Chemistry of CVD Graphene. *J. Mater. Chem. C* 6, 6082–6101. doi:10.1039/C8TC00463C

Ryu, S. H., Kim, S., Kwon, Y. T., Park, Y. K., Kang, S. O., Cho, H. B., et al. (2020). Decorating Surface Charge of Graphite Nanoplate Using an Electrostatic Coupling Agent for 3-dimensional Polymer Nanocomposite. *J. Appl. Polym. Sci.* 137, 48390. doi:10.1002/app.48390

Singh, T., Öz, S., Sasinska, A., Frohnhoven, R., Mathur, S., and Miyasaka, T. (2018). Sulfate-Assisted Interfacial Engineering for High Yield and Efficiency of Triple Cation Perovskite Solar Cells with Alkali-Doped TiO 2 Electron-Transporting Layers. *Adv. Funct. Mater.* 28, 1706287. doi:10.1002/adfm.201706287

Tai, F. C., Wei, C., Chang, S. H., and Chen, W. S. (2010). Raman and X-ray Diffraction Analysis on Unburned Carbon Powder Refined from Fly Ash. *J. Raman Spectrosc.* 41, 933–937. doi:10.1002/jrs.2532

Tanguy, N. R., N'Diaye, J., Arjmand, M., Lian, K., and Yan, N. (2020). Facile One-Pot Synthesis of Water-Dispersible Phosphate Functionalized Reduced Graphene Oxide toward High-Performance Energy Storage Devices. *Chem. Commun.* 56, 1373–1376. doi:10.1039/C9CC07613A

Terayama, H., Hirota, K., Yoshimura, T., and Esumi, K. (2003). Effect of Dilution on Aqueous Dispersion of Drug Particles. *Colloids Surf. B: Biointerfaces.* 27, 177–180. doi:10.1016/S0927-7765(02)00072-3

Wang, H. S., Tian, S. Y., Yang, S. W., Wang, G., You, X. F., Xu, L. X., et al. (2018). Anode Coverage for Enhanced Electrochemical Oxidation: a green and Efficient Strategy towards Water-Dispersible Graphene. *Green. Chem.* 20, 1306–1315. doi:10.1039/c7gc03345a

Wu, Y., Wang, Z., Liu, X., Shen, X., Zheng, Q., Xue, Q., et al. (2017). Ultralight Graphene Foam/Conductive Polymer Composites for Exceptional Electromagnetic Interference Shielding. *ACS Appl. Mater. Inter.* 9, 9059–9069. doi:10.1021/acsami.7b01017

Yang, S., Lohe, M. R., Müllen, K., and Feng, X. (2016). New-Generation Graphene from Electrochemical Approaches: Production and Applications. *Adv. Mater.* 28, 6213–6221. doi:10.1002/adma.201505326

Yang, W., Chen, G., Shi, Z., Liu, C.-C., Zhang, L., Xie, G., et al. (2013). Epitaxial Growth of Single-Domain Graphene on Hexagonal boron Nitride. *Nat. Mater* 12, 792–797. doi:10.1038/nmat3695

Ye, J., He, F., Nie, J., Cao, Y., Yang, H., and Ai, X. (2015). Sulfur/carbon Nanocomposite-Filled Polyacrylonitrile Nanofibers as a Long Life and High Capacity Cathode for Lithium-Sulfur Batteries. *J. Mater. Chem. A.* 3, 7406–7412. doi:10.1039/c4ta06976e

Yuan, S., Liao, P., and Alshawabkeh, A. N. (2014). Electrolytic Manipulation of Persulfate Reactivity by Iron Electrodes for Trichloroethylene Degradation in Groundwater. *Environ. Sci. Technol.* 48, 656–663. doi:10.1021/es404535q

Conflict of Interest: S-WP and S-OK were employed by MExplorer Co., Ltd.

The remaining authors declare that the research was conducted in the absence of any commercial or financial relationships that could be construed as a potential conflict of interest.

The handling Editor declared a past co-authorship with one of the authors (YC).

frontiers in Chemistry

ORIGINAL RESEARCH
published: 01 September 2021
doi: 10.3389/fchem.2021.694726

Aqueous Electrodeposition of SmCo Alloys: II. Direct Current Studies

Jei C. Wei[1], **Morton Schwartz**[1†], **Ken Nobe**[1†] **and Nosang V. Myung**[2*]

[1]University of California at Los Angeles, Los Angeles, CA, United States, [2]University of Notre Dame, Notre Dame, IN, United States

Previously, we reported the aqueous electrodeposition of rare earth - iron group alloys. A key factor was the complexation of the metal ions with various coordination compounds (*e.g.,* aminoacetic acids), without which only the ferrous metal and rare earth hydroxides/ oxides are deposited. In this work, samarium cobalt (SmCo) alloys were synthesized using direct current (DC) aqueous electrodeposition. The basic electrolyte solution consisted of 1 M samarium sulfamate, 0.05 M cobalt sulfate, and 0.15 M glycine, resulting in deposits containing >30 at% Sm at 60°C with current density of 500 mA/cm^2. Supporting electrolytes (*i.e.,* ammonium salts) decreased the Sm content in the deposit. Crystallinity of deposited films altered from nanocrystalline to amorphous as the Sm content increased. Deposits with high Sm content (32 at%) became isotropic with reduction in magnetic saturation (M_S) and coercivity (H_c). A deposition mechanism involving stepwise reduction of the complexed Sm-Co ions by depositing hydrogen atoms was proposed.

Keywords: electrodeposition, samarium cobalt, magnetic thin films, glycine, aqueous

Edited by:
Cheng Zhong,
Tianjin University, China

Reviewed by:
Abhishek Lahiri,
Brunel University London,
United Kingdom
Dillip K. Panda,
Clemson University, United States

***Correspondence:**
Nosang V. Myung
nmyung@nd.edu

†Deceased

Specialty section:
This article was submitted to Electrochemistry, a section of the journal Frontiers in Chemistry

Received: *13 April 2021*
Accepted: *21 June 2021*
Published: *01 September 2021*

Citation:
Wei JC, Schwartz M, Nobe K and Myung NV (2021) Aqueous Electrodeposition of SmCo Alloys: II. Direct Current Studies. Front. Chem. 9:694726. doi: 10.3389/fchem.2021.694726

INTRODUCTION

High-performance permanent magnets such as samarium-cobalt (SmCo) and neodymium-iron-boron (NdFeB) alloys are playing an increasingly prominent role in miniaturizing electrical and electronic machines and devices. Although the rare earth-transition metals (RE-TM) alloys are substantially more expensive than the hard, magnetic ferrites, their superior magnetic properties drive the RE-TM permanent magnets' growing usage (Strnat and Strnat, 1991). A sharp decline in their manufacturing costs would lead to an increasingly dominant position in worldwide applications of nano- and micro-scale systems.

Compared to SmCo, NdFeB permanent magnets (PM) have a higher energy product ($(BH)_{max}$) and coercivity (H_c), but a lower Curie temperature (T_C) and chemical stability in aggressive environments. As a result, SmCo PMs have application in high temperature and aggressive environments such as those encountered by military and aeronautical / aerospace systems (du Trémolet Lacheisserie et al., 2002). So far, fabrication of nanostructured SmCo alloys have been restricted to physico-chemical deposition methods. Therefore, development of an aqueous electrodeposition process would dramatically reduce manufacturing costs (Dini, 1993).

In a series of preliminary studies, we reported on the aqueous electrodeposition of alloys of RE mischmetals, La, Ce, Nd, Gd and Sm with the iron group metals (e.g., Ni, Co, and Fe). The key factor is the complexation of the metal ions with aminocarboxylates (Chen et al., 1996; Myung et al., 1999; Schwartz et al., 1999; Schwartz et al., 2004; Wei et al., 2006; Wei et al., 2008; Wei et al., 2009). The present work reports on the aqueous DC electrodeposition of SmCo alloys using parallel electrodes. The solution constituents and compositions as well as the deposition

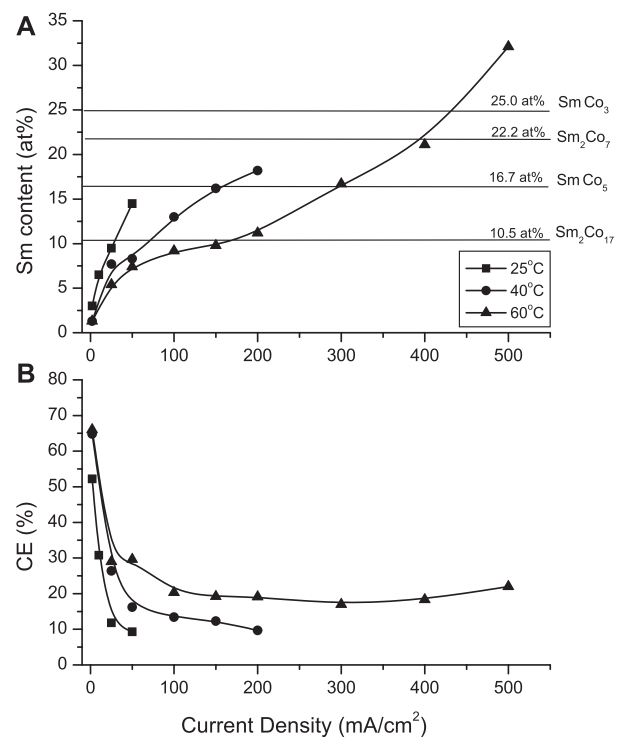

FIGURE 1 | Effect of current density and solution temperature on **(A)** deposit samarium content and **(B)** current efficiency (CE).

variables were selected as a result of preliminary parametric studies using Hull Cells (HC) (Wei et al., 2008).

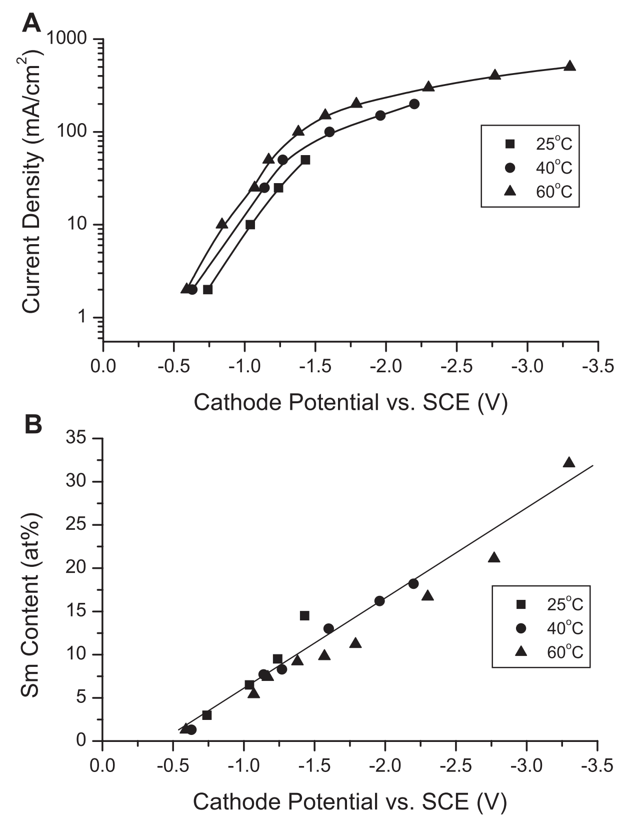

FIGURE 2 | (A) Cathodic polarization curves in the electrodeposition of Sm-Co alloys at various current densities and solution temperature and **(B)** dependence of Sm content on cathodic potential.

EXPERIMENTAL

The electrodeposition cell consisted of two parallel electrodes (brass cathode, 2 × 2 cm, and a platinum anode, 3 × 6 cm), which were 4 cm apart. A shielding panel with a 2 cm by 2 cm window was inserted equidistant between the electrodes to provide a more uniform current distribution. A saturated calomel electrode (SCE) measured the cathode potential. A potentio/gavalno-stat (EG & G 273) served as the power source with a coulometer measuring charge (50 C). Solution volume was kept at 240 ml. The basic solution consisted of 1 M Sm sulfamate, 0.05 M Co sulfate, and 0.15 M glycine, unless otherwise noted. The plating conditions were varied within the following ranges: current density from 2 to 500 mA/cm^2, temperature from 25 to 60°C, pH range from 2 to 6. The solutions were not agitated during electrodeposition.

Prior to plating, the brass cathode was mechanically cleaned by immersing in 0.1 M NaOH, rinsing with deionized (DI) water, dipping in 10 vol. % HCl (30 s) and then rinsed with DI water. The plated cathodes were rinsed and dried with nitrogen. Disk specimens (0.64 cm diameter) were fabricated for analysis and characterization.

Sm and Co contents in the deposits were determined by energy dispersive X-ray spectroscopy (EDS). Co content was measured separately by atomic absorption spectrophotometry (AAS, Perkin Elmer). Deposit structure, crystal orientation, phase identification and grain size were determined by powder X-ray diffraction (XRD). Deposit surface morphology and microstructure were observed with scanning electron microscopy (SEM). Magnetic properties were determined by a vibrating sample magnetometer (VSM, Digital Measurement Systems Model 1660) with an applied magnetic field scanning between −10 and +10 KOe. In-phase (//) and perpendicular (⊥) measurements represent the field applied to the specimen's plane, respectively. The deposit magnetic properties were obtained from BH loops. All measurements and data reported were on deposits with metallic appearance, unless otherwise noted. CD$_{\max}$ is the maximum current density, beyond which deposits appeared non-metallic. Minimum duplicate runs were performed.

RESULTS AND DISCUSSION

Confirming trends of the Hull Cell (HC) studies (Wei et al., 2008), the deposit Sm content increased with increasing temperature and applied current density (**Figure 1A**). At 25°C, the CD$_{\max}$ was 50 mA/cm^2 with deposit containing approximately 14.5 at% Sm (*i.e.,* 30.2 wt%). Increased

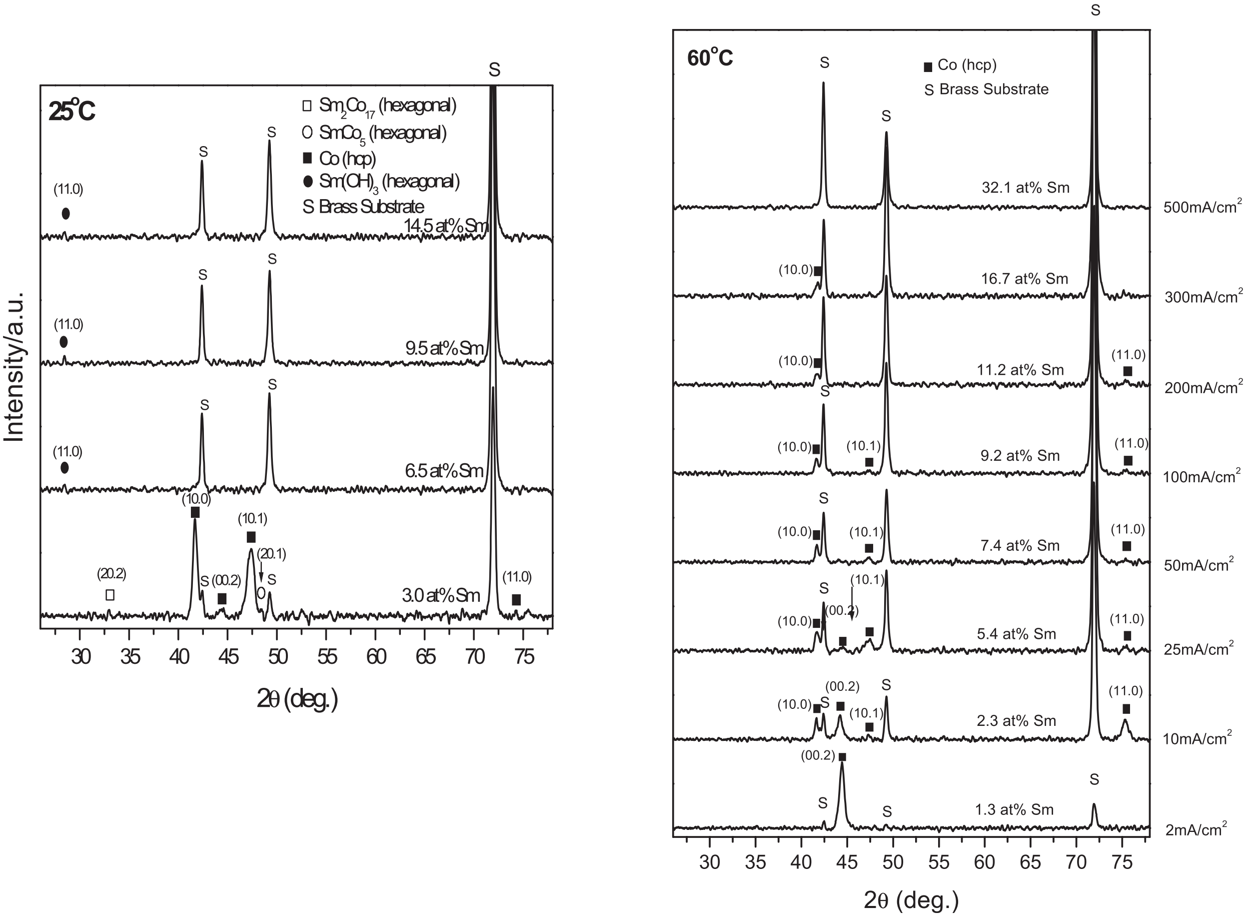

FIGURE 3 | XRD patterns of electrodeposits obtained at different temperature (i.e., 25 and 60°C) and various CDs.

solution temperature (60°C) extended the $\mathrm{CD}_{\max}$ to 500 mA/cm^2, resulting in the deposit Sm content of approximately 30 at% (*i.e.,* 55 wt%), sufficient for a series of stoichiometric SmCo intermetallic compounds (after appropriate annealing): $\mathrm{Sm_2Co_{17}}$, $\mathrm{SmCo_5}$, $\mathrm{SmCo_7}$ and $\mathrm{SmCo_3}$. The current efficiencies (CEs) initially decreased sharply, leveling with CD exceeding 50 mA/cm^2 (**Figure 1B**).

While the cathode potential became more negative with increased CD, it was less negative with increased solution temperature (**Figure 2A**). The deposit Sm content increased linearly with more negative potentials, apparently independently of solution temperature (**Figure 2B**). However, co-deposition of SmCo initiating a potential less negative than the equilibrium potential of Sm ($\mathrm{E^{o}_{Sm/Sm}}{}^{3+} = -2.65$ vs SCE) indicated a deposition mechanism involving a potential resulting from complexation rather than direct electrodeposition from aqueous ions.

X-ray diffraction spectra (XRD) of **Figure 1** deposits indicated structures changing from crystalline to noncrystalline (amorphous) with increasing Sm content (**Figure 3**). The crystolites consisted of α-Co phases (hexagonal close packed (hcp)) or Sm (rhombohedral) phases were observed. Deposits formed at 25°C were essentially amorphous with low $\mathrm{Sm(OH)_3}$ content. Low CD (2 mA/cm^2, 3 at% Sm) deposit showed strong 10.0 and 10.1 α-Co (hcp) peaks and weak (20.1), (20.2) $\mathrm{SmCo_5}$ and $\mathrm{Sm_2Co_{17}}$ (hcp) peaks, respectively (**Figure 3**).

XRD spectra of 60°C electrodeposits (not shown) indicated a slight shift in the Bragg angles (α-Co 0.002 and 10.0 peaks) with increasing Sm content. Differing atomic radii of Co (1.25 Å) and Sm (1.81 Å) suggested a misfit, (RSm-RCo) = 0.45], which could result in Co lattice distortion, which tends to elongate the Co lattice while compressing it along the basic plane and likely generate residual stresses in the SmCo deposit contributing to microcracks (**Figure 4**).

Figure 4 shows the SEM images of SmCo alloys electrodeposited at 60°C and 100 mA/cm^2, which revealed a cracked nodular surface. At higher magnification, fibrous nanorods with varying random orientation emanating from individual nodules (**Figures 4B,C**) were observed, as with other electrodeposited cobalt and cobalt alloys (Cavallotti et al., 1983). The estimated nodule diameters ranged

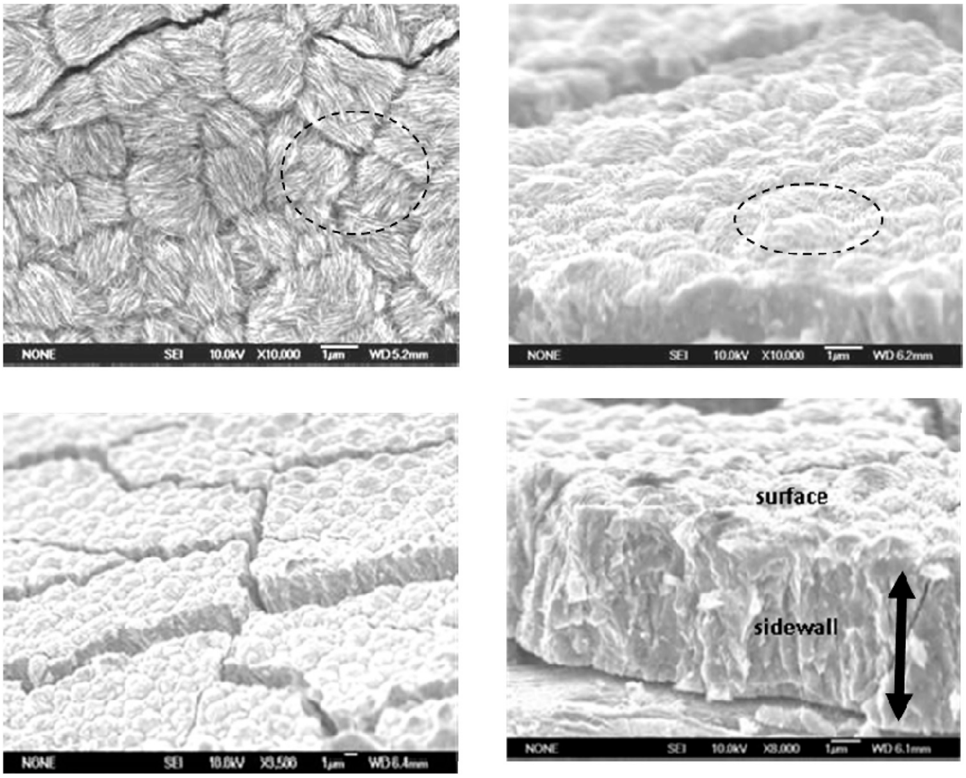

FIGURE 4 | Top and cross-sectional scanning electron microscopic images of Sm-Co electrdeposits at different magnification; 9.2 at% Sm, ~ 5 μm, pH 5.7, 60°C, 100 mA/cm^2.

approximately from 1.5 to 2.5 μm, the crack widths from 0.12 to 0.15 μm with an estimated density of approximately 1,000 cracks/cm^2. The texture of the mechanically fractured sidewall was indicative of the deposit's brittleness (**Figure 4D**). It is suggested that the deposit nanocrystalline or amorphous structure and columnar growth may be the result of coalescing or bundling fibers (**Figure 4C**). Experience with electrodeposits of chromium (Cr) and electroless nickel (Ni) indicated that fine-grained nanocrystalline or amorphous deposit surfaces generally contain nodules (Ruan and Schuh, 2008).

Figures 5, **6** show the effects of deposition variables on deposit composition and magnetic properties. Hysteresis loops indicated magnetic saturation (M_s) was easier along the in-plane direction (easy axis) than the perpendicular direction (hard axis). The in-plane and perpendicular directions approached each other as deposit Sm content increased, while M_s and H_c decreased as CD increased. At constant CD and increased solution temperature (25°C–60°C), M_s and H_c increased, reflecting changing alloy compositions and structures (**Figure 5**)

Magnetization (M_s) decreased linearly with increased deposit Sm content (**Figure 6B**), similar to sputtered deposits (Cho et al., 1997). Magnetic saturation of Co (M_s = 169 emu/g) (Bozorth, 1978) is higher than Sm (M_s = 0.3 emu/g) (Adachi et al., 1994), and the decreased M_s of the alloy was the result of decreased Co content. The deposit's structure changed from crystallinity to non-crystallinity with increased Sm content (**Figure 6**). Deposits with low Sm contents exhibited (002) plane orientation (*c*-axis), resulting in anisotropy.

As the deposit structure changes from crystallinity to non-crystallinity (increased Sm content), the deposits become more isotropic (**Figure 5**), and M_s and $H_{c||}$ decreased. Deposits with low Sm contents exhibit 00.2 plane orientation (*c*-axis), resulting in anisotropy ($H_{c\perp} >> H_{c||}$) (**Figure 6C**). Deposits with increased Sm have decreased hcp 00.2 peak intensity with decreased $H_{c\perp}$. Deposits with high Sm content (32 at%) are non-crystalline and isotropic ($H_{c\perp} \approx H_{c||}$) as shown in **Figure 6C** with reduced M_s (**Figure 6B**).

Deposit coercivities in the in-plane direction (100 Oe) varied only slightly with deposit composition, but in the perpendicular direction, higher H_c (600–800 Oe) was obtained at low Sm content, decreasing sharply with increasing deposit Sm content. We note that as-deposited room temperature sputtered stoichiometric SmCo films also exhibited low coercivities (~100 Oe), which did not increase substantially with subsequent annealing unless deposited on a Cr underlayer, promoting nanocrystalline c-axis texture in the SmCo deposit, increasing in-plane anisotropy (H_c > 40 KOe) (Prados and Hadjipanayis, 1998; Prados and Hadjipanayis, 1999).

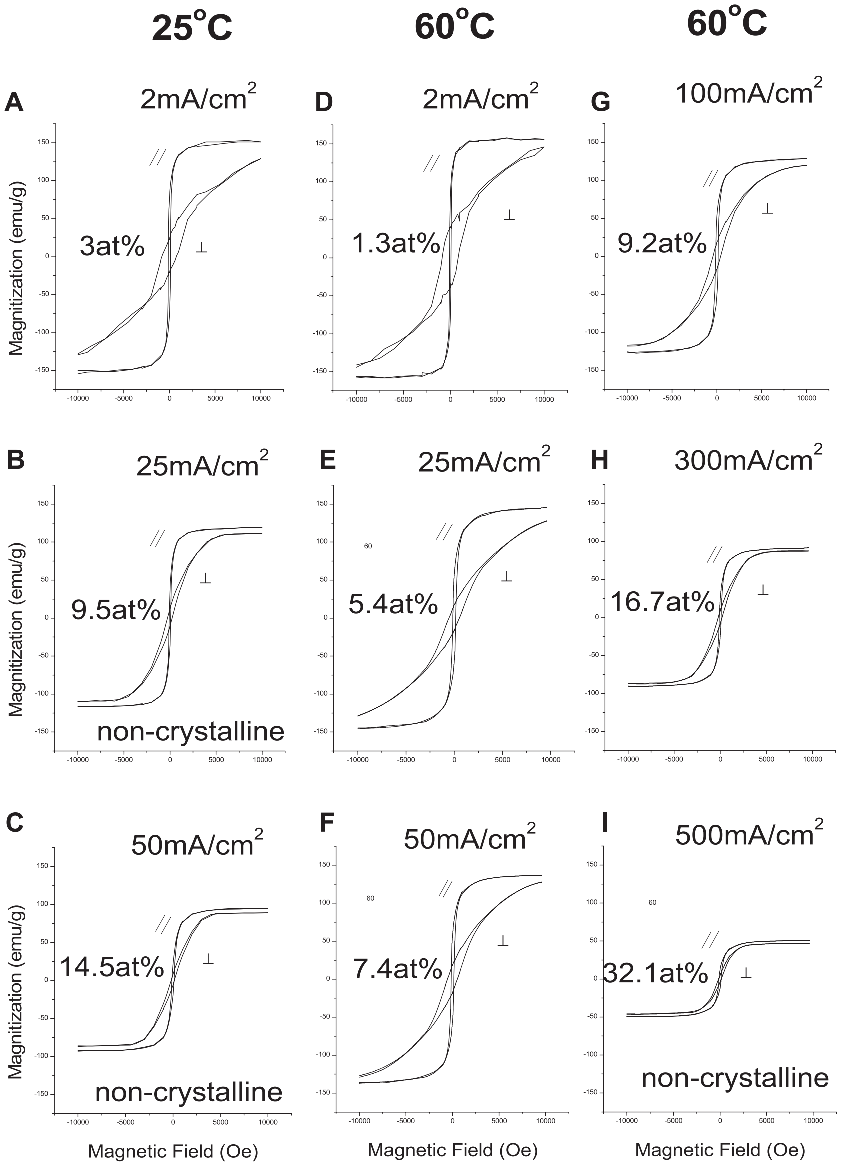

FIGURE 5 | Magnetic hysteresis loops of Sm-Co deposits at 25 and 60°C, and various CDs.

In-plane coercivities remained constant regardless of the deposit Sm content; coercivity in the perpendicular direction, however, decrease with increased Sm content (**Figure 6C**). The squareness of the deposits appeared to be reversed (**Figure 6D**).

Deposit particle size decreased as Sm content increased, result of increased CD and/or decreased solution temperature (**Figure 6A**). Cavallotti *et al.* reported similar results for electrodeposited Co and Co alloys (Cavallotti et al., 1983).

Figure 7A shows the dependence of Sm content on pH at various CDs (10 and 50 mA/cm^2) at room temperature. Sm contents were higher than at 60°C but at the latter temperature maxima deposit Sm content were higher between pH 4 (12 at%, 100 mA/cm^2) and pH 5 (28 at. %, 300 mA/cm^2), respectively. Lower current densities and higher solution temperatures resulted in higher current efficiencies (CEs), but dependence on solution pH was not substantial (**Figure 7B**).

Hull cell experiments (Wei et al., 2008) showed Co and $Sm(OH)_3$ are electrodeposited from glycene-free solution, indicating a complex was essential for deposition of SmCo alloys. At 25°C, maximum deposit Sm contents were obtained at 25 mA/cm^2 (~11 at%) and 50 mA/cm^2 (~14 at%) with glycine concentration of 0.1 and 0.15 M , respectively; below 0.1 M, non-metallic deposits were formed. Increased solution temperature (60°C) and higher CDs resulted in increased Sm contents (*e.g.*, 300 mA/cm^2, 0.1 M glycine to ~18 at%) initially,

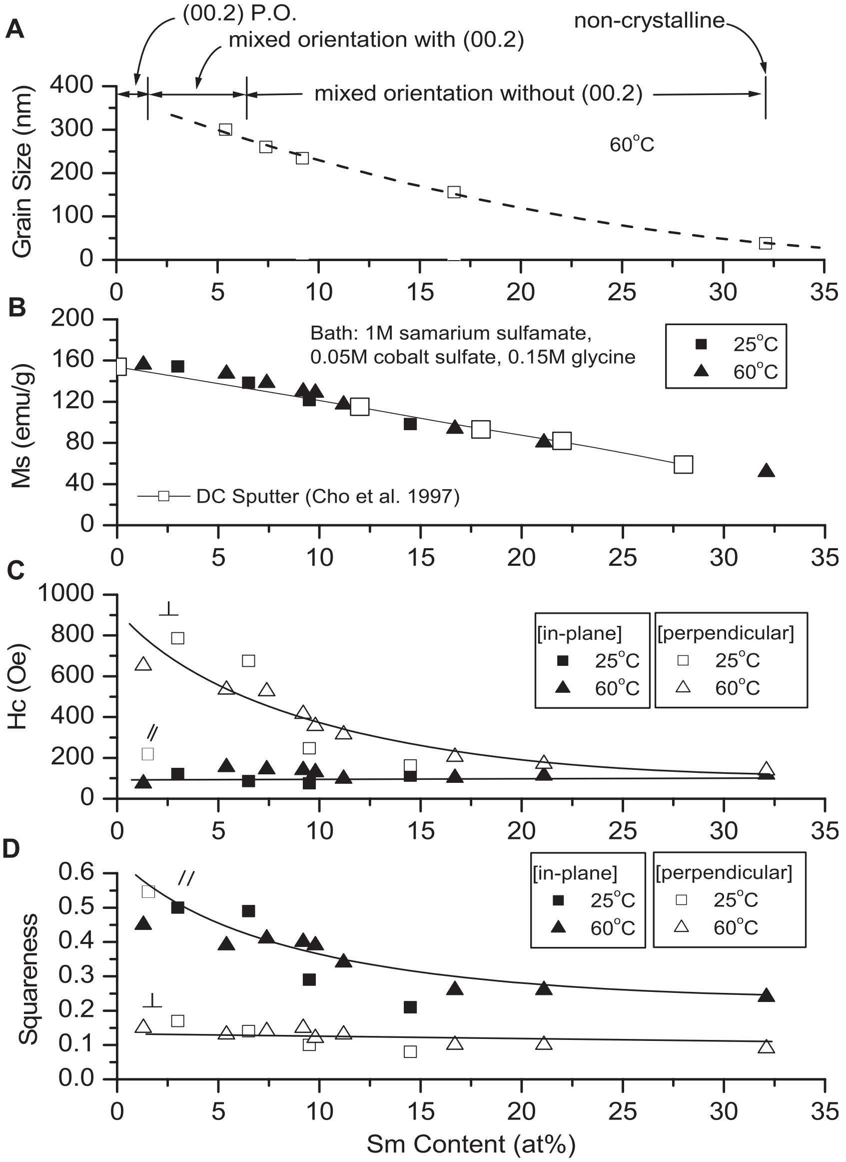

FIGURE 6 | Effect of Sm deposit content and temperature on grain size and magnetic properties.

decreasing with increased glycine concentration (>0.1 M). High deposit Sm contents were obtained with 2 to 3:1 glycine to Co ratios in the presence of excess Sm^{3+} (**Figure 8A**).

Current efficiencies (CEs) of 25°C deposits increased to 15% with increased CD and glycine concentrations. At 60°C, there appeared to be no significant CE dependence, although CE increased to 30% at higher CDs (**Figure 8B**).

XRD spectra (not shown) indicated that 0.15 M glycine containing solutions produced nanocrystalline or amorphous deposits with a weak 11.0 $Sm(OH)_3$ peak at 25°C but none at 60°C. This confirmed observations of the HC studies (Wei et al., 2008), *i.e.,* glycine inhibited formation of hydroxides in agreement with Diven et al. (2003) that glycinato-Co complexes inhibit formation of $Co(OH)_2$ in aqueous solutions. Interestingly, XRD spectra of deposits from solutions with 0.05 M or 0.5 M glycine concentrations show the presence of $Sm(OH)_3$ and $Co(OH)_2$ 11.0 peaks, which suggested an optimum concentration of complexant: M (metal ion) ratio, minimizing or inhibiting hydroxide/oxide inclusions. At 60°C, deposits also exhibited several Co (hcp) peaks which did not appear in 25°C deposit spectra.

Figure 9 shows the effects of selected complexants (0.15 M) on the deposit Sm contents. In 25°C solutions, only the amino acids appeared to be effective complexants (**Table 1**), while the other tested complexants resulted in burnt or powdery deposits containing hydroxides/oxides. Increasing solution temperature to 60°C resulted in extending the CD ranges and permitted co-deposition with other amino acids and hydroxycarboxylic acids,

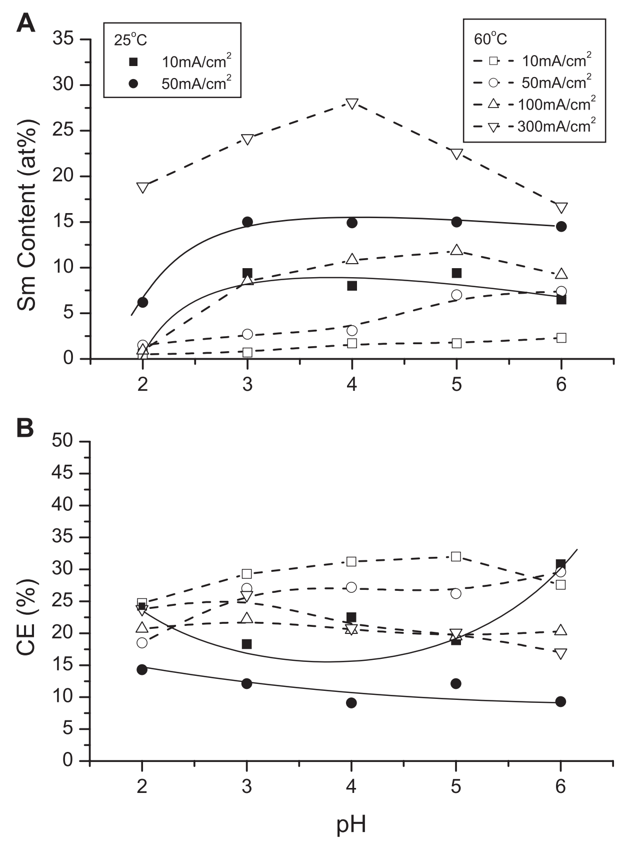

FIGURE 7 | Effect of solution pH on **(A)** Sm deposit content and **(B)** current efficiency different temperature (25 and 60°C) and various CDs.

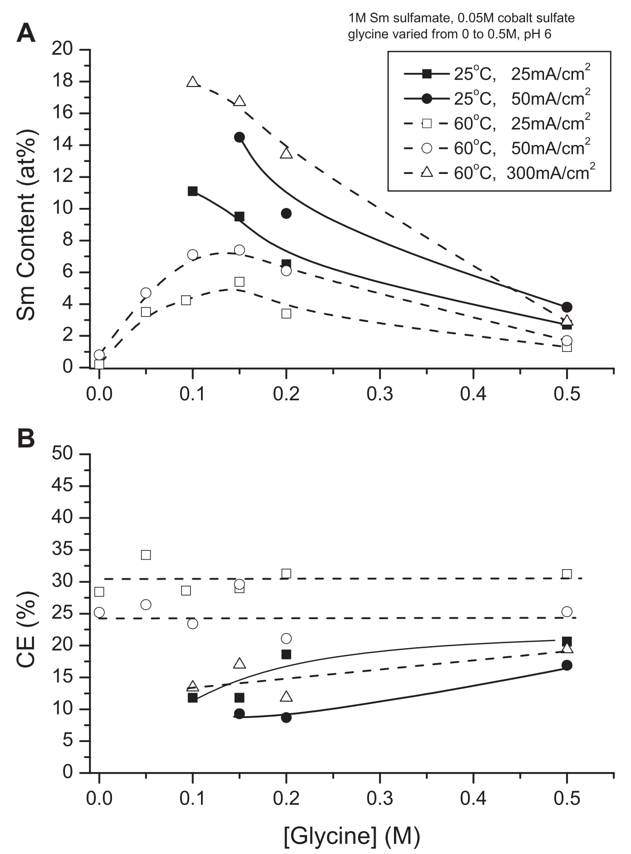

FIGURE 8 | Effect of glycine concentration on **(A)** samarium deposit content and **(B)** current efficiency at 25 and 60°C.

analogous to glycine and alanine (glycolic and lactic acids) with decreased CD_{max} (**Table 1**). Substitution of other complexants for glycine indicated glycine provided higher deposit Sm contents, but polycarboxylic acids (e.g., citric acid, EDTA) presumably resulted in stronger complexes which prevented deposition of SmCo alloys. These results suggested the bond strengths and/or structures of the various (aqueous) coordination compounds and their interdependence with the deposition variables are paramount in the co-deposition of the alloys, their compositions and magnetic properties.

Supporting electrolytes (SE) are frequently added as solution components to increase solution conductivity, stabilize solution pH, and permit higher CDs, affecting deposit composition and properties. **Figure 10** shows the effect of KCl, NH_4Cl and NH_4 sulfamate on deposit Sm content. At 25°C, KCl increased the deposit Sm content up to 18 at%, which was higher than that in the absence of supporting electrolyte (15–14 at%), while NH_4Cl and NH_4 sulfamate decreased the Sm content to 9.7 at% and 8.1 at %, respectively. CD increased substantially at 60°C in both the absence and presence of supporting electrolytes (**Figure 10**).

Ammonium compounds are widely added to plating solutions as these SE may participate in complexation of the depositing ions. Ammonium sulfamate was investigated as SE in the SmCo solutions (**Figure 11**). Increasing additions of NH_4^+ (0–1 M) decreased the deposit Sm contents from solutions at both 25°C and 60°C. This effect was more pronounced at the higher temperature: Sm deposit contents decreased from ~32 at. % Sm (no NH_4^+) to ~11 at% Sm (1 M NH_4^+) at 500 mA/cm², with similar decreases at lower CDs. This might be attributed

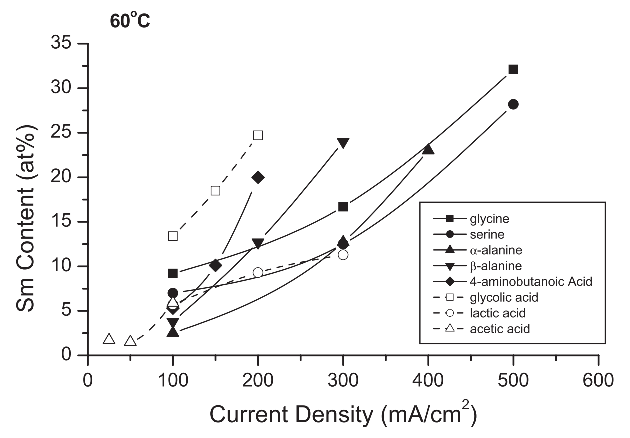

FIGURE 9 | Effect of various complexes on samarium deposit content at 60°C (pH = 5.8).

TABLE 1 | Summary of CD_{max} and max. Sm contents obtained from solutions containing different complexers.

	25°C		60°C	
Complexer	**CD_{max} (mA/cm^2)**	**Max. Sm content (at%)**	**CD_{max} (mA/cm^2)**	**Max. Sm content (at%)**
Acetic acid	nd	nd	100	6
Glycine	50	15	500	32
Serine	50	13	500	28
α-alanine	50	12	400	23
β-alanine	nd	nd	300	24
4-aminobutanoic acid	nd	nd	200	20
Glycolic acid	nd	nd	200	25
Lactic acid	nd	nd	300	11
Citric acid	nd	nd	nd	nd
EDTA	nd	nd	nd	nd

nd, non metallic deposit.

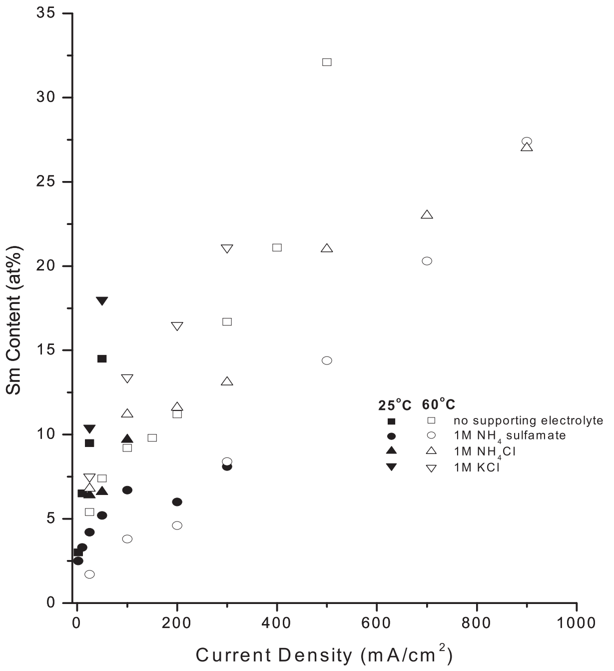

FIGURE 10 | Effect of supporting electrolyte on samarium deposit content at **(A)** 25°C (closed pts) and **(B)** 60°C (open pts) [Note- draw continuous and dashed connecting line].

to the deprotonation of ammonium ($NH_4^+ \rightarrow NH_3 + H^+$), which could form other competing complexes such as cobalt hexammine ion ($Co(NH_3)_6^{2+}$), favoring Co deposition. Furthermore, NH_3 could modify the proposed heteronuclear-glycinato-complexes (Schwartz et al., 2004) with the inclusion of bridging NH_3 ligands, which are not conductive to facilitate electron transfer in redox reactions (Taube and Gould, 1969).

Proposed Deposition Mechanism

Coordination compounds, such as inorganic complexes (ligands)—cyanide, halide, hydroxide, and phosphate complexes—, have been employed in electroplating systems since the early 1800s and are increasingly involved in many commercial processes. Organic ligands including polycarboxylic, hydroxycarboxylic, aminocarboxylic and heterocyclic compounds are also well-known complexing agents for the electrodeposition of single metals and alloys from aqueous plating solutions. Tartrates, citrates, hydroxyacetates, hydroxypropionates and glycinates are extensively employed in electroless deposition and electrodeposition of alloys.

In addition to engineering, electronic, and magnetic applications of these electrodeposited alloys, there is increasing interest in applying compatible samarium (Torres et al., 2001; Torres et al., 2003; Kremer et al., 2005), vanadium (Tsaramyrsi et al., 2001; Kaliva et al., 2002a; Kaliva et al., 2002b), molybdenum and tungsten (Kiss et al., 1995; Zhou et al., 1999; Zhou et al., 2000; Zhang et al., 2003; Zhou et al., 2004; Kustin et al., 2007) coordination compounds in biological (physiological) systems. Citrate ions participate in essential physiological processes (e. g., Krebs cycle) and as natural chelator for various metal ions; compatible amino acid and peptide complexes may interact with bodily citrate fluids and independently have enhanced effects as active biological agents for metalloenzyme processes and oncological treatments.

Yukawa and coworkers stressed the relevance of the coordination chemistry of amino acids and peptides in understanding interaction of trace metals with enzyme and other biological systems in bioinorganic and medicinal chemistry (Komiyama et al., 2008).

Franklin considered possible effects of complexation on electrodeposition mechanisms and deposition rates including adsorption or inclusion of complexed ions or molecules, complexation resulting in catalyzing deposition rate through ion bridging or ion pairing (Franklin, 1987).

The following observations pertinent to the proposed deposition mechanism were considered: only metallic Co and $Sm(OH)_3$ deposited from Sm-Co solutions. Complexation with glycine or other ligand is a required constituent for electrodeposition of Sm-Co alloys. The structure and geometrics of the complex, along with the deposition variables determined the deposition rates of both Co and Sm, the resultant alloy composition, grain size and other properties. The extensive industrial application of chromium plating was used for

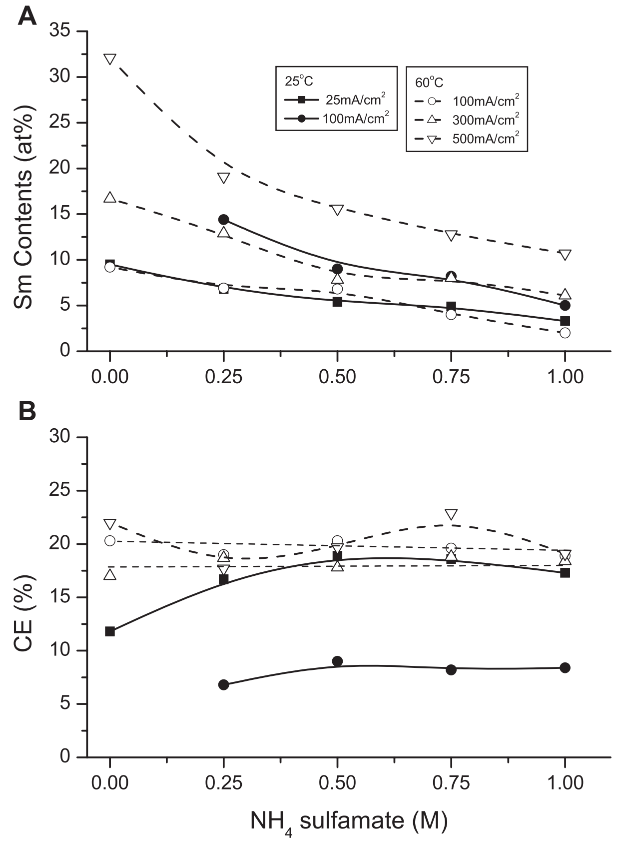

FIGURE 11 | Effect of NH$_4$ sulfamate concentration on **(A)** samarium deposit content and **(B)** current efficiency at 25 and 60°C.

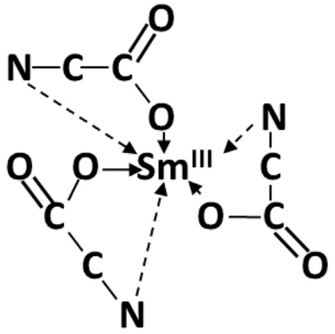

FIGURE 12 | Sm glycine chelate complexes adapted from Prados and Hadjipanayis (1999).

comparison (Hoare, 1989). Although the toxic Cr(VI) regularly electroplates to Cr, much less toxic Cr(III) cannot. Mandich reported that Cr(III) is a strongly hydrated ion, which precludes its electrodeposition to metallic Cr (Mandich, 1997). However, complexed with a suitable organic ligand, Cr(III) deposits to Cr (Danilov and Protsenko, 2001; Song and Chin, 2002).

Yukawa showed the versatility of glycine and other amino acids and peptides as complexing chelated molecules (Komiyama et al., 2008). The versatility of glycine is based, in part, on various protonation/deprotonation configurations. Sm glycino-complexes either as chelated monomeric Smgly$_3$ (**Figure 12**) or dimeric coordinated compounds, i.e., complexes resulting in high stability constants, possibly preventing electrodeposition (Torres et al., 2001; Torres et al., 2003; Kremer et al., 2005).

Zvaginsteva and Goncharov considered the polymerization of glycine as peptides (Zvaginstev and Goncharov, 1963). It is envisioned that quasi-peptides structures developed as a result of H-bonded bridges by O...H. . .N bonds. The presence of Co ions possibly inhibited Sm-glycine chelated complexes, resulting in catenated heteronuclear trisglycino- complexes coordinating cis oriented Co and Sm ions through the glycine carbonato- and amino- groups, respectively (**Figure 13**).

In gas phase catalysis, hydrogenation of organics usually proceeds by adsorbed hydrogen atoms on surfaces; this generally requires high temperatures and/or pressures as contrasted with aqueous phase hydrogenation (Ceyer, 2001). Further, in aqueous phase electrocatalysis, adsorbed hydrogen atoms readily reduce and hydrogenate organics and promote polymerization (Parravano, 1951; Park et al., 1985; Li et al., 2012).

H atoms generated and adsorbed at the cathode surface provided the electrons for the reduction and deposition of metal from the complex. The adsorbed hydrogen atoms reduced Sm^{3+} to Sm^{2+}, modifying the complex. Continued stepwise reduction by hydrogen atoms resulted in zero-valent Co^0 and Sm^0 complex, which deposited on the electrode surface, resulting in an intimately mixed deposit constituting the equivalent of an alloy, Sm$_x$Co$_y$, with variable composition, depending on deposition conditions (**Figures 13**, **14**).

Low CD deposition resulted in low Sm content and the presence of Co crystallites in the deposit. The reduction series of Co and Sm in the polymeric glycine- complexes and reaction flowchart (**Figures 13**, **14**) show the suggested stepwise reduction process, culminating in the SmCo alloy.

SUMMARY

Samarium cobalt alloys were electrodeposited from aqueous solutions containing 1 M samarium sulfamate, 0.05 M cobalt sulfate, 0.15 M glycine, in presence and absence of supporting electrolytes. While they contribute to the solution stability, the supporting electrolytes used in this work decreased the Sm content in the deposit. Glycine or other coordination compounds were essential constituents in promoting co-deposition of Sm and Co; without complexing species, only Co metal and Sm hydroxide or oxide deposited. Glycine was a preferred ligand, resulting in higher deposit Sm contents while effectively inhibiting or minimizing occluded hydroxide/oxides in the deposit.

Polarization curves showed a linear dependence of deposit Sm content on cathodic potential with higher Sm content obtained at more negative potentials than the equilibrium potential of Sm, indicating complex species were involved in the co-deposition mechanism.

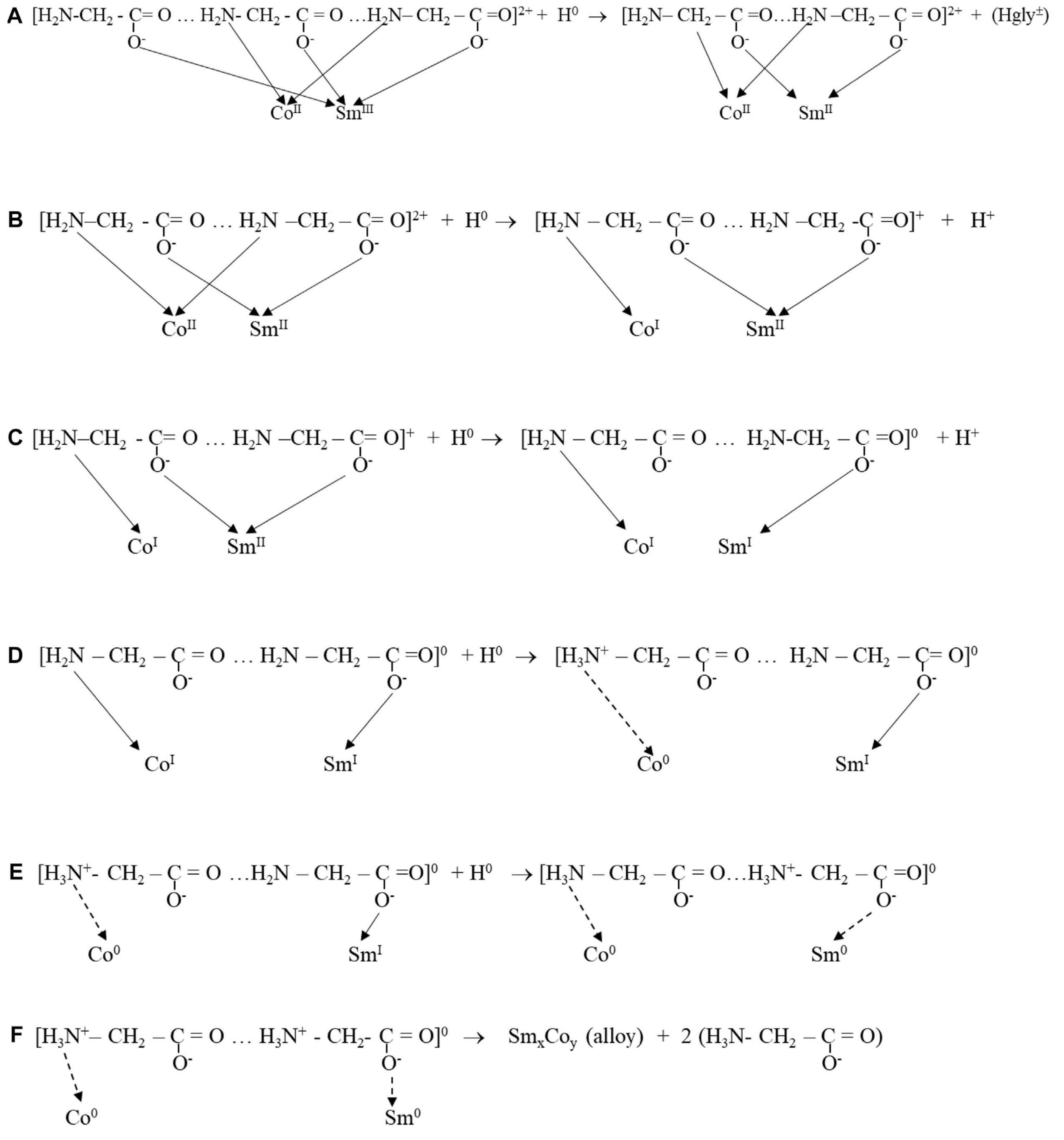

FIGURE 13 | Incremental atomic H reduction of Sm-Co ions in glycine structure.

Increased solution temperature extended the CD_{max} from 50 mA/cm^2 (25°C) to 500 mA/cm^2 (60°C), resulting in high deposit Sm contents (32 at%), which satisfied the potential stoichiometric SmCo alloy compositions after annealing. The preferred solution pH range was between 2 and 6; $pH > 6$ resulted in nonmetallic deposits.

Magnetic saturation (M_s) of deposits decreased with increased Sm content, becoming isotropic with deposits containing >30 at% Sm. Electrodeposited SmCo alloys and as-sputtered $SmCo_5$ films exhibited low coercivities (i.e., H_c of ~100 Oe as deposited).

Crystalline deposits became noncrystalline (amorphous) with increased deposit Sm content. Lower temperature and lower CD favor noncrystalline deposits with weak $Sm(OH)_3$ peaks; no $Sm(OH)_3$ peaks are observed in deposits from elevated temperatures.

A deposition mechanism involving the sequential stepwise reduction of the Sm and Co ions complexed with glycine (or other compatible ligand) by atomic hydrogen deposited at the cathode surface is proposed. Without complexation, only metallic Co and non-metallic Sm hydroxide/ oxide co-deposit.

1) $Co^{2+} + Sm^{3+} + 3\,(Hgly^{\pm}) \rightarrow [Co^{II}\,Sm^{III}\,gly^{-3}]^{2+} + 3H^{+}$

2) $[Co^{II}\,Sm^{III}gly^{-}_{3}]^{2+} + H^{0} \rightarrow [Co^{II}\,Sm^{II}\,gly^{-2}]^{2+} + (Hgly^{\pm})$

3) $[Co^{II}\,Sm^{II}gly^{-}_{2}]^{2+} + H^{0} \rightarrow [Co^{II}\,Sm^{II}gly^{-2}]^{2+} + H^{+}$

4) $[Co^{I}\,Sm^{II}gly^{-}_{2}]^{+} + H^{0} \rightarrow [Co^{I}\,Sm^{I}\,gly^{-2}]^{0} + H^{+}$

5) $[Co^{I}Sm^{I}gly^{-}_{2}]^{0} + H^{0} \rightarrow [Co^{0}Sm^{I}(gly^{-}\,Hgly^{\pm})]^{0}$

6) $[Co^{0}\,Sm^{I}\,(gly^{-}\,Hgly^{\pm})]^{0} + H^{0} \rightarrow [Co^{0}\,Sm^{0}\,Hgly^{\pm 2}]$

7) $[Co^{0}\,Sm^{0}\,Hgly^{\pm 2}] \rightarrow$ CoSm (alloy) + 2 $(Hgly^{\pm})$

FIGURE 14 | Proposed stepwise reduction of Sm-Co glycine complexes by H atoms.

AUTHOR'S NOTE

This manuscript is dedicated to the pioneering research accomplishments of Dr. Ken Nobe and Mr. Morton Schwartz, who recently passed away. They were world-renowned electrochemical engineers and electroplaters known for their research on electrochemical processes including kinetics and mechanisms of electrodissolution, electrodeposition, corrosion, electrochemical energy systems, and bioelectrochemistry. This manuscript was the last manuscript they worked on together.

DATA AVAILABILITY STATEMENT

The original contributions presented in the study are included in the article/supplementary material, further inquiries can be directed to the corresponding author.

AUTHOR CONTRIBUTIONS

JW conducted most of the experimental work. NM is assisted the submission process, revised the manuscript during review and has agreed to serve as corresponding author.

FUNDING

This work was supported in part by the NSF XYZ on a chip program (Award #0089095).

ACKNOWLEDGMENTS

Special thanks to J. Schwartz for assistance with the figures and submission. KN has not seen this submitted version; MS and NM are responsible for any errors.

REFERENCES

Adachi, H., Kimura, K., and Ino, H. (1994). Magnetic Properties of Metastable h.c.P. Samarium. *Mater. Sci. Eng. A* 181, 864–867. doi:10.1016/0921-5093(94)90757-9

Bozorth, R. M. (1978). *Ferromagnetism*. New York: IEEE Press.

Cavallotti, P., Galbiati, E., and Chen, T. (1983). *Electroplating Engineering and Waste Recycle*. Pennington, NJ: Electrodeposition Division, Electrochemical Society.

Ceyer, S. T. (2001). The Unique Chemistry of Hydrogen beneath the Surface: Catalytic Hydrogenation of Hydrocarbons. *Acc. Chem. Res.* 34 (9), 737–744. doi:10.1021/ar970030f

Chen, L., Schwartz, M., and Nobe, K. (1996). Electrodeposited Magnetic Thin Films, Electrochemically Deposited Thin Films III, in PV 96-19. Editors M. Paunovic and D. A. Scherson (San Antonio, TX: The Electrochemical Society Proceedings Series).

Cho, H. S., Salem, J. R., Kellock, A. J., and Beyers, R. B. (1997). Magnetic and Electrical Properties of Co-sm Thin Films Deposited by Dc Magnetron Sputtering. *IEEE Trans. Magn.* 33 (5), 2890–2892. doi:10.1109/20.617788

Danilov, F. I., and Protsenko, V. S. (2001). Kinetics and Mechanism of Chromium Electroplating from Cr(III) Baths. *Prot. Met.* 37 (3), 223–228. doi:10.1023/a:1010490126064

Dini, J. (1993). An Electroplater's View of PVD Processing. *Plating Surf. finishing* 80, 26.

Diven, C. F., Wang, F., Abukhdeir, A. M., Salah, W., Layden, B. T., Geraldes, C. F. G. C., et al. (2003). Evaluation of [Co(gly)3]-As a35Cl-NMR Shift Reagent for Cellular Studies. *Inorg. Chem.* 42 (8), 2774–2782. doi:10.1021/ic0258680

du Trémolet Lacheisserie, É., Gignoux, D., and Schlenker, M. (2002). *Magnetism: II-Materials and Applications*. US: Springer.

Franklin, T. C. (1987). Some Mechanisms of Action of Additives in Electrodeposition Processes. *Surf. Coat. Technol.* 30 (4), 415–428. doi:10.1016/0257-8972(87)90133-2

Hoare, J. P. (1989). An Electrochemical Mystery story: a Scientific Approach to Chromium Plating. *Plat. Surf. Finish.* 76 (9), 46–52.

Kaliva, M., Giannadaki, T., Salifoglou, A., Raptopoulou, C. P., and Terzis, A. (2002a). A New Dinuclear Vanadium(V)−Citrate Complex from Aqueous Solutions. Synthetic, Structural, Spectroscopic, and pH-dependent Studies in Relevance to Aqueous Vanadium(V)−Citrate Speciation. *Inorg. Chem.* 41 (15), 3850–3858. doi:10.1021/ic010971v

Kaliva, M., Kyriakakis, E., and Salifoglou, A. (2002b). Reactivity Investigation of Dinuclear Vanadium(IV,V)−Citrate Complexes in Aqueous Solutions. A Closer Look into Aqueous Vanadium−Citrate Interconversions. *Inorg. Chem.* 41 (26), 7015–7023. doi:10.1021/ic020323r

Kiss, T., Buglyó, P., Sanna, D., Micera, G., Decock, P., and Dewaele, D. (1995). Oxovanadium(IV) Complexes of Citric and Tartaric Acids in Aqueous Solution. *Inorg. Chim. Acta* 239 (1), 145–153. doi:10.1016/0020-1693(95)04750-6

Komiyama, T., Igarashi, S., and Yukawa, Y. (2008). Synthesis of Polynuclear Complexes with an Amino Acid or a Peptide as a Bridging Ligand. *Curr. Chem. Biol.* 2, 18. doi:10.2174/187231308784220509

Kremer, C., Torres, J., Dominguez, S., and Mederos, A. (2005). Structure and Thermodynamic Stability of Lanthanide Complexes with Amino Acids and Peptides. *Coord. Chem. Rev.* 249 (5), 567–590. doi:10.1016/j.ccr.2004.07.004

Kustin, K., Pessoa, J. C., and Crans, D. C. (2007). "Vanadium: the Versatile Metal," in *ACS Symposium Series 974.* Editors K. Kustin (Brandeis University), J. C. Pessoa (IST-Technical University of Lisboa), and D. C. Crans (Colorado State University) (Washington, D.C.: American Chemical Society), 4206. 978-0-8412-7446-4. (distributed by Oxford University Press).

Li, Z., Kelkar, S., Lam, C. H., Luczek, K., Jackson, J. E., Miller, D. J., et al. (2012). Aqueous Electrocatalytic Hydrogenation of Furfural Using a Sacrificial Anode. *Electrochimica Acta* 64, 87–93. doi:10.1016/j.electacta.2011.12.105

Mandich, N. V. (1997). Chemistry & Theory of Chromium Deposition: Part I - Chemistry. *Plating Surf. Finishing* 84 (5), 108–115.

Myung, N. V., Schwartz, M., and Nobe, K. (1999). *Fundamental Aspects of Electrochemical Deposition and Dissolution*. NJ: Pennington.

Park, K., Pintauro, P. N., Baizer, M. M., and Nobe, K. (1985). Flow Reactor Studies of the Paired Electro-Oxidation and Electroreduction of Glucose. *J. Electrochem. Soc.* 132 (8), 1850–1855. doi:10.1149/1.2114229

Parravano, G. (1951). Polymerization Induced by Hydrogen in Metals*. *J. Am. Chem. Soc.* 73 (2), 628–630. doi:10.1021/ja01146a039

Prados, C., and Hadjipanayis, G. C. (1998). Magnetic and Structural Properties of High Coercivity Sm(Co, Ni, Cu) Sputtered Thin Films. *J. Appl. Phys.* 83 (11), 6253–6255. doi:10.1063/1.367804

Prados, C., and Hadjipanayis, G. C. (1999). Sm(Co, Cu, Ni) Thin Films with Giant Coercivity. *Appl. Phys. Lett.* 74 (3), 430–432. doi:10.1063/1.123051

Ruan, S., and Schuh, C. A. (2008). Mesoscale Structure and Segregation in Electrodeposited Nanocrystalline Alloys. *Scripta Materialia* 59 (11), 1218–1221. doi:10.1016/j.scriptamat.2008.08.010

Schwartz, M., et al. 1999.

Schwartz, M., Myung, N. V., and Nobe, K. (2004). Electrodeposition of Iron Group-Rare Earth Alloys from Aqueous Media. *J. Electrochem. Soc.* 151 (7), C468. doi:10.1149/1.1751196

Song, Y. B., and Chin, D.-T. (2002). Current Efficiency and Polarization Behavior of Trivalent Chromium Electrodeposition Process. *Electrochimica Acta* 48 (4), 349–356. doi:10.1016/s0013-4686(02)00678-3

Strnat, K. J., and Strnat, R. M. W. (1991). Rare Earth-Cobalt Permanent Magnets. *J. Magnetism Magn. Mater.* 100 (1), 38–56. doi:10.1016/0304-8853(91)90811-n

Taube, H., and Gould, E. S. (1969). Organic Molecules as Bridging Groups in Electron-Transfer Reactions. *Acc. Chem. Res.* 2 (11), 321–329. doi:10.1021/ar50023a001

Torres, J., Kremer, C., Kremer, E., Pardo, H., Russi, S., Mombrú, Á., et al. (2003). Sm(III) Complexation with Small Peptides. Crystal Structure of [Sm2(Gly-Val) 4(H2O)8](ClO4)6·2H2O. *Inorg. Chim. Acta* 355, 442–448. doi:10.1016/s0020-1693(03)00373-6

Torres, J., Kremer, C., Kremer, E., Pardo, H., Suescun, L., Mombru, Á., et al. (2001). Sm(III) Complexation with α-amino Acids. *J. Alloys Compd.* 323-324, 119–124. doi:10.1016/s0925-8388(01)00979-3

Tsaramyrsi, M., Kaliva, M., Salifoglou, A., Raptopoulou, C. P., Terzis, A., Tangoulis, V., et al. (2001). Vanadium(IV)−Citrate Complex Interconversions in Aqueous Solutions. A pH-dependent Synthetic, Structural, Spectroscopic, and Magnetic Study. *Inorg. Chem.* 40 (23), 5772–5779. doi:10.1021/ic010276n

Wei, J. C., Schwartz, M., and Nobe, K. (2008). Aqueous Electrodeposition of SmCo Alloys. *J. Electrochem. Soc.* 155 (10), D660. doi:10.1149/1.2961013

Wei, J. C., Schwartz, M., and Nobe, K. (2006). Parametric Aqueous Electrodeposition Studies of Co-sm Alloys. *ECS Trans.* 1 (4), 273–278.

Wei, J., Schwartz, M., and Nobe, K. (2009). DC Aqueous Electrodeposition of Sm-Co Permanent Magnets. *ECS Trans.* 16 (45), 129.

Zhang, H., Zhao, H., Jiang, Y.-Q., Hou, S.-Y., Zhou, Z.-H., and Wan, H.-L. (2003). pH- and Mol-Ratio Dependent Tungsten(VI)-citrate Speciation from Aqueous Solutions: Syntheses, Spectroscopic Properties and crystal Structures. *Inorg. Chim. Acta* 351, 311–318. doi:10.1016/s0020-1693(03)00177-4

Zhou, Z.-H., Hou, S.-Y., and Wan, H.-L. (2004). Peroxomolybdate(vi)-citrate and -malate Complex Interconversions by pH-Dependence. Synthetic, Structural and Spectroscopic Studies. *Dalton Trans.* (9), 1393–1399. doi:10.1039/b315280d

Zhou, Z.-H., Wan, H.-L., and Tsai, K.-R. (1999). Bidentate Citrate with Free Terminal Carboxyl Groups, Syntheses and Characterization of Citrato Oxomolybdate(VI) and Oxotungstate(VI), Δ/Λ-Na2[MO2(H2cit)2]·3H2O (M = Mo or W). *J. Chem. Soc. Dalton Trans.* (24), 4289–4290. doi:10.1039/a908739g

Zhou, Z.-H., Wan, H.-L., and Tsai, K.-R. (2000). Syntheses and Spectroscopic and Structural Characterization of Molybdenum(VI) Citrato Monomeric Raceme and Dimer, K4[MoO3(cit)]·2H2O and K4[(MoO2)2O(Hcit)2]·4H2O. *Inorg. Chem.* 39 (1), 59–64. doi:10.1021/ic990042s

Zvaginstev, O. E., and Goncharov, E. V. (1963). *Russ. Inorg. Chem.* 8, 179.

Conflict of Interest: The authors declare that the research was conducted in the absence of any commercial or financial relationships that could be construed as a potential conflict of interest.

frontiers in Chemistry

ORIGINAL RESEARCH
published: 10 September 2021
doi: 10.3389/fchem.2021.733383

Magnetic Properties of Electrodeposited Cobalt-Platinum (CoPt) and Cobalt-Platinum-Phosphide (CoPtP) Thin Films

D.-Y. Park[1]* and N. V. Myung[2]

[1]Department of Advanced Materials Engineering, Hanbat National University, Daejeon, South Korea, [2]Department of Chemical and Biomolecular Engineering, University of Notre Dame, Notre Dame, IN, United States

CoPt and CoPtP thin films were synthesized using direct current (DC) aqueous electrodeposition from weak alkaline solutions. The basic plating solutions of binary CoPt thin films consisted of cobalt pyrophosphate [$Co_2P_2O_7$] and chloroplatinic acid [H_2PtCl_6]. Various amounts of sodium hypophosphite [NaH_2PO_2] was added to deposit ternary CoPtP thin films. The film composition was adjusted by varying the several electrodeposition parameters including electrolyte composition, solution pH, and current density and correlated to their microstructure and magnetic property (*i.e.* coercivity and squareness). For the binary CoPt thin films, the maximum coercivities [in-plane coercivity ($H_{c,//}$) = ~1,600 Oe, and perpendicular coercivity ($H_{c,\perp}$) = ~2,500 Oe] were obtained from electrolytes containing 0.01 M H_2PtCl_6 + 0.04 M $Co_2P_2O_7$ at current density (CD) of 7.5 mA cm^{-2}. In the case of ternary CoPtP electrodeposits, the maximum coercivities ($H_{c,//}$ = ~2,600 Oe, and $H_{c,\perp}$ = ~3,800 Oe) were achieved from baths containing 0.015 M H_2PtCl_6, 0.07 M $Co_2P_2O_7$, 0.8 M NaH_2PO_2 at CD of 7.5 mA cm^{-2} and solution pH 9. It was suggested that microstructure and magnetic properties are affected not only by the type of substrate but also by chemical compositions and electrodeposition conditions.

Keywords: cobalt-platinum, cobalt-platinum-phosphide, electrodeposition, magnetic thin film, hard magnetic material

Edited by:
Xiaopeng Han,
Tianjin University, China

Reviewed by:
Edward Gillan,
The University of Iowa, United States
Yunpei Zhu,
King Abdullah University of Science and Technology, Saudi Arabia

***Correspondence:**
D.-Y. Park
dypark@hanbat.ac.kr

Specialty section:
This article was submitted to Electrochemistry, a section of the journal Frontiers in Chemistry

Received: *30 June 2021*
Accepted: *30 August 2021*
Published: *10 September 2021*

Citation:
Park D-Y and Myung NV (2021) Magnetic Properties of Electrodeposited Cobalt-Platinum (CoPt) and Cobalt-Platinum-Phosphide (CoPtP) Thin Films. Front. Chem. 9:733383. doi: 10.3389/fchem.2021.733383

INTRODUCTION

CoPt and CoPtP alloys are promising hard magnetic materials due to their high magnetocrystalline anisotropy and magnetic saturation (Bozorth, 1963; Myung et al., 2003). $Co_{50}Pt_{50}$ alloy has tetragonal $L1_O$ ordered phase material and shows very high coercivities (>10,000 Oe) (Coffey et al., 1995). Because of their excellent hard magnetic properties, they are of interest in the areas such as magnetic sensors and magnetic microelectromechanical systems (mag-MEMS) (Myung et al., 2003; Park et al., 1995; Vieux-Rochaz et al., 2006).

CoPt thin films were mostly obtained using vacuum processes such as molecular-beam epitaxy (MBE) (Lee et al., 1991), and sputtering (Coffey et al., 1995; Carcia et al., 1993; Farrow and Marks, 1998). In these vacuum processes, CoPt was deposited as multilayered structures and followed by post thermal treatment to make ordered phases. The requirement of post thermal treatment limited

TABLE 1 | Bath compositions and operating conditions (unless otherwise noted) for binary CoPt thin films (M = mol dm^{-3}).

Chemical/condition	Concentration/unit				
Pt^{4+} (as $H_2PtCl_6{\cdot}6H_2O$) (M)	0.01	0.005–0.025	0.015	0.01	0.015
Co^{2+} (as $Co_2P_2O_7$ referred to **Table 2**) (M)	0.005–0.1	0.07	0.07	0.02	0.07
$Na_3PO_4{\cdot}12H_2O$ (M)	0.365	0.365	0.365	0.365	0.365
$NaH_2PO_2{\cdot}H_2O$ (M)	—	—	—	0 or 0.1	0.01–0.8
Solution pH	8	8	7–10	8	9
Current density (mA·cm^{-2})	7.5	7.5	7.5–100	7.5–100	7.5
Deposit charge (C) (deposit time) (sec)	15 (2,000)	15 (2,000)	15 (2,000)	15 (2,000)	15 (2,000)
Corresponding figures	1 and 2	3 and 4	3 and 5	6, 7 and 8	9

the applications including mag-MEMS since most of MEMS structure cannot survive at these high temperatures (e.g., 500–700 °C). Therefore, an alternative near room temperature deposition process such as electrodeposition is needed. Electrodeposition process over vacuum processes has many benefits such as easy scale up and maintenance, lower operating temperature, low cost, the ability of tailoring microstructure and properties. Therefore, it was widely used in many research fields including thin film, nanostructures including nanocrystals, nanorod etc. (Park et al., 1995; Myung et al, 2003; Zhu et al., 2015a; Zhu et al., 2015b).

Despite the needs for integration of magnetic CoPt and CoPtP alloys by electrodeposition at near room temperature, limited works were carried out for electrodeposition baths and conditions. Tabakovic et al. and Dragos-Pinzaru et al. conducted electroanalytical study and electroplating parameters (e.g., electrodeposition time, Co^{2+} concentration, additive, solution pH etc.) on film composition and magnetic properties (Tabakovic et al., 2015; Tabakovic et al., 2016; Dragos-Pinzaru et al., 2017). Kim et al. also investigated magnetic properties (*e.g.,* coercivity, magnetic moment etc.) to film thickness (Kim et al., 2013). Guillamat et al. electrodeposited CoPt thin film from deep eutectic solvent (Guillamat et al., 2012) whereas Hnida et al. electrodeposited nanowires using template directed method (Hnida et al., 2016). Eagleton et al. reported coercivity of 2,000–4,000 Oe for 50 nm–10 μm thick CoPtP films (Eagleton et al., 2005). Vieux-Rochaz et al. integrated hard magnetic CoPtP material into mag-MEMS (Vieux-Rochaz et al., 2006).

In this study, magnetic CoPt and CoPtP thin film alloys were systematically electrodeposited using the various plating solutions containing chloroplatinic acid, cobalt pyrophosphate and sodium hypophosphite. Dependence of various electrodeposition parameters including solution composition (e.g $[Pt^{4+}]$ $[Co^{2+}]$ and $[H_2PO_2^-]$), solution pH, current density on current efficiency, magnetic properties, and microstructure were investigated.

EXPERIMENTAL

For binary CoPt thin films, the dependence of deposit contents, current efficiencies, and extrinsic magnetic properties (*i.e.,* coercivity and squareness) on Co^{2+} ion concentration in plating baths was investigated. The bath compositions and operating conditions are listed in **Table 1** (conditions for **Figures 1,2**). Co^{2+} concentration in the bath was controlled using Co-pyrophosphate solution as shown in **Table 2** (conditions for **Figures 1,2**). After the optimum Co^{2+} concentration in the bath for the best coercivity ($H_{c,\perp}$ and $H_{c,//}$) of CoPt thin film was determined, the dependence of current efficiency and coercivity in CoPt thin films on concentration of Pt^{4+} in plating bath was studied. The bath compositions and operating conditions are listed in **Table 1** (conditions for **Figures 3,4**). Both Co^{2+} and Pt^{4+} concentrations for the optimum coercivity of CoPt thin film were determined as 0.07 and 0.015 M, respectively and listed in **Table 1** (conditions for **Figures 3,5**). Dependence of current efficiencies in the CoPt thin films on solution pH was also studied. Then a better bath composition and solution pH (conditions for **Figures 6,7,8**) was determined as shown in **Table 1**. The optimum current density for the best coercivity of CoPt thin film was tested using the bath compositions and conditions of **Table 1** with/without NaH_2PO_2 concentration (as P source). Finally, the optimum electroplating conditions for the best coercivity of CoPt thin film as shown in **Table 1** (conditions for **Figure 9**) was obtained. Magnetic properties [parallel (in-plane) and perpendicular (out-of-plane) coercivity ($H_{c,//}$ and $H_{c,\perp}$), and parallel (in-plane) and perpendicular (out-of-plane) squareness ($S_{//}$ and $S_\perp$)] were examined by varying the NaH_2PO_2 concentration from 0.01 to 0.8 M. All the CoPt and CoPtP thin films were electrodeposited on brass substrates; Pt (mesh) coated

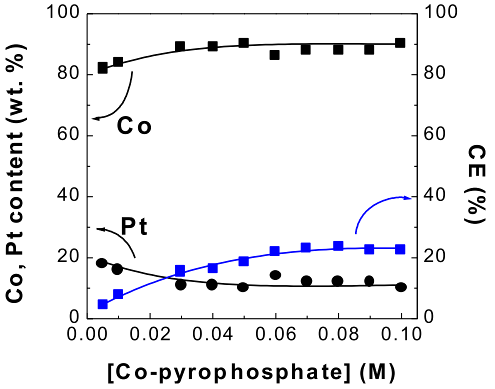

FIGURE 1 | Dependence of Co, Pt contents and current efficiency (CE) of CoPt thin film on Co-pyrophosphate concentration.

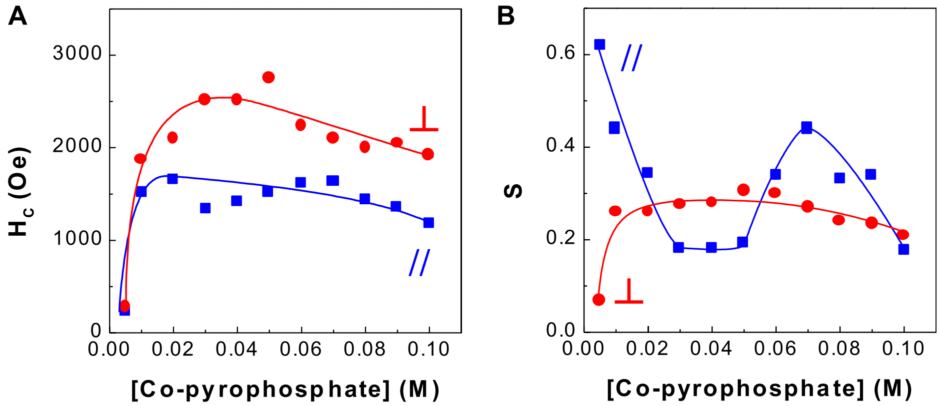

FIGURE 2 | Dependence of coercivity and squareness of CoPt thin films on Co-pyrophosphate concentration **(A)** coercivity and **(B)** squareness.

TABLE 2 | Bath compositions (unless otherwise noted) for Co-pyrophosphate solution (M = mol dm^{-3}).

Chemical/condition	Concentration (M)/unit
Co^{2+} (as $CoSO_4 \cdot 7H_2O$)	0.120 M
$Na_4P_2O_7$	0.451 M
NH_4OH	1 ml/L
Solution pH	8.5

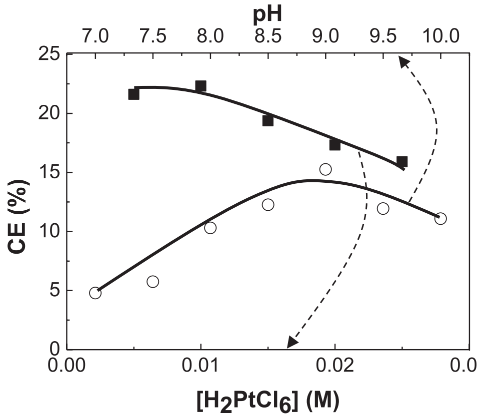

FIGURE 3 | Dependence of current efficiency (CE) of CoPt thin films on H_2PtCl_6 concentration and solution pH.

on Ti core was used as an insoluble anode. Brass substrates were used because they exhibit no magnetic property, specially coercivity and squareness, at all. Solutions were exposed to air. All the films were electrodeposited without stirring at room temperature.

Deposit Co and Pt contents in CoPt and CoPtP thin films were analyzed using atomic absorption spectroscopy (AAS). P content in the CoPtP thin films could not be analyzed using both AAS and energy dispersive spectroscopy (EDS) because of interference between Pt and P elements. Magnetic properties such as coercivity (H_C) and squareness ($S = M_r/M_S$) were measured using a vibrating sample magnetometer (VSM) (Model 880, ADE technologies Inc.). Microstructures of CoPt and CoPtP thin films were examined using an X-ray diffractometer (XRD) (Model 42202, Norelco, North American Phillips Company Inc.) with K_α radiation to identify the phases. Conditions of XRD were a scanning range of 20–100° with 0.03° increments and a one second dwell time.

RESULTS AND DISCUSSION

Figure 1 shows the dependence of Co and Pt contents in electrodeposits and current efficiency (CE) on Co^{2+} concentrations. Deposited Co content in electrodeposits increased from 82 to 90 wt% with increasing Co^{2+} concentration from 0.005 to 0.1 M, while Pt content decreased from 19 to 10 wt%. Current efficiency increased from 4 to 22%. Very limited work for deposit Co content and current efficiency in CoPt alloy was reported. Dragos-Pinzaru et al. electrodeposited CoPt films from hexachloroplatinate solutions: 0.4 M H_3BO_3, 0.3 M NH_4Cl, 0.1 M $CoSO_4 \cdot 7H_2O$, 0.00386 M H_2PtCl_6 with/without 3.89 mM saccharin (Dragos-Pinzaru et al., 2017). They reported deposit Co content of 28.8–66.9 wt% (56–87 at%) with the change of deposit time from 10 s to 300 s. Deposit Co content of 82–90 wt% in this study is significantly higher than that (28.8–66.9 wt%) in the article reported by Dragos-Pinzaru et al. (Dragos-Pinzaru et al., 2017). Also, they investigated the effect of deposit time on current efficiency at different pH and different Co^{+2} ion concentration and reported the current efficiency of 55–68% and 55–78% with the change of deposit time, respectively. They reported about 2.5–20 times higher current efficiency (55–78%) than that (4–22%) of this study. Relatively low current efficiency in this study compared to that reported by Dragos-Pinzaru et al. (Dragos-Pinzaru et al., 2017) may be attributed to the different chemical compositions. That is, the applied current in this paper was used very much in side reactions such as the evolution of hydrogen gases on cathode and oxygen gases on anode.

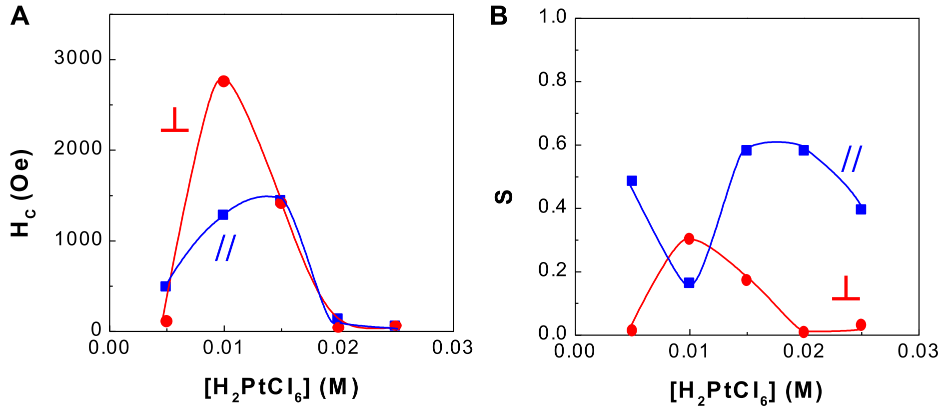

FIGURE 4 | Dependence of coercivity and squareness of CoPt thin films on H_2PtCl_6 concentration **(A)** coercivity and **(B)** squareness.

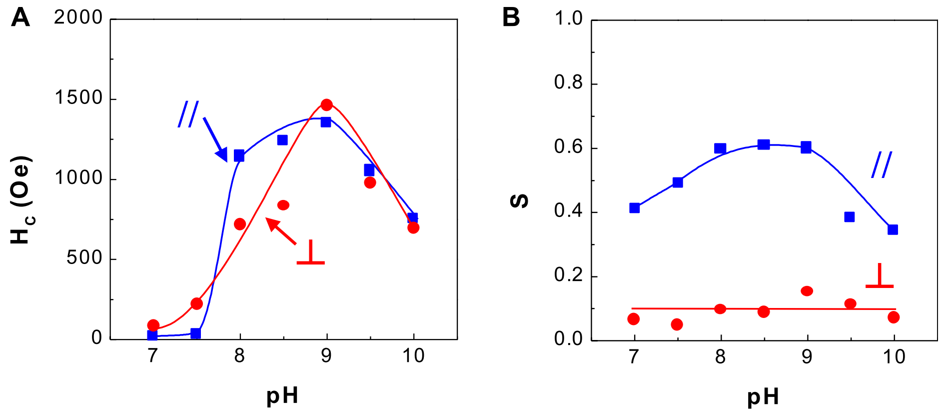

FIGURE 5 | Dependence of coercivity and squareness of CoPt thin films and solution pH **(A)** coercivity and **(B)** squareness.

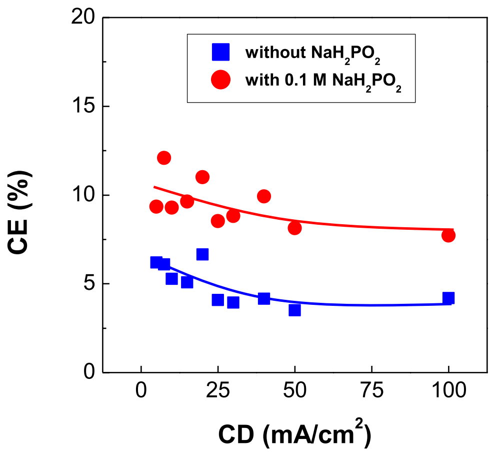

FIGURE 6 | Dependence of current efficiency (CE) of CoPt thin films on current density (CD) (The values of CE in the red curve are similar or lower than that in **Figures 1**, **3**).

Figure 2 shows the dependence of hard magnetic properties (*i.e.*, coercivity and squareness) of binary CoPt electrodeposits. The optimum Co^{2+} concentrations with high coercivity were observed in the range of 0.03–0.07 M. In this range of Co^{2+} concentrations, parallel coercivities ranged from ~1,400 to ~1,600 Oe whereas perpendicular coercivities ranged from ~2,200 to ~2,800 Oe. On the other hand, parallel and perpendicular squareness ($S_{//}$ and $S_{\perp}$) were measured to be ranged from ~0.2 to ~0.5 and about 0.25, respectively. Tabakovic et al. obtained the coercivity of $H_{C,//}$ = 221 Oe and $H_{C,\perp}$ = 254 Oe from $Co_{80}Pt_{20}$ films deposited on Cu substrate [oxidized Si wafer/Ta (5 nm)/Cu (200 nm)/CoPt (15–20 nm)] (Tabakovic et al., 2016). Also the coercivity of $H_{C,//}$ = 629 Oe and $H_{C,\perp}$ = 1,220 Oe in $Co_{80}Pt_{20}$ films deposited on Ru substrate [oxidized Si wafer/Ta (5 nm)/Ru (200 nm)/CoPt (15–20 nm)] was reported. It is well known that perpendicular anisotropy of CoPt films obtained either by electrodeposition or vacuum deposition highly depend on the underlayer types such as Cu and Ru (Wierman et al., 2002; Pattanaik et al., 2006; Vokoun et al.,

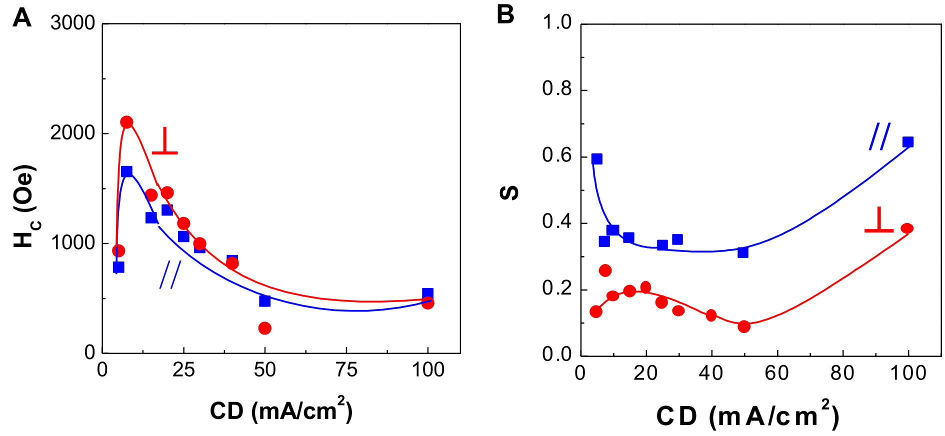

FIGURE 7 | Dependence of coercivity and squareness of CoPt thin films on current density (CD) **(A)** coercivity and **(B)** squareness.

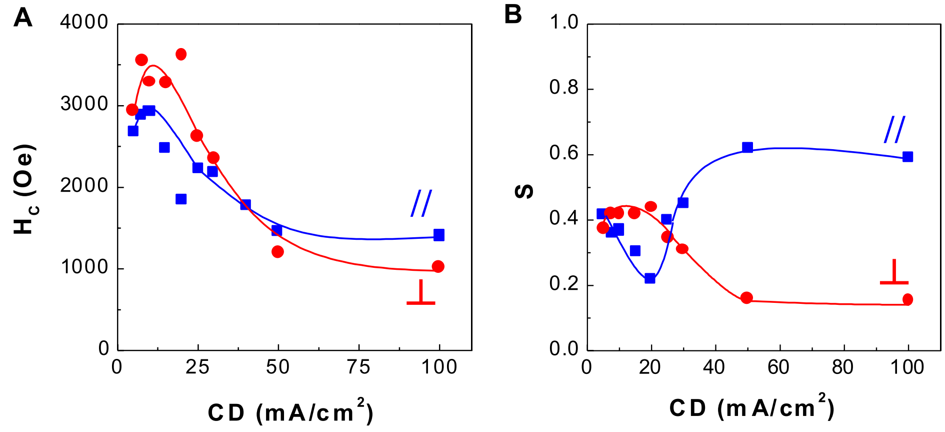

FIGURE 8 | Dependence of coercivity and squareness of CoPtP thin films on current density (CD) **(A)** coercivity and **(B)** squareness.

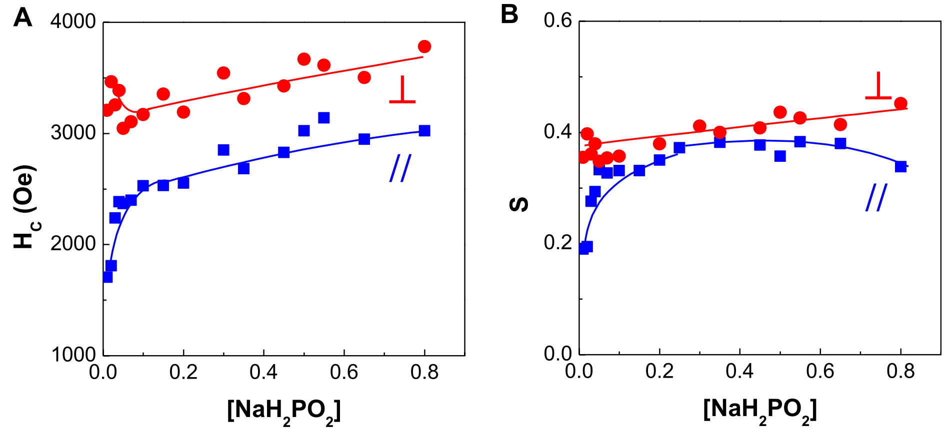

FIGURE 9 | Dependence of coercivity and squareness of CoPtP thin films on NaH_2PO_2 concentration **(A)** coercivity and **(B)** squareness.

2006; Wodarz et al., 2016). Because, in this study, brass substrate was used and parallel coercivities ranged from ~1,400 to ~1,600 Oe and perpendicular coercivities ranged from ~2,200 to ~2,800 Oe were obtained, we can suggest that the type of substrate strongly affects coercivities of CoPt films.

Figure 3 shows the dependence of current efficiency on H_2PtCl_6 concentration and solution pH in the baths. Current efficiency decreased from 22 to 17% with increasing H_2PtCl_6 concentration. No work for the dependence of the change of H_2PtCl_6 concentration on current efficiency in CoPt alloy was reported as far as we know. Current efficiency as a function of $CoSO_4$ concentration (0.1 and 0.25 M) in the bath for electrodeposited CoPt films was measured by Dragos-Pinzaru et al. (Dragos-Pinzaru et al., 2017). They reported that the bath with higher concentration of 0.25 M $CoSO_4$ exhibits the current efficiency of about 61–65%, while the bath with lower concentration of 0.1 M $CoSO_4$ shows the current efficiency of about 55–60%. The change of $CoSO_4$ concentration in the bath resulted in the decrease of about 6% in current efficiency. However, it was reported that deposit Co content in CoPt films was almost the same as 66.9 wt% (87 at%) for both concentrations of 0.1 and 0.25 M $CoSO_4$ in the bath. Therefore, some decrease of current efficiency from 22 to 17% with increasing H_2PtCl_6 concentration in this study is expected. Because the increase of Co^{2+} concentration in the bath (see **Figure 1**) from 0 to 0.1 M results in the decrease of deposit Pt content and the increase of deposit Co content in the CoPt films, we can suggest that more Co^{2+} concentration in the bath means more deposit Co content in CoPt films; more H_2PtCl_6 concentration in the bath gives more deposit Pt content in the CoPt films, resulting in the decrease of current efficiency.

The dependence of current efficiency on solution pH is also shown in **Figure 3**. Maximum current efficiency (~20%) was obtained at pH 9. Dragos-Pinzaru et al. investigated the influence of solution pH (2.5 and 5.5) on the current efficiency of electrodeposited CoPt films from hexachloroplatinate solutions (Dragos-Pinzaru et al., 2017). They reported that the current efficiency in the bath with pH 2.5 and 5.5 was measured to be about 62 and 66%, respectively. We believe from **Figure 1** that about three times higher current efficiency of CoPt films reported by Dragos-Pinzaru et al. (Dragos-Pinzaru et al., 2017) than that of this study may be attributed to the different chemical compositions in the baths. The change of solution pH somewhat has an influence on the current efficiency. The current efficiency highly depends on the chemical compositions in the baths rather than solution pH.

Figure 4 shows the dependence of coercivity and squareness of binary CoPt thin film alloys on H_2PtCl_6 concentration. This experimental work was carried out in order to find higher coercivity of CoPt films in the bath compositions and operating conditions as shown in **Table 1**. The optimum coercivity ($H_{C,//}$ = ~1,000 Oe and $H_{C,\perp}$ = ~2,700 Oe) was obtained at 0.01 M Pt concentration, while parallel and perpendicular squarenesses were measured as ~0.18 and ~0.3, respectively.

Figure 5 shows the dependence of coercivity and squareness of CoPt alloys on solution pH. The optimum coercivity ($H_{C,//}$ = ~1,250 Oe and $H_{C,\perp}$ = ~1,300 Oe) was obtained at solution pH 8–9. Parallel and perpendicular squarenesses at solution pH 8–9 were measured as ~0.6 and ~0.1, respectively. It was observed that the change of solution pH has a considerable effect on the coercivity of CoPt films.

Figure 6 exhibits the dependence of current efficiency of binary CoPt and ternary CoPtP electrodeposits on current density. The current efficiencies were slightly decreased with increasing current density for both CoPt and CoPtP electrodeposits. The addition of 0.1 M NaH_2PO_2 in the plating bath resulted in the slight decrease of current efficiency from 10 to 7%. Dragos-Pinzaru et al. investigated the influence of saccharin (with/without 3.89 mM) as an additive on current efficiency of CoPt films electrodeposited from hexachloroplatinate solutions (Dragos-Pinzaru et al., 2017). Higher current efficiency (78%) was observed in CoPt films electrodeposited from the bath containing no saccharin, while CoPt films electrodeposited from the bath containing 3.89 mM saccharin exhibits lower current efficiency (66%). Therefore, we can suggest that the current efficiency obtained in CoPt films electrodeposited from hexachloroplatinate solutions was influenced by the type of additive such as saccharin (Dragos-Pinzaru et al., 2017) or sodium hypophosphite (NaH_2PO_2) (this study). In this study, the current efficiency was measured as 22% at the most or less. Therefore, we can summarize from **Figures 1**, **3**, **6** that current efficiency obtained in CoPt films electrodeposited from hexachloroplatinate solutions much depend on the bath compositions rather than the type of additives, solution pH, $CoSO_4$, and H_2PtCl_6. That is, current efficiencies in the baths used by Dragos-Pinzaru et al. (Dragos-Pinzaru et al., 2017) were much higher than that in the baths used by this study.

Figures 7, **8** show the corresponding coercivity and squareness of binary CoPt (**Figure 7**; electrodeposited from the bath

TABLE 3 | Comparison of some important results representing high coercivities in CoPt/CoPtP thin films.

Coercivity (Oe)		Alloy/substrate	References
$H_{c,//}$	$H_{c,\perp}$		
629	1,220	CoPt/Ru	Tabakovic et al. (2016)
221	254	CoPt/Cu	
—	4,500–6,700	CoPt (10–30 nm thick)/Ru	Dragos-Pinzaru et al. (2017)
1700–3,000	3,200–3,700	CoPt/brass	This study

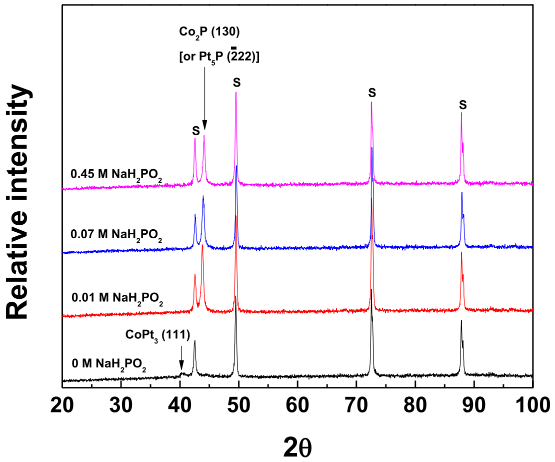

FIGURE 10 | XRD patterns of CoPt and CoPtP thin films electrodeposited on brass substrate with the change of NaH_2PO_2 concentration in the plating baths; relative intensity vs NaH_2PO_2 concentration (S: substrate).

containing no NaH_2PO_2) and ternary CoPtP electrodeposits (**Figure 8**; electrodeposited from bath containing 0.1 M NaH_2PO_2). **Figures 7**, **8** were carried out at optimum conditions (using the conditions from **Table 1**; Co^{2+} and Pt^{4+} concentrations, solution pH, and current density) in order to get the best coercivity in CoPt films. In binary CoPt electrodeposits, high coercivity ($H_{C,//}$ = ~1,600 Oe and $H_{C,\perp}$ = ~2,100 Oe) was obtained at the current density of 7.5 mA/cm^2. On the other hand, parallel and perpendicular squarenesses at the current density of 7.5 mA/cm^2 were measured as ~0.35 and ~0.2, respectively. There is no research work for the effect of adding sodium hypophosphite (NaH_2PO_2) into the baths for binary CoPt thin films. In ternary CoPtP electrodeposits of this study (**Figure 8**), high coercivity ($H_{C,//}$ = ~3,000 Oe and $H_{C,\perp}$ = ~3,500 Oe) was obtained from 7.5 to 20 mA/cm^2. Also, parallel and perpendicular squarenesses at the current density of 7.5–20 mA/cm^2 were measured as ~0.4 and 0.2–0.4, respectively.

Figure 9 shows the dependence of coercivity and squareness of CoPtP alloys on NaH_2PO_2 concentration in the plating baths. Parallel coercivity increased from ~1,700 to ~2,700 Oe with increasing NaH_2PO_2 concentration from 0.01 to 0.8 M, while perpendicular coercivity was maintained at the range of 3,000–3,500 Oe. Perpendicular squareness was slightly increased and parallel squareness was increased from ~0.2 to 0.37 with increasing NaH_2PO_2 concentration. The addition effect of NaH_2PO_2 concentration in the bath for electrodeposited CoPt films was much higher in parallel coercivity than in perpendicular coercivity. Also, the similar effect both for parallel and perpendicular squarness was observed.

Figure 10 shows XRD patterns of binary CoPt and CoPtP thin film alloys with increasing NaH_2PO_2 concentration in the baths. For the binary CoPt thin film, it is analyzed that CoPt thin films consist of mainly amorphous crystalline and small intensity of $CoPt_3$ (111) phases (JCPDS file #: 29–499). For the ternary CoPtP thin film, CoPtP thin films consist of both amorphous crystalline and Co_2P (130) (JCPDS file #: 6–306) [or Pt_5P_2 ($\bar{2}22$) (JCPDS file #: 23–465)] peaks. The addition of NaH_2PO_2 into the baths for the binary CoPt films results in the considerable increase of intensity of Co_2P (130) (JCPDS file #: 6–306) [or Pt_5P_2 ($\bar{2}22$) (JCPDS file #: 23–465)] peaks. Tabakovic et al. investigated the influence of different substrates (Cu and Ru) on the peaks in XRD patterns in CoPt films electrodeposited from hexachloroplatinate solutions (Tabakovic et al., 2016). Zana et al. also reported the same results of XRD using electrodeposited CoPt on Cu seed layer (Zana and Zangari, 2004). It was reported that CoPt films electrodeposited on Cu substrate [oxidized Si wafer/Ta (5 nm)/Cu (200 nm)/CoPt (15–20 nm)] consists of hcp CoPt (10.0), (00.2) and (10.1), at 41.2°, 43.4°, 46.4° 2θ values, respectively (Tabakovic et al., 2016). On the other hand, CoPt films electrodeposited on Ru substrate [oxidized Si wafer/Ta (5 nm)/Ru (200 nm)/CoPt (15–20 nm)] exhibits hcp CoPt (10.0) and (00.2) at 41.2° and 43.4° 2θ values, respectively (Tabakovic et al., 2016).

It was reported that Ru underlayer results in both the improvement of the microstructure [absence of hcp CoPt (00.2)] and enhancement of perpendicular anisotropy ($H_{C,//}$ = 629 Oe and $H_{C,\perp}$ = 1,220 Oe) in CoPt films (Tabakovic et al., 2016). The same results were observed in CoPt films obtained either by vacuum deposition or electrodeposition (Tabakovic et al., 2016; Pattanaik et al., 2006; Wodarz et al., 2016; Wierman et al., 2002; Vokoun et al., 2006). Also, Dragos-Pinzaru et al. reported that very high perpendicular coercivity ($H_{C,\perp}$ = 4,500–6,700 Oe) in CoPt films is attributed to both Ru substrate and thickness (10–30 nm) of CoPt film (Dragos-Pinzaru et al., 2017). They suggested that high perpendicular coercivity of $Co_{71}Pt_{21}$ film (~15 nm thickness) deposited on Ru seed layer is resulted from the addition of saccharin in the baths, resulting in the dramatic improvement of hcp (00.2) crystal structure. However, in this study, the binary CoPt film electrodeposited on brass substrate mainly consists of nanocrystalline with only a very small intensity of $CoPt_3$ (111) peak (JCPDS file #: 29–499). On the other hand, the ternary CoPtP film electrodeposited in the baths containing NaH_2PO_2 showed the dramatic improvement of Co_2P (130) [or Pt_5P_2 ($\bar{2}22$)] peaks, resulting in the increase of parallel coercivity from ~1,700 Oe to ~3,000 Oe and the increase of perpendicular coercivity from ~3,200 Oe to ~3,700 Oe. These results in this study may be attributed to the different substrate (brass) and the different bath compositions compared to previous papers reported by another researcher (Tabakovic et al., 2016; Dragos-Pinzaru et al., 2017). Some important results in CoPt/CoPtP films (for high coercivities) were tabulated in **Table 3** to compare each other.

In summary, it is believed that the coercivity and XRD patterns [**Figures 9**, **10**] in this study are affected not only by the type of substrate but also by chemical composition and operating conditions in the baths for electrodeposition. Although there is neither SEM image nor optical microscope image in this study, the smooth, bright and shiny surfaces of all the CoPt and CoPtP thin films were observed.

CONCLUSION

Magnetic CoPt and CoPtP thin film alloys were fabricated by electrodeposition process from the baths containing chloroplatinic acid, cobalt pyrophosphate and sodium hypophosphite. Influence of several electrodeposition parameters such as solution compositions (e.g [Pt^{4+}] [Co^{2+}] and [NaH_2PO_2]), solution pH, current density on current efficiency, magnetic properties, and microstructure was systematically investigated. It is believed that relatively low current efficiency in this article compared to that reported by Dragos-Pinzaru et al. (Dragos-Pinzaru et al., 2017) may be attributed to the different chemical compositions because of much more current consumption in the evolution of side reactions in this study. Parallel coercivities ranged from ~1,400 to ~1,600 Oe and perpendicular coercivities ranging from ~2,200 to ~2,800 Oe for binary CoPt films in this article were obtained. It is believed that the type of substrate strongly affects coercivities of CoPt films. Also, more Co-pyrophosphate concentration in the bath results in more deposit Co content in CoPt films; more H_2PtCl_6 concentration in the bath more deposit Pt content. Current efficiency obtained in CoPt films electrodeposited from hexachloroplatinate solutions much depend on the bath compositions rather than the type of additives, solution pH, $CoSO_4$, and H_2PtCl_6. In summary, the XRD patterns and coercivity in this study are affected by both the type of substrates and chemical composition and operating conditions in the baths for electrodeposition.

DATA AVAILABILITY STATEMENT

The original contributions presented in the study are included in the article/**Supplementary Material**, further inquiries can be directed to the corresponding author.

AUTHOR CONTRIBUTIONS

All authors listed have made a substantial, direct, and intellectual contribution to the work and approved it for publication.

SUPPLEMENTARY MATERIAL

The Supplementary Material for this article can be found online at: https://www.frontiersin.org/articles/10.3389/fchem.2021.733383/full#supplementary-material

REFERENCES

Bozorth, R. M. (1963). *Ferromagnetism*. Princeton, NJ: D. Van Nostrand Comp. (Chapter 5).

Carcia, P. F., Li, Z. G., and Zeper, W. B. (1993). Effect of Sputter-Deposition Processes on the Microstructure and Magnetic Properties of Pt/Co Multilayers. *J. Magnetism Magn. Mater.* 121, 452–460. doi:10.1016/0304-8853(93)91245-3

Coffey, K. R., Parker, M. A., and Howard, J. K. (1995). High Anisotropy L1/sub 0/ Thin Films for Longitudinal Recording. *IEEE Trans. Magn.* 31 (6), 2737–2739. doi:10.1109/20.490108

Dragos-Pinzaru, O., Ghemes, A., Chiriac, H., Lupu, N., Grigoras, M., Riemer, S., et al. (2017). Magnetic Properties of CoPt Thin Films Obtained by Electroeposition from Hexachloroplatinate Solution. Composition, Thickness and Substrate Dependence. *J. Alloys Comp.* 718, 319–325. doi:10.1016/j.jallcom.2017.05.186

Dragos-Pinzaru, O., Riemer, S., and Tabakovic, I. (2017). Composition Gradient in Electrodeposition of Thin CoPt Films from the Quiescent Hexachloroplatinate Solutions. *J. Electrochem. Soc.* 164 (2), D30–D38. doi:10.1149/2.0361702jes

Eagleton, T. S., Mallet, J., Cheng, X., Wang, J., Chien, C.-L., and Searson, P. C. (2005). Electrodeposition of Co[sub x]Pt[sub 1−x] Thin Films. *J. Electrochem. Soc.* 152 (1), C27–C31. doi:10.1149/1.1836128

Farrow, R. F., and Marks, R. F. (1998). Method for Making a Chemically-Ordered Magnetic Metal Alloy Film. U.S. Patent #5,792,510.

Guillamat, P., Cortés, M., Vallés, E., and Gómez, E. (2012). Electrodeposited CoPt Films from a Deep Eutectic Solvent. *Surf. Coat. Technol.* 206, 4439–4448. doi:10.1016/j.surfcoat.2012.04.093

Hnida, K. E., Żywczak, A., Gajewska, M., Marciszko, M., Sulka, G. D., and Przybylski, M. (2016). Tuning the Magnetic Properties of Multilayered CoPt-Pt Nanowires via Thickness of Magnetic Segments. *Electrochimica Acta* 205, 29–37. doi:10.1016/j.electacta.2016.04.076

Kim, H. S., Jeong, S. Y., and Suh, S. J. (2013). Current Density and Thickness Effects on Magnetic Properties of Electrodeposited CoPt Magnetic Films. *J. Magnetics* 18 (4), 417–421. doi:10.4283/jmag.2013.18.4.417

Lee, C. H., Farrow, R. F. C., Hermsmeier, B. D., Marks, R. F., Bennet, W. R., Lin, C. J., et al. (1991). Molecular Beam Epitaxial Growth and Magnetic Properties of Co-pt Superlattices Oriented along the [001], [110] and [111] axes of Pt*. *J. Magnetism Magn. Mater.* 93, 592–596. doi:10.1016/0304-8853(91)90407-2

Myung, N. V., Park, D.-Y., Yoo, B.-Y., and Sumodjo, P. T. A. (2003). Development of Electroplated Magnetic Materials for MEMS. *J. Magnetism Magn. Mater.* 265, 189–198. doi:10.1016/S0304-8853(03)00264-6

Park, S. E., Jung, P. Y., and Kim, K. B. (1995). Magnetic Properties and Microstructural Analysis of Sputter-deposited and Annealed Co-Pt Alloys. *J. Appl. Phys.* 77, 2641–2647. doi:10.1063/1.358730

Pattanaik, G., Zangari, G., and Weston, J. (2006). Perpendicular Anisotropy in Electrodeposited, Co-rich Co-Pt Films by Use of Ru Underlayers. *Appl. Phys. Lett.* 89, 112506. doi:10.1063/1.2339070

Tabakovic, I., Qiu, J.-M., and Dragos, O. (2016). Electrodeposition of Thin CoPt Films with Very High Perpendicular Anisotropy from Hexachloroplatinate Solution: Effect of Saccharin Additive and Electrode Substrate. *J. Electrochem. Soc.* 163 (7), D287–D294. doi:10.1149/2.0491607jes

Tabakovic, I., Qiu, J.-M., and Riemer, S. (2015). Electrodeposition of CoPt Alloys from the Stable Hexachloroplatinate Solution: Electrochemical Studies. *J. Electrochem. Soc.* 162, D291–D299. doi:10.1149/2.0861507jes

Vieux-Rochaz, L., Dieppedale, C., Desloges, B., Gamet, D., Barragatti, C., Rostaing, H., et al. (2006). Electrodeposition of Hard Magnetic CoPtP Material and Integration into Magnetic MEMS. *J. Micromech. Microeng.* 16, 219–224. doi:10.1088/0960-1317/16/2/005

Vokoun, D., Lai, C.-H., Liao, Y.-Y., Lin, M.-S., Jiang, R.-F., Huang, R.-T., et al. (2006). Effects of Tb⁄Pt⁄Ru Underlayer on Microstructure and Magnetic Properties of CoPtCr-SiO2 Perpendicular Media. *J. Appl. Phys.* 99, 08E703. doi:10.1063/1.2164410

Wierman, K. W., Klemmer, T. J., Lu, B., Ju, G., Howard, K. J., Roy, A. G., et al. (2002). Ru[sub x]Cr[sub 1−x]/Ta Underlayer for Co-alloy Perpendicular Magnetic Recording. *J. Appl. Phys.* 91, 8031–8033. doi:10.1063/1.1447498

Wodarz, S., Abe, J., and Homma, T. (2016). Analysis and Control of the Initial Electrodeposition Stages of Co-Pt Nanodot Arrays. *Electrochimica Acta* 197, 330–335. doi:10.1016/j.electacta.2015.11.136

Zana, I., and Zangari, G. (2004). Magnetic Properties of Electrodeposited Co-pt Thin Films with Very High Perpendicular Magnetic Anisotropy. *J. Magnetism Magn. Mater.* 272-276, 1698–1699. doi:10.1016/j.jmmm.2003.12.262

Zhu, Y.-P., Liu, Y.-P., Ren, T.-Z., and Yuan, Z.-Y. (2015a). Self-Supported Cobalt Phosphide Mesoporous Nanorod Arrays: a Flexible and Bifunctional Electrode for Highly Active Electrocatalytic Water Reduction and Oxidation. *Adv. Funct. Mater.* 25, 7337–7347. doi:10.1002/adfm.201503666

Zhu, Y.-P., Xu, X., Su, H., Liu, Y.-P., Chen, T., and Yuan, Z.-Y. (2015b). Ultrafine Metal Phosphide Nanocrystals *In Situ* Decorated on Highly Porous Heteroatom-Doped Carbons for Active Electrocatalytic Hydrogen Evolution. *ACS Appl. Mater. Inter.* 7, 28369–28376. doi:10.1021/acsami.5b09092

Conflict of Interest: The authors declare that the research was conducted in the absence of any commercial or financial relationships that could be construed as a potential conflict of interest.

frontiers in Chemistry

ORIGINAL RESEARCH
published: 21 October 2021
doi: 10.3389/fchem.2021.763508

Study of Cu Electrochemical Polishing Mechanism With Observation of Water Acceptor Diffusion

Kimoon Park[1†], Jinhyun Lee[2†], Youjung Kim[3], Sangwha Yoon[2] and Bongyoung Yoo[1,2,3*]*

[1]Department of Advanced Material Science & Engineering, Hanyang University, Ansan-si, South Korea, [2]Department of Materials Engineering, Hanyang University, Ansan-si, South Korea, [3]Department of Material Science and Chemical Engineering, Hanyang University, Ansan-si, South Korea

The salt-film and water acceptor mechanisms were generally accepted mechanisms for Cu electrochemical polishing (ECP) theory. These mechanisms of Cu ECP are still controversial for a long time. Conventional and new electrochemical analysis methods were used to investigate the mechanisms and behaviors of Cu electrochemical polishing. Two cases of Cu dissolution, with and without polishing, were classified by results of linear scan voltammetry (LSV) and scanning electron microscopy (SEM). The electrochemical impedance spectroscopy (EIS) results showed the main difference in these two cases was in the low-frequency region. However, it was hard to distinguish between the salt-film and water acceptor mechanisms by conventional electrochemical analysis. A scanning electrochemical microscopy (SECM) system, a new electrochemical analysis method that measures the electrolysis currents of the water acceptors along with a set distance from the substrate, was used to investigate the Cu ECP mechanism. Accordingly, the diffusion of the water acceptors was successfully confirmed for the first time. Finally, the mechanisms of the Cu ECP are definitively described by using all analysis results.

Keywords: electropolishing, copper, water acceptor, scanning electrochemical microscopy, diffusion

Edited by:
Elizabeth J. Podlaha,
Clarkson University, United States

Reviewed by:
Yao Yang,
Shanghai Jiao Tong University, China
Yunpei Zhu,
King Abdullah University of Science and Technology, Saudi Arabia

****Correspondence:***
Sangwha Yoon
indada@naver.com
Bongyoung Yoo
byyoo@hanyang.ac.kr

[†]These authors contributed equally to this work and share first authorship

Specialty section:
This article was submitted to Electrochemistry, a section of the journal Frontiers in Chemistry

Received: *24 August 2021*
Accepted: *11 October 2021*
Published: *21 October 2021*

Citation:
Park K, Lee J, Kim Y, Yoon S and Yoo B (2021) Study of Cu Electrochemical Polishing Mechanism With Observation of Water Acceptor Diffusion. Front. Chem. 9:763508. doi: 10.3389/fchem.2021.763508

INTRODUCTION

Cu electrochemical polishing (ECP) is an electrochemical process that makes a Cu surface smooth when Cu electrodes are anodically polarized in the ECP electrolytes. This Cu ECP method has several advantages, such as a solution-based process that uses simple equipment, selectivity for the conductive substrate, and causing no mechanical damages. Due to these unique properties, the Cu ECP process can be used in various applications that treat surfaces for cosmetic purposes (Du and Suni, 2004), for substrates for graphene growth (Zhang et al., 2012), for TEM and EBSD samples (Sun et al., 2005; Lapeire et al., 2013), and for Cu planarization in semiconductor interconnections (Chang et al., 2002; Chang et al., 2003; Padhi et al., 2003; Liu et al., 2005; Suni and Du, 2005; West et al., 2005; Liu et al., 2006; Liu et al., 2006). Despite the many potentials of Cu ECP, its actual mechanisms are still controversial.

Abbreviations: ECP, electrochemical polishing; EIS, electrochemical impedance spectroscopy; LSV, linear scan voltammetry; SEM, scanning electron microscopy; SECM; scanning electrochemical microscopy; FSW, finite space Warburg; OCP, open circuit potential.

The simple mechanism of Cu ECP in concentrated phosphoric acid solutions was first suggested by Jacquet's viscous film theory (Jacquet, 1936). A bluish viscous layer forms on the Cu substrate and the thickness of this layer is different between its protrusions and valleys. This difference means that the resistances at the protrusions are different from those in the valleys, and therefore ECP occurs. This theory was challenged by Elmore's diffusion theory (Elmore, 1939; Elmore, 1940), wherein the thicknesses of the diffusion layer of Cu ions from the Cu surface to the bulk electrolyte are different at the protrusions and in the valleys. These different diffusion layer thicknesses affect the limiting current of Cu dissolution reaction. The limiting current is higher at the protrusions, while that is lower at the valleys. Therefore, these phenomena cause the ECP. Then, in contrast to this theory, Edwards (1953) proposed acceptor diffusion theory wherein the ECP is governed by the diffusion of anionic acceptors such as $(PO_4)^{3-}$, $(HPO_4)^{2-}$, and $(H_2PO_4)^-$ into the Cu surface from the bulk electrolyte. The ECP rates are dependent on the diffusion of the acceptors into the Cu surface; the diffusion rate is high at the protrusions and low in the valleys.

After these mechanisms were thoroughly evaluated, the salt-film mechanism and the water acceptor mechanism came to be considered the main processes that explained the behavior of Cu ECP. Landolt. (1987) first described the salt-film mechanism, whereby salts are precipitated when the concentration of metal ions on the Cu surface produced by the dissolution reaction exceeds the solubility limit; the precipitated salt film forms on the Cu surface. Due to this salt film, metal dissolution is limited by the diffusion of metal ions from the film to the bulk electrolyte. In contrast, the water acceptor mechanism is similar to Edward's acceptor diffusion theory except that the acceptor is water instead of anionic acceptors. And unlike in the salt-film mechanism, the most important factor for the polishing effect is not the diffusion of Cu ions into the bulk electrolyte, but, rather, the diffusion of water acceptors into the Cu surface.

Between these two mechanisms, the water acceptor mechanism has been more accepted by electrochemical impedance spectroscopy (EIS) studies (Glarum and Marshall, 1985a, Glarum and Marshall, 1985b; Vidal and West, 1995a, Vidal and West, 1995b), which indicated that the water depletion layer acts as a viscous film, so the mass transfer control reaction of the water acceptors becomes a critical factor. Wagner. (1954) mathematically analyzed an ideal Cu ECP process based on the water acceptor mechanism, and various other studies proposed mechanisms to explain Cu ECP behavior (Hoar and Rothwell, 1964; Kojima and Tobias, 1973; Pointu et al., 1981; Pointu et al., 1983a, Pointu et al., 1983b). The water acceptor mechanism has remained the most accepted based on previous studies. However, Cu ECP mechanisms are still controversial because the ECP process is complicated, which is many factors such as metal ion, anions, and acceptors affect the process. Therefore, new analyses are required for the direct explanation and confirmation of Cu ECP behavior.

Accordingly, in this paper we report on the mechanisms and behaviors of Cu ECP using the conventional electrochemical analysis methods and a new electrochemical analysis method. So, the electrochemical behaviors of Cu ECP at various ECP potentials were compared and studied. In addition to these conventional analyses, quantities of water at various distances from the Cu substrate were estimated by measuring the water electrolysis reaction currents using a scanning electrochemical microscopy (SECM) system for the direct observation and verification of Cu ECP behavior based on the water acceptor mechanism. Based on the data, we here discuss the mechanisms, behaviors, and critical factors of Cu ECP.

MATERIALS AND METHODS

We first conducted typical analysis and experiments in a 100 ml cell with a conventional three-electrode system. The three-electrode system consisted of an electrodeposited Cu substrate as the working electrode, a Pt-coated Ti plate as the counter electrode, and a saturated Ag/AgCl electrode (3M KCl saturated) as the reference electrode. For preparing the working electrodes, Ti (20 nm)/Cu (200 nm) seed layers were deposited on an Si wafer by the evaporation method, and Cu film was galvanostatically electrodeposited at $-50\ \mathrm{mA/cm^2}$ for 300 s on Si/Ti (20 nm)/Cu (200 nm) substrates with an area of $1 \times 1\ \mathrm{cm^2}$.

Reagent-grade chemicals were utilized for the all of the Cu electrodepositions and Cu ECP experiments. The electrolytes for Cu electrodeposition consisted of 1.0 M copper sulfate ($CuSO_4$, 99.5%, YAKURI, Japan), 0.58 M sulfuric acid (H_2SO_4, 95%, Daejung Chemicals & Metals, Korea), and 1.9 mM hydrochloric acid (HCl, 35%, Daejung Chemicals & Metals, Korea) in 100 ml of 18.6 MOhm deionized water. 85% phosphoric acids (H_3PO_4) were utilized as electrolytes for the Cu ECP.

Conventional electrochemical analysis, deposition, and polishing were carried out using a potentiostat/galvanostat (VersaSTAT 4, AMETEK Inc., United States). For analysis of electrochemical behavior and appropriate ECP potential selection, LSV analysis was conducted at the potential range between the open circuit potential (OCP) to 2.5 V vs Ag/AgCl with a scan rate of 10 mV/s without agitation. After selection of the ECP potentials at 0.25, 0.375, 0.50, 0.90, and 1.30 V, Cu substrates were electrochemically polished at the potential of 1.3 V in 85% phosphoric acid without agitation. The surfaces of the electrochemically polished Cu substrates were observed using field emission scanning electron microscopy (FESEM; MIRA3, TESCAN Orsay Holding, a.s., Czech Republic). EIS analysis was also conducted at the selected ECP potentials with an amplitude of 10 mV in the frequency range of 50 kHz to 10 Hz so as to understand the Cu ECP behavior. EIS and SECM were performed after "preconditioning" that applying the selected potential for 60 s to the Cu substrates in phosphoric acid to establish a steady-state interface condition on the Cu substrates (Grimm et al., 1992).

To estimate the water acceptor quantities along various distances from the Cu substrate, electrolysis currents were measured with the SECM system's electrochemical scanning probe tool. The cell configuration for this analysis is illustrated in **Figure 1**. The electrodes consisted of the Pt tip probe

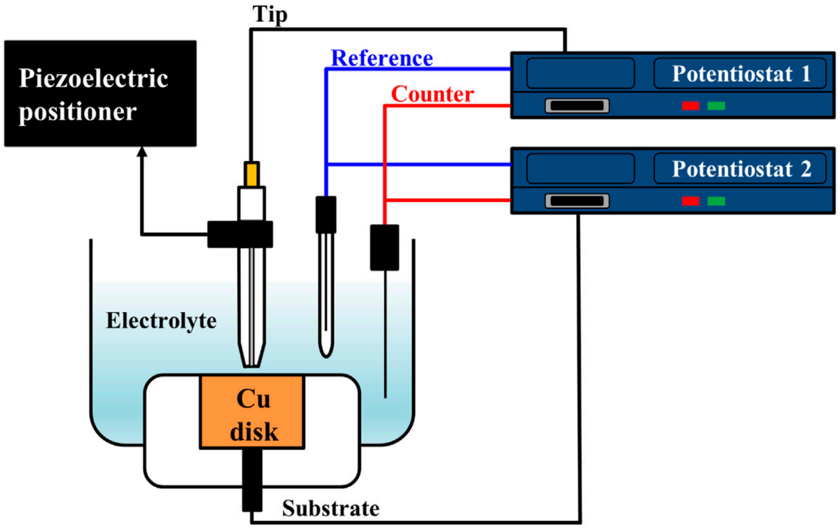

FIGURE 1 | Scheme of cell configuration for water electrolysis current measurement using SECM system.

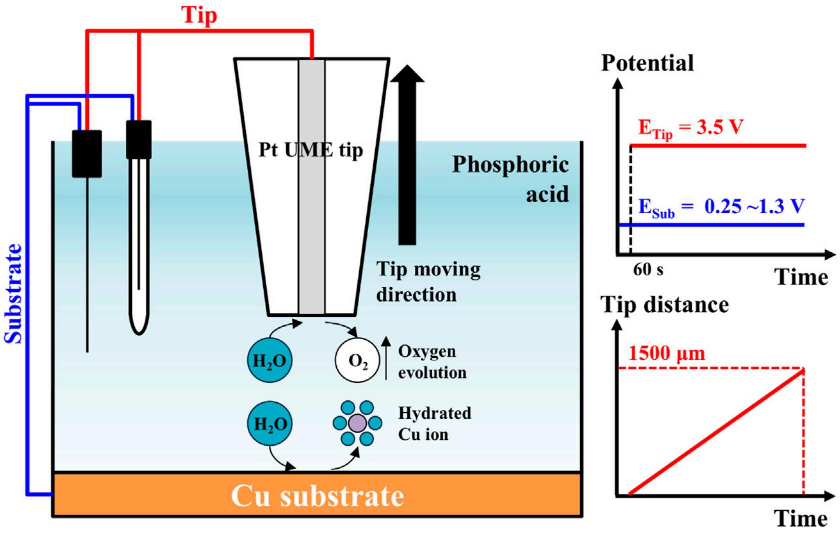

FIGURE 2 | Measurement scheme of electrode reactions for water electrolysis current measurement in SECM system. The Cu ions were dissolved from Cu substrate by applied potential from 0.25 to 1.3 V. The water molecules hydrated the dissolved Cu ions. Oxygen evolution occurs on Pt tip by applied potential 3.5 V after preconditioning for 60 s. A Pt tip moved with 5 μm/s of scan speed.

(10 μm diameter) and the Cu substrate for the working electrode, a Pt wire for the counter-electrode, and Ag/AgCl electrode (3 M KCl saturated) for the reference electrode. The Pt tip probe and the Cu substrate were arranged with each potentiostat as working electrodes. These configurations were identical with typical configuration of SECM analysis. Based on the configuration of the electrodes, the solutions and the reactions for the analysis are illustrated in **Figure 2**. The 85% phosphoric acid was utilized to analyze the solutions, and the process details are as follows. First, when the potential of the Cu substrate was applied to 0.25~1.3 V, the Cu dissolution reaction occurred at the surface of the Cu substrate with these two-step reactions (Matlosz et al., 1994; Han and Fang, 2019):

$$Cu \rightarrow Cu_{ad}^{2+} + 2e^{-} \qquad (1)$$

$$Cu_{ad}^{2+} + 6H_2O \rightarrow [Cu(H_2O)_6]^{2+} \qquad (2)$$

After 60 s of preconditioning time, the potential of the Pt tip probe was applied to 3.5 V at the Cu substrate to achieve steady-state for the water acceptor diffusion. The oxygen evolution reaction from the decomposition of the water occurred at the surface of the Pt tip probe with following reaction:

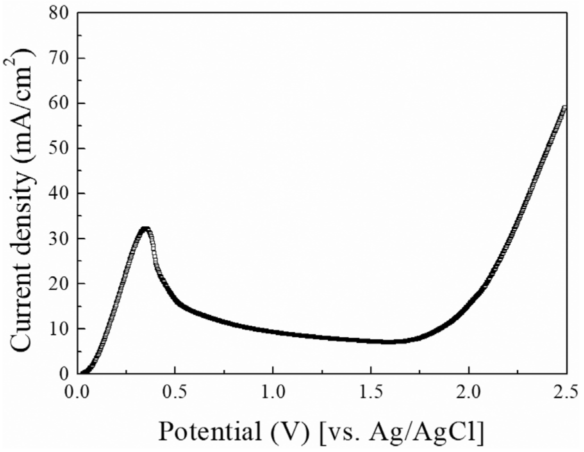

FIGURE 3 | Linear scan voltammogram of Cu substrate in 85% phosphoric acid. A sweep was done with a scan rate of 10 mV/s.

$$2H_2O \rightarrow O_2\uparrow + 4H^+ + 4e^- \quad (3)$$

These water electrolysis currents were dependent on the water acceptor quantities, and these currents were measured at various Pt tip distances from the Cu substrate. The initial tip distance from the Cu substrate was set to 1 μm to prevent direct current from passing current between the Pt tip and the Cu substrate; then the tip distance was varied from 1 μm to 1,500 μm with 5 μm/s of scan speed. All electrochemical analyses were performed at 20°C.

RESULTS AND DISCUSSION

LSV is a fundamental and powerful analysis method to study the electrochemical behavior of Cu ECP. Therefore, we first conducted LSV analysis in 85% phosphoric acid, and the resulting the voltammogram is shown in **Figure 3**. At the initial potential range, anodic current began to increase until 0.375 V. According to Shieh et al. (2004), these anodic current in this potential range are related to the direct dissolution of Cu, resulting in dully etched surfaces. Over 0.375 V, the anodic current was decreased to 0.50 V. This phenomenon indicates generating a passivation layer on the anodic surface. When the ECP potential was applied over 0.50 V, the current remained nearly constant up to 1.7 V. This current plateau region is generally considered the Cu ECP reaction (Jacquet, 1936; Elmore, 1939; Glarum and Marshall, 1985a; Landolt, 1987; Han and Fang, 2019). After that current plateau, the current was increased again from the potential above 1.7 V by the oxygen evolution reaction (Shieh et al., 2004), which caused severe etch pits.

In addition to interpreting previous papers, we selected five potential points for the exact interpretation of the LSV results: 1) 0.25 V as the potential before the peak point, 2) 0.375 V as the potential at the peak point, 3) 0.50 V as the potential after the peak point, 4) 0.90 V and 5) 1.30 V as the potentials in the plateau region. Then the Cu substrates were anodically polarized at the five potential points with a charge density of 2.5 C/cm^2; their top SEM images are presented in **Figure 4**. Compared with the SEM images of Cu substrate before polarized (**Figure 4A**), the Cu ECP effect was observed at all of the ECP potentials (**Figures 4C–F**) except at 0.25 V, where dully etched Cu was observed (**Figure 4B**). These results indicate that the Cu dissolution reaction on Cu substrate or interphase between the Cu substrate and the phosphoric acid began to change as the peak potential. Accordingly, we analyzed the difference in dissolution reactions or interphase conditions between the potential before the peak point and the potentials after the peak point.

Previous researchers reported the two models describing the interface condition at the Cu surface during ECP (Glarum and Marshall, 1985a, Glarum and Marshall, 1985b; Landolt, 1987; Vidal and West, 1995a, Vidal and West, 1995b). One is the salt-film model in which Cu salts are precipitated on the Cu substrate when the Cu dissolution exceeds the dissolution limit of the Cu salts. The other is the water-acceptor diffusion model in which water acceptors are diffused toward the Cu substrate. However, in both models, the ECP mechanism is still controversial. Therefore, to precisely determine the interface condition of the Cu surface during ECP, we conducted EIS analysis at the five potential points described earlier.

Figure 5 shows schematic Nyquist plots in the whole frequency range, where R_s is the solution resistance from the left intercept of the semicircle, R_p is the polarization resistance from the diameter of the semicircle, and C_{dl} is the double layer capacitance calculated from the relation $\omega_{max} = 1/R_pC_{dl}$. ω_{max} represents the frequency when Z_{img} is at maximum value in the semicircle. In the low-frequency region, the angle of the line increased from about 45^o to 90^o (vertical) as the polishing potentials were increased. This result may be related to the diffusion of the water acceptor and will be discussed later. The Nyquist plots of Cu ECP in the 85% phosphoric acid according to ECP potential were obtained at two preconditioning times, 0 s and 60 s, corresponding with **Figure 6A** and **Figure 6B**, respectively.

The fitting results of the Nyquist plots are summarized in **Table 1**. In the high-frequency region, the R_s values were almost consistent with 6.0 Ω cm^2 regardless of the polishing potential and preconditioning time. These results, which is R_s not changed, were evidence of water acceptor diffusion because in the salt-film model the R_s changed with the polishing potential (Vidal and West, 1995a). However, the R_p was increased, and the C_{dl} was decreased as the anodic potential was increased. These changes of the R_p and C_{dl} with the various polishing potentials were different from the EIS results of the water-acceptor mechanism measured by Vidal and West (1995a). Our R_p and C_{dl} values changed when the preconditioning times were varied. These changes associated with potentials and preconditioning times can be explained by changes in both the salt-film thickness and the depletion layer thickness in the salt film model and the water acceptor model, respectively (Grimm et al., 1992).

The low-frequency regions of our Nyquist plots were significantly affected by the potentials and preconditioning times. When the Nyquist plots were obtained as the polishing

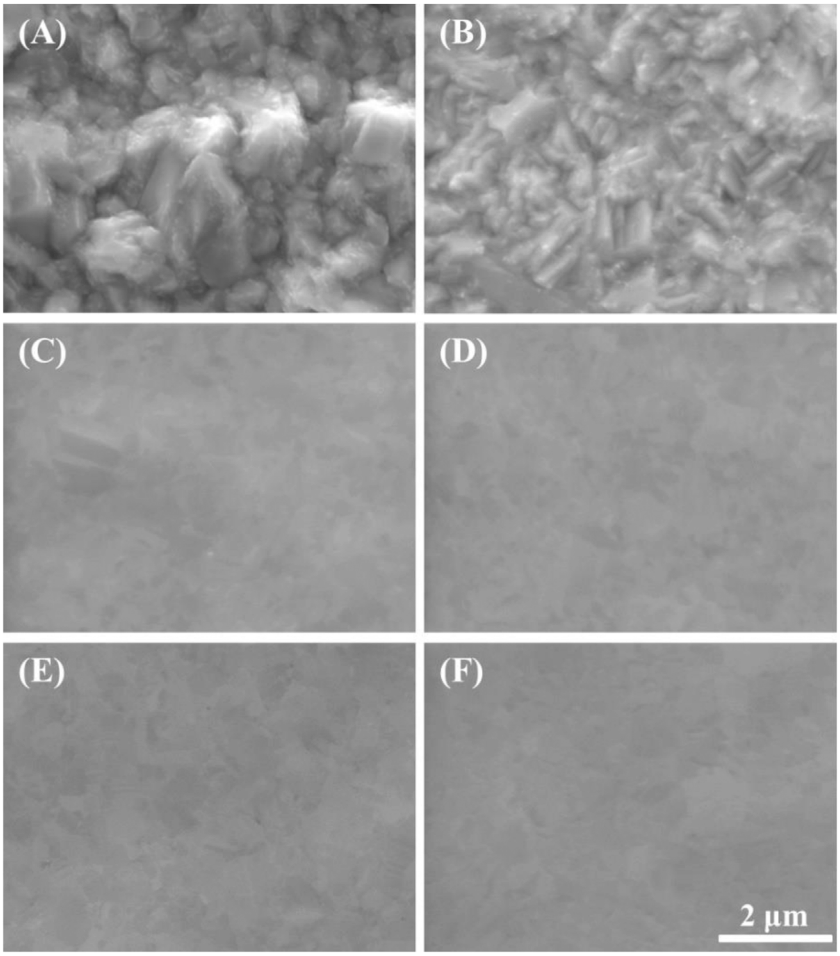

FIGURE 4 | SEM images of anodically polarized Cu substrates in 85% phosphoric acid at various potentials with a charge density of 2.5 C/cm^2: **(A)** before polarized, **(B)** 0.25 V, **(C)** 0.375 V, **(D)** 0.50 V, **(E)** 0.90 V, and **(F)** 1.30 V.

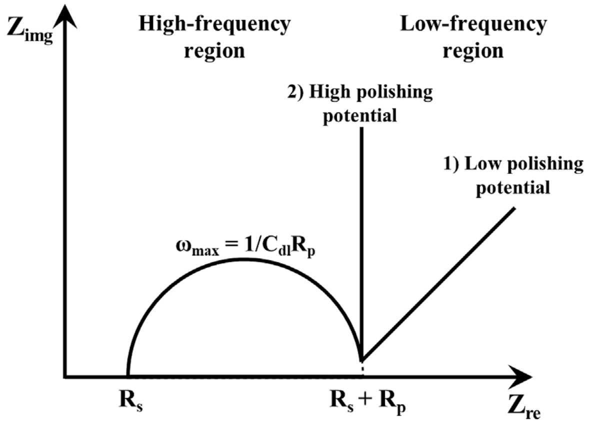

FIGURE 5 | Schematic Nyquist plot according to frequency region.

potentials were applied without preconditioning (**Figure 6A**), the line in the low-frequency region started to exhibit Warburg impedance from 0.50 to 1.30 V. The angle changed to 90° in low-frequency regions when the polishing potentials exceeded 0.90 V. In the Nyquist plots obtained with the preconditioning time of 60 s (**Figure 6B**), Warburg impedance was observed from the peak potential, 0.375 V, as seen in **Figure 3**. When we compared Nyquist plots in the condition of 0.375 V between the preconditioning times of 0 s (**Figure 6A**) and 60 s (**Figure 6B**), the Cu ECP occurred when the Cu dissolution reaction was governed by a mass transfer control reaction of the water acceptors. The vertical lines were observed as the anodic potentials exceeded 0.50 V.

These results confirmed that all lines of the low-frequency region were related to the diffusion process due to Warburg impedance. Especially, the vertical lines in the low-frequency region at the high ECP potentials were related to the finite space Warburg (FSW) elements, in which the diffusion condition is a limited diffusion layer and a limited electroactive substance (Oldenburger et al., 2019). This indicated two possible diffusion conditions, one being a porous salt film and the other being a depleted water acceptor layer (Grimm et al., 1992; Matlosz et al., 1994). However, there was no explanation

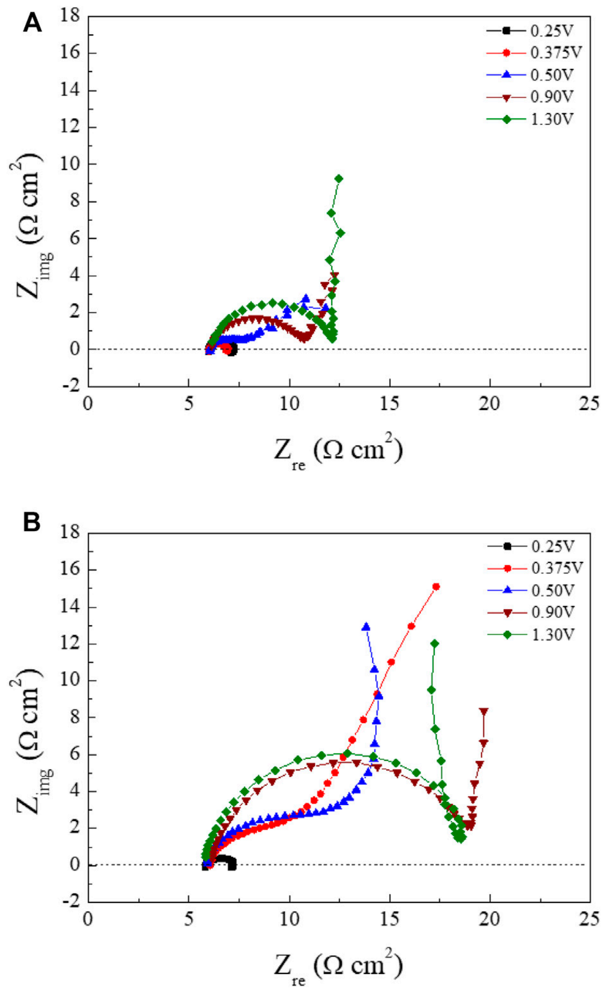

FIGURE 6 | Nyquist plots of the Cu substrates at various polishing potentials in 85% phosphoric acid measured according to preconditioning time **(A)** 0 s and **(B)** 60 s. Frequencies were set on between 50 kHz and 10 Hz.

TABLE 1 | Fitting results of the Nyquist plots according to preconditioning time and applied potentials.

(V)	R_s (Ω cm^2)		R_p (Ω cm^2)		C_{dl} (F/cm^2)	
	0 s	60 s	0 s	60 s	0 s	60 s
0.25	6.155	6.003	1.110	1.058	7.66×10^{-5}	1.33×10^{-4}
0.375	5.947	6.031	0.536	1.903	9.58×10^{-5}	1.59×10^{-5}
0.50	6.017	5.964	1.139	3.617	5.76×10^{-5}	1.42×10^{-5}
0.90	6.200	6.267	2.36	10.62	1.09×10^{-5}	7.65×10^{-6}
1.30	6.139	5.869	2.73	10.69	6.30×10^{-6}	6.33×10^{-6}

about the low-frequency region in previous reports by Vidal and West. (1995a), Vidal and West. (1995b), leaving it still unclear which mechanism was correct. More analysis was required to interpret these results, so we designed a new analysis method that can directly observe water acceptor diffusion.

To observe the water acceptor diffusion at various distances from the Cu substrate, we measured the water electrolysis current resulting from the oxygen evolution reaction by using the SECM system. The cell configuration of the measurement system and the scheme of the measurement method are presented in **Figures 1**, **2**, respectively. In the three-electrode system, two working electrodes (the Pt tip and the Cu substrate) were installed in the measurement cell. At the Cu substrate, the Cu dissolution reaction occurred when the potentials were anodically applied. At the Pt tip electrode, the water acceptor quantities were estimated by using the oxygen evolution reaction, which was observed in the LSV in **Figure 3** when the potentials exceeded 1.7 V. Therefore, the potential at the Pt tip electrode was set to 3.5 V for sufficient electrolysis of the rest of the water acceptors, and the oxygen evolution reaction could occur without dissolution of the Pt electrode.

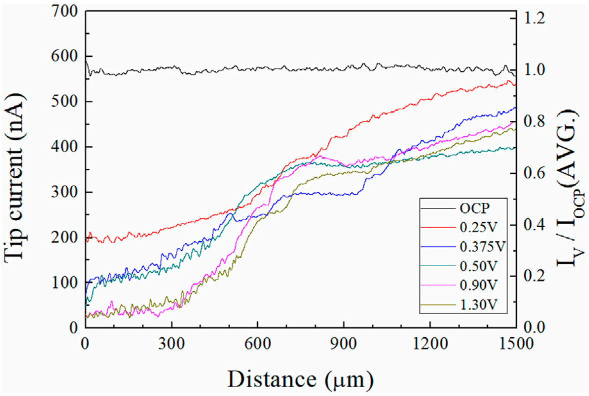

FIGURE 7 | Profiles of water electrolysis currents measured by SECM in 85% phosphoric acid **(left)** tip currents, and **(right)** I_V/I_{OCP}(AVG.) along the tip distance from the Cu substrate. I_V and I_{OCP} mean the tip currents at the applied potential "V" and OCP of the Cu substrate. The measurement system was illustrated in **Figure 2**.

First, the potential to the Cu substrate was applied for 60 s (the preconditioning described earlier). Then the potential to the Pt tip was applied and the current of the Pt tip were measured with movements from the surface of the Cu substrate to the bulk electrolyte. The two water electrolysis profiles from this experiment are presented in **Figure 7**. The tip current-tip distance and the I_V/I_{OCP}(Avg.)-tip distance profiles are shown in the left side and right side of **Figure 7**, respectively. The I_V/I_{OCP}(Avg.)-tip distance is the ratio of the tip current at applied potential "V" on the Cu substrate and the average tip current at the open circuit potential (OCP) of the Cu substrate.

These profiles revealed that the tip current profile varied with the potential of the Cu substrate. At the OCP of the Cu substrate, the current was almost constant, regardless of the position of the tip electrode, because the water acceptors were not consumed for the Cu dissolution reaction. As the ECP potentials on the Cu substrate were increased, the tip currents were decreased; tip currents at the Cu surface (distance between the Pt tip and the Cu substrate: 1 μm) were 590 nA, 200 nA, 72 nA, 45 nA, 23 nA, and 21 nA when the ECP potential was OCP, 0.25, 0.375, 0.50, 0.90, and 1.30 V, respectively. The tip currents increased when the Pt tip moved toward the bulk electrolyte direction at all anodic potentials. These results indicated that the quantity of the water

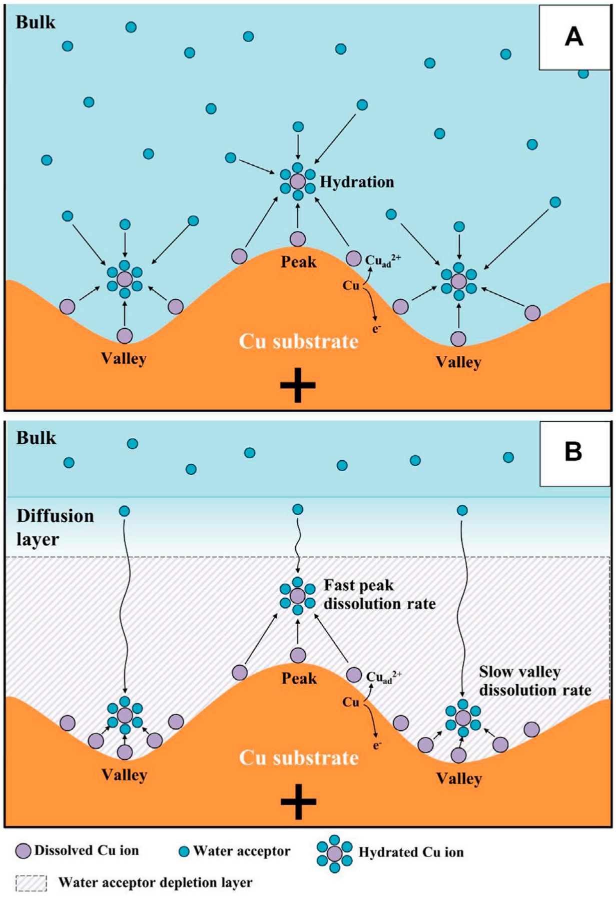

FIGURE 8 | Mechanism scheme of Cu electrochemical polishing: **(A)** initial state, and **(B)** steady state.

acceptors was affected by the ECP potentials because the magnitude of the tip current is proportional to the quantities of water acceptors. Therefore, profiles were evidence of the water acceptor diffusion mechanism.

Using these water electrolysis profiles and the evidenced mechanism of water acceptor diffusion, the results of LSV and EIS can be also explained. In the LSV in **Figure 3**, the polishing phenomena occurred at the peak potential of 0.375 V. This LSV behavior might seem to be anodic passivation behavior, but this peak occurred due to the depletion of the water acceptors. Additionally, the polishing phenomena were observed after the potential region at which depletion and diffusion of the water acceptors occurred on the Cu surface; therefore, the diffusion of the water acceptor was closely related with the Cu polishing effects. The results of the Nyquist plots (**Figure 6**) can be also explained by water acceptor diffusion. In the high-frequency region, the C_{dl} was decreased and the R_p was increased as the ECP potential was increased, because the thickness of the diffusion layer of the water acceptor was increased as the ECP potential was increased. Therefore, the difficulty of the Cu dissolution reaction was increased due to the insufficient amount of water acceptors. The presence of the vertical line in the low-frequency region indicates that these conditions correspond with the FSW diffusion condition wherein the viscous diffusion layer and the water acceptors were matched with the limited diffusion layer and the water-limited electroactive substance, respectively. Therefore, the FSW diffusion behavior was caused by this significant and viscous diffusion layer of the water acceptors. These novel electrochemical measurements revealed the Cu ECP mechanism scheme, which is presented in **Figure 8**. In the initial state of Cu ECP (**Figure 8A**), when a potential above 0.375 V was applied to the Cu substrate, significant Cu dissolution reactions occurred in both protrusions and the valleys of Cu substrate because many water acceptors hydrated the Cu ions. However, the concentration of the water acceptors rapidly decreased on the Cu surface as the potential was applied; the water acceptors were eventually depleted by hydration for the Cu ions, and the Cu dissolution reaction was governed by a mass transfer control reaction of the water acceptors. Therefore, the water acceptors were preferentially diffused to the surface protrusions, which were more rapidly dissolved than the valleys (**Figure 8B**). As a result of the rapid dissolution rate at the protrusions, the Cu surface was flattened.

CONCLUSION

We successfully identified the mechanism of Cu ECP using various standard electrochemical analysis methods as well as our novel electrochemical analysis method. From the LSV analysis, the Cu polishing effect was observed when the potential was higher than 0.375 V. Anodic potentials were selected for EIS and SECM analyses. The low-frequency region of the resulting Nyquist plots indicated that the diffusion of the water acceptors was related to the Cu polishing phenomena in EIS analyses. Then the profiles of water electrolysis currents and distance enabled the observation of the diffusion of water acceptors for the first time from SECM analyses. These profiles were evidence that the water acceptor mechanism is most likely to explain the polishing phenomena. Knowing the exact mechanism of Cu ECP will be helpful for new interpretations, designs, and applications of ECP.

DATA AVAILABILITY STATEMENT

The original contributions presented in the study are included in the article/supplementary files, further inquiries can be directed to the corresponding authors.

AUTHOR CONTRIBUTIONS

KP and JL contributed equally to this work and share first authorship. YK especially contributed to setup equipment and do the experiments. SY and BY are the main organizer and advisor of this work.

FUNDING

This research was supported by the Basic Science Research Program through the National Research Foundation of Korea (NRF) funded by the Ministry of Science, ICT & Future Planning (No. 2015R1A5A1037548). This research was also supported by the National Research Foundation of Korea (NRF) (No. NRF-2020R1A2C2009462). This work was also supported by the Technology Innovation Program (Development of non cyanide gold bump solution and plating process for semiconductor device bonding process, 20017189) funded By the Ministry of Trade, Industry; Energy (MOTIE, Korea).

REFERENCES

Chang, S.-C., Shieh, J.-M., Dai, B.-T., Feng, M.-S., Li, Y.-H., Shih, C. H., et al. (2003). Superpolishing for Planarizing Copper Damascene Interconnects. *Electrochem. Solid-state Lett.* 6 (5), G72–G74. doi:10.1149/1.1565853

Chang, S.-C., Shieh, J.-M., Huang, C.-C., Dai, B.-T., and Feng, M.-S. (2002). Pattern Effects on Planarization Efficiency of Cu Electropolishing. *Jpn. J. Appl. Phys.* 41 (12), 7332–7337. doi:10.1143/Jjap.41.7332

Du, B., and Suni, I. I. (2004). Mechanistic Studies of Cu Electropolishing in Phosphoric Acid Electrolytes. *J. Electrochem. Soc.* 151 (6), C375–C378. doi:10.1149/1.1740783

Edwards, J. (1953). The Mechanism of Electropoiishing of Copper in Phosphoric Acid Solutions. *J. Electrochem. Soc.* 100 (7), 189C–C194. doi:10.1149/1.2781122

Elmore, W. C. (1939). Electrolytic Polishing. *J. Appl. Phys.* 10 (10), 724–727. doi:10.1063/1.1707257

Elmore, W. C. (1940). Electrolytic Polishing. II. *J. Appl. Phys.* 11 (12), 797–799. doi:10.1063/1.1712738

Glarum, S. H., and Marshall, J. H. (1985a). The Anodic Dissolution of Copper into Phosphoric Acid: I . Voltammetric and Oscillatory Behavior. *J. Electrochem. Soc.* 132 (12), 2872–2878. doi:10.1149/1.2113686

Glarum, S. H., and Marshall, J. H. (1985b). The Anodic Dissolution of Copper into Phosphoric Acid: II . Impedance Behavior. *J. Electrochem. Soc.* 132 (12), 2878–2885. doi:10.1149/1.2113687

Grimm, R. D., West, A. C., and Landolt, D. (1992). AC Impedance Study of Anodically Formed Salt Films on Iron in Chloride Solution. *J. Electrochem. Soc.* 139 (6), 1622–1629. doi:10.1149/1.2069467

Han, W., and Fang, F. (2019). Fundamental Aspects and Recent Developments in Electropolishing. *Int. J. Machine Tools Manufacture* 139, 1–23. doi:10.1016/j.ijmachtools.2019.01.001

Hoar, T. P., and Rothwell, G. P. (1964). The Influence of Solution Flow on Anodic Polishing. Copper in Aqueous O-Phosphoric Acid. *Electrochimica Acta* 9 (2), 135–150. doi:10.1016/0013-4686(64)85001-5

Jacquet, P. A. (1936). On the Anodic Behavior of Copper in Aqueous Solutions of Orthophosphoric Acid. *Trans. Electrochem. Soc.* 69 (1), 629–655. doi:10.1149/1.3498234

Kojima, K., and Tobias, C. W. (1973). Interpretation of the Impedance Properties of the Anode-Surface Film in the Electropolishing of Copper in Phosphoric Acid. *J. Electrochem. Soc.* 120 (9), 1202–1205. doi:10.1149/1.2403661

Landolt, D. (1987). Fundamental Aspects of Electropolishing. *Electrochimica Acta* 32 (1), 1–11. doi:10.1016/0013-4686(87)87001-9

Lapeire, L., Martinez Lombardia, E., Verbeken, K., De Graeve, I., Kestens, L. A. I., and Terryn, H. (2013). Effect of Neighboring Grains on the Microscopic Corrosion Behavior of a Grain in Polycrystalline Copper. *Corrosion Sci.* 67, 179–183. doi:10.1016/j.corsci.2012.10.017

Liu, F. Q., Du, T., Duboust, A., Tsai, S., and Hsu, W.-Y. (2006a). Cu Planarization in Electrochemical Mechanical Planarization. *J. Electrochem. Soc.* 153 (6), C377–C381. doi:10.1149/1.2186180

Liu, S.-H., Shieh, J.-M., Chen, C., Dai, B.-T., Hensen, K., and Cheng, S.-S. (2005). Two-additive Electrolytes for Superplanarizing Damascene Cu Metals. *Electrochem. Solid-state Lett.* 8 (3), C47–C50. doi:10.1149/1.1854124

Liu, S.-H., Shieh, J.-M., Chen, C., Hensen, K., and Cheng, S.-S. (2006b). Roles of Additives in Damascene Copper Electropolishing. *J. Electrochem. Soc.* 153 (6), C428–C433. doi:10.1149/1.2193348

Matlosz, M., Magaino, S., and Landolt, D. (1994). Impedance Analysis of a Model Mechanism for Acceptor-Limited Electropolishing. *J. Electrochem. Soc.* 141 (2), 410–418. doi:10.1149/1.2054741

Oldenburger, M., Bedürftig, B., Gruhle, A., Grimsmann, F., Richter, E., Findeisen, R., et al. (2019). Investigation of the Low Frequency Warburg Impedance of Li-Ion Cells by Frequency Domain Measurements. *J. Energ. Storage* 21, 272–280. doi:10.1016/j.est.2018.11.029

Padhi, D., Yahalom, J., Gandikota, S., and Dixit, G. (2003). Planarization of Copper Thin Films by Electropolishing in Phosphoric Acid for ULSI Applications. *J. Electrochem. Soc.* 150 (1), G10–G14. doi:10.1149/1.1523415

Pointu, B., Braizaz, M., Poncet, P., and Rousseau, J. (1981). Photoeffects on the Cu/H3PO4 Interface. *J. Electroanalytical Chem. Interfacial Electrochemistry* 122, 111–131. doi:10.1016/S0022-0728(81)80144-1

Pointu, B., Braizaz, M., Poncet, P., and Rousseau, J. (1983a). Photoeffects on the Cu/H3PO4 Interface: Part II. Band Model of the Interface in Darkness. *J. Electroanalytical Chem. Interfacial Electrochemistry* 151 (1), 65–77. doi:10.1016/S0022-0728(83)80424-0

Pointu, B., Braizaz, M., Poncet, P., and Rousseau, J. (1983b). Photoeffects on the Cu/H3PO4 Interface: Part III. Interpretation of Photocurrents at the Interface. *J. Electroanalytical Chem. Interfacial Electrochemistry* 151 (1), 79–87. doi:10.1016/S0022-0728(83)80425-2

Shieh, J.-M., Chang, S.-C., Wang, Y.-L., Dai, B.-T., Cheng, S.-S., and Ting, J. (2004). Reduction of Etch Pits of Electropolished Cu by Additives. *J. Electrochem. Soc.* 151 (7), C459–C462. doi:10.1149/1.1757461

Sun, B. B., Wang, Y. B., Wen, J., Yang, H., Sui, M. L., Wang, J. Q., et al. (2005). Artifacts Induced in Metallic Glasses during TEM Sample Preparation. *Scripta Materialia* 53 (7), 805–809. doi:10.1016/j.scriptamat.2005.06.007

Suni, I. I., and Du, B. (2005). Cu Planarization for ULSI Processing by Electrochemical Methods: A Review. *IEEE Trans. Semicond. Manufact.* 18 (3), 341–349. doi:10.1109/Tsm.2005.852091

Vidal, R., and West, A. C. (1995a). Copper Electropolishing in Concentrated Phosphoric Acid: I . Experimental Findings. *J. Electrochem. Soc.* 142 (8), 2682–2689. doi:10.1149/1.2050074

Vidal, R., and West, A. C. (1995b). Copper Electropolishing in Concentrated Phosphoric Acid: II . Theoretical Interpretation. *J. Electrochem. Soc.* 142 (8), 2689–2694. doi:10.1149/1.2050075

Wagner, C. (1954). Contribution to the Theory of Electropolishing. *J. Electrochem. Soc.* 101(5), 225–228. doi:10.1149/1.2781235

West, A. C., Deligianni, H., and Andricacos, P. C. (2005). Electrochemical Planarization of Interconnect Metallization. *IBM J. Res. Dev.* 49(1)**,** 37–48. doi:10.1147/rd.491.0037

Zhang, B., Lee, W. H., Piner, R., Kholmanov, I., Wu, Y., Li, H., et al. (2012). Low-Temperature Chemical Vapor Deposition Growth of Graphene from Toluene on Electropolished Copper Foils. *Acs Nano* 6 (3), 2471–2476. doi:10.1021/nn204827h

Conflict of Interest: The authors declare that the research was conducted in the absence of any commercial or financial relationships that could be construed as a potential conflict of interest.

frontiers in Chemistry

ORIGINAL RESEARCH
published: 13 December 2021
doi: 10.3389/fchem.2021.781838

Electrocatalytic Properties of Pulse-Reverse Electrodeposited Nickel Phosphide for Hydrogen Evolution Reaction

Woohyeon Jo[1,2], Dasol Jeong[1], Jaebum Jeong[1], Taegeon Kim[1,3], Seungyeon Han[1,2], Minkyu Son[1], Yangdo Kim[2], Yong Ho Park[2]† and Hyunsung Jung[1]*†*

[1]Nano Convergence Materials Center, Korea Institute of Ceramic Engineering & Technology (KICET), Jinju, South Korea, [2]Department of Materials Science and Engineering, Pusan National University, Busan, South Korea, [3]Departments of Materials and Chemical Engineering, Hanyang University, 55 Hanyangdaehak-ro, Sangnok-gu, Ansan, South Korea

Nickel phosphide (Ni-P) films as a catalytic cathode for the hydrogen evolution reaction (HER) of a water splitting were fabricated by a pulse-reverse electrodeposition technique. The electrochemical behaviors for the electrodeposition of Ni-P were investigated by the characterization of peaks in a cyclic voltammogram. The composition of the electrodeposited Ni-P alloys was controlled by adjusting duty cycles of the pulse-reverse electrodeposition. The HER electrocatalytic properties of the Ni-P electrodeposits with an amorphous phase as a function of phosphorous contents existing in Ni-P were electrochemically characterized by the analysis of overpotentials, Tafel slopes, and electrochemical impedance spectrometry. Additionally, the elemental Ni-embedded crystalline Ni_3P was prepared by an annealing process with the amorphous $Ni_{69}P_{31}$ electrodeposit with high contents of phosphorus. The crystalline structure with Ni inclusions in the matrix of Ni_3P was formed by the precipitation of excess Ni. The electrocatalytic properties of crystalline Ni_3P with elemental Ni inclusions were also investigated by electrochemical characterization.

Keywords: nickel phosphide, pulse-reverse electrodeposition, hydrogen evolution reaction, Ni precipitate, volmer-heyrovsky route

Edited by:
Bongyoung Yoo,
Hanyang University, South Korea

Reviewed by:
Ligang Feng,
Yangzhou University, China
Xiaoguang Wang,
Taiyuan University of Technology, China

Correspondence:
Hyunsung Jung
hsjung@kicet.re.kr
Yong Ho Park
yhpark@pusan.ac.kr

†These authors have contributed equally to this work

Specialty section:
This article was submitted to Electrochemistry, a section of the journal Frontiers in Chemistry

Received: *23 September 2021*
Accepted: *16 November 2021*
Published: *13 December 2021*

Citation:
Jo W, Jeong D, Jeong J, Kim T, Han S, Son M, Kim Y, Park YH and Jung H (2021) Electrocatalytic Properties of Pulse-Reverse Electrodeposited Nickel Phosphide for Hydrogen Evolution Reaction. Front. Chem. 9:781838. doi: 10.3389/fchem.2021.781838

INTRODUCTION

Research on environmentally friendly renewable energy has been conducted to replace fossil fuels with limited reserves. Hydrogen energy (H_2) with high gravimetric density has been researched as a candidate for an environmentally friendly sustainable energy source (Kapdan and Kargi, 2006; Nikolaidis and Poullikkas, 2017). Nowadays, hydrogen was dominantly produced by the steam reforming of natural gases with the emission of carbon dioxide as a by-product (Muradov and Veziroğlu, 2005). Electrochemical water splitting operating in a sustainable manner, such as wind and solar power, has been applied to produce green hydrogen as a promising approach. Water splitting is a chemical reaction in which water is separated into hydrogen and oxygen by applying an electric current. The representative technologies of electrochemical water splitting can be categorized in alkaline water electrolysis (AEL), proton exchange membrane electrolysis (or polymer electrolyte membrane) (PEMEL), and solid oxide electrolysis (SOEL) (Brisse et al., 2008; Carmo et al., 2013; David et al., 2019; Shiva Kumar and Himabindu, 2019; Brauns and Turek, 2020). The water splitting reaction was typically performed in the corrosive media of an acidic or alkaline electrolyte. The fabrication of stable and efficient electrocatalysts with low overpotentials for both hydrogen evolution reaction (HER) and oxygen evolution reaction (OER) in water splitting is still a challenging issue. Pt for HER and Ir/Ru oxides as commercial electrocatalytic materials have been utilized. However, the high cost of noble materials is a key limiting factor for application to a large-scale system. Non-noble materials such as metal oxides, chalcogenides, sulfides, nitrides, carbides, and phosphides have been investigated to replace precious electrocatalytic materials (Brown et al., 1984; Raj and Vasu, 1990; Liu and Rodriguez, 2005; McKone et al., 2011; Merki and Hu, 2011; Vrubel and Hu, 2012; Jiang et al., 2014; Kucernak and Sundaram, 2014; Pu et al., 2014; Pan et al., 2015a; Pan et al., 2015b; Wang et al., 2015; Chen et al., 2018; Zhao et al., 2020). Among them, nickel phosphide (Ni-P) compounds have been attracting attention as one of the promising candidates for both HER and OER electrocatalysts. The Ni-P compounds typically exist in the crystalline phases of Ni_3P, $Ni_{12}P_5$, Ni_2P, and Ni_5P_4. The relatively higher positive charges of $Ni^{\delta+}$ and the stronger ensemble effect of phosphorous with increasing contents of phosphorous in Ni-P compounds have been reported to improve the catalytic activities especially for HER due to the easier desorption of H_2 (Pan et al., 2015b; Menezes et al., 2017). The Ni-P electrocatalysts for water splitting have been fabricated by various approaches, such as colloidal synthesis, phosphorylation, physical vapor deposition, chemical vapor deposition, plasma spraying method, and electrodeposition (Wu and Duh, 2003; Mahalingam et al., 2007; Panneerselvam et al., 2008; Wu and Wu, 2013; Cai et al., 2015; Kornienko et al., 2017; Hasannaeimi and Mukherjee, 2019; Kim et al., 2019; Suryawanshi et al., 2020). The electrodeposition technique can be performed to deposit homogeneous Ni-P electrocatalysts in low temperature and atmospheric pressure without high-cost facilities. The contents of phosphorous in Ni-P electrodeposits have been controlled to enhance the electrocatalytic performance by adjusting electrochemical parameters such as the concentration of phosphorus acid, the applied voltage, the applied current, and deposition time (Bonino et al., 1997; Bai et al., 2003; Krolikowski et al., 2006; Mahalingam et al., 2007; Pu et al., 2014; Jiang et al., 2016; Hasannaeimi and Mukherjee, 2019). However, the phosphorous contents in Ni-P electrodeposits are difficult to increase with typical potentiostatic or galvanostatic deposition techniques, since the deposition was conducted by the indirect electrodeposition mechanism called induced co-deposition (Mahalingam et al., 2007; Hasannaeimi and Mukherjee, 2019). Compared to the potentiostatic/galvanostatic and typical pulse electrodeposition techniques with the limited phosphorous contents in Ni-P compounds, a pulse-reverse electrodeposition technique can be employed as the efficient approach to increase the contents of phosphorous in Ni-P compounds. The relative phosphorous contents in Ni-P electrocatalysts can be increased by the selective dissolution of Ni elements in an anodic reaction for the reverse pulse. Therefore, the composition of Ni-P electrocatalysts can be minutely controlled by tailoring a duty cycle of pulse-reverse electrodeposition. A few studies for Ni-P pulse-reverse electrodeposition have been reported (Wu and Wu, 2013; Wu et al., 2015; Kim et al., 2019).

In this paper, the electrochemical behavior of the Ni-P compound was analyzed by cyclic voltammetry. Ni-P compounds as a HER electrocatalyst for the water splitting were fabricated by utilizing a pulse-reverse electrodeposition technique. Compared to the typical Ni-P prepared by a potentiostatic deposition and a pulse electrodeposition, the composition of the amorphous Ni-P electrocatalysts was systematically controlled by controlling the duty cycle of applied pulses in the pulse-reverse electrodeposition. The electrocatalytic properties and the electrochemical behaviors of Ni-P compounds for HER of water splitting in acidic media were intensely investigated as a function of the tailored contents of phosphorous in Ni_xP_y by polarization curves, Tafel plots, and Nyquist plots. Additionally, the electrodeposited Ni-P electrocatalysts with an amorphous phase were annealed. The electrocatalytic properties of the crystallized Ni-P compound were systematically analyzed.

MATERIALS AND METHODS

The Ni-P films were fabricated by pulse-reversed electrodeposition at 30°C using a typical three-electrode configuration with a platinum (Pt) mesh and a saturated calomel electrode (SCE) as the counter electrode and reference electrode, respectively. Fluorine-doped tin oxide glasses (~7 Ω/sq., Sigma-Aldrich, St. Louis, MO, USA) with an area of 25 × 25 mm were employed as the working electrode. Fluorine-doped tin oxide (FTO) glass substrates were ultrasonically cleaned with deionized water (18 MΩ-cm) and a mixture of ethanol and acetone (v/v ratio 1:1) for 20 min and then dried at 80°C for 30 min under air. The electrolyte for the Ni-P electrodeposition consisted of 0.5 M nickel(II) acetate tetrahydrate (Sigma-Aldrich), 0.29 M phosphorous acid (Daejung Chemical, Siheung, South Korea), 0.65 M phosphoric acid (Junsei Chemical, Tokyo, Japan), and 5 wt.% N-methylformamide (NMF, Sigma-Aldrich) with a pH of 3.4. The pulse-reverse electrodeposition was performed by the periodic application of a voltage of -0.85 V (vs. SCE) for the cathodic Ni-P co-deposition reaction and a reverse voltage of -0.2 V (vs. SCE) for the anodic Ni dissolution reaction. The composition of Ni-P electrodeposits was controlled with the varied duty cycles (duty cycle = $\frac{t_{cathodic}}{t_{cathodic}+t_{anodic}} \times 100$). The numbers of periodic cycles for the fixed film thickness of about 500 nm were determined by Faraday's law. The crystalline Ni-P catalyst was prepared by an annealing process at 500 °C in Ar(g) for 1 h with a heating rate of 5°C/min.

Material characterization was carried out with an X-ray diffractometer (XRD, D8 Advance, Bruker, Billerica, MA, USA) with Cu-Kα radiation (λ = 1.5418 nm), field-emission scanning electron microscope (FE-SEM, JSM-6700, JEOL, Tokyo, Japan), transmission electron microscope (TEM, Titan Themis Z, FEI), and energy-dispersive x-ray spectroscope (EDS) equipped with TEM and SEM. Electrochemical analysis was performed with an electrochemical workstation (PMC-1000, AMETEK, Berwyn, PA, USA). The cyclic voltammetry was measured with the scan range of -1.0–1.0 V (vs. SCE) at the scan rate of 50 mV/s in the Ni-P electrolyte. Polarization curves, Tafel plots, and Nyquist plots for the analysis of HER electrocatalytic properties were measured in the acidic solution of 0.5 M H_2SO_4. The linear sweep voltammetry for polarization curves and Tafel plots was swept from 0 to -0.62 V (vs. RHE) at the scan rate of 5 mV/s. Electrochemical impedance spectrometry was performed by applying a potential at -325 mV with an amplitude of 10 mV in the frequency range of 10 kHz to 1 Hz. The electrochemical capacitance surface area (ECSA) was calculated by the double-layer capacitance (C_{dl}) obtained from the cyclic voltammetry at scan rates from 10 to 800 mV/s in the non-Faraday region nearest to the HER-evolving potentials. Specific capacitance (C_s) was assumed to be 40 μF/cm² (Han et al., 2019). The accelerated degradation test (ADT) was performed by sweeping for 2,500 cycles at the scan rate of 100 mV/s with the potential range of 0 to -0.62 V (vs. RHE) in the acidic solution of 0.5 M H_2SO_4.

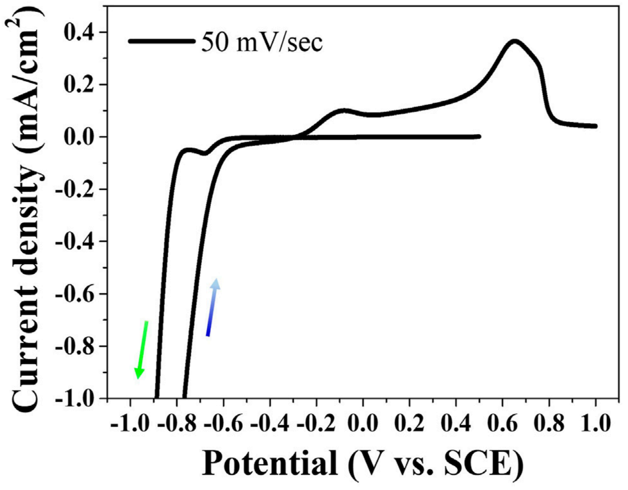

FIGURE 1 | Cyclic voltammetry behavior for Ni-P electrodeposition.

RESULTS AND DISCUSSION

Phosphorous in aqueous solutions cannot be electrodeposited alone due to the high cathodic reduction potential over HER. However, the metal phosphides including the phosphorous element can be electrodeposited by the process defined as the induced co-deposition. **Figure 1** shows the cyclic voltammetry behavior swept at the scan rate of 50 mV/s on an FTO substrate in the aqueous electrolyte including $Ni(OCOCH_3)_2 \cdot 4H_2O$, H_3PO_3, H_3PO_4, and N-CH_3NHCHO. The reduction peak at approximately -0.68 V (vs. SCE) in the cathodic sweep appeared indicating the electrodeposition of Ni-P alloy. Although the mechanism of Ni-P induced co-deposition is still unclear, the electrodeposition of Ni-P has been proposed by an indirect mechanism, as described in **Eqs 1–3**. The formation of Ni-P is achieved by the reaction of Ni^{2+} ions with PH_3 as an intermediate (Mahalingam et al., 2007; Hasannaeimi and Mukherjee, 2019). Two peaks for oxidation reactions were observed in the anodic scan. The first peak at about -0.08 V (vs. SCE) and the second peak at about 0.65 V (vs. SCE) indicate the oxidation of Ni and the dissolution of Ni-P, respectively (Crousier et al., 1993).

$$6H^+ + 6e^- \rightarrow 6H_{ads} \tag{1}$$

$$H_3PO_3 + 6H_{ads} \rightarrow PH_3 + 3H_2O \tag{2}$$

$$2PH_3 + 3Ni^{2+} \rightarrow 3Ni + 2P + 6H^+ \tag{3}$$

Based on the cyclic voltammetry study for the electrochemical behavior of Ni-P, Ni-P electrodeposits with the tailored contents of phosphorous were prepared by pulse-reverse electrodeposition with the controlled duty cycles for the cathodic reaction of the Ni-P co-deposition and the anodic reaction of the dissolution of Ni. **Figures 2A–D** show the morphologies of the Ni-P compounds pulse-reverse electrodeposited at the tailored duty cycles of 50%, 60%, 80%, and 100% (DC), respectively. The thickness of Ni-P electrodeposits was controlled at about 527 ± 12.2 nm, as shown in insets of **Figures 2A–D**. The surface morphologies of Ni-P electrodeposits display the grained structures. Image analyses of the average grain size were accomplished by a linear intercept method. The average grain size of Ni-P electrodeposits decreased with the decrease in the applied duty cycle, as shown in **Figure 2E**. The increased ion diffusion on a cathode at the lower duty cycle with the longer anodic reaction time can induce the frequent adsorption of ionic species. Therefore, the decrease in the duty cycle of the pulse-reverse Ni-P electrodeposition can lead to the increase in the nucleation rate and the inhibition of the grain growth (Chandrasekar and Pushpavanam, 2008; Wahyudi et al., 2019). The average grain size of Ni-P electrodeposits decreased from 401 nm for the duty cycle of 100% to 263 nm for the duty cycle of 50%. Additionally, the EDS analysis of Ni-P electrodeposited as a function of the tailored duty cycles is described in the graph of **Figure 2F**. The phosphorous contents in the Ni-P electrodeposit increased with the decrease in the duty cycle. Ni-P electrodeposits at the duty cycles of 100%, 80%, 60%, and 50% indicated the phosphorous contents of 24.7, 25.6, 27.0, and 30.6 at.%, respectively. The phosphorous content of 30.6% in Ni-P pulse-reverse electrodeposited at the duty cycle of 50% showed the relatively high 30.6 at.%, compared to the phosphorous contents in the Ni-P compounds prepared with conventional DC electrodeposition methods ranging from 12 to 28 at.% (Bonino et al., 1997; Bai et al., 2003; Krolikowski et al., 2006; Mahalingam et al., 2007; Hasannaeimi and Mukherjee, 2019). The increase in phosphorous contents of Ni-P prepared at the lower duty cycle of the pulse-reverse electrodeposition can be attributed to the increased Ni dissolution reaction due to the longer anodic reaction time. The dissolution of Ni in the electrodeposited Ni-P compounds can increase the relative content of phosphorous. Furthermore, the indirect phosphorous co-deposition with Ni requires the indispensable presence of nascent hydrogen to produce PH_3, as described in **Eqs 1–3**. The increased contents of phosphorous at the lower duty cycle might be attributed to the increased H^+ ions adsorbed on a cathode required for the PH_3 formation, because the longer anodic reaction time can effectively remove the reduced

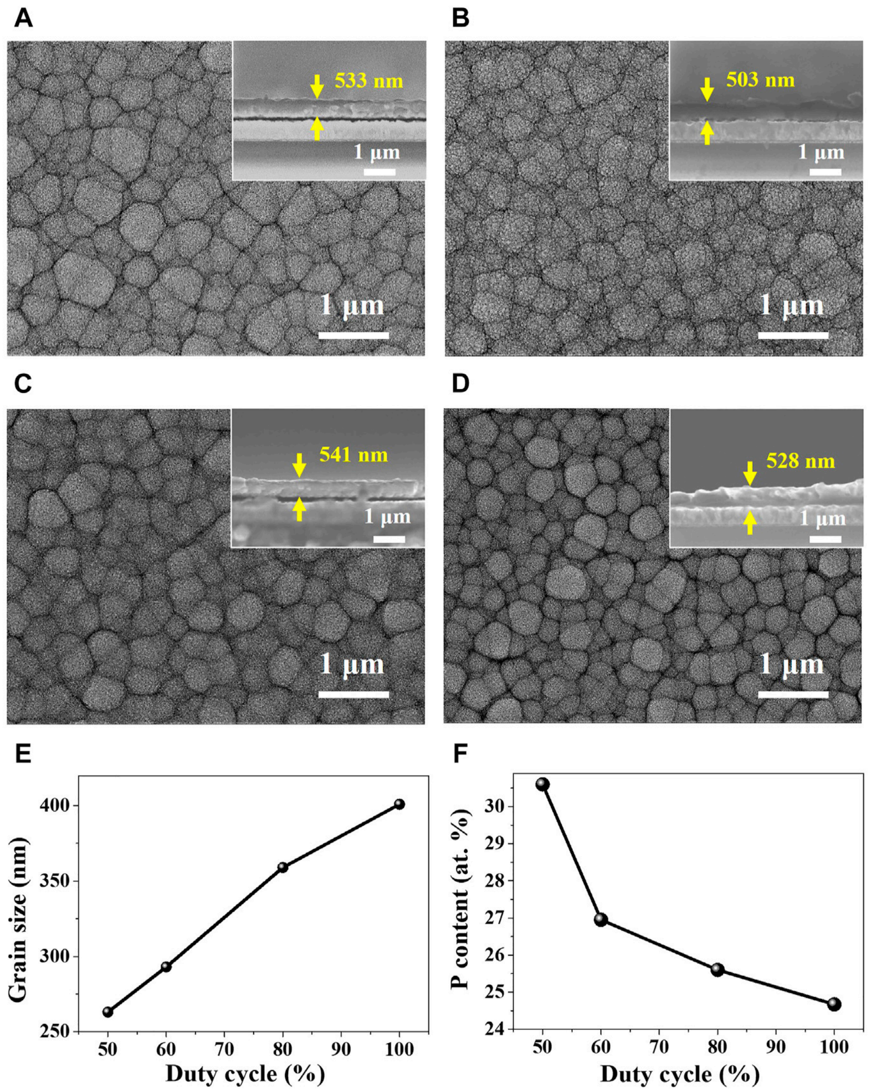

FIGURE 2 | Surface morphologies of Ni-P pulse-reverse electrodeposited at tailored duty cycles: **(A)** 100% (DC), **(B)** 80%, **(C)** 60% and **(D)** 50% (insets: cross-sectional views), and **(E)** the average grain size and **(F)** the phosphorous contents of the Ni-P electrodeposits as a function of duty cycles.

species such as H_2 from the cathode surface (Hasannaeimi and Mukherjee, 2019).

Figure 3 shows the XRD spectra of the pulse-reverse electrodeposited Ni-P at the tailored duty cycles. The well-developed peaks in the diffraction patterns indicate the crystal planes of SnO_2 in FTO substrates. The diffraction peaks were defined as the (110), (101), (200), (211), (310), and (301) planes of SnO_2 (JCPDS, no. 46-1088). The diffraction patterns of the Ni-P electrodeposits were observed as a broad peak at about 44 for the (111) plane of Ni (JCPDS, no. 87-0712). The induced co-deposited phosphorous atoms with Ni for the Ni-P electrodeposition were incorporated into the Ni lattices. Compared to the XRD patterns of the polycrystalline Ni electrodeposit with well-developed peaks, the Ni-P electrodeposits showed the amorphous phase indicating the broad peaks at about 44°. As the contents of phosphorous in Ni-P electrodeposits increase, the crystallinity of Ni-P becomes poor. Additionally, the application of a pulse to enable interference in the continuous crystal growth can aggravate the short-range ordered crystallinity. Therefore, the Ni-P electrodeposits with the induced co-deposition mechanism typically exhibited the poor crystallinity or amorphous phase. Furthermore, the increase in phosphorous contents in Ni-P with decrease in duty cycles intuitively showed the gradual diminution of the intensity for the broad amorphous peak.

The electrocatalytic properties of amorphous Ni-P electrodeposits with tailored compositions were characterized as shown in **Figure 4**. Polarization curves were measured to characterize the overpotential for HER of amorphous Ni-P compounds in the acidic electrolyte of 0.5 M H_2SO_4 (**Figure 4A**). The electrocatalytic activity of a bare FTO substrate without Ni-P electrodeposits for HER was not

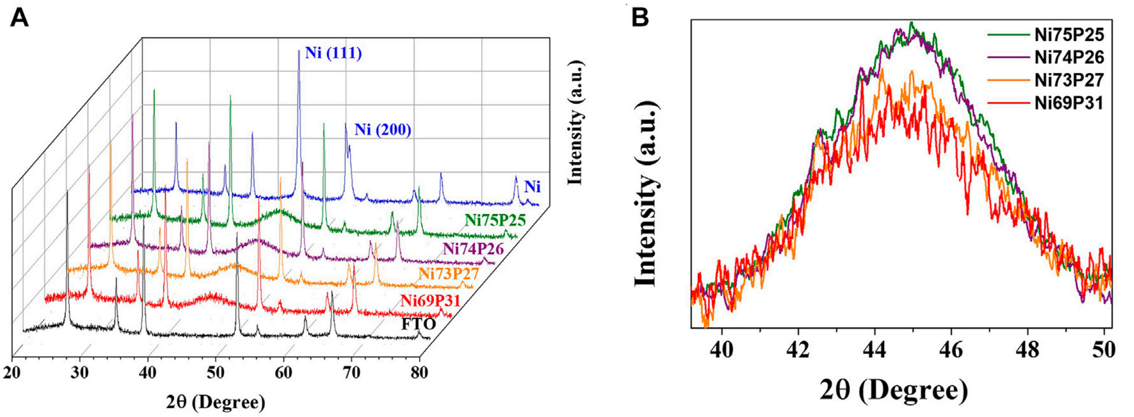

FIGURE 3 | (A) XRD patterns of the pulse-reversed electrodeposited Ni-P with tailored composition and **(B)** the broad peaks around 44° with amorphous phase as a function of phosphorous contents.

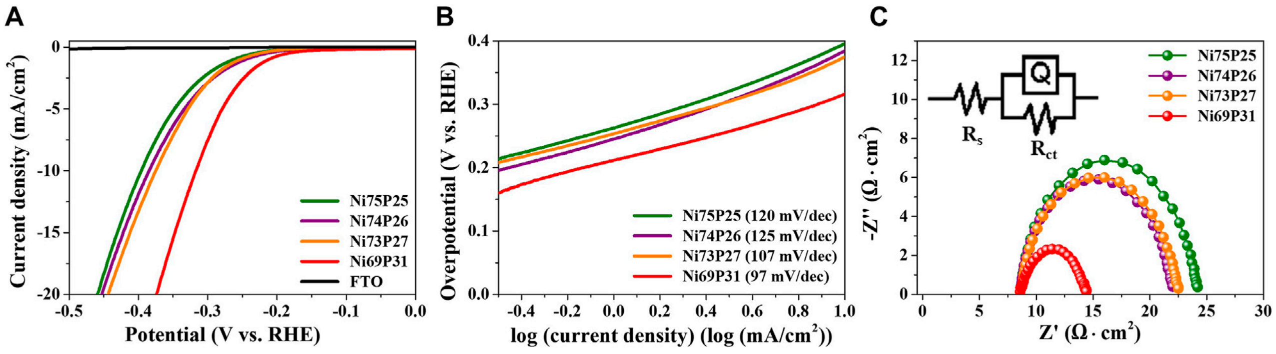

FIGURE 4 | Electrocatalytic properties of the amorphous Ni-P electrodeposits as a function of contents of phosphorous: **(A)** polarization curves, **(B)** Tafel plots, and **(C)** Nyquist plots.

observed. The overpotential of the commercial Pt/C for HER has been reported to be approximately -14 mV at -10 mA/cm^2 (Kim et al., 2019). The overpotentials of $Ni_{69}P_{31}$, $Ni_{73}P_{27}$, $Ni_{74}P_{26}$, and $Ni_{75}P_{25}$ with the controlled compositions indicated -317, -375, -385, and -396 mV at -10 mA/cm^2, respectively. The overpotential of amorphous Ni-P electrodeposits for HER was gradually reduced with the increase in the phosphorous contents. The enhanced electrocatalytic properties for HER might be attributed to the lower desorption energy of H_2 due to the reduced negative charge on the surface of phosphorous to trap protons with increasing contents of phosphorous in Ni-P electrodeposits, as well as to the decreased active sites of Ni to reduce the H_2 desorption energy (ensemble effect) (Pan et al., 2015b; Menezes et al., 2017). The kinetics of Ni-P electrodeposits for HER as a function of composition was investigated by Tafel analysis, as shown in **Figure 4B**. The Tafel slopes of $Ni_{69}P_{31}$, $Ni_{73}P_{27}$, $Ni_{74}P_{26}$, and $Ni_{75}P_{25}$ decreased with the increase in the contents of phosphorous, indicating 97, 107, 125, and 120 mV/dec, respectively. The mechanism for HER in acidic solutions can be described with three processes of the formation step of H_{ads} *via* the adsorption of H^+ (Volmer reaction), the desorption step (Heyrovsky reaction), and the combination step (Tafel reaction), as described in **Eqs 4–6**.(Zeng and Li, 2015). The HER in acidic solutions can be determined by two successive steps of the Volmer–Tafel route or/and the Volmer–Heyrovsky route. The Tafel slopes of Volmer reaction, Heyrovsky reaction, and Tafel reaction as the rate-determining step are 118, 39, and 29.5 mV/dec (Zeng and Li, 2015). The Tafel slope of the Pt electrocatalyst for HER has been reported to be about 30 mV/dec indicating a Volmer–Tafel route with the Tafel reaction as a rate-determining step following the fast initial Volmer reaction. The HER process of Ni-P electrocatalysts has been typically described as Volmer–Heyrovsky route with the Tafel slopes of about 40–75 mV/dec (Pu et al., 2014; Pan et al., 2015b; Zhao et al., 2020). The Tafel slopes of the amorphous Ni-P electrodeposits indicated that the rate-determining step is the Volmer reaction in the mixed kinetic mechanism. The reduction in Tafel slopes with the increase in the contents of phosphorous implied the faster adsorption of intermediate hydrogen atoms on the surface of Ni-P catalysts. Electrochemical impedance spectrometry as a further

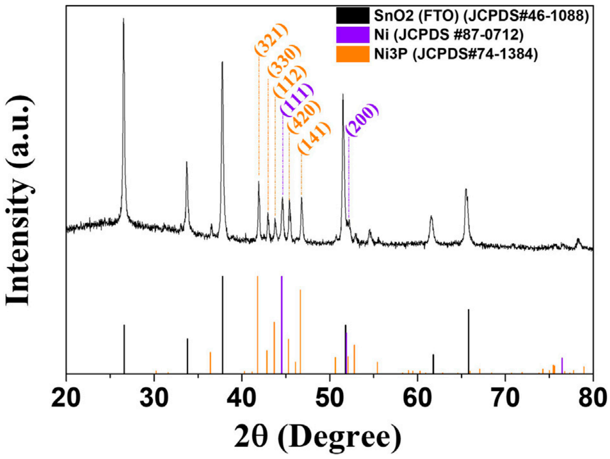

FIGURE 5 | XRD patterns of the annealed $Ni_{69}P_{31}$ electrodeposit.

kinetic study for HER was analyzed as a function of the composition of Ni-P electrodeposits. The charge transfer resistance of the interface between the Ni-P catalyst and electrolyte was drastically reduced in $Ni_{69}P_{31}$ with the highest contents of phosphorous. The enhanced charge transfer of the $Ni_{69}P_{31}$ electrocatalyst was in agreement with the results of the analyses of overpotentials and Tafel plots (**Figure 4C**).

$$H^+ + e^- \rightarrow H_{ads}\,(\text{Volmer reaction}) \tag{4}$$

$$H_{ads} + H^+ + e^- \rightarrow H_{2\,(g)}\ (\text{Heyrovsky reaction}) \tag{5}$$

$$H_{ads} + H_{ads} \rightarrow H_{2\,(g)}\,(\text{Tafel reaction}) \tag{6}$$

The Ni-P electrodeposits had amorphous phases as shown in **Figure 3**. Lowering of the duty cycles in the pulse-reverse electrodeposition induced Ni-P electrodeposits to become further amorphous, aggravating the short-range ordered crystallinity due to the brief periodic deposition time and increase in phosphorous contents. The amorphous $Ni_{69}P_{31}$ electrodeposited at the duty cycle of 50% was annealed at 500°C in Ar 7(g) for 1 h. **Figure 5** shows the XRD patterns of the annealed $Ni_{69}P_{31}$ electrodeposit. Compared to the XRD pattern of the bare $Ni_{69}P_{31}$ electrodeposit, the diffraction patterns of annealed $Ni_{69}P_{31}$ shows the well-developed peaks, indicating the crystallization of amorphous $Ni_{69}P_{31}$. The diffraction peaks were defined as the (301), (321), (330), (112), (420), (141), and (321) planes of Ni_3P (JCPDS, no. 74-1384) and the (111) and (220) planes of Ni (JCPDS, no. 87-0712). As described in XRD analysis, the amorphous $Ni_{69}P_{31}$ electrodeposit was transformed into two crystal structures of Ni_3P and Ni by the annealing process.

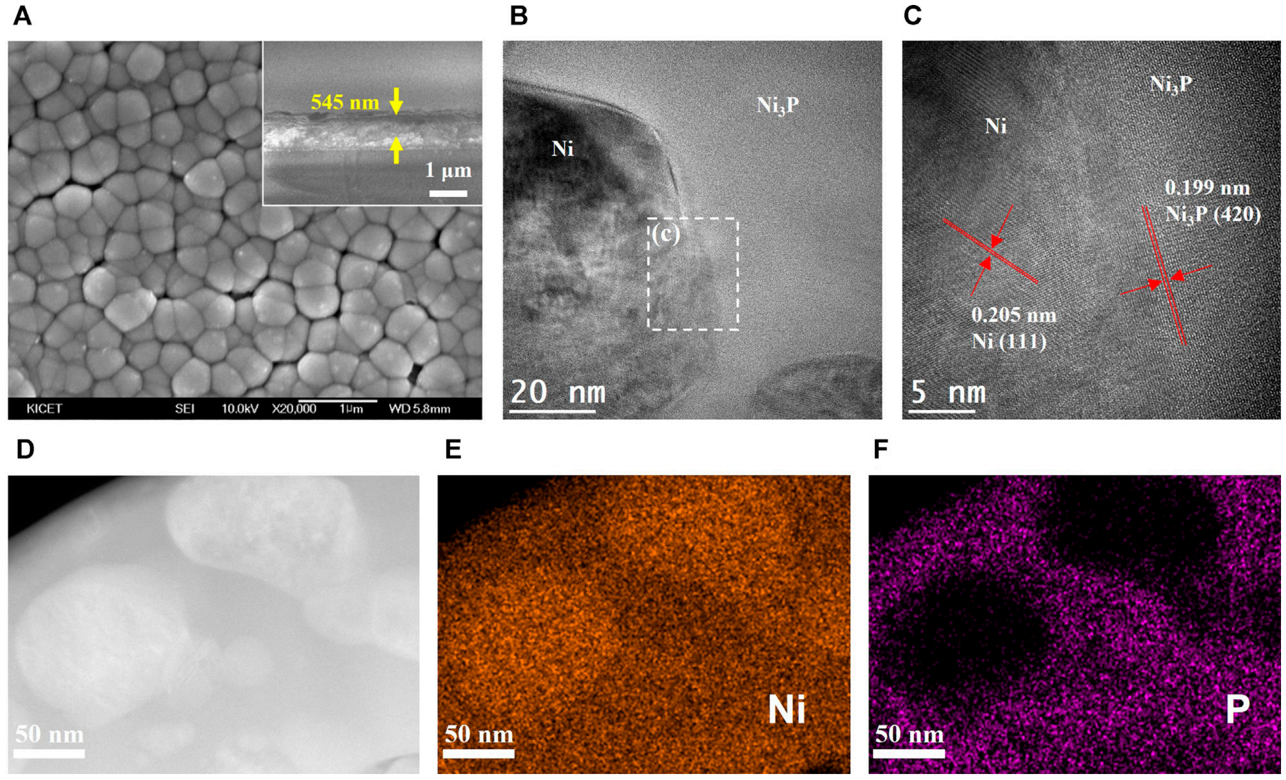

FIGURE 6 | Structural characterization of the crystalline Ni_3P with elemental Ni inclusions prepared by annealing of amorphous $Ni_{69}P_{31}$ electrodeposit: **(A)** FE-SEM image (SEM scale bar and thickness display), **(B)** bright-field TEM image, **(C)** HRTEM image, **(D)** STEM image, and **(E, F)** EDS elemental mapping for Ni and phosphorous.

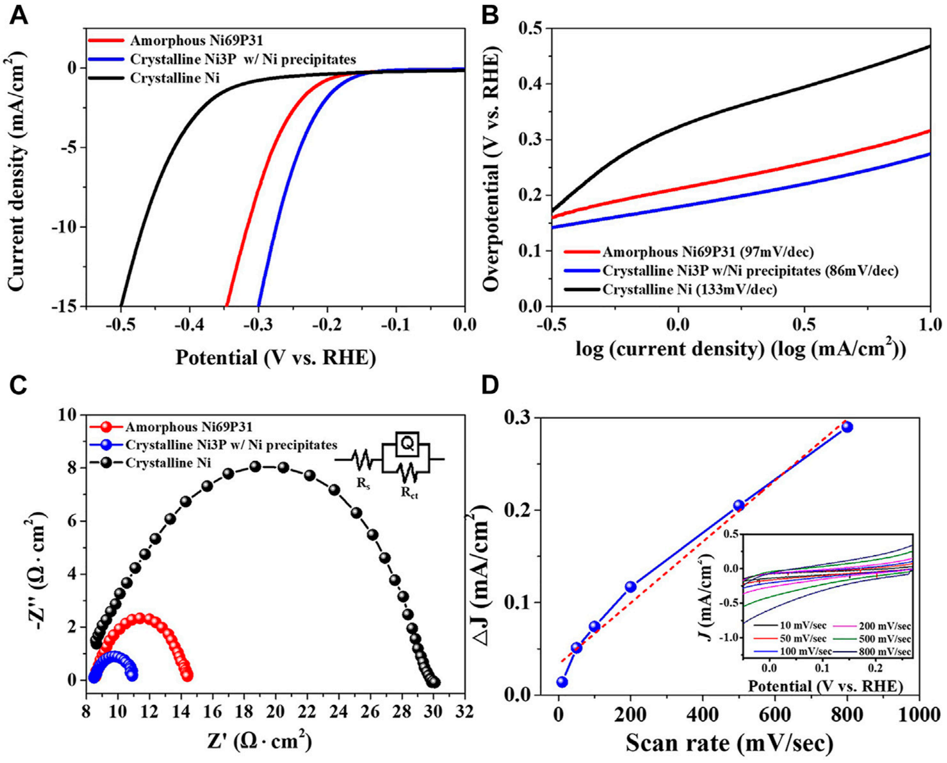

FIGURE 7 | Electrocatalytic properties of the crystalline Ni_3P with elemental Ni inclusions prepared by annealing of amorphous $Ni_{69}P_{31}$ electrodeposit: **(A)** polarization curves, **(B)** Tafel plots, **(C)** Nyquist plots, and **(D)** ECSA estimation based on the capacitive current at 250 mV (vs. RHE) (inset: cyclic voltammograms crystalline Ni_3P with elemental Ni inclusions as a function of scan rate).

SEM and TEM analyses of the annealed $Ni_{69}P_{31}$ electrodeposit was conducted as shown in **Figure 6**. The surface morphology of the crystallized $Ni_{69}P_{31}$ electrodeposit was similar to the surface of the as-deposited amorphous $Ni_{69}P_{31}$ with the grain boundaries, as shown in **Figure 6A**. Corresponding with the XRD analysis, TEM images of the annealed $Ni_{69}P_{31}$ electrodeposit clearly showed the interface between the Ni precipitates and Ni_3P with well-developed lattice structures. The HRTEM image revealed a crystalline structure for Ni precipitates with a lattice spacing of 0.205 nm and for Ni_3P with a lattice spacing of 0.199 nm, corresponding to the (111) planes of Ni (JCPDS, no. 87-0712) and the (420) planes of Ni_3P (JCPDS, no. 74-1384). The elemental precipitation of Ni in the matrix of Ni_3P can be obviously confirmed from STEM and EDS elemental mapping analysis, indicating the compositional distribution of Ni_3P/Ni. The excess elemental Ni over Ni_3P with the stoichiometric composition in $Ni_{69}P_{31}$ might be precipitated for the annealing process.

The electrocatalytic properties of crystalline Ni_3P with elemental Ni inclusions were characterized as shown in **Figure 7**. The crystalline Ni_3P with elemental Ni inclusions indicated the lower overpotential of -275 mV at -10 mA/cm^2 for HER, compared to the HER overpotential of -317 mV in the amorphous $Ni_{69}P_{31}$ and the overpotential of -468 mV in the crystalline Ni film. The Tafel slope of the crystalline Ni_3P with elemental Ni inclusions indicated 86 mV/dec which is smaller than the Tafel slope of 97 mV/dec and 133 mV/dec in the amorphous $Ni_{69}P_{31}$ and crystalline Ni film, respectively. Based on the Tafel slope of 86 mV/dec in the crystalline Ni_3P with elemental Ni inclusions, the rate-determining step is still predicted to be the Volmer reaction in the Volmer–Heyrovsky route. However, the adsorption energy of intermediate hydrogen atoms on the surface of crystalline Ni_3P with elemental Ni inclusions can be anticipated to be reduced, compared to the adsorption energy in the amorphous $Ni_{69}P_{31}$. The analysis of electrochemical impedance spectrometry showed the reduced charge transfer resistance of the interface between elemental Ni-embedded crystalline Ni_3P and electrolyte. The electrocatalytic performance of Ni-P compounds for HER can be improved by the balanced control of the Volmer reaction for the adsorption of protons and the Heyrovsky reaction for the desorption of H_2, considering the exposure of active sites with low energy barrier. The improved overpotential, Tafel slope, and charge transfer in the crystalline Ni_3P with elemental Ni inclusions might be attributed to the lower desorption energy of hydrogen for Heyrovsky reaction and the lower adsorption energy for Volmer reaction. The energy for the H_2 desorption (Heyrovsky reaction) in the crystalline Ni_3P with Ni inclusions prepared from amorphous $Ni_{69}P_{31}$ with the highest phosphorous content was decreased by the enhanced ensemble effect. Moreover, the strong hydride formation in the Ni hollow sites of the crystallized Ni_3P with Ni inclusions reduced the adsorption

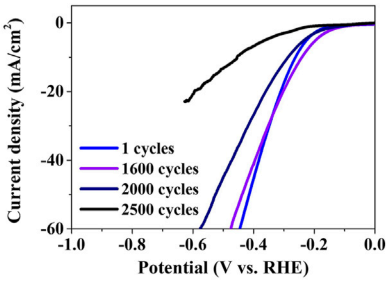

FIGURE 8 | ADT of the crystalline Ni_3P with elemental Ni inclusions up to 2,500 cycle.

energy for proton adsorption reaction (Volmer reaction) called the ligand effect (Liu and Rodriguez, 2005; Chen et al., 2017). Additionally, the ECSA of the crystalline Ni_3P with elemental Ni inclusions was characterized with the double-layer capacitance of the catalytic surface (McCrory et al., 2013). The double-layer capacitance (C_{dl}) indicated 331.48 μF/cm^2, which was calculated with the non-Faradaic double-layer charging current from the cyclic voltammograms at the varied scan rates. The calculated ECSA of the crystalline Ni_3P with elemental Ni inclusions was 8.29 cm^2 corresponding to the ECSA of typical electrodeposited Ni film with about 8.13 cm^2 (Zhou et al., 2017).

The ADT was performed to evaluate the stability of the crystalline Ni_3P with elemental Ni inclusions for the HER electrocatalyst, as shown in **Figure 8**. The ADT polarization curves showed the degradation of the electrocatalytic properties with the increase in the number of cycles. The cycle-dependent overpotentials in the current density of 10 mA/cm^2 indicated -262 mV at 1 cycle, -241 mV at 1,600 cycles, -287 mV at 2,000 cycles, and -455 mV at 2,500 cycles, respectively. The polarization curve of 1,600 cycles slightly deviated with the overpotential of -241 mV, compared to the initial curve of 1 cycle with the overpotential of -262 mV. The severe deviation of the polarization curve with the overpotential of -455 mV after 2,500 cycles indicated the significant loss of the electrocatalytic properties.

CONCLUSION

The electrochemical behaviors for the Ni-P electrodeposition were characterized by cyclic voltammetry, indicating the Ni-P co-deposition in cathodic sweep, the oxidation of Ni, and the dissolution of Ni-P in anodic sweep. The pulse-reverse electrodeposition including the Ni-P co-deposition and the dissolution of Ni was utilized to deposit Ni-P films with tailored compositions. $Ni_{69}P_{31}$, $Ni_{73}P_{27}$, $Ni_{74}P_{26}$, and $Ni_{75}P_{25}$ electrodeposits with the amorphous phase were prepared by adjusting the duty cycles of pulse-reverse electrodeposition. The overpotentials at -10 mA/cm^2 and Tafel slopes of the amorphous Ni-P electrodeposits for HER were reduced from -396 and 120 mV/dec to -317 and 97 mV/dec, as the contents of phosphorous in Ni-P increased from $Ni_{75}P_{25}$ to $Ni_{69}P_{31}$. The analysis of electrochemical impedance spectrometry also showed the reduction of charge transfer resistance of the interface between Ni-P and electrolyte with increase in the contents of phosphorous. The improvement of electrocatalytic properties in amorphous Ni-P electrodeposits with increase in the contents of phosphorous can be achieved by the reduction of the H_2 desorption energy. Additionally, crystalline elemental Ni-embedded Ni_3P were prepared by the annealing of the amorphous $Ni_{69}P_{31}$ electrodeposit. The electrocatalytic properties of the crystalline Ni_3P with elemental Ni inclusions for HER indicated the lower overpotential of -275 mV at -10 mA/cm^2, the gentler Tafel slope of 86 mV/dec, and the reduced charge transfer resistance, compared to the properties of the amorphous $Ni_{69}P_{31}$. Compared to the HER catalytic properties in the amorphous $Ni_{69}P_{31}$, the enhanced electrocatalytic properties in the crystalline Ni_3P with Ni inclusions might be attributed to the lower desorption energy of hydrogen for Heyrovsky reaction and the lower adsorption energy for Volmer reaction. The improved hydrogen desorption and proton adsorption processes for HER catalytic properties can be described by an ensemble effect and a ligand effect, respectively. The crystalline Ni_3P with elemental Ni inclusions demonstrated the continuous stability for HER catalytic properties up to 1,600 cycles in acidic solution.

DATA AVAILABILITY STATEMENT

The original contributions presented in the study are included in the article/Supplementary Material; further inquiries can be directed to the corresponding author.

AUTHOR CONTRIBUTIONS

HJ and YP contributed to the conception and design of the study. WJ, DJ, and JJ conducted the experiments. SH and TK conducted TEM analysis. MS and YK conducted the statistical analysis.

FUNDING

This research was supported by the National Research Foundation of Korea (NRF) funded by the Ministry of Science and ICT (NRF-2020M3H4A3081760).

REFERENCES

Bai, A., Chuang, P.-Y., and Hu, C.-C. (2003). The Corrosion Behavior of Ni-P Deposits with High Phosphorous Contents in Brine media. *Mater. Chem. Phys.* 82 (1), 93–100. doi:10.1016/s0254-0584(03)00193-7

Bonino, J.-P., Bruet-Hotellaz, S., Bories, C., Pouderoux, P., and Rousset, A. (1997). Thermal Stability of Electrodeposited Ni–P Alloys. *J. Appl. electrochemistry* 27 (10), 1193–1197. doi:10.1023/a:1018423701791

Brauns, J., and Turek, T. (2020). Alkaline Water Electrolysis Powered by Renewable Energy: A Review. *Processes* 8 (2), 248. doi:10.3390/pr8020248

Brisse, A., Schefold, J., and Zahid, M. (2008). High Temperature Water Electrolysis in Solid Oxide Cells. *Int. J. Hydrogen Energ.* 33 (20), 5375–5382. doi:10.1016/j.ijhydene.2008.07.120

Brown, D. E., Mahmood, M. N., Man, M. C. M., and Turner, A. K. (1984). Preparation and Characterization of Low Overvoltage Transition Metal alloy Electrocatalysts for Hydrogen Evolution in Alkaline Solutions. *Electrochimica Acta* 29 (11), 1551–1556. doi:10.1016/0013-4686(84)85008-2

Cai, Z.-x., Song, X.-h., Wang, Y.-r., and Chen, X. (2015). Electrodeposition-Assisted Synthesis of Ni2P Nanosheets on 3D Graphene/Ni Foam Electrode and its Performance for Electrocatalytic Hydrogen Production. *ChemElectroChem* 2 (11), 1665–1671. doi:10.1002/celc.201500239

Carmo, M., Fritz, D. L., Mergel, J., and Stolten, D. (2013). A Comprehensive Review on PEM Water Electrolysis. *Int. J. Hydrogen Energ.* 38 (12), 4901–4934. doi:10.1016/j.ijhydene.2013.01.151

Chandrasekar, M. S., and Pushpavanam, M. (2008). Pulse and Pulse Reverse Plating-Conceptual, Advantages and Applications. *Electrochimica Acta* 53 (8), 3313–3322. doi:10.1016/j.electacta.2007.11.054

Chen, Y.-q., Zhang, J.-f., Wan, L., Hu, W.-b., Liu, L., Zhong, C., et al. (2017). Effect of Nickel Phosphide Nanoparticles Crystallization on Hydrogen Evolution Reaction Catalytic Performance. *Trans. Nonferrous Met. Soc. China* 27 (2), 369–376. doi:10.1016/s1003-6326(17)60041-4

Chen, Z., Wu, R., Liu, Y., Ha, Y., Guo, Y., Sun, D., et al. (2018). Ultrafine Co Nanoparticles Encapsulated in Carbon-Nanotubes-Grafted Graphene Sheets as Advanced Electrocatalysts for the Hydrogen Evolution Reaction. *Adv. Mater.* 30 (30), 1802011. doi:10.1002/adma.201802011

Crousier, J., Hanane, Z., and Crousier, J. P. (1993). A Cyclic Voltammetry Study of the NiP Electrodeposition. *Electrochimica Acta* 38 (2), 261–266. doi:10.1016/0013-4686(93)85137-N

David, M., Ocampo-Martínez, C., and Sánchez-Peña, R. (2019). Advances in Alkaline Water Electrolyzers: A Review. *J. Energ. Storage* 23, 392–403. doi:10.1016/j.est.2019.03.001

Han, H., Choi, H., Mhin, S., Hong, Y.-R., Kim, K. M., Kwon, J., et al. (2019). Advantageous Crystalline-Amorphous Phase Boundary for Enhanced Electrochemical Water Oxidation. *Energy Environ. Sci.* 12 (8), 2443–2454. doi:10.1039/c9ee00950g

Hasannaeimi, V., and Mukherjee, S. (2019). Highly Catalytic Amorphous Ni-P Synthesized via Pulsed Electrodeposition. *Adv. Eng. Mater.* 21 (7), 1801122. doi:10.1002/adem.201801122

Jiang, N., You, B., Sheng, M., and Sun, Y. (2016). Bifunctionality and Mechanism of Electrodeposited Nickel-Phosphorous Films for Efficient Overall Water Splitting. *ChemCatChem* 8 (1), 106–112. doi:10.1002/cctc.201501150

Jiang, P., Liu, Q., and Sun, X. (2014). NiP2nanosheet Arrays Supported on Carbon Cloth: an Efficient 3D Hydrogen Evolution Cathode in Both Acidic and Alkaline Solutions. *Nanoscale* 6 (22), 13440–13445. doi:10.1039/c4nr04866k

Kapdan, I. K., and Kargi, F. (2006). Bio-hydrogen Production from Waste Materials. *Enzyme Microb. Technology* 38 (5), 569–582. doi:10.1016/j.enzmictec.2005.09.015

Kim, H., Park, H., Kim, D.-K., Choi, I., and Kim, S.-K. (2019). Pulse-electrodeposited Nickel Phosphide for High-Performance Proton Exchange Membrane Water Electrolysis. *J. Alloys Compounds* 785, 296–304. doi:10.1016/j.jallcom.2019.01.192

Kornienko, E., Bezrukova, V., Kuz'min, V., Lozhkin, V., and Tutunkova, M. (2017). Fine Structure Study of the Plasma Coatings B4C-Ni-P. *IOP Conf. Ser. Mater. Sci. Eng.* 286, 012006. doi:10.1088/1757-899X/286/1/012006

Królikowski, A., Karbownicka, B., and Jaklewicz, O. (2006). Anodic Dissolution of Amorphous Ni-P Alloys. *Electrochimica acta* 51 (27), 6120–6127. doi:10.1016/j.electacta.2006.01.070

Kucernak, A. R. J., and Naranammalpuram Sundaram, V. N. (2014). Nickel Phosphide: the Effect of Phosphorus Content on Hydrogen Evolution Activity and Corrosion Resistance in Acidic Medium. *J. Mater. Chem. A.* 2 (41), 17435–17445. doi:10.1039/c4ta03468f

Liu, P., and Rodriguez, J. A. (2005). Catalysts for Hydrogen Evolution from the [NiFe] Hydrogenase to the Ni2P(001) Surface: The Importance of Ensemble Effect. *J. Am. Chem. Soc.* 127 (42), 14871–14878. doi:10.1021/ja0540019

Mahalingam, T., Raja, M., Thanikaikarasan, S., Sanjeeviraja, C., Velumani, S., Moon, H., et al. (2007). Electrochemical Deposition and Characterization of Ni–P alloy Thin Films. *Mater. Characterization* 58 (8-9), 800–804. doi:10.1016/j.matchar.2006.11.023

McCrory, C. C. L., Jung, S., Peters, J. C., and Jaramillo, T. F. (2013). Benchmarking Heterogeneous Electrocatalysts for the Oxygen Evolution Reaction. *J. Am. Chem. Soc.* 135 (45), 16977–16987. doi:10.1021/ja407115p

McKone, J. R., Warren, E. L., Bierman, M. J., Boettcher, S. W., Brunschwig, B. S., Lewis, N. S., et al. (2011). Evaluation of Pt, Ni, and Ni-Mo Electrocatalysts for Hydrogen Evolution on Crystalline Si Electrodes. *Energ. Environ. Sci.* 4 (9), 3573–3583. doi:10.1039/c1ee01488a

Menezes, P. W., Indra, A., Das, C., Walter, C., Göbel, C., Gutkin, V., et al. (2017). Uncovering the Nature of Active Species of Nickel Phosphide Catalysts in High-Performance Electrochemical Overall Water Splitting. *ACS Catal.* 7 (1), 103–109. doi:10.1021/acscatal.6b02666

Merki, D., and Hu, X. (2011). Recent Developments of Molybdenum and Tungsten Sulfides as Hydrogen Evolution Catalysts. *Energ. Environ. Sci.* 4 (10), 3878–3888. doi:10.1039/c1ee01970h

Muradov, N., and Vezirolu, T. (2005). From Hydrocarbon to Hydrogen?carbon to Hydrogen Economy. *Int. J. Hydrogen Energ.* 30 (3), 225–237. doi:10.1016/j.ijhydene.2004.03.033

Nikolaidis, P., and Poullikkas, A. (2017). A Comparative Overview of Hydrogen Production Processes. *Renew. Sustainable Energ. Rev.* 67, 597–611. doi:10.1016/j.rser.2016.09.044

Pan, Y., Hu, W., Liu, D., Liu, Y., and Liu, C. (2015a). Carbon Nanotubes Decorated with Nickel Phosphide Nanoparticles as Efficient Nanohybrid Electrocatalysts for the Hydrogen Evolution Reaction. *J. Mater. Chem. A.* 3 (24), 13087–13094. doi:10.1039/c5ta02128f

Pan, Y., Liu, Y., Zhao, J., Yang, K., Liang, J., Liu, D., et al. (2015b). Monodispersed Nickel Phosphide Nanocrystals with Different Phases: Synthesis, Characterization and Electrocatalytic Properties for Hydrogen Evolution. *J. Mater. Chem. A.* 3 (4), 1656–1665. doi:10.1039/c4ta04867a

Panneerselvam, A., Malik, M. A., Afzaal, M., O'Brien, P., and Helliwell, M. (2008). The Chemical Vapor Deposition of Nickel Phosphide or Selenide Thin Films from a Single Precursor. *J. Am. Chem. Soc.* 130 (8), 2420–2421. doi:10.1021/ja078202j

Pu, Z., Liu, Q., Tang, C., Asiri, A. M., and Sun, X. (2014). Ni2P Nanoparticle Films Supported on a Ti Plate as an Efficient Hydrogen Evolution Cathode. *Nanoscale* 6 (19), 11031–11034. doi:10.1039/c4nr03037k

Raj, I. A., and Vasu, K. I. (1990). Transition Metal-Based Hydrogen Electrodes in Alkaline Solution ? Electrocatalysis on Nickel Based Binary alloy Coatings. *J. Appl. Electrochem.* 20 (1), 32–38. doi:10.1007/bf01012468

Shiva Kumar, S., and Himabindu, V. (2019). Hydrogen Production by PEM Water Electrolysis - A Review. *Mater. Sci. Energ. Tech.* 2 (3), 442–454. doi:10.1016/j.mset.2019.03.002

Suryawanshi, U. P., Ghorpade, U. V., Lee, D. M., He, M., Shin, S. W., Kumar, P. V., et al. (2020). Colloidal Ni2P Nanocrystals Encapsulated in Heteroatom-Doped Graphene Nanosheets: A Synergy of 0D@ 2D Heterostructure toward Overall Water Splitting. *Chem. Mater.* 33 (1), 234–245. doi:10.1021/acs.chemmater.0c03543

Vrubel, H., and Hu, X. (2012). Molybdenum Boride and Carbide Catalyze Hydrogen Evolution in Both Acidic and Basic Solutions. *Angew. Chem. Int. Ed. Engl.* 51 (ARTICLE), 12703–12706. doi:10.1002/anie.201207111

Wahyudi, S., Soepriyanto, S., and Mubarok, M. (2019). Effect of Pulse Parameters on the Particle Size of Copper Powder Electrodeposition. *IOP Conf. Ser. Mater. Sci. Eng.* 547, 012020. doi:10.1088/1757-899X/547/1/012020

Wang, X., Kolen'ko, Y. V., Bao, X. Q., Kovnir, K., and Liu, L. (2015). One-Step Synthesis of Self-Supported Nickel Phosphide Nanosheet Array Cathodes for Efficient Electrocatalytic Hydrogen Generation. *Angew. Chem.* 127 (28), 8306–8310. doi:10.1002/ange.201502577

Wu, F.-B., and Duh, J.-G. (2003). Mechanical Characterization of Ni–P-Based Ternary Coatings by RF Magnetron Sputtering. *Thin Solid Films* 441 (1-2), 165–171. doi:10.1016/s0040-6090(03)00970-2

Wu, M.-S., Chung, C.-J., and Ceng, Z.-Z. (2015). Cyclic Voltammetric Deposition of Discrete Nickel Phosphide Clusters with Mesoporous Nanoparticles on Fluorine-Doped Tin Oxide Glass as a Counter Electrode for Dye-Sensitized Solar Cells. *RSC Adv.* 5 (6), 4561–4567. doi:10.1039/c4ra13130d

Wu, M.-S., and Wu, J.-F. (2013). Pulse-reverse Electrodeposition of Transparent Nickel Phosphide Film with Porous Nanospheres as a Cost-Effective Counter Electrode for Dye-Sensitized Solar Cells. *Chem. Commun.* 49 (93), 10971–10973. doi:10.1039/c3cc45670f

Zeng, M., and Li, Y. (2015). Recent Advances in Heterogeneous Electrocatalysts for the Hydrogen Evolution Reaction. *J. Mater. Chem. A.* 3 (29), 14942–14962. doi:10.1039/C5TA02974K

Zhao, X., Chen, X., Wang, Y., Song, P., and Zhang, Y. (2020). High-efficiency Ni-P Catalysts in Amorphous and Crystalline States for the Hydrogen Evolution Reaction. *Sustainable Energ. Fuels* 4 (9), 4733–4742. doi:10.1039/d0se00201a

Zhou, Z., Wei, L., Wang, Y., Karahan, H. E., Chen, Z., Lei, Y., et al. (2017). Hydrogen Evolution Reaction Activity of Nickel Phosphide Is Highly Sensitive to Electrolyte pH. *J. Mater. Chem. A.* 5 (38), 20390–20397. doi:10.1039/c7ta06000a

Conflict of Interest: The authors declare that the research was conducted in the absence of any commercial or financial relationships that could be construed as a potential conflict of interest.

frontiers in Chemistry

REVIEW
published: 21 December 2021
doi: 10.3389/fchem.2021.762896

Comprehensive Review on Thermoelectric Electrodeposits: Enhancing Thermoelectric Performance Through Nanoengineering

Tingjun Wu[1]*, Jiwon Kim[2]*, Jae-Hong Lim[3], Min-Seok Kim[3] and Nosang V. Myung[4]

[1]Shanghai Institute of Microsystem and Information Technology, Chinese Academy of Sciences, Shanghai, China, [2]Materials Science and Chemical Engineering Center, Institute for Advanced Engineering, Yongin-si, Korea, [3]Department of Materials Science and Engineering, Gachon University, Seongnam-si, Korea, [4]Department of Chemical and Biomolecular Engineering, University of Notre Dame, Notre Dame, IN, United States

Edited by:
Yong-Ho Choa,
Hanyang University, South Korea

Reviewed by:
Kun-Jae Lee,
Dankook University, South Korea
Hyo-Ryoung Lim,
Pukyong National University, South Korea

*Correspondence:
Tingjun Wu
tingjun.wu@hotmail.com
Jiwon Kim
jkim@iae.re.kr

Specialty section:
This article was submitted to Electrochemistry,
a section of the journal Frontiers in Chemistry

Received: *23 August 2021*
Accepted: *04 October 2021*
Published: *21 December 2021*

Citation:
Wu T, Kim J, Lim J-H, Kim M-S and Myung NV (2021) Comprehensive Review on Thermoelectric Electrodeposits: Enhancing Thermoelectric Performance Through Nanoengineering. Front. Chem. 9:762896. doi: 10.3389/fchem.2021.762896

Thermoelectric devices based power generation and cooling systemsystem have lot of advantages over conventional refrigerator and power generators, becausebecause of solid-state devicesdevices, compact size, good scalability, nono-emissions and low maintenance requirement with long operating lifetime. However, the applications of thermoelectric devices have been limited owingowing to their low energy conversion efficiency. It has drawn tremendous attention in the field of thermoelectric materials and devices in the 21st century because of the need of sustainable energy harvesting technology and the ability to develop higher performance thermoelectric materials through nanoscale science and defect engineering. Among various fabrication methods, electrodeposition is one of the most promising synthesis methods to fabricate devices because of its ability to control morphology, composition, crystallinity, and crystal structure of materials through controlling electrodeposition parameters. Additionally, it is an additive manufacturing technique with minimum waste materials that operates at near room temperature. Furthermore, its growth rate is significantly higher (*i.e.,* a few hundred microns per hour) than the vacuum processes, which allows device fabrication in cost effective matter. In this paper, the latest development of various electrodeposited thermoelectric materials (*i.e.,* Te, PbTe, Bi_2Te_3 and their derivatives, BiSe, BiS, Sb_2Te_3) in different forms including thin films, nanowires, and nanocomposites were comprehensively reviewed. Additionally, their thermoelectric properties are correlated to the composition, morphology, and crystal structure.

Keywords: electrodeposition, electroplating, thermoelectrics, nanoengineering, defect engineering

OVERVIEW OF THERMOELECTRICS

Thermoelectric power generators and coolers are based on the Seebeck and the Peltier effect, respectively, where the Seebeck effect allows direct conversion of temperature gradient into electricity (**Figure 1**). When establishing temperature gradient at the two sides of materials, charge carriers (*i.e.,* electronsin *n*-type semiconductor and holes in p-type semiconductor) would transfertransfer from

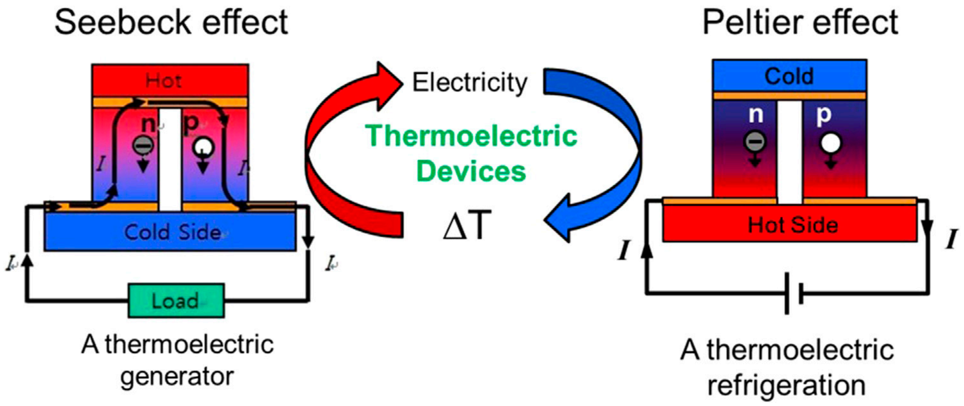

FIGURE 1 | Schematic illustration of thermoelectric effect including the Seebeck effect and Peltier effect.

hot side to cold side, which would create a voltage. voltage. The generated voltage, ΔV, is given by ΔV = S·ΔT, where S is the Seebeck coefficient and ΔT is the temperature difference. On the other hand, the Peltier effect is the generation of temperature gradient by applying electric energy. When electric energy is applied to the materials, charge carriers flow to one end of the thermoelectric materials. The charge carriers also transport energy, resulting in a temperature difference between the two ends.

In thermoelectric devices, the performance can be characterized by the dimensionless thermoelectric figure-of-merit (ZT), which is defined asas following equation:

$$ZT = \frac{S^2\sigma}{\kappa}T \tag{1}$$

where S is the Seebeck coefficient (V/K), σ is the electrical conductivity (S/m), κ is the thermal conductivity (W/mK) and T is the absolute temperature (K). (Zebarjadi et al., 2012) $S^2\sigma$ is defineddefined as the thermoelectric power factor (P. F.).

Additionally, the maximum energy conversion efficiency (η) of a thermoelectric device is defined as the energy produced toproduced the workwork (W) divided by the thermal energy consumed at the hot junction (Q), which is dependent on dependent onZT as well as the temperature difference of the hot and cold side (T_H, T_C). (Nolas et al., 2001; Snyder and Ursell, 2003; Sootsman et al., 2009; Zebarjadi et al., 2012).

$$\eta = \frac{W}{Q} = \frac{T_H - T_C}{T_H}\frac{\sqrt{1+ZT}-1}{\sqrt{1+ZT}+\frac{T_H}{T_C}} \tag{2}$$

Based on the definitions, high energy efficiency would be achieved by improving the thermoelectric power factor ($S^2\sigma$) and suppressing the thermal conductivity. However, Seebeck coefficient, electrical conductivity and thermal conductivity are interdependent to each other, lead to significant difficulties to enhancing the energy efficiency (Szczech et al., 2011). For example, the Seebeck coefficient (S) is a function of the charge carrier (i.e., electrons or holes) effective mass and charge carrier concentration as shown in **Eq. 3**,

$$S = \frac{8\pi^2 k_B^2}{3eh^2}m^*T\left(\frac{\pi}{3n}\right)^{\frac{2}{3}} \tag{3}$$

where e is the elementary carrier charge, k_B is Boltzmann constant, m* is the charge carrier effective mass, h is Planck's constant, and n is the charge carrier concentration. The electrical conductivity (σ) is proportional to the product of carrier concentration and carrier mobility represented (**Eq. 4**).

$$\sigma = e\left(n_e\mu_e + n_h\mu_h\right) \tag{4}$$

where e is the elementary charge; n_e and n_h are the carrier concentrations of electrons and holes, respectively; μ_e and μ_h are the carrier mobility of electrons and holes, respectively. Based on these two equations, increasing the carrier concentration enhances the electrical conductivity, but decreases the Seebeck coefficient.

The electrical conductivity (σ) and thermal conductivity (k) are also interdependent since thermal conductivity (κ) is combination of the lattice thermal conductivity (κ_l) and electrical thermal conductivity (κ_e). κ_e is proportional to the electrical conductivity ($\kappa_e = \sigma LT$), by Wiedemann-Franz law (Szczech et al., 2011). Thus, increasing the carrier concentration increases both electrical conductivity and thermal conductivity. **Figure 2** shows the interdependency of the Seebeck coefficient, the electrical conductivity and the thermal conductivity (Snyder and Toberer, 2008; Szczech et al., 2011).

In order to overcome this intrinsic demerit, numerous researchers endeavored to independently control these parameters by utilizing quantum confinement effect, phonon scattering effect, and energy filtering effect. Historical approaches to enhance the ZT have been focused on altering phonon scattering mechanism, called phonon-glass electron-crystal (PGEC), by introducing complex lattice structures such as skutterudites, superlattices, heterostructure, and nanocomposites. The enhancement of ZT in these systems was mainly achieved by reducing the thermal conductivity due to the increased phonon scattering at the interfaces. (Poudel et al., 2008). However, there is a limit for reducing the lattice thermal conductivity. Recent advancements have been

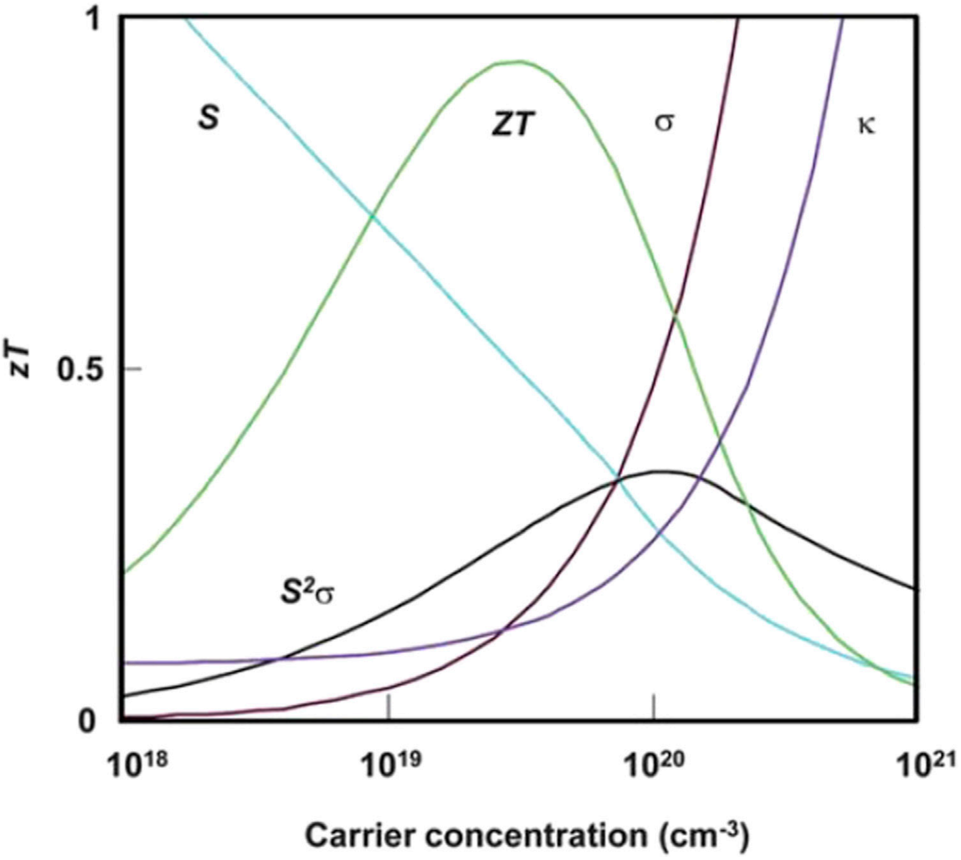

FIGURE 2 | Interdependence of the Seebeck coefficient (S), electrical conductivity (σ), and thermal conductivity (κ) (Snyder and Toberer, 2008; Szczech et al., 2011).

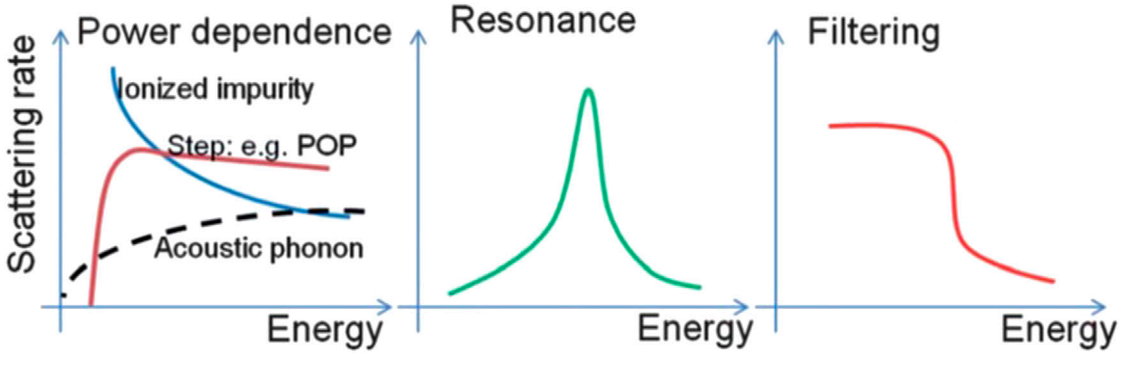

FIGURE 3 | Several possible behaviors of total relation rate (1/τ(E)) in a few k_BT window. (Zebarjadi et al., 2012).

achieved by incorporating metallic and/or semiconducting nanoparticles in thermoelectric matrices. (Hsu et al., 2004; Zeng et al., 2007; Zide et al., 2006). The distortions of the density of states (DOS) near Fermi level as results of carrier localization, resonant state, and carrier filtering effect fulfilled the sharp increase of the Seebeck coefficient without suppressing electrical conductivity. As shown in **Figure 3**, the large Seebeck coefficient can be dependent on the behavior of the scattering rates (1/τ) as a function of energy in the materials (Zebarjadi et al., 2012). The 1/τ, which is inverse function of the energy dependence of the relaxation times ($\tau = \tau_0$Er), where the exponent r is called the scattering parameter. This scattering parameter, which is determined by different scatterings for example, in the case of acoustic phonon scattering, the r is -1/

TABLE 1 | Correlation of material composition and microstructure with electrical and thermoelectric properties.

Ref	Materials	Morphology	Microstructure (Crystalline\diameter)	Preferred orientation	Grain size (nm)	Seebeck coefficient (μV K^{-1})	Electrical conductivity (S cm^{-1})	Thermal conductivity (W m^{-1} K^{-1})	Power factor (μW K^{-2} m^{-1})	ZT	Measure-temp.(K)
Abad et al. (2015)	Te	Thin film	Poly-crystalline		27 ± 3	285	12.5	1	280	0.09	RT
		Thin film	Poly-crystalline		43 ± 4	285	43.7	1	82	0.03	RT
Jiang et al. (2012)	Te	Thin film		(003)		342					473
Wu et al. (2016a)	$Pb_{49}Te_{51}$	Thick film		(220)		524	0.14		3.9		296
Lee et al. (2008)	Bi_2Te_3	Nanowires		(110)		30					RT
Li and Wang, (2009)	$Bi_{0.22}Sb_{1.48}Te_{3.30}$	Thin film				119	78.7		111.5		RT
Diliberto et al. (2008)	$Bi_{1.93}Te_{3.07}$	Film		(110)		−65	833.3		352		RT
Suresh et al. (2009)	Bi_2Te_3	Thin film		(111)	83	−28.1					313
Kim and Oh, (2009)	Bi_2Te_3	Film		(110)		−51.6			710		RT
	Sb_2Te_3	Film				52.1			170		RT
Mannam et al. (2009)	n-Bi_2Te_3	Nanowires		(110)		−318.7					300
	p-Bi_2Te_3	Nanowires		(110)		117					300
Kim and Oh (2010a)	$Bi_{39}Te_{61}$	Film				−67	1,204.8		540		RT
	$Sb_{35}Te_{65}$	Film				63	179.5		70		RT
Lee et al. (2010)	Bi_2Te_3	Nanowires				53	1,690		476.3		RT
Richoux et al. (2010)	$Bi_{0.38}Sb_{1.43}Te_{3.19}$	Film			40	230	54.3		287		RT
Li and Wang, (2010)	$Bi_{0.49}Sb_{1.53}Te_{2.98}$	Film		(015)		185	299.4				RT
Chen et al. (2010)	Bi_2Te_3	Nanowires				−65		0.75		0.45	300
	Bi_2Te_3	Nanowires				−75		0.75		0.9	350
Li et al. (2010a)	$Bi_{0.5}Sb_{1.5}Te_3$	Film				85					RT
Rostek et al. (2011)	$Bi_{39.6}Te_{60.4}$	Thin film				−55					RT
Ma et al. (2011)	$Bi_{39.3}Te_{60.7}$	Thin film				−58.3	1,036		352.2		RT
Pinisetty et al. (2011a)	Te-rich Bi_2Te_3	Nanowire				−48 ± 2.3					RT
	Te-rich Bi_2Te_3	Nanotube				−63 ± 1.9					RT
Zhu and Wang, (2012)	$Bi_{0.40}Sb_{1.28}Te_{3.14}Se_{0.18}$	Thin film				158	138.9				RT
Zou et al. (2012)	$Bi_2Te_{2.7}Se_{0.5}$	Thin film				−92	95.0		80.4		RT
Kim and Oh (2013)	$Bi_{39.5}Te_{60.5}$	Thick film				−59.8	1,408.5		506		RT
	$Sb_{42.9}Te_{57.1}$	Thick film				485.4	210.5		4,960		RT
Manzano et al. (2013)	$Bi_{46}Te_{54}$	Film		(110)		−72	851.1		440		380
Rashid et al. (2013)	Bi_2Te_3	Film		(110)	43.1	−169.49			1737		RT
	Bi_2Te_3			(110)	21.1	112.3			443		RT
Cao et al. (2013)	Bi_2Te_3	Thin film				−140	600		1,247		RT
Wu et al. (2013)	Bi_2Te_3	Film				−120					RT
Yoo et al. (2013a)	$Bi_{11}Te_{10}$	Thin film		(015)		−70			336.2		RT
Wang et al. (2013)	$Bi_{0.47}Sb_{1.44}Te_{3.09}$	Film				145			220		RT
	$Bi_{1.98}Te_{2.73}Se_{0.29}$	Film				−83.2			210		RT
Rashid and Chung, (2013)	$Bi_{1.9}Te_{3.1}$	Thin film		(110)	28	−61.215			820		RT
Zou et al. (2014)	$Bi_2Te_{2.65}Se_{0.44}$	Film		(110)		−88	142		110.0		RT
Maas et al. (2014)	Bi_2Te_3	Thick film				−90	512.8		500		RT
Szymczak et al. (2014)	Bi_2Te_3	Film		(110)		−70	75.2				RT
Jiang et al. (2014)	Bi_2Te_3/PEDOT:PSS/Bi_2Te_3	Film				16	402.5	0.17		0.017	RT
Caballero-Calero et al. (2014)	$Bi_{37.7}Te_{62.3}$	Film		(110)		−80					358
Matsuoka et al. (2015)	$Bi_{54}Te_{46}$/BiSe				38/15	−46			144		RT

(Continued on following page)

TABLE 1 | (*Continued*) Correlation of material composition and microstructure with electrical and thermoelectric properties.

Ref	Materials	Morphology	Microstructure (Crystalline\diameter)	Preferred orientation	Grain size (nm)	Seebeck coefficient (μV K^{-1})	Electrical conductivity (S cm^{-1})	Thermal conductivity (W m^{-1} K^{-1})	Power factor (μW K^{-2} m^{-1})	ZT	Measure-temp.(K)
		Layered structure									
Caballero-Calero et al. (2015)	$Bi_{1.7}Te_{3.1}Se_{0.2}$	Thin film		(110)		–100					353
Zhou et al. (2015)	Bi_2Te_3	Thin film		(110)		–81	520		340	0.16	RT
Li et al. (2015)	$Bi_{0.5}Sb_{1.5}Te_3$	Nanowires	Dia. 67nm	(110)		143	480	0.28		1.14	330
Uda et al. (2015)	$Bi_{37.5}Te_{62.5}$	Film				–81.9	526.3		354		RT
Chang et al. (2015)	$Bi_{39}Te_{61}$	Nanowires	Dia. 60nm			71	390		195.8		300
Shin and Oh (2015)	$Bi_{39.4}Te_{60.6}$	Film				–59.5	1,587.3		559		RT
	$Sb_{43.1}Te_{56.9}$	Film				441.2	281.7		5,480		RT
Kulsi et al. (2015)	$Bi_{1.6}Te_{3.4}$	Thin film		(018)	55	–29	4,033		340	0.28	RT
Lei et al. (2016a)	Bi_2Te_3	Thick film		(110)		–200	400		1,600		RT
Yang et al. (2016)	Te-Bi-Sb	Film				32.9			34		RT
Na et al. (2016)	$Bi_{2.17}Te_{2.83}$	Film		(110)	35.7	–146	691		1,473		RT
Kulsi et al. (2016)	Bi-Te	Film			127	–32	1,247	0.46	130	0.08	RT
Lei et al. (2016b)	Bi_2Te_3	Thick film		(110)	17	–80	330				RT
Manzano et al. (2016)	Bi_2Te_3	Film		(110)		–-58	670		225	0.056	300
Jagadish et al. (2015)	$Bi_2Te_{2.53}$	Film				–20					RT
Lal et al. (2017)	$(Sb_{0.68}Bi_{1.10})_2Te_{3.25}$	Film			17.6	11					RT
Kang et al. (2017)	Bi_2Te_3	Thick film				–72.3	1,408		732		RT
Lei et al. (2017)	$Bi_{0.5}Sb_{1.5}Te_3$	Thick film		(015)	17	150	100		230		RT
Wu et al. (2017b)	Bi_2Te_3-silica particle	Film				78					RT
Xiaolong and Zhen, (2014)	Bi_2Se_3	Thick film				20	1,309		52.57		RT
Jagadish et al. (2016)	$Bi_2S_{2.34}$	Film				–16.3					RT
Kim and Oh, (2010b)	Sb_2Te_3	Thin film				322					RT
Pinisetty et al. (2011b)	Sb_2Te_3	Nanowires	Dia. 100nm		36	359					300
	Sb_2Te_3	Nanotubes	Dia. 400nm		43	332					300
Lim et al. (2011)	Sb_2Te_3	Film		(015)		118					RT
Qiu et al. (2011)	Sb_2Te_5	Thin film				532			1,580		RT
Schumacher et al. (2012)	$Sb_{39.08}Te_{60.92}$	Film		(015)	543	161	280		726		RT
Lim et al. (2012b)	Sb_5Te_8	Thin film		(015)		118			44.2		473
Yoo et al. (2013c)	Sb_2Te_3	Thin film				280			100		RT
Kim et al. (2016)	$AgSbTe_2$	Thin film	Nano-crystalline			300			553		RT

2, and weak impurity scattering, the r is 3/2. Therefore, an increase of the scattering parameter leads to an increase in the slope of the differential conductivity, thus also in the Seebeck coefficient.

Recently, the energy filtering effect where the creation of band bending induced by charge transfer at the interfaces causes the energy-dependent scattering of charge carriers was used to decouple S and σ. In the concrete, a barrier height (E_b) can be generated on the pathways of charge carriers by interfaces, where the charge carriers with higher energy would pass though but the charge carriers with low energy would be scattered. The carrier charge scattering, which is dependent on energy, would improve Seebeck coefficient, owing to its correlation with the energy derivative of the relaxation time at the Fermi energy;

$$S = \frac{\pi^2 kB^2 T}{3e}\left(\frac{\partial lnN(E)}{\partial E} + \frac{\partial ln\tau(E)v(E)^2}{\partial E}\right)E_F \tag{5}$$

$$\tau^{-1}(E) = \frac{V_b^2 x}{R}E^{-3/2} = \frac{e\mu}{m^*} \tag{6}$$

Where $v(E)$ is the velocity of average charge, $N(E)$ is the density of states, $\tau(E)$ is the charge carrier relaxation time. Furthermore, as shown in **Eq. 6**, the carrier relaxation time is proportional to the barrier potential (V_b) by inversion, which means tailoring a potential barrier to an effective height can be utilized to enhancing the Seebeck coefficient. (Faleev and Léonard, 2008; Martin et al., 2009; Ko et al., 2011; Sumithra et al., 2011; Narducci et al., 2012; Zhang et al., 2012).

ELECTRODEPOSITION OF THERMOELECTRIC MATERIALS

Xiao et al. (2008) and Boulanger (2010) reviewed the advances in the electrodeposition of thermoelectric materials in 2008 and 2010, respectively, where major focus was devoted to electrochemistry of thermoelectric materials. Rostek et al. (2015) and others (Snyder et al., 2003; Wang et al., 2013; Roth et al., 2014; Shin and Oh, 2015; Uda et al., 2015; Pelz et al., 2016) reviewed the advancement of electrodeposition of $Bi_2(Te,Se)_3$ and $(Bi,Sb)_2Te_3$ thin films and electrodeposition-based processes to form TE microdevices.

Here, the latest development of various electrodeposited thermoelectric thin films and nanostructured materials (*i.e.*, Te, PbTe, Bi_2Te_3, BiSe, BiS, Sb_2Te_3, Cu_2Se, $CoSb_3$, Ag_8SnS_6, and their derivatives) were comprehensively reviewed in last 10 years. Especially, their thermoelectric properties were summarized and correlated to their composition, morphology, and crystal structure (**Table 1**).

Electrodeposition of Tellurium

Electrodeposition of tellurium has been investigated in both acidic and alkaline media. Qiu et al. (1989) electrodeposited Te thin films with a thickness up to 4 μm on monocrystalline tellurium substrate from a TeO_2-saturated aqueous solution. The thickness was relatively uniform. The needle-like surface morphology with random crystal orientation was observed when deposited on (10 $\bar{1}$ 0) surfaces. At high current densities, polycrystalline films consisting of 1 μm blades with random crystal orientation were produced (Qiu and Shih, 1989).

Suggs et al. (1991) investigate the electrochemical nucleation and growth of Te on gold (Au) (100) surface in acidic sulfate baths (*i.e.*, 0.4 mM TeO_3^{2-} in X M H_2SO_4). Under potentiodynamic deposition, Te initially electrodeposited under underpotential deposition (UPD). As the deposition potential becomes more cathodic, Te electrodeposits under overpotential deposition (OPD) to from three dimensional nuclei. (Suggs and Stickney, 1991).

Ikemiya et al. (1996) electrodeposited Te films on Au (100) and Au (111) from acidic sulfate solutions (0.1 mM $HTeO_2^+$ + 0.05 M H_2SO_4). The atomic structures and growth morphologies of the films were investigated by *in situ* atomic force microscopy. Accordingly, the atomic structure of the Te deposits was independent to the substrate crystal orientation, this support the conclusion that the surface diffusion process of Te adsorbed atoms is rate-limiting steps (Ikemiya et al., 1996).

Yagi et al. (1996) electrodeposited Te in acidic perchlorate solutions with 0.1 M $HClO_4$ and 0.5 mM TeO_2 using polycrystalline gold as substrate. AuAdditionally, *in situ* optical second harmonic (SH) generation at two different excitation wavelengths was utilized. On 1,064 nm excitation, the SH signal varied with the surface coverage of Te (Yagi et al., 1996).

Sorenson et al. synthesized tellurium atomic layers on Au (110) by electrodeposition in the acidic bath (*i.e.*, 0.25 mM TeO_2 + 20 mM H_2SO_4). Additionally, the phase transitions associated with those layers was investigated. The voltammetry indicates two sub-monolayer deposition features and one for bulk. The result of the slow deposition kinetics is that surfaces composed of a single atomic layer structure are not observed. (Sorenson et al., 1999; Sorenson et al., 2001)

Jiang et al. electrodeposited Te film on polyaniline-coated macroporous phenolic foam in the solution with 1 M HNO_3 and 10 mM $HTeO_2^+$. The deposited film was composed of columnar structures and had a growth direction along c-axis direction (Jiang et al., 2011). The highest Seebeck coefficient achieved for the macroporous Te film is 342 μV/K at 473 K (Jiang et al., 2012).

Abad et al. (2015) electrodeposited Te films from acidic nitrate baths (*e.g.*, 10 mM $HTeO_2^+$ and 1 M HNO_3) with sodium lignosulfonate (SLS) as additives. The presence of SLS reduced the average grain size resulted in higher electrical resistivity (~798 μΩ m) compared to Te electrodeposits (~229 μΩ m) in the absence of SLS. The Seebeck coefficient values were about 285 μV/K for both samples which resulted in the power factor of 280 μW/(mK^2) and 82 μW/(mK^2) without SLS and with SLS, respectively, at room temperature (Abad et al., 2015).

Ha et al. (2000) reported the electrochemical behavior of tellurium in alkaline baths (*e.g.*, 10 mM TeO_3^{2-} in2.5 M NaOH). In this bath, Te was able to electrodeposit between -0.8 V and -0.95 V vs. Hg/HgO, but the Te morphology was porous with needle-like radial growth (Ha et al., 2000).

Sadeghi et al. (2008) electrodeposited Te using a nickel-coated copper as substrate in alkaline plating baths. The influence of current density, temperature, and pH were systematically studied. They found that the optimum conditions to electrodeposit Te was: 6 g/L (37.6 mM) TeO_2, pH of 10, and DC current density of 8.55 mA/cm^2 at room temperature (Sadeghi et al., 2008).

Our group also demonstrated the ability to electrodeposit thick Te films from alkaline baths (Wu et al., 2017a) where the applied potentials were optimized to electrochemically reduced TeO_3^{-2} (*aq*) to $Te_{(s)}$ without further reduction of Te to Te_2^{2-} (*aq*). The XRD data revealed that the preferred orientation of thick Te films altered from (001) to (101) as the applied potential varied from −0.9 V to −1.0 V. The optimum pH ranges to deposit compact thick films was between 11.3 and 12.5. Additionally, sufficient magnetic agitation is also essential to deposit compact films. The average grain size ranged from 66 to 135 nm where larger grain size resulted in lower carrier concentration (*e.g.*, $n = 7.1 \times 10^{18}$ cm^{-3}) which might be due to lower defect density. The Highest deposition rate (upto 130 μm/h) with high current efficiency (upto 85%) was achieved by adjusting deposition conditions. Additionally, galvanic displacement reaction which is another facile method to synthesize various nanostructured Te was investigated (Chang et al., 2010; Chen et al., 2010; Hangarter et al., 2010; Lee et al., 2011; Jung et al., 2012; Elazem et al., 2013; Park et al., 2013; Suh et al., 2014; Suh et al., 2017).

Electrodeposition of Lead Telluride Based Materials

PbTe is also a narrow band-gap semiconductor with E_g of 0.31 eV measured at room temperature and a rock-salt crystal structure. PbTe can be n-type or p-type as a result of departures from stoichiometry (*n*-type for Pb-rich PbTe, while p-type for Te-rich PbTe). (Dughaish, 2002). The state-of-the-art commercially available PbTe based thermoelectric materials have the highest ZT of ~0.8 at ~ 600 K, which makes the materials a good candidate for thermoelectric application in the middle-high temperature range.

The Electrodeposition of PbTe was investigated by several groups. Saloniemi et al. reported electrodeposition of Te-rich PbTe thin films in alkaline electrolytes containing TeO_2, disodium salt of ethylenediaminetetraacetic acid (EDTA), and $Pb(CH_3COO)_2$ethylenediaminetetraacetic. They utilized various electrochemical analysis methods including cyclic voltammetry and quartz crystal microbalance to investigate the electrodeposition of PbTe. They observed that Te-rich PbTe deposition through UPD of Pb on Te *via* six electron reduction (Saloniemi et al., 1998). The reduction of the $PbEDTA^{2-}$ complex to $Pb_{(0)}$ was a two-electron reaction whereas Te deposits *via* a four-electron reaction. As the potential becomes more negative, the film becomes powdery and $Te_{(0)}$ further reduced to Te_2^{2-} as the deposition potential becomes more negative (Saloniemi et al., 2000).

Miranda et al. electrodeposited polycrystalline PbTe thin films on porous silicon from alkaline solutions with EDTA as a complexing agent for Pb. They were able to deposit PbTe thin films with the average grain size of 100 nm (Miranda et al., 2004).

Qiu et al. (2005) synthesized uniform and single-crystalline PbTe nanorods with a diameter in the sub-10-nm regime at ambient conditions using sonoelectrochemical method. In the experiment, the Pb^{2+} and TeO_3^{2-} ions concentration were fixed at 10 mM, and the solution pH was kept at approximately 8. Nitrilotriacetic acid (NTA) was used as a complex reagent. The composition of PbTe can be controlled by ratio of precusor ion/ligand concentration. When the $[Pb^{2+}]/[NTA]$ changed from 0.20:1 to 0.10:1 to 0.05:1, the composition of deposits changed from pure PbTe to a mixture of PbTe/Te to pure Te (Qiu et al., 2005).

Yang et al. (2008) electrodeposited PbTe nanowire arrays using template which is patterned by lithographic method. The cross-section of the synthesized PbTe nanowires is rectangular, and the width and height of the nanowires can be tuned from 60 to 400 nm and 20–100 nm, respectively. Polycrystalline PbTe with face centered cubic crystal structure and was produced by a cyclic electrodeposition-stripping method, which have grain size ranged from 10 to 20 nm. The nanowires have a length over 1 mm (Yang et al., 2008).

Erdogan et al. (2009) electrodeposited stoichiometric PbTe thin films on Au (111) substrates from alkaline baths containing EDTA, Pb^{2+}, and TeO_3^{2-} ions. They observed two dimensional nucleation and growth with the preferred orientation of (200) (Erdoğan et al., 2009).

Li et al. (2008a) electrodeposited symmetrical PbTe dendritic structures in the solution containing 10 mM Na_2TeO_3, 5 mM $Pb(NO_3)_2$ and 0.1 M tartaric acid. The formation of the PbTe dendritic structure is affected by the potential oscillation. The morphology of particle with dendritic structures were star-like or trigonal, and the size of the particles were varied from 100 to 500 nm. The deposited PbTe structures had a band gap energy of about 0.272 eV (Li et al., 2008a).

Additionally, many other groups reported the results of characterization of PbTe electrodeposits based on various experimental conditions which are summarized on the **Table 1**. (Banga et al., 2008; Diliberto et al., 2008; Jung et al., 2011; Ni et al., 2011; Frantz et al., 2015; Wu et al., 2016a; Frantz et al., 2016; Bae et al., 2017).

Electrodeposition of Bismuth Telluride (Bi_2Te_3) Based Materials Including BiTe, BiSbTe, BiTeSe and BiSbTeSe

Bi_2Te_3 with a bandgap of 0.16 eV is an excellent candidate for TE application near room temperature range (**Figure 4**). Electrodeposition of Bi_2Te_3 was investigated by various groups.

Wang et al. (2008) synthesized high-density thermoelectric Bi_2Te_3/Sb heterostructure nanowire arrays with diameter of tens using AAO template-directed pulsed electrodeposition. The electrolyte included 12 mM TeO_2, 4 mM $Bi(NO_3)_3$, 0.1 M Sb_2O_3, 0.5 M $K_2C_6H_5O_7$, 1 M $C_6H_8O_7$, and 2 M HNO_3. Additionally, was used as template (Wang et al., 2008).

Li et al. synthesized the hierarchical Bi_2Te_3 nanostructures by electrodeposition in the solution with 10 mM Na_2TeO_3, 5 mM $Bi(NO_3)_3$, 10 mM tartaric acid and 1 M HNO_3 at room temperature (Li et al., 2008b; Li et al., 2008c).

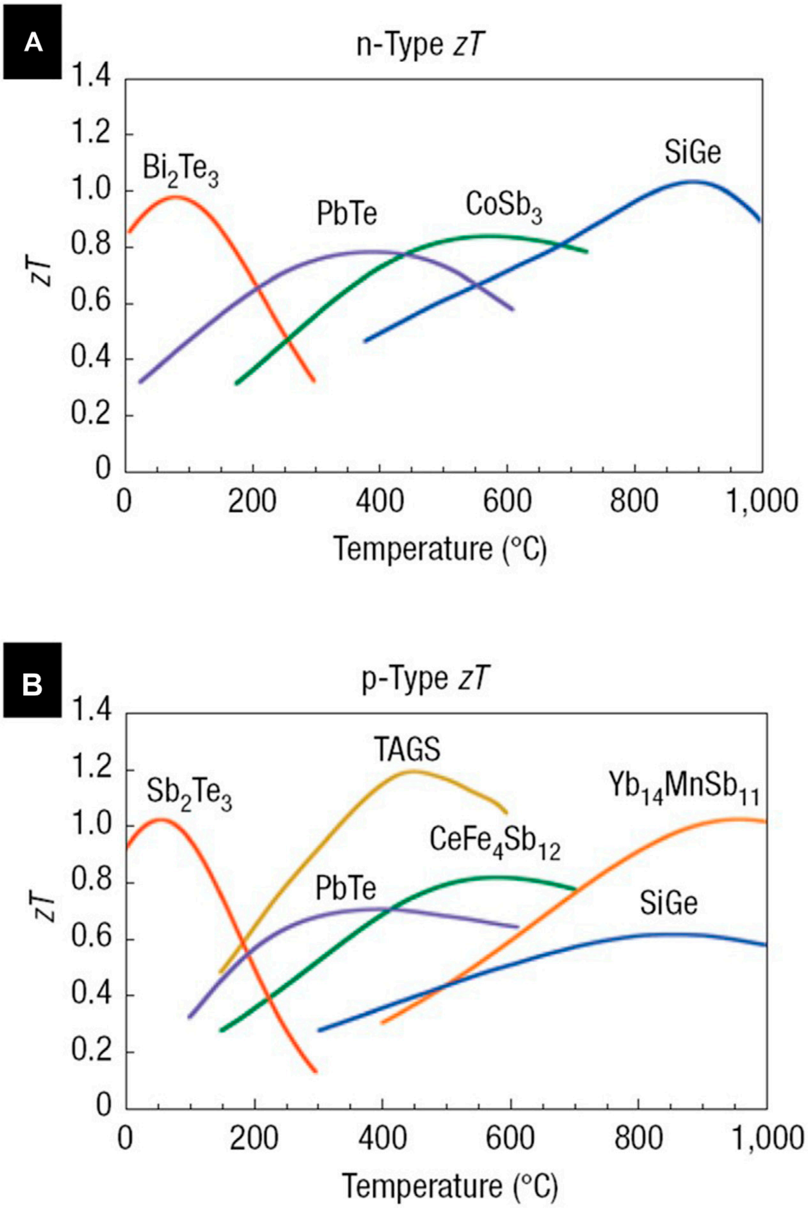

FIGURE 4 | Thermoelectric performance (ZT) of the state-of-art commercial thermoelectric materials: **(A)** n-type and **(B)** p-type, as function of temperature (Snyder and Toberer, 2008).

Liu and Li (2008) reported that electrodeposited Bi_2Te_3 films had a preferential orientation of (110) and platelet grain morphology. The grain morphology changed from single-to multi-order platelets, and the texture decreased when the deposition potential became more negative, which was explained by considering geometrical selection growth and (1ī010) (ī 105) twinning of Bi_2Te_3 crystals (Liu and Li, 2008).

Glatz et al. (2008) electrodeposited $Bi_{2+x}Te_{3-x}$ by combining potential controlled deposition pulses with galvanostatic-controlled resting pulses. The deposited had a uniform stoichiometry composition along the entire thickness. A deposition rates of 50 µm/h was achieved, and Layers thickness of 800 µm was obtained. The composition of $Bi_{2+x}Te_{3-x}$ can be controlled by varying Bi ion concentration in the electrolyte with 80 mM $HTeO_2^+$ and 2 M HNO_3. Bath n-type and p-type $Bi_{2+x}Te_{3-x}$, which is determined by Seebeck coefficients, was deposited (Glatz et al., 2008).

Lee et al. (2008) electrodeposited Bi_2Te_3 nanowires arrays using AAO as template by potentiostatic, galvanostatic, and pulsed method in aqueous solution at room temperature. Uniform Bi_2Te_3 nanowire arrays with highly oriented crystalline structure was synthesized, The bandgap of the deposited can be controlled from 0.21 to 0.29 eV by different relaxation times in the pulsed electrodeposition. The electrical resistances increased slightly with increasing temperatures, which was owing to enhanced carrier-phonon scattering. All samples showed a positive Seebeck coefficient (12–33 μV/K). (Lee et al., 2008).

Li et al. electrodeposited $Bi_xSb_{2-x}Te_y$ in nitric acid and hydrochloric acid solutions. A composition of $Bi_{0.5}Sb_{1.5}Te_3$ was gained in both acid solutions with significantly different morphology. The $Bi_{0.47}Sb_{1.36}Te_{3.17}$ thin film prepared in the nitric acid solution has the highest Seebeck coefficient of 213 μV/K. The $Bi_{0.22}Sb_{1.48}Te_{3.30}$ film prepared in the hydrochloric acid solution has the highest power factor of 111.5 $\mu W/(mK^2)$, which had an electrical resistivity of 1.27×10^{-4} Ω m and Seebeck coefficient of 119 μV/K (Li and Wang, 2009).

Diliberto et al. (2008) synthesized Bi_2Te_3 thin films using pulsed electrodeposition from electrolytes of 20 mM Te(IV) ion and 1 M HNO_3. The Bi ion concentration was varied, where increasing Bi concentration in the electrolyte would lead to higher Bi composition. The results also indicated that pulsed electrodeposition would improve the morphology and the electrical conductivity of films compared to direct electrodeposition. The film near stoichiometry ($Bi_{1.93}Te_{3.07}$) have a Seebeck coefficient of -65 μV/K (Diliberto et al., 2008).

Zhu et al. (2008) synthesized Bi_2Te_3 thin sheets on Au by electrochemical atomic layer epitaxy method using Bi solution with 0.25 mM $Bi(NO_3)_3$ and 0.1 M $HClO_4$, and Te solutions with 0.25 mM TeO_2 and 0.1 M $HClO_4$. The bandgap of the Bi_2Te_3 film was 0.33 eV measured by Fourier transform infrared spectroscopy. Compared to the bulk Bi_2Te_3 single crystal, the bandgap is blue shifted (Zhu et al., 2008).

Mavrokefalos et al. (2009) reported electrodeposition of n-type Bi_2Te_3 nanowires (NW). The results showed that monocrystalline NWs have higher electrical conductivity and thermal conductivity than polycrystalline NWs. Additionally, the carrier mobility of the monocrystalline NW is about 2.5 times higher than that of the polycrystalline NW, but it about 19% lower than that of bulk materials. The electron mean-free path was decreased from 61 nm for bulk materials to 40 nm for the 52 nm nanowires, which is owing to electron scattering specularity parameter by nanowire surface is 0.7. Furthermore, the thermal conductivity of the polycrystalline nanowires is lower. The ZT is about 0.1 at 400 K for both monocrystalline and polycrystalline NWs (Mavrokefalos et al., 2009).

Li et al. electrodeposited $Bi_{0.5}Sb_{1.5}Te_3$ thin film from nitric acid baths. The results show that electrodeposition mechanism varied with applied potential, where at low applied potential, Te was deposited because of electrochemical reduction of $HTeO_2^+$, while at more negative applied potential the reduction reaction of Bi^{3+} with Te occurred with formation of Bi_2Te_3. Additionally, when the applied potential is negative enough, formation of $Bi_{0.5}Sb_{1.5}Te_3$ compound took place (Köse et al., 2009).

Li et al. examined the electrodeposition of Bi_2Te_3 in a solution containing $TeCl_4$, $Bi(NO_3)_3$ and dimethyl sulfoxide (DMSO) by combining cyclic voltammetry with electrochemical quartz crystal microbalance. The results indicated Te^{4+} concentrations in and applied potential had an effect on Bi_2Te_3 composition. Bi_2Te_3 was electrodeposited in applied potential between −0.2 and −0.8 V vs. Ag/AgCl with 10 mM Te^{4+} and 7.5 mM Bi^{3+}. However, Te-rich Bi_2Te_3 were electrodeposited at applied potential between -0.2 and -0.8 V vs. Ag/AgCl in the solution with 50 mM Te^{4+} and 37.5 mM Bi^{3+} (Li, 2009).

Suresh et al. (2009) electrodeposited Bi_2Te_3 thin films at various pH values in HNO_3 solution of Bi $(NO_3)_3$ and TeO_2. The increase in pH resulted in a decrease in grain size and the film morphology transformed from dispersed nanoparticles to connected chain-like nanostructures as pH was increased. At the temperature between 300 and 425 K, the data showed a four-times increase in Seebeck coefficient between its maximum and minimum value as the solution pH changes from 1 to 3.5, which is attributed to the improved connectivity of the nanostructures at higher pH (Suresh et al., 2009).

Kim and Oh (2009) electrodeposited n-type Bi_2Te_3 and p-type Sb_2Te_3 films. The n-type Bi_2Te_3 had a power factor of 7.1×10^{-4} $W/(K^2 \cdot m)$ with a Seebeck coefficient of −51.6 μV/K, which was electrodeposited at applied potential of −0.05 V with 25 mM Bi ion and 25 mM Te ion. Additionally, The p-type Sb_2Te_3 film had a power factor of 1.7×10^{-4} $W/(K^2 \cdot m)$ with a Seebeck coefficient of 52.1 μV/K, which is deposited at applied potential of 0.02 V in the solution containing 63 mM Sb ion and 7 mM Te ion. (Kim and Oh, 2009).

Mannam et al. (2009) electrodeposited Bi_xTe_y nanowires from aqueous acidic solutions containing different $[Bi^{3+}]/[HTeO_2^+]$ (20/20 and 20/10 mM) with 2.5 M HNO_3. The nanowires deposited at low applied potentials had a dominant orientation of (110) according to the XRD pattern. In both electrolytes, n-type nanowires were deposited. However, p-type nanowires can be deposited only in the $[Bi^{3+}]/[HTeO_2^+]$ = 20/10 mM solution. Nanowires formed in the 20/10 mM electrolyte showed at transition from intrinsic to extrinsic. The Seebeck coefficient of -318.7 and 117 μV/K were achieved for n-type and p-type Bi_xTe_y nanowires, respectively (Mannam et al., 2009).

Kuleshova et al. (2010) electrodeposited BiSbTe films in nitric acid baths. In the electrolyte, sodium ligninsulfonate was added as surfactant, which would improve uniformity of the films as well as the thermoelectric properties. Additionally, the surfactant would also affect the composition of films, where $Bi_{0.32}Sb_{1.33}Te_3$ was deposited in the solution with surfactant and $Bi_{0.35}Sb_{1.33}Te_3$ was deposited without surfactant in the solution with 10 mM $HTeO_2^+$, 1 mM Bi^{3+}, 20 mM Sb^{3+}, 1 M HNO_3, 0.1 M H_3Cit and 50 mM Na_3Cit (Kuleshova et al., 2010).

Ma et al. (2010) electrodeposited Bi_2Te_3 on stainless steel, in which the reaction mechanism and the effect of deposition parameters on composition and morphology were investigated. The CV results showed that onset potential for Bi_2Te_3 is more positive than Bi and Te deposition. Furthermore, the Te reduction reaction is kinetically hindered with the presence of Bi ions. (Ma et al., 2010).

Kim and Oh (2010a) synthesized p-type Sb_xTe_y and n-type Bi_xTe_y films by electrodeposition. The Bi_xTe_y film with a thickness of 5.3 μm was electrodeposited in 1 M HNO_3 solution at -0.05 V, which contained 50 mM Bi and Te ion. Moreover, the Bi/(Bi + Te) mole ratio is 0.5. The Sb_xTe_y film with a thickness of 5.2 μm was electrodeposited at 0.02 V in the electrolyte, where the total concentration of Sb and Te ion is

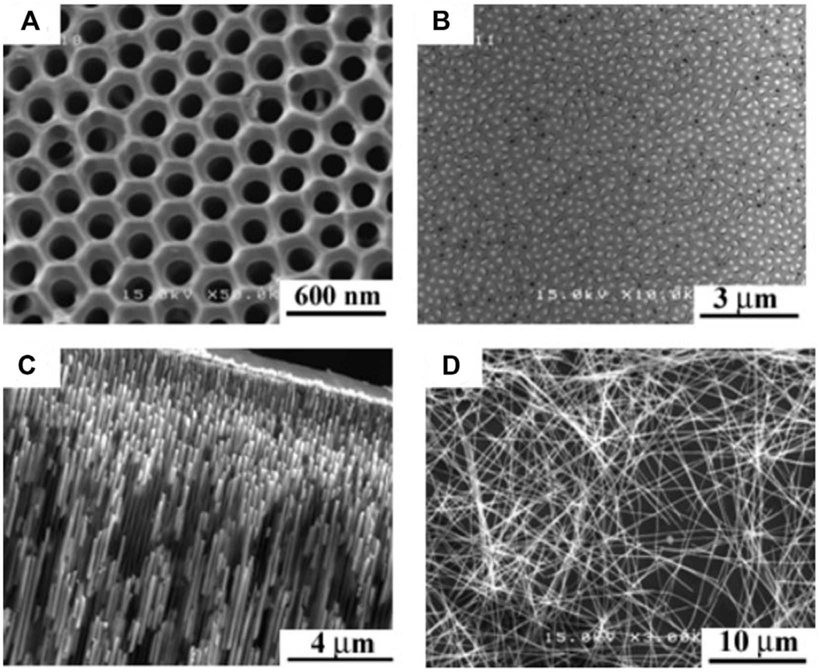

FIGURE 5 | Scanning electron micrographs of AAO template and Bi_2Te_3 nanowires array: **(A)** AAO, **(B)** Top view of Bi_2Te_3 nanowires array, **(C)** Side view of Bi_2Te_3 nanowires array, **(D)** individual nanowires after dissolving AAO (Chen et al., 2010).

70 mM and Sb/(Sb + Te) mole ratio is 0.9. The Bi_xTe_y and Sb_xTe_y films have an electrical conductivity of -67 and 63 μV/K(Kim and Oh, 2010a).

Lee et al. (2010) electrodeposited Bi_2Te_3 nanowires in AAO templates. They claimed the electrical conductivity can be improved from 0.053 to 0.169 × 10^6 S/m by tailoring the structural properties. Meanwhile, the Seebeck coefficient can be enhanced from 46.6 μV/K to 55 μV/K. As a result, a power factor of 476.3 μW/(K^2·m) was achieved (Lee et al., 2010).

Richoux et al. (2010) synthesized p-type $(Bi_{1-x}Sb_x)_2Te_3$ thermoelectric compounds by pulsed electrodeposition in the electrolyte with 1 M $HClO_4$ and 0.1 M tartaric acid. The deposited film had a Seebeck coefficient of 150 μV/K. Additionally, pulsed electrodeposition method can be used to reduce resistivity of the films, where 200 μΩ m was achieved by pulsed electrodeposition method, compared to 5,000 μΩ m by direct-current electrodeposition method (Richoux et al., 2010).

Li et al. electrodeposited $Bi_xSb_{2-x}Te_y$ film by potentiodynamic electrodeposition technique from mixed dimethyl sulfoxide solution containing $Bi(NO_3)_3{\cdot}5H_2O$, $TeCl_4$ and $SbCl_3$. Their results showed that electrodeposition of $Bi_xSb_{2-x}Te_y$ can be realized in a wide range of applied potential. However, the films deposited at applied potential of -0.2 to -0.4 V achieved the highest S of 185 μV/K and the lowest electrical resistivity of 3.34 × 10^{-5} Ω m after annealing. Additionally, the deposited nano-crystalline $Bi_{0.49}Sb_{1.53}Te_{2.98}$ film had a preferred orientation of (015) (Li and Wang, 2010).

Chen et al. (2010) fabricated Te-rich n-type Bi_xTe_y films and nanowires array with rhombohedral structure (**Figure 5**) by potentiostatically electrodeposition from nitric baths. The Seebeck coefficient was about -70 μV/K at 300 K and decreased monotonically with temperature. Additionally, thermal conductivity of 0.75 W/(mK) was obtained at 300 K. Aa a result, The ZT Bi_2Te_3 nanowire was 0.45 at 300 K and 0.9 at 350 K for (Chen et al., 2010).

Frantz et al. (2010) also synthesized polycrystalline Bi_2Te_3 nanowires with rhombohedral phase by electrodeposition using porous polycarbonate as template. Their results showed that dimethyl sulfoxide would help to increase the filling ratio to 80%. Moreover, DMSO in the electrolyte can help to improve the electrical conductivity of the nanowires (Frantz et al., 2010).

Gan et al. (2010) investigated Nanoscale Bi-Te particles with thermoelectric properties electrodeposited on copper substrate in 2.0 M HNO_3. The atomic ratio 1:1 for Bi:Te in the alloy, which is equivalent to the weight percentage of Bi:Te = 62%:38% was confirmed from the EDS data (Gan et al., 2010).

Li et al. (2010a) investigated the electrochemical behavior $Bi_xSb_{2-x}Te_y$ in the solution consisting of 20 mM $TeCl_4$, 20 mM $Bi(NO_3)_3$, 20 mM $SbCl_3$, DMSO, and 0.1 mM KNO_3. A smooth morphology was obtained for $Bi_xSb_{2-x}Te_y$ films deposited at different applied potential. The resistances reduced to about 0.04 Ω by post-annealing process. Seebeck coefficient of 85 μV/K was obtained for $Bi_{0.49}Sb_{1.53}Te_{2.98}$ film (Li et al., 2010a).

Li et al. (2010b) electrodeposited $Bi_2Te_{2.7}Se_{0.3}$ nanowire arrays using AAO as template in the electrolyte composing of 2 mM TeO_2, 2.5 mM $Bi(NO_3)_3$, 0.3 mM SeO_2 and 0.1 M HNO_3. The post-annealing process was carried out at 300°C under an argon atmosphere. The single crystalline nanowires with diameter of about 14 nm were obtained (Li et al., 2010b).

Golgovici et al. (2010) synthesized BiSbTe films by electrodeposition in choline chloride (ChCl) and malonic acid based ionic liquids with a molar ratio of 1:1. The reaction temperature was controlled between 80 and 85°C. The concentration of Bi, Sb and Te ions ranged from 1.5 to 50 mM. The CV data showed that the Te reduction reaction happened first, followed by formation of binary or ternary compounds by codeposition. Furthermore, pulsed electrodeposition technique was also used to synthesize BiSbTe films (Golgovici et al., 2010).

Rostek et al. (2011) synthesized n-type Bi_2Te_3 films by electrochemical deposition. The films with composition near stoichiometric was deposited in the solution containing 20 mM Te ions and 30 mM Bi ions at a current density of 3.75 mA/cm^2. The Seebeck coefficient of as-deposited Bi_2Te_3 films is about -55 μV/K. However, after annealed at 250°C for 60 h, the Seebeck coefficient increased to -130 μV/K(Rostek et al., 2011).

Ma et al. (2011) electrodeposited thin Bi_2Te_3 film onto stainless steel from acidic nitrate baths. The carrier concentration of the deposited films was ten times higher than the bulk Bi_2Te_3, while the Seebeck coefficient and Hall mobility is lower than bulk Bi_2Te_3 (Ma et al., 2011).

Erdogan et al. (2009) synthesized Bi_2Te_3 nanofilm and nanowire by electrodeposition. The acidic electrolyte containing 1 mM TeO_2 and 1 mM $Bi(NO_3)_3$ with a pH of 1.5, in which Bi_2Te_3 nanofilm was deposited with a preferential orientation of (015). Additionally, the alkaline electrolyte containing 2 mM $Bi(NO_3)_3$, 1 mM TeO_2, and 10 mM EDTA with a pH of 9.0, in which nanowire was deposited with (110) as preferential orientation. They claimed that the EDTA in the basic solution leading to the 2D growth mechanism. Furthermore, the band gap energy of Bi_2Te_3 nanostructures can be tuned by size and morphology of the nanostructures, as shown in the reflection absorption Fourier transform infrared spectroscopy (Erdoan and Demir, 2011).

Li et al. (2011a) electrodeposited polycrystalline Bi_2Te_3 nanowire arrays using AAO templates by a pulse electrodeposition method from a electrolyte containing DMSO. The results showed that the applied potential can be used to tune the composition of the nanowires. The Bi_2Te_3 nanowire array have a preferential orientation of (110). Additionally, Bi_2Te_3/Te multilayered nanowires were electrodeposited by the same method (Li et al., 2011a).

Kose et al. (2009) electrodeposited thin $Bi_2Te_{3-y}Se_y$ films in the solution containing 2 mM TeO_2, 2.5 mM $Bi(NO_3)_3$, 0.3 mM SeO_2 and 0.1 M HNO_3 on Au (111) at room temperature. $Bi_2Te_{2.7}Se_{0.3}$ films was obtained at applied potential of −0.02 V vs. Ag/AgCl (3 M NaCl), which has micron-sized granular crystallites (Köse et al., 2009).

Lim et al. (2009) synthesized BiSbTe films *via* electrodeposition in the electrolyte containing 0.5 mM Bi^{3+}, 32 mM SbO^+, 2 mM $HTeO_2^+$, 0.2 M citric acid, 30 mM EDTA and 1 M HNO_3. A Seebeck coefficient of 71 μV/K and a power factor 1.2 × 10^{-4} W/(K^2·m) was achieved for BiSbTe films. Additionally, the amorphous Sb_2Te_3 films was electrodeposited at 0.01–0.03 V in the electrolyte containing 70 mM Bi^{3+}, 70 mM SbO^+, 3.5 M perchloric acid and 0.35 M tartaric acid. A Seebeck coefficient of 250 μV/K and a power factor 57 × 10^{-4} W/(K^2·m) was achieved for Sb_2Te_3 films (Lim et al., 2009).

Kim et al. (2018a) electrodeposited $Bi_xSb_{2-x}Te_y$ films in the solution with 2.4 mM TeO_2, 3.6 mM Sb_2O_3, 400–1,000 μM $Bi(NO_3)_35H_2O$, 33 mM L-tartaric acid, and 1 M HNO_3 at fixed applied potential of −0.1 V (vs. SCE). The composition of the films were controlled by [Sb]/[Bi] ratio. The results showed that the substitution of Bi with Sb would improve the mobility, while suppress the carrier concentration. The deposited $Bi_{10}Sb_{30}Te_{60}$ film has a high Seebeck coefficient, which results in a power factor (PF) of ~490 μW/m K^2 (Kim et al., 2018a).

Ma et al. (2010) electrodeposited $Bi_{1-x}Sb_x$ and $Bi_{2-x}Sb_xTe_3$ thin films at 25°C with different morphologies, such as thin sheets, rods, dendrites, and spherical particles. The $Bi_{1-x}Sb_x$ film was deposited in the electrolyte containing 2 mM $Bi(NO_3)_3$, 1 mM $SbCl_3$, 0.2 M $C_4H_6O_6$, and 0.1 M HNO_3. Additionally, The $Bi_{2-x}Sb_xTe_3$ film was deposited in the electrolyte containing 0.3 mM TeO_2, 0.2 mM $Bi(NO_3)_3$, 1 mM $SbCl_3$, 0.2 M $C_4H_6O_6$, and 0.1 M HNO_3. Furthermore, the results indicated that the underpotential deposition mechanism would lead to the formation of $(Bi_{0.5}Sb_{0.5})_2Te_3$, however the overpotential deposition would result in the formation of $Bi_{0.5}Sb_{1.5}Te_3$. Meanwhile different deposition mechanism can be triggered by applied potential (Ma et al., 2010).

Jin and Wang (2010) electrodeposited n-Type thin $Bi_2Te_{3-y}Se_y$ films using Au, Bi, and $Bi_2Te_{3-y}Se_y$ as substrates. The electrolyte contained 8 mM $HTeO_2^+$, 8 mM Bi^{3+}, 1 mM H_2SeO_3, and 1 M HNO_3. The substrates have significant effect on the morphology of films, as well as the crystal orientation. The preferred orientation of (015) with rhombohedral structure was obtained when using $Bi_2Te_{3-y}Se_y$ as substrate. Additionally, the films deposited on the $Bi_2Te_{3-y}Se_y$ substrate showed the highest power factor after annealing (Jin and Wang, 2010).

Golgovici et al. (2011) investigated electrodeposition of Bi_2Te_3, Sb_2Te_3, BiSb, and BiSbTe films in an aqueous solution containing 5 M NaCl and 1 M HCl or an ionic liquid with choline chloride and malonic acid mixture. The concentrations of Bi, Sb and Te ion were controlled between 10 and 90 mM. Morphology and composition of BiSbTe was modified by increasing the current pulses (Golgovici et al., 2011).

Liu et al. electrodeposited Bi_2Te_3 pillars using multi-channel glass molds as template. The results showed that pulsed electrodeposition method is helpful to achieve high aspect ratio filling. The n-type Bi_2Te_3 arrays with aspect ratio exceeding ten was obtained at a pulse circle of −0.2 V for 4 s, +0.5 V for 1 s, and 0 mV for 3 s (vs. SCE). The precursor concentration in the electrolyte includes 7.5 mM Bi^{3+} and 10 mM $HTeO_2^+$. Furthermore, the electrical conductivity of as-deposited Bi_2Te_3 pillars is the same magnitude as bulk Bi_2Te_3 (Liu and Li, 2011).

Li et al. (2011b) synthesized heterogeneous thermoelectric nanowire arrays of multilayer Bi_2Te_2Se/Te using template direction electrodeposition. The thickness of the Te section can be modulated by tailoring Te ion concentration. The diameter of the heterogeneous nanowires is from 60 to 85 nm. Additionally, the Bi_2Te_2Se segment can change to Bi_2Se_2Te by lowing the Te ion concentration to a certain level (Li et al., 2011b).

Pinisetty et al. (2011a) fabricated polycrystalline Bi_2Te_3 nanowires and nanotubes arrays by electrodeposition. The applied potential had effect on the composition, where both Bi-rich (p-type)and Te-rich (n-type) nanowires or nanotubes can be deposited. The lamellar thickness of bath morphologies were about 17–24 nm. The nanowires and nanotubes had a Seebeck coefficient of 11.5 and 17 μV/K, respectively, which were deposited at −0.4 V. However, when applied potential was −0.065 V, Seebeck coefficient of −48 and −63 μV/K were obtained for the nanowires and nanotubes, respectively (Pinisetty et al., 2011a).

Lim et al. (2012a) synthesized $Bi_xSb_{2-x}Te_3$ films by electrodeposition in an electrolyte containing 0.8 mM TeO_2, 0.2 mM $Bi(NO_3)_3$, 0.8 mM Sb_2O_3, 33 mM tartaric acid, and 1 M HNO_3. The composition of the thin films can be controlled by applied potential, where stoichiometry can be achieved from −0.10 to −0.15 V vs. SCE. Additionally, at more negative applied potential, the thermoelectric property of $Bi_xSb_{2-x}Te_3$ films was degraded, which might owing to higher defect density. The electrical and thermoelectric properties can be enhanced by annealing in reducing environment (Lim et al., 2012a).

Peranio et al. (2012) synthesized Bi_2Te_3 nanowires by a potential-pulsed electrodeposition using AAO as template in a solution with 15 mM $HTeO_2^+$, 10 mM Bi^{3+} and 1 M HNO_3. The nanowires had a stoichiometric composition with diameters of 50–80 nm and a length of 56 μm. The nanowires are single-crystalline with no grain boundaries. The XRD pattern revealed that growth direction of the nanowires were (110) and (210). Additionally, the c axis of the Bi_2Te_3 crystal was perpendicular to nanowire axis (Peranio et al., 2012).

Frantz et al. (2012) electrodeposited bismuth telluride nanowires from an electrolyte with1.5 mM Bi^{3+}, 15 mM $HTeO_2^+$ and DMSO using polycarbonate as template. The DMSO would shift the reduction potential to more negative side and inhibit the cation diffusion. The nanowires deposited -0.1 V vs Ag/AgCl at have a diameter of 60 nm diameter with stoichiometric composition. The crystal structure of the nanowires was polycrystalline with a preferential orientation perpendicular to the (015) planes (Frantz et al., 2012).

Ma et al. (2012a) synthesized thin Sb_2Te_3 and Bi_2Te_3 films using goldthe Au-coated silicon as substrate in an acidic bath with $Bi(NO_3)_3{\cdot}5H_2O$, TeO_2, Sb_2O_3, 1 M HNO_3 and 0.5 M tartaric acid at room temperature by electrochemical deposition. The as-deposited Bi_2Te_3 films were polycrystalline, but the Sb_2Te_3 films were amorphous. Additionally, the Sb_2Te_3 films showed both Sb_2Te_3 and Te phase after annealing (Ma et al., 2012a).

Zhu et al. (2008) electrodeposited p-type quaternary thin BiSbTeSe films using Au as substrate in a acidic solution with 0.5 mM Se(IV), 12 mM Te(IV), 2.5 mM Bi(III), 10 mM Sb(III), 0.67 M tartaric acid at room temperature. The thickness of the films was controlled to 8 μm. The applied potential can be used to tailoring the composition of the films. The as-deposited films were amorphous, however they changed to polycrystalline after annealing based on the XRD patterns. A maximum power factor of 620 $\mu W/(K^2{\cdot}m)$ was achieved for the thin BiSbTeSe films after post-annealing with Seebeck coefficients of 116–133 μV/K (Zhu and Wang, 2012).

Banga et al. (2012) fabricated $Bi_2Te_3/Bi_{2-x}Sb_xTe_3$ heterostructure by pulsed potentiostatic electrodeposition method. The solution consisted Na_2TeO_3, $Bi(NO_3)_3$, Sb(III), 2 M nitric acid, and 0.3 M tartaric acid. The heterostructure had a layer periodicity in the range of 10–30 nm. The XRD data showed that the multilayer films possessed a (015) texture (Banga et al., 2012).

Zhu et al. (2008) synthesized n-type $Bi_2Te_{3-y}Se_y$ films using ITO-coated glass as substrates in the acidic solution containing 10.0 mM $HTeO_2^+$, 7.5 mM Bi^{3+}, 1.1 mM SeO_3^{2-} and 0.5 M HNO_3 at room temperature by pulsed electrodeposition. The smooth and compact $Bi_2Te_{3-y}Se_y$ films were obtained. Increasing the cathodic current density would decrease the grain size of the films. The $Bi_2Te_{3-y}Se_y$ films had a Seebeck coefficient of about -92 μV/K and electrical resistivity of about 109.4 μΩ m (Zou et al., 2012).

Naylor et al. (2012) synthesized Bi_2Te_3 films with stoichiometric composition Bi_2Te_3 in the electrolyte consisting of 10 mM Te(IV), 7.5 mM Bi(III), sodium lignosulfonate (SL) and 1 M HNO_3. The sodium lignosulfonate acted as a surfactant, which would improve morphology and roughness of the Bi_2Te_3 films and achieve better alignment in the (110) plane. The optimal concentration of SL is from 60 to 80 mg/L at a deposition potential of -0.1 V vs SCE (Naylor et al., 2012).

Limmer et al. (2012) reported the electrodeposition of 75 nm diameter nanowire arrays with a composition of $Bi_2(Te_{0.95}Se_{0.05})_3$ onto Si substrates using AAO as template in the electrolyte containing 80 mM $Bi(NO_3)_3{\bullet}5H_2O$, 40–80 mM $TeCl_4$, 0.8–1.2 mM SeO_2 and 0.1 M $KClO_4$ in dimethyl sulfoxide. The nanowires are polycrystalline with grain size of 5–10 nm (Limmer et al., 2012).

Ma et al. (2012b) synthesized ternary compounds $(Bi_xSb_{1-x})_2Te_3$ and $Bi_2(Te_{1-y}Se_y)_3$ by electrodeposition using gold-coated silicon as substrates in the electrolyte with TeO_2, $Bi(NO_3)_3{\cdot}5H_2O$, $SbCl_3$ and Na_2SeO_3, 1 M HNO_3 and 0.67 M tartaric acid at room temperature. The p-type $(Bi_xSb_{1-x})_2Te_3$ films had the highest power factor obtained with composition close to $Bi_{0.5}Sb_{1.5}Te_3$ deposited at a relatively large negative potential. In addition, $Bi_2(Te_{1-y}Se_y)_3$ thin films showed n-type behaviors with composition close to $Bi_2Te_{2.7}Se_{0.3}$ (Ma et al., 2012b).

Fu et al. (2013) fabricated Ag/Bi_2Te_3 multilayer nanowires by pulse electrochemical deposition using AAO as the template in the electrolyte consisted of 0.1 M $HTeO_2^+$, 75 mM $Bi(NO_3)_3$, 10 mM $AgNO_3$, and 1 M HNO_3. The deposited the Bi_2Te_3 had a rhombohedral lattice phase and Ag had a cubic lattice phase. The length of each layer ranged from 25 to 45 nm (Fu et al., 2013).

Nguyen et al. (2012) investigated the electrodeposition of Bi_2Te_3 film in the electrolyte consisting of 50 mM of 50 mM $TeCl_4$, $Bi(NO_3)_3$, 0.5 M lithium nitrate, and ethylene glycol. The results showed that the electrochemical reduction reaction of both Bi^{3+} and Te^{4+} ions were carried out at applied potential more negative than 0.2 and 0.55 V vs. SHE, and the reaction is one step without the formation of intermediates. The Bi and Te ions had the similar diffusion coefficients and the reaction rate constants.

Bi_2Te_3 films stoichiometric composition were deposited at current densities up to 5 A/dm^2 (Nguyen et al., 2012).

Agapescu et al. (2013) electrodeposited of Bi, Te, and Bi_2Te_3 films in an ionic liquids consisting of 10 mM $BiCl_3$ and TeO_2, choline chloride, and oxalic acid (ChCl–OxA) at 60°C.

Kim and Oh (2013) fabricated a thermoelectric device using n-type Bi_2Te_3 and p-type Sb_2Te_3 thin films as basic element legs. The device has a cross-plane configuration with 242 pairs of legs by flip-chip bonding of top electrodes. The thickness of both Bi_2Te_3 and Sb_2Te_3 films were about 20 μm. Additionally, the n-type Bi_2Te_3 and p-type Sb_2Te_3 films showed Seebeck coefficients of -59 μV/K and 485 μV/K, respectively. Furthermore, an open-circuit voltage of 0.294 V and a maximum output power of 5.9 μW were achieved at a temperature difference of 22.3 K (Kim and Oh, 2013).

Manzano et al. (2013) electrodeposited Bi_2Te_3 films with preferentially oriented of (110) direction in the electrolyte containing 10 mM $HTeO_2^+$, 7.5 mM Bi^{3+} and 1 M HNO_3 at applied potential of 0.02 V vs. Ag/AgCl on a Pt substrate. When using pulsed electrodeposition method, the results indicated that at a pulse of on-time = off-time = 0.1 s the films achieved a Seebeck coefficient of −72 μV/K and power factor of 440 μW/(K^2·m), which is measured at 107°C. Additionally, when using potentiostatic method, a Seebeck coefficient of -73 μV/K at 107°C and power factor of 600 μW/(K^2·m) was obtained at 107°C (Manzano et al., 2013).

Zhou et al. (2013) electrodeposited n-type phosphorus-doped Bi_2Te_3 films on a stainless-steel electrode in the solution containing 10 mM TeO_2, 8 mM $Bi(NO_3)_3$, 4 mM H_3PO_4 and 1 M HNO_3. The as-prepared films had the thermal conductivity of 0.47 W/(mK) and the electrical conductivity of 280 S/cm (Zhou et al., 2013).

Rashid et al. (2013) synthesized Bi_2Te_3 films by galvanostatic electrodeposition in a solution containing 8 mM $HTeO_2^+$, 8 mM Bi^{3+} and 1 M nitric acid. The results indicated that annealing process would enhance the carrier mobility while suppressing the carrier concentration. Additionally, the Seebeck coefficient can be enhanced from -57 to -169.49 μV/K and the power factor can be enhanced from 2.74 to 1737 μW/(K^2·m) by post annealing process for p-type Bi_2Te_3 film. Moreover, the Seebeck coefficient can be improved from 28 to 112.3 μV/K and the power factor can be improved from 2.57 to 443 μW/(K^2·m) by post-annealing process (Rashid et al., 2013).

Cao et al. (2013) fabricated thin Bi_2Te_3 films by electrodeposition in the solution with 10 mM $HTeO_2^+$, 8 mM Bi^{3+} and 1 M HNO_3 at room temperature. The substrates used during the deposition had an epitaxial seed layer, which would help to reduce the lattice mismatch between Bi_2Te_3 and Silicon. Moreover, more uniform structure and better crystallinity can be achieved. Both doped and intrinsic silicon were used as substrate, while the results showed that a more compact thin Bi_2Te_3 film with preferential orientation of (001) was obtained for intrinsic silicon, which also showed better thermoelectric performance and smoother surface morphology. Compared to the thin film with preferential orientation of (110), the electrical conductivity is about 72% higher and the power factors is about 45% higher. Additionally, the electrical conductivity and Seebeck coefficient was suppressed by reducing the seed layer thickness from 40 to 20 nm, which can be attributed to the insufficient charge transfer during electrodeposition (Cao et al., 2013).

Wu et al. (2013) investigated the effect of chloride on the electrodeposition of Bi_2Te_3 films in the solution containing $TeCl_4$, $Bi(NO_3)_3·5H_2O$ and ethylene glycol. The results indicated that the presence of chloride could enhance the reduction reaction rate of Te significantly, where the reaction rate with chloride in the solution is three orders of magnitude higher than the rate without chloride. Additionally, Bi_2Te_3 films with stoichiometric composition and smooth morphology were electrodeposited in certain potential window. A Seebeck coefficient of -120 μV/K was achieved for the Bi_2Te_3 films (Wu et al., 2013).

Yoo et al. (2013a) electrodeposited Bi_xTe_y thin films from nitric acid baths with 2.5–10 mM $Bi(NO_3)_3$, 10 mM TeO_2, and 1.5 M HNO_3 using Au/Ni/Si as substrates. The films with surface morphologies of granular and needle-like structures were deposited at different Te content. Higher of Bi ions concentration in electrolytes would result in higher power factor. Additionally, the power factor was not improved significantly owing to the interdependence of the electrical conductivity and the Seebeck coefficient (Yoo et al., 2013a).

Wang et al. (2013) synthesized $Bi_2Te_{2.7}Se_{0.3}$ and $Bi_{0.5}Sb_{1.5}Te_3$ by electrodeposition combined with post annealing. The solution to electrodeposit n-type $Bi_2Te_{2.7}Se_{0.3}$ contained 8 mM $HTeO_2^+$, 8 mM Bi^{3+}, 1 mM H_2SeO_3 and 1 M HNO_3, while the electrolyte to electrodeposit p-type $Bi_{0.5}Sb_{1.5}Te_3$ contained 2 mM Bi^{3+}, 10 mM $HTeO_2^+$, 100 mM Sb(III) and 1 M HNO_3. The as-deposited films possess amorphous structure and can be transferred to nanocrystalline after annealing. The annealed films show a preferred orientation of (015). The maximum power output of 77 μW was achieved with open-circuit voltage of 660 mV with a temperature difference of 20 K at 25°C. Additionally, a power density of 770 μW/cm^3 was obtained (Wang et al., 2013).

Rashid et al. (2013) synthesized n-type Bi_2Te_3 films with a prominent orientation of (110) in the acidic solution with TeO_2 and $Bi(NO_3)_3$ on gold electrode. The Bi_2Te_3 films are nanocrystalline with grain size ranged from 21 to 45 nm. The results showed that the electrodes distance could be used to tune electrical and thermoelectric properties of the films, thus improving carrier charge mobility without varying of the Seebeck coefficient and carrier concentration. The highest power factor of 820 μW/K^2·m was achieved with an electrical conductivity of 2.13 × 10^3 S/cm and Seebeck coefficient of -61.2 μV/K (Rashid and Chung, 2013).

Yoo et al. (2013b) synthesized $Bi_xSb_{2-x}Te_3$ films use potentiostatic electrodeposition method at room temperature in an acidic electrolyte containing 0.8 mM TeO_2, 0.2 mM $Bi(NO_3)_3$, 0.8 mM Sb_2O_3, 1 M HNO_3, and 33 mM tartaric acid. When the applied potential was controlled between -0.10 and -0.15 V versus SCE, thin films with composition near stoichiometric were deposited. Additionally, reducing the applied potentials would result in suppressing the electrical and thermoelectric properties, probably owing to higher defect density (Yoo et al., 2013b).

Ng et al. (2014) fabricated the binary Bi_2Te_3 and ternary BiSbTe nanowires using template (AAO) directed electrodeposition method in a solution compose of 10 mM TeO_2, 20 mM $Bi(NO_3)_3 \cdot 5H_2O$ and 1 M HNO_3,. The results showed that reducing the applied potentials can increase the Sb composition, while increasing the applied potentials would facilitate the formation of Bi_2Te_3 (Ng et al., 2014).

Zou et al. (2014) investigated electrodeposition of n-type $Bi_2Te_{3\text{-}y}Se_y$ film in the solution containing 10.0 mM $HTeO_2^+$, 1.1 mM SeO_3^{2-}, 7.5 mM Bi^{3+}, and 1 M HNO_3 at room temperature. The nucleation and growth mechanism were examined. The electrochemical reaction rate was controlled by diffusion and irreversible with the limiting current density of 1.78 mA/cm^2. A flocculent film was deposited when the applied potential was larger than limiting current without agitation. However, $Bi_2Te_{3\text{-}y}Se_y$ film with smooth morphology was deposited at 4 mA/cm^2 with agitation. $Bi_2Te_{3\text{-}y}Se_y$ film deposited at 1 mA/cm^2 have relatively high power factor and electrical conductivity (Zou et al., 2014).

Maas et al. (2014) electrodeposited Bi_2Te_3 in acidic solution with 20 mM $HTeO_2^+$ and 20 mM Bi^{3+}. The anode is Bi_2Te_3 as a sacrificial the source of cations. A homogeneous Bi_2Te_3 film with a thickness of 300 μm was deposited using Bi_2Te_3 as anode, while without Bi_2Te_3 as anode the thickness can be obtained is 10 times thinner. A power factor of 500 μW/(K^2·m) was achieved (Maas et al., 2014).

Szymczak et al. (2014) electrodeposited n-type Bi_2Te_3 films in an ionic liquid with 1-ethyl-1-octyl-piperidinium bis(trifluoromethylsulfonyl)imide (EOPipTFSI) and 1-ethyl-1-octyl- piperidinium bromide (EOPipBr). The atomic ratio of EOPipTFSI and EOPipBr is 95:5. According to the result, this ionic liquid is stable at high cathodic applied potential, which provide a larger window to deposited Bi_2Te_3 compound. The morphology of the Bi_2Te_3 film can be tuned by precursor concentration, in which mirror-like films can be deposited with good uniformity. Additionally, an electrical resistivity of 133 μΩ m and Seebeck coefficient of -70 μV/K were achived (Szymczak et al., 2014).

Jiang et al. (2014) fabricated Bi_2Te_3/PEDOT:PSS/Bi_2Te_3 composite film by electrodeposition of Bi_2Te_3 onto poly (3,4-ethylenedioxythiophene): poly (styrenesulfonate) (PEDOT:PSS) film. The solution contained TeO_2, $Bi(NO_3)_3$, and 1 M HNO_3. A thermal conductivity of 0.169–0.179 W/(mK) was obtained. ZT value of 1.72×10^{-2} was achieved for Bi2Te3/PEDOT:PSS/Bi_2Te_3 composite film with electrical conductivity of 403.5 S/cm (Jiang et al., 2014).

Caballero-Calero et al. (2014) electrodeposited Bi_2Te_3 films in a solution with 10 mM $HTeO_2^+$, 7.5 mM Bi^{3+}, 1 M HNO_3. The Bi_2Te_3 films have a preferred orientation of (110) with c-axis parallel the substrate. Additionally, the effect of sodium lignosulfonate as surfactant on morphology was examined. Seebeck coefficient was determined to be -80 ± 6 μV/K (Caballero-Calero et al., 2014).

Wu et al. (2014) electrodeposited SbBi, Sb_2Te_3, and BiSbTe alloys in the electrolyte containing $TeCl_4$, $SbCl_3$, $Bi(NO_3)_3$, and ethylene glycol. The electrochemical reaction mechanism of Sb in chloride-free ethylene glycol was investigated. The results showed that the diffusion coefficients of Sb(III), Te(IV) and Bi(III) were comparable in ethylene glycol. Additionally, the onset potential of Sb is more negative than that of Te. During the electrodeposition of BiSbTe alloys, BiTe was deposited first followed by increase of Sb composition at more negative applied potential. (Wu et al., 2014).

Patil et al. (2015) electrodeposited fern shaped Bi_2Te_3 thin film in the solution containing 10 mM Te(IV), 7 mM $Bi(NO_3)_3$, and 1 M HNO_3.

Matsuoka et al. (2015) electrodeposited Bi_2Te_3/Bi_2Se_3 multiplayer heterostructure in two baths sequentially. The layer thickness was fixed to about 1 μm and the number of layers were varied from 2 to 10. The deposited multilayer structure is n-type with nanocrystalline. The boundaries between different layers were not clear planar. The number of the layers had a dramatic effect on the electrical conductivity, where more layers resulted in higher electrical conductivity, while Seebeck coefficient remained unchanged. The 10-layer Bi_2Te_3/Bi_2Se_3 heterostructure has a power factor of 144 μW/(K^2·m), which is about 3 times higher than that of the 2-layer heterostructure (Matsuoka et al., 2015).

Caballero-Calero et al. (2015) electrodeposited $Bi_2Te_{3\text{-}y}Se_y$ films in a conventional three electrode cell in the solution containing 9 mM $HTeO_2^+$, 7.5 mM Bi^{3+}, 1 mM H_2SeO_3, and 1 M HNO_3. The influence of additives (*i.e.,* sodium signosulfonate (SLS) and EDTA) in morphology, stoichiometry, structure and Seebeck coefficient was studied. The films synthesized with SLS had high crystallographic orientation and better morphology, while films deposited in the presence of EDTA had higher content of bismuth. The combination of both additives would improve the quality of stoichiometric $Bi_2Te_{2.7}Se_{0.3}$ films, namely denser morphology, higher orientation and higher Seebeck coefficients (60% larger) when compared with films deposited without additives. (Caballero-Calero et al., 2015).

Zhou et al. (2015) synthesized Bi_2Te_3 thin films by the pulsed electrodeposition method in the solution consisting of 40 mM $HTeO_2^+$, 30 mM Bi^{3+} and 1.7 M HNO_3. The effect of deposition parameters on the composition and microstructure was investigated. The results indicated that the stoichiometry and morphology can be improved by a large pulse off-to-on ratio with a pulsed applied potential of 0 mV vs. Ag/AgCl. Additionally, larger pulse off-to-on ratio would enhance the ZT of Bi_2Te_3 films owing to suppressing the thermal conductivity and improving the Seebeck coefficient. The highest ZT value was 0.16 obtained at a pulse off-to-on ratio of 50 (Zhou et al., 2015).

Li et al. (2015) reported the electrodeposition of BiSbTe nanowires in the electrolyte containing 15 mM $HTeO_2^+$, 40 mM SbO^+, 2 mM Bi^{3+}, 0.3 M tartaric acid and 1 M HNO_3. Their data showed that the pulse electrodeposit method would help to improve the uniformity and crystallinity of $Bi_{0.5}Sb_{1.5}Te_3$ nanowires, which resulted in higher electrical and thermal conductivity, compared to the direct current deposited nanowires. Additionally, the pulse electrodeposit method would also enhance the Seebeck coefficient of nanowires, which was attributed to a more homogeneous distribution of the elements. The highest ZT value was 1.14 at 330 K achieve by pulse-deposited $Bi_{0.5}Sb_{1.5}Te_3$ nanowires (Li et al., 2015).

Song et al. (2015) synthesized thin Bi_2Te_3 films in a acidic bath with 7.5 mM $Bi(NO_3)_3$, 10 mM TeO_2, cetyltrimethylammonium bromide (CTAB) and 1.5 M HNO_3 at room temperature. CTAB acted as a surfactant. The results indicated that the presence of CTAB would help to improve the surface morphology and mechanical properties Bi_2Te_3 films. However, the electrical and thermoelectric properties were preserved (Song et al., 2015).

Uda et al. (2015) fabricated Bi_2Te_3 thermoelectric micro-device by electrodeposition in an electrolyte composing of $Bi(NO_3)_3{\cdot}5H_2O$, TeO_2, and HNO_3. The size effect of electrode was examined. The cross-section of the TE units is 50×50 μm^2 with depth of 20 μm. Additionally, the device had a eight arrays, which composed of 110 TE units. A maximum power output of 0.96 μW was achieved with an open-circuit voltage of 17.6 mV (Uda et al., 2015).

Chang et al. (2015) examined the electrodeposition of individual n-type Bi_2Te_3 nanowires (NWs) using polycarbonate membranes (PCM) as templates in the solution 10 mM $HTeO_2^+$, 15 mM Bi^{3+}, 1 M HNO_3 and 50 v/v % DMSO. The electrodeposition conditions, such as the applied potential can be used to control the composition of Bi_2Te_3. Additionally, increase the Te composition would increase the average grain size of NWs, as well as the electrical conductivity. The maximum power factor of 195.8 μW/(mK^2) was achieved at 300 K for the Te-rich NW with diameter of 162 nm (Chang et al., 2015).

Shin and Oh (2015) fabricated a thermoelectric device based on thin film by combining electrodeposition and the flip-chip process. The thermoelectric materials used in the device are the n-type Bi_2Te_3 and p-type Sb_2Te_3 thin film, which is deposited on Ti/Cu/Au substrate in the solutions with 25 mM Bi ion, 25 mM Te ion and 1 M HNO_3 for Bi_2Te_3 and 63 mM Sb ion, 7 mM Te ion. The device with 242 pairs thermoelectric legs have a internal resistance of 21.4 Ω, which have a output voltage of 320 mV and output power of 1.1 mW at 39.7 K temperature difference. Additionally, the calculated power density of 3.84 mW/cm^2 (Shin and Oh, 2015).

Abellán et al. (2015) synthesized thin Bi_2Te_3 films containing $TeCl_4$, $Bi(NO_3)_3$ and dimethyl sulfoxide. Different substrates were used, such as CdTe/FTO and SnO_2:F coated glasses. Additionally, the deposits films were n-type semiconductors with trigonal crystal structure and stoichiometric composition dimethyl sulfoxide (Abellán et al., 2015).

Kulsi et al. (2015) synthesized thin Bi_2Te_3 films with preferred crystal orientation of (018) in the solution consisting of 15 mM TeO_2 and 10 mM Bi $(NO_3)_3$. The effect of different surfactant on the morphology was examined, including sodium dodecyl sulfate (SDS) and polyvinylpyrrolidone (PVP). The results indicated that improving the surface morphology would help to enhancing the carrier mobility. A ZT value of 0.28 was achieved using SDS as surfactant, which was measured at room temperature (Kulsi et al., 2015).

Şişman and Başoğlu (2016) fabricated thin $Bi_2Te_{3\text{-}y}Se_y$ films by electrodeposition in the solution containing 2 mM TeO_2, 2.5 mM $Bi(NO_3)_3$, SeO_2 and 0.1 M HNO_3 with Au as substrate. The Se composition was controlled to be 0.3 to 2.5. The results showed that replacement of Te by Se atoms would push the XRD diffraction peaks positions $Bi_2Te_{3\text{-}y}Se_y$ to higher angle, which is attributed to the change of crystal lattice constant (Şişman and Başoğlu, 2016).

Lei et al. (2016a) synthesized of 600 μm-thick n-type Bi_2Te_3 films by pulsed and potentiostatic electrodeposition in the electrolyte consisting of 70 mM TeO_2, 52.5 mM Bi^{3+}, 2 M nitric acid and polyvinyl alcohol (PVA). The results indicated that compact and uniform Bi_2Te_3 films was electrodeposited which composition near stoichiometric and hexagonal crystal structure. Moreover, the film growth can reach 100 μm/h. Additionally, a Seebeck coefficient of -200 μV/K and an electrical conductivity of 400 S/cm were achieved, resulting in a power factor of 1.6×10^3 μW/(mK^2) (Lei et al., 2016a).

Yang et al. (2016) electrodeposited p-type BiSbTe thin films using ITO glasses as substrate in the electrolyte composing of 2 mM TeO_2, 0.5 mM Bi_2O_3, 3.5 M $HClO_4$, 1 M HNO_3 and 0.35 M $C_4H_6O_6$. The Sb^{3+} concentration and current density were the variables during the electrodeposition. Thin BiSbTe films showed different morphologies, such as ball-type, mixed-type and acicular-type. The Seebeck coefficient of 32.89 μV/K was obtained (Yang et al., 2016).

Patil et al. (2016) electrodeposited thin Bi_2Te_3 film in a solution with 10 mM Te(IV), 7 mM $Bi(NO_3)_3{\cdot}5H_2O$ and 1 M HNO_3. The XRD pattern showed that the Bi_2Te_3 film was nanocrystalline with grain size of 18.08 nm and had a preferred orientation of (015) with rhombohedral crystal structure (Patil et al., 2016).

Na et al. (2016) electrodeposited n-type Bi_2Te_3 films in the electrolyte with 10 mM $HTeO_2^+$, 8 mM Bi^{3+} and 1 M HNO_3 on a flexible substrate. The effect of applied potential on the crystal structure and thermoelectric properties were systematically studied. The Bi_2Te_3 film with preferred orientation of (110) is deposited. The highest power factor of 1,473 μW/(K^2·m) was achieved for the film electrodeposited at applied potential of 0.02 V with electrical conductivity of 691 S/cm. The effect of applied potential and grain size on the electrical and thermoelectric properties were shown in **Figure 6**. A flexible thermoelectric device was fabricated using Bi_2Te_3 as n-type material and poly (3,4-ethylene dioxythiophene)s as p-type material. The generator achieved a output voltage of 5 mV and output power of 56 nW with temperature difference of 12 K (Na et al., 2016).

Lal et al. (2017) synthesized p-type $(Bi_xSb_{1\text{-}x})_2Te_3$ thin films using pulsed electrodeposition in the electrolyte consisting of 15 mM $HTeO_2^+$, 5 mM Sb_2O_3, 5 mM $Bi(NO_3)_3$, 0.2 M tartaric acid, sodium dodecyl sulfate (SDS) and dimethyl sulfoxide. The results indicated that the present of SDS would improve the Seebeck coefficient and power factor of the films as shown in **Figure 7**. (Lal et al., 2017).

Additionally, many other groups reported the results of characterization of BiTe/Se electrodeposits based on various experimental conditions which are summarized on **Table 1**. (Jagadish et al., 2015; Lei et al., 2016b; Wu et al., 2016b; Hasan et al., 2016; Kulsi et al., 2016; Manzano et al., 2016; Wu et al., 2017b; Kang et al., 2017; Lal et al., 2017; Lei et al., 2017).

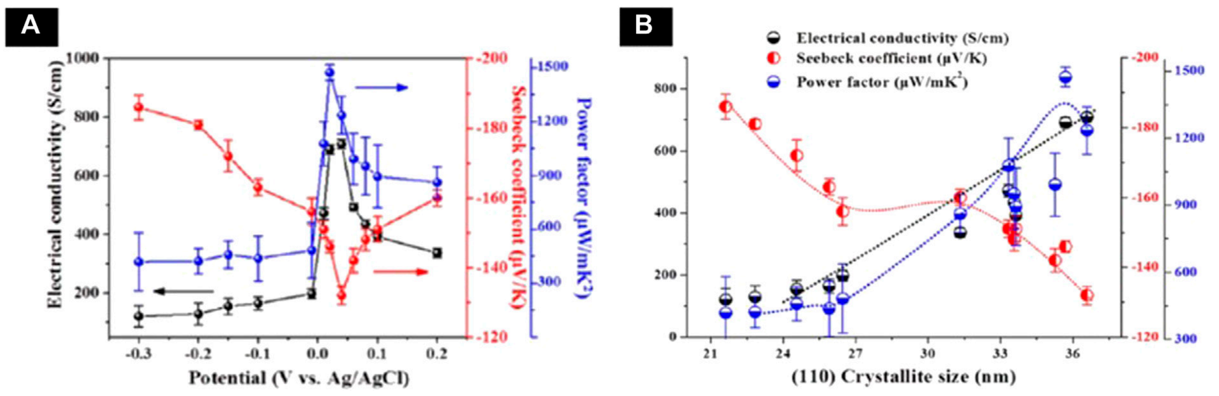

FIGURE 6 | (A) Corelation of electrical conductivity (black circle), Seebeck coefficient (red circle), and power factor (blue circle) with different applied potentials (V vs Ag/AgCl) **(B)** Corelation of the electrical conductivity (black), Seebeck coefficient (red), and power factor (blue) with (110) crystallite size (Na et al., 2016).

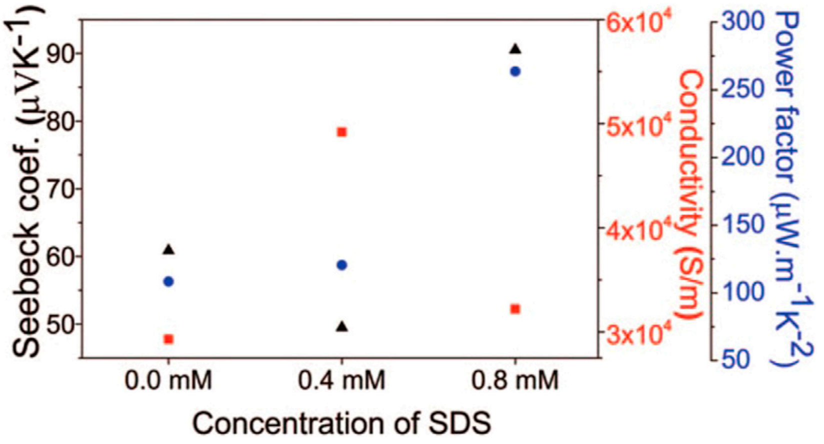

FIGURE 7 | Electrical resistivity (square), Seebeck coefficient (triangle), and power factor (circle) of annealed films deposited with different concentrations of SDS (Lal et al., 2017).

Electrodeposition of Bi_xSb_y Based Materials

Dou et al. (2008) synthesize Bi/BiSb superlattice nanowires by template-directed electrodeposition method, in which AAO was used as template. The electrolyte for electrodeposition contains a mixture of 80 mM $SbCl_3$, 40 mM $BiCl_3$, 50 g/L citric acid, 40 g/L tartaric acid, 70 g/L NaCl, 100 g/L glycerol and 1.0 M HCl at pH value of 0.82 (Dou et al., 2008).

Weber et al. (2008) electrodeposited high density nanowire arrays in AAO templates from the electrolyte of 50 mM Bi^{3+} + 50 mM Sb^{3+} in dimethyl sulfoxide.

Dou et al. (2009) synthesized Bi/BiSb multilayer nanowires by pulsed electrodeposition with small bilayer thickness. The electrolyte for the deposition contained a mixture of 80 mM $SbCl_3$, 40 mM $BiCl_3$, 0.24 M citric acid, 0.27 M tartaric acid, 1.2 M NaCl, 0.1 M glycerol and 1.0 M HCl. Additionally, the modulating time was used to control the segment length and layer thickness of the nanowires (Dou et al., 2009).

Muller et al. (2012) synthesized $Bi_{1-x}Sb_x$ nanowires with Sb composition in the range from 0.05 to 0.40 and diameter in the range from 20 to 100 nm. The results showed that applied potential and ratio of Bi/Sb ions would influence the composition of $Bi_{1-x}Sb_x$ nanowires (Müller et al., 2012).

Limmer et al. (2015) electrodeposited Bi_xSb_y in the non-aqueous baths consisting of Sb salts, $Bi(NO_3)_3{\cdot}5H_2O$, dimethyl sulfoxide and $KClO_4$. The effect of different Sb salts on the crystalline quality and preferred orientations were investigated. The results showed that nanowire arrays synthesized with SbI_3-based bath were polycrystalline. However, nanowire arrays synthesized with $SbCl_3$-based bath have a trigonal orientation, and composition of these nanowires remained constant along the nanowires. Additionally, there was a composition gradient along the radius of the nanowires array, where nanowires of $Bi_{0.75}Sb_{0.25}$ were obtained in the center area and nanowires of $Bi_{0.70}Sb_{0.30}$ were obtained in the edge region (Limmer et al., 2015).

Electrodeposition of Bi_2Se_3 Based Materials

Xiao et al. (2009) electrodeposited thin Bi_2Se_3 films using Pt as substrate by atomic layer epitaxy. The electrochemical reaction mechanism of Bi and Se alone were investigated by cyclic voltammetry. The electrodeposition mechanism Bi_2Se_3 is underpotential deposition (UPD). The synthesized Bi_2Se_3 films had an orthorhombic structure with stoichiometric composition. Additionally, the bandgap of Bi_2Se_3 films the was 0.35 eV. (Xiao et al., 2009).

Li et al. (2010c) synthesized Bi_2Se_3 thin films by electrodeposition in the solution containing SeO_2, $Bi(NO_3)_3$, and HNO_3 using Ti and indium tin oxide-coated glass as substrates at room temperature. The results indicated that the substrate had dramatic effect on the crystal structure of Bi_2Se_3 thin films. Pure rhombohedral crystal structure was obtained on the indium tin oxide-coated glass substrate, while both rhombohedral and orthorhombic crystal structure was obtained on Ti (Li et al., 2010c).

Xue et al. (2014) fabricated Bi_2Se_3/Bi multilayered nanowire arrays by pulsed electrodeposition using AAO as template in the electrolyte with 7.5 mM H_2SeO_3, 25 mM Bi^{3+} and 7 mM HNO_3. Each layer of Bi or Bi_2Se_3 had a thickness of about 100 nm, and the total length of the nanowire was 10 μm with a diameter of 50 nm (Xue et al., 2014).

Li et al. electrodeposited thick Bi_2Se_3 films using ITO-coated glass as substrate in a acidic solution containing 25 mM SeO_2, 25 mM $Bi(NO_3)_3$ and 1.3 M HNO_3. The results showed that the as-deposited films were p-type Bi_2Se_3 films. The power factors of 52.57 $\mu W/mK^2$ were obtained for the as-deposited films (Xiaolong and Zhen, 2014).

Tumelero et al. (2016) electrodeposited Bi_2Se_3 using Si (100) substrate as substrate in the electrolyte consisting of 1.5 mM SeO_2, 1 mM $Bi(NO_3)_3$ and 0.5 M nitric acid. The results indicated that Bi_2Se_3 with single orthorhombic phase and stoichiometric composition can be deposited by tuning the applied potential, while the potential window was narrow. Additionally, the deposited Bi_2Se_3 had a bandgap of 1.25 eV (Tumelero et al., 2016).

Souza et al. (2017) synthesized Bi_2Se_3 films by potentiostatic electrodeposition method in the electrolyte consisting of 1.5 mM SeO_2, 0.5 mM Bi_2O_3 and 1.0 M $HClO_4$ using silicon (100) as substrate. The deposited Bi_2Se_3 films is compact with uniform and smooth morphology. The as-deposited films had a dominant orthorhombic phase with mixture of rhombohedral and amorphous phases. However, pure rhombohedral structure was obtained after annealing (Souza et al., 2017).

Electrodeposition of Bi_2S_3 Based Materials

Jagadish et al. (2016) synthesized n-type Bi_2S_3 films in the solution consisting of 20.6 mM $Bi(NO_3)_3$, 0.54 M of lactic acid, 0.78 M of nitric acid and 140.8 mM Na_2SO_4. Virgin carbon fiber and recycled carbon fiber were used as substrates. The deposited Bi_2S_3 had a composition near stoichiometry. The surface morphology and the Seebeck coefficient of Bi_2S_3 films can be tuned by post annealing process. The Bi_2S_3 films had Seebeck coefficient of -16.3 and -12.4 μV/K deposited on virgin carbon fiber and recycled carbon fiber, respectively (Jagadish et al., 2016).

Electrodeposition of Sb_2Te_3 Based Materials

Ueda et al. (2008) synthesized Sb_2Te_3 alloy in the $AlCl_3$-NaCl-KCl molten salt electrolyte containing 10 mM $TeCl_4$ and 7 mM $SbCl_3$, at the temperature of 423 K and applied potential of 0.85 V vs. Al/Al(III). The composition of Sb can be controlled by concentration ratio of the Sb(III) to [Sb(III) + Te(IV)]. The morphology of deposited Sb_2Te_3 alloy is disk-like granule, which had a size of around 10 μm (Ueda et al., 2008).

Park et al. (2009) electrodeposited thin Sb_xTe_y films and nanowires at room temperature in an acidic electrolyte. Pt/Si and Au were used as substrate. The applied voltage and film thickness had significant effect on the morphology and grain size of the Sb_xTe_y films. Amorphous Sb_xTe_y films was electrodeposited, while the films became the rhombohedral R3m structure after annealing (Park et al., 2009).

Kim and Oh (2010b) investigated the crystallization behavior of the electrodeposited Sb_2Te_3 film in the electrolyte containing 7 mM Te ion, 63 mM Sb ion, 3.5 M perchloric acid, 0.35 M tartaric acid. The transition crystal structure from amorphous to crystalline would influence the Seebeck coefficient. Moreover, the addition of Cu can improve the thermal stability of the Sb_2Te_3 film, where CuSbTe film had a crystallization temperature of 149.5°C (Kim and Oh, 2010b).

Pinisetty et al. (2011b) electrodeposited polycrystalline Sb_2Te_3 nanowires and nanotubes arrays in the electrolyte consisting of 0.7 mM TeO_2, 1.6 mM Sb_2O_3, 33 or 330 mM tartaric acid, and 3 M HNO_3. The nanowires and nanotube had an average lamellar thickness of 36 and 43 nm, respectively (Pinisetty et al., 2011b).

Lim et al. (2011) electrodeposited *p*-tyape Sb_xTe_y thin films in an acidic solutions. The effect of TeO_2 concentrations was investigated. Sb_2Te_3 films with composition near stoichiometry was deposited with a rhombohedral structure and preferred orientation of (015). The films had a carrier concentration of 5.8×10^{18} cm^{-3} and mobility of 54.8 $cm^2/(Vs)$. Additionally, more negative applied potential would reduce the carrier concentration and mobility, which is possibly owing to increase in defects. A Seebeck coefficient of 118 μV/K was obtained at room temperature for the as-deposited Sb_2Te_3 film (Lim et al., 2011).

Qiu et al. (2011) synthesized Sb_2Te_x (2 < × < 6) films in the alkaline solution with TeO_3^{2-}, SbO_2^-, diaminourea polymer and triethanolamine. The solution was pretreated by argon gas to fully deaerate, which would enhance the Seebeck coefficient of the films by reducing oxygen contamination in the deposited films. The Sb_2Te_x films were amorphous before annealing. A maximum power factor 1.58 mW/mK^2 was achieved with a Seebeck coefficient of 532 μV/K after annealing (Qiu et al., 2011).

Schumacher et al. (2012) electrodeposited Sb_2Te_3 films in the electrolyte composing of 10 mM TeO_2, 5.6 mM Sb_2O_3, 0.84 M tartaric acid and 1 M nitric acid with pH of 1. Both Au and stainless steel were used as substrates. The results showed that morphology and composition of the films could be improved by pulsed electrodeposition methods. The p-type Sb_2Te_3 films fabricated by pulsed electrodeposition methods achieved a power factors of about 700 $\mu W/(mK^2)$ at room temperature

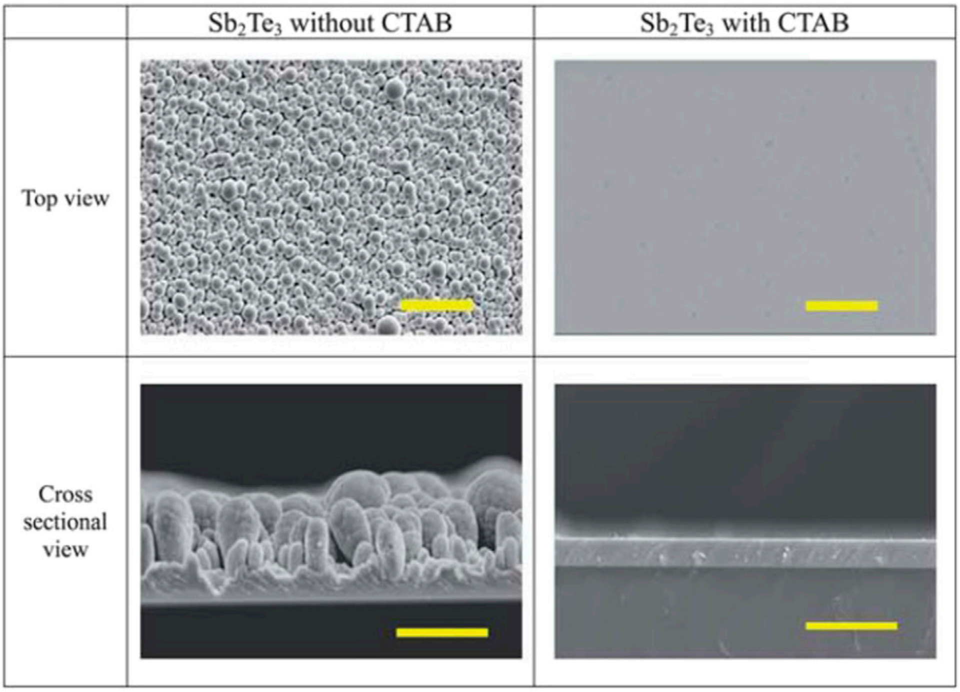

FIGURE 8 | Comparison of the top view (scale bar = 30 μm) and the cross-sectional (scale bar = 20 μm) SEM images of the Sb_2Te_3 films electrodeposited with and without CTAB (Yoo et al., 2013c).

with the electrical conductivity of 280 S/cm and Seebeck coefficients of 160 μV/K. Additionally, a maximum power factors obtained is 852 μW/(mK^2) after annealing (Schumacher et al., 2012).

Li et al. (2012) electrodeposited Sb_xTe_y films in a nonaqueous electrolyte containing 20 mM $SbCl_3$, 20 mM $TeCl_4$ and 0.1 M KNO_3. The Sb_xTe_y films had a smooth morphology, which is independent of applied potential. The composition obtained nearest to stoichiometry is $Sb_{1.87}Te_{3.13}$. Additionally, all the films were p-type after annealing (Li et al., 2012).

Lim et al. (2012b) synthesized Sb_xTe_y films in the electrolyte with 2.4 mM $HTeO_2^+$, 0.8 mM SbO^+, 33 mM tartaric acid, and 1 M HNO_3 by electrodeposition. The thin Sb_2Te_3 films with composition near stoichiometry were deposited in the applied potential range of -0.15 to -0.30 V vs. SCE. The post-annealing process would reduce the FWHM of the major diffraction peaks and enhance the electrical conductivity. Additionally, the power factor was improved from 44.2 to 372.1 mW/(mK^2) by annealing (Lim et al., 2012b).

Lensch-Falk et al. (2012) electrodeposited thin Sb_2Te_3 films in the electrolyte consisting of 7 mM sodium tellurite (IV), 16 mM antimony (III) oxide, 0.3 M tartaric acid, and 2 M nitric acid at room temperature by pulsed electrodeposition method. The results showed that the pulse duration have a significant effect on the texture and microstructure of films, where lamellar microstructure was deposited at short pulse durations, while equiaxed and randomly oriented microstructure was deposited at relative long pulse durations. Additionally, reducing pulse duration would also help to suppress the thermal conductivity of the films, where thermal conductivity of less than 2 W/(Km) was obtained (Lensch-Falk et al., 2012).

Nguyen et al. (2013) fabricated Sb, Te and Sb_xTe_y from molten salts containing acetamide - antimony chloride and tellurium chloride by electrodeposition. The Te composition of Sb_xTe_y alloy films is ranged from 20 to 81 at%, which is obtained in the electrolyte with $SbCl_3$ up to 0.48 M and $TeCl_4$ up to 0.12 M (Nguyen et al., 2013).

Yoo et al. (2013c) synthesized Sb_2Te_3 films in the solution consisting of 2.4 mM TeO_2, 0.8 mM Sb_2O_3, 33 mM tartaric acid, and 1 M HNO_3 at room temperature. Additionally, cetyltrimethylammonium bromide (CTAB) was used as surfactant to improve the surface morphology, where the effect of CTAB on the morphology of Sb_2Te_3 films was shown in **Figure 8**. Moreover, CTAB would also help to enhance the adhesion of Sb_2Te_3 films to substrate. Post-annealing at 200°C can improve electrical conductivity and Seebeck coefficient of the Sb_2Te_3 films, which was attributed to Te nanodots formation within the Sb_2Te_3 crystal structure. A power factor of 716.0 mW/mK^2 was obtained for Sb_2Te_3 films with 10–20 nm Te nanodots (Yoo et al., 2013c).

Kim et al. (2015) synthesized Te-rich Sb_2Te_3 film in a solution with 3.6 mM Sb_2O_3, 2.4 mM TeO_2, 33 mM L-tartaric acid, 1 M HNO_3. The as deposited films were amorphous, while γ-SbTe embedded nanocrystalline Sb_2Te_3 film was obtained by post annealing process because of solid-state phase transition. The results indicated that γ-SbTe embedded Sb_2Te_3 had higher Seebeck coefficient and P.F. than single phase Sb_2Te_3 film. This was attributed to strong energy-dependent charge

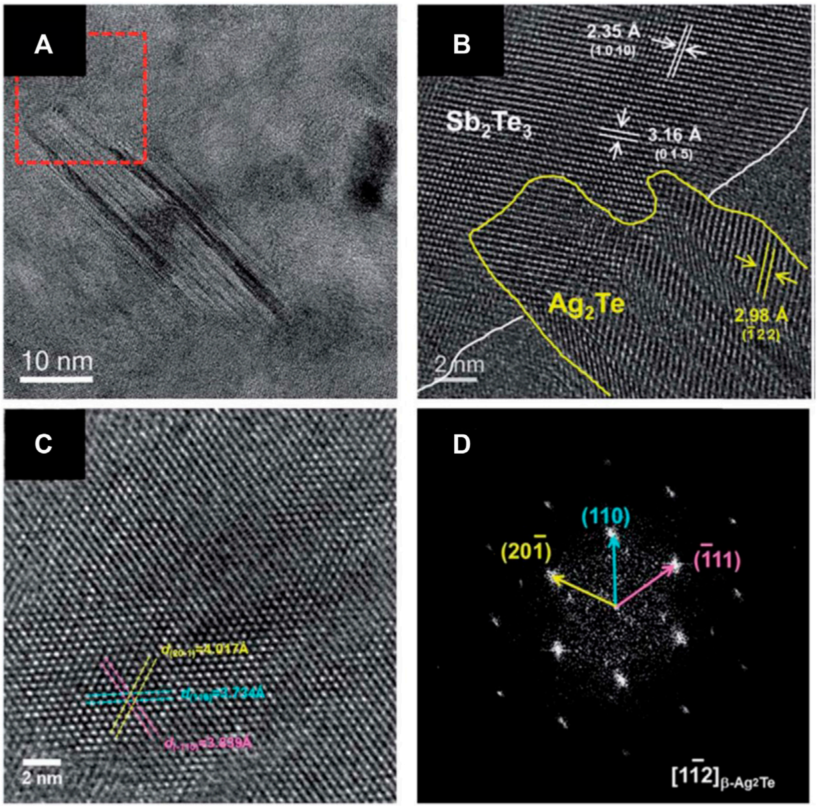

FIGURE 9 | Microstructure of the precipitated Ag2Te phase embedded in Sb2Te3 film. **(A)** HRTEM image and **(B)** a lattice image showing the precipitated Ag2Te nanodots within the Sb_2Te_3 matrix. **(C)** HRTEM image taken at a (Nolas et al., 2001; Snyder and Ursell, 2003; Hsu et al., 2004; Zide et al., 2006; Zeng et al., 2007; Faleev and Léonard, 2008; Poudel et al., 2008; Snyder and Toberer, 2008; Sootsman et al., 2009; Ko et al., 2011; Szczech et al., 2011; Zebarjadi et al., 2012) zone axis and **(D)** the corresponding FFT image (Kim et al., 2018b).

scattering, which is confirmed by UPS analysis showing 90 meV valence band difference between Sb_2Te_3 and γ-SbTe nanocrystalline. As a consequence, a Seebeck coefficient of 320 μV/K was obtained for γ-SbTe/Sb_2Te_3 nanocomposite (Kim et al., 2015).

Kim et al. (2018b) also electrodeposited Ag_2Te nanoprecipitates embedded p-type Sb_2Te_3 films (**Figure 9**). The same electrolyte condition and applied potential (0.1 vs. SCE) was applied to deposit the films except adding 100 μM $AgNO_3$ as Ag sources. The results indicated that the presence of the β-Ag_2Te phase would improve the Electrical property Sb_2Te_3 films dramatically, which was attributed to energy-dependent charge carrier filtering effect at the β-Ag_2Te/Sb_2Te_3 interface. Additionally, density of states effective mass ($m^* \sim 1.8\ m_0$) increased, leading to a high power factor of 1870 mW/mK^2 at 300 K without any dramatic suppression of electrical conductivity (Kim et al., 2018b).

Catrangiu et al. (2016) electrodeposited Sb_2Te_3 film in the ionic liquid with 4–10 mM TeO_2, 4–10 mM $SbCl_3$, choline chloride and oxalic acid. The composition of the films can be controlled by precursor concentration and applied potential. The electrodeposited mechanism is that Te layer was deposited followed by the deposition of Sb_xTe_y compounds at more negative applied potential (Catrangiu et al., 2016).

Hatsuta et al. (2016) synthesized Sb_2Te_3 thin films in the solution consisting of 1.6 mM TeO_2, 1.3 mM SbF_3, and 0.39 M HCl by electrodeposition using stainless steel as substrate. The results indicated that a stoichiometric atomic composition was achieved for the as-deposited thin film. Moreover, the composition of thin film kept at stoichiometry after annealed at the temperature below 250°C. However, when the annealing temperature go up to 300°C, a portion a of alien element, including Fe, Cr, Ni, was detected in the film, which lead to lower Seebeck coefficient and higher electrical conductivity. As a consequence, a maximum power factor of 13.6 μW/(cmK^2) was obtained for the Sb_2Te_3 film (Hatsuta et al., 2016).

Kim et al. (2016) electrodeposited thin $AgSbTe_2$ films. The deposited amorphous $Ag_{15}Sb_{27}Te_{58}$ film showed a Seebeck coefficient of 1,270 μV/K. The carrier concentration of about 10^{16} to 10^{19} cm^{-3} was obtained. For deposited nanocrystalline film, The power factors of 90–553 mW/mK^2 was obtained owing to higher Hall mobility and Seebeck coefficients (Kim et al., 2016).

CONCLUSION

Electrochemical deposition is a cost effective and manufacturable synthesis method, which can be used to deposit thermoelectric materials with controlled morphology, composition and crystal structures. The electrodeposition baths including aqueous solution (*e.g.,* acidic and alkaline solutions), ionic liquid, deep eutectic solvents solutions were used to deposit TE materials. Most of the papers investigated the electrodeposition mechanism and kinetics, and the control of morphology, composition and crystal structure of the deposits by electrodeposition parameters, such as precursor concentration, solution pH in aqueous solution, agitation, additives, temperature, applied potential/current, substrate and so on. The correlation between electrodeposition parameters and TE properties was reported, which is indirect correlation because the material properties (*e.g.,* morphology, composition and crystal structure) are the direct effects on the TE properties. The correlation between material properties and TE properties was also discussed by various groups.

Thermoelectric micro-devices have a great potential to serve as a generator/cooler for portable electronic devices. Electrodeposition have an advantage to be utilized to fabricate TE micro-devices, attributed to its ability to deposit thick films, which can be used to fabricate cross-plane devices, with controlled morphology, composition, and crystal structure. The performance of the TE micro-devices are for now limited because of low efficiency. More researches about thermoelectric properties of electrodeposited materials and the performance of devices need to be further studied for wide applications.

AUTHOR CONTRIBUTIONS

JK, J-HL, and NM contributed conception and design of the study; TW and M-SK organized the database; TW and JK performed the statistical analysis; TW and JK wrote the draft of the manuscript. All authors contributed to manuscript revision, read and approved the submitted version.

FUNDING

This work was supported by the Technology Innovation Program (No. 20010638, No. 20016338) funded By the Ministry of Trade, Industry and Energy (MOTIE, Korea).

REFERENCES

Abad, B., Rull-Bravo, M., Hodson, S. L., Xu, X., and Martin-Gonzalez, M. (2015). Thermoelectric Properties of Electrodeposited Tellurium Films and the Sodium Lignosulfonate Effect. *Electrochimica Acta* 169, 37–45. doi:10.1016/j.electacta.2015.04.063

Abellán, M., Schrebler, R., and Gómez, H. (2015). Electrodeposition of Bi2Te3 Thin Films onto FTO Substrates from DMSO Solution. *Int. J. Electrochem. Sci.* 10 (9), 7409–7422.

Agapescu, C., Cojocaru, A., Cotarta, A., and Visan, T. (2013). Electrodeposition of Bismuth, Tellurium, and Bismuth telluride Thin Films from Choline Chloride-Oxalic Acid Ionic Liquid. *J. Appl. Electrochem.* 43 (3), 309–321. doi:10.1007/s10800-012-0487-0

Bae, S., Lee, S., Sohn, H.-S., and Lee, H. S. (2017). Synthesis and Characteristics of PbTe1−xSex Thin Films Formed via Electrodeposition. *Met. Mater. Int.* 23 (5), 1056–1061. doi:10.1007/s12540-017-7009-x

Banga, D., Lensch-Falk, J. L., Medlin, D. L., Stavila, V., Yang, N. Y. C., Robinson, D. B., et al. (2012). Periodic Modulation of Sb Stoichiometry in Bi2Te3/Bi2-xSbxTe3Multilayers Using Pulsed Electrodeposition. *Cryst. Growth Des.* 12 (3), 1347–1353. doi:10.1021/cg2014418

Banga, D. O., Vaidyanathan, R., Xuehai, L., Stickney, J. L., Cox, S., and Happeck, U. (2008). Formation of PbTe Nanofilms by Electrochemical Atomic Layer Deposition (ALD). *Electrochimica Acta* 53 (23), 6988–6994. doi:10.1016/j.electacta.2008.02.108

Boulanger, C. (2010). Thermoelectric Material Electroplating: A Historical Review. *J. Elec Materi* 39 (9), 1818–1827. doi:10.1007/s11664-010-1079-6

Caballero-Calero, O., Díaz-Chao, P., Abad, B., Manzano, C. V., Ynsa, M. D., Romero, J. J., et al. (2014). Improvement of Bismuth Telluride Electrodeposited Films by the Addition of Sodium Lignosulfonate. *Electrochimica Acta* 123, 117–126. doi:10.1016/j.electacta.2013.12.185

Caballero-Calero, O., Mohner, M., Casas, M., Abad, B., Rull, M., Borca-Tasciuc, D. A., et al. (2015). Improvements on Electrodeposited Bi2Te3-ySey Films by Different Additives. *Mater. Today Proc.* 2 (2), 620–628. doi:10.1016/j.matpr.2015.05.087

Cao, Y., Zeng, Z., Liu, Y., Zhang, X., Shen, C., Wang, X., et al. (2013). Electrodeposition and Thermoelectric Characterization of (00L)-Oriented Bi2Te3Thin Films on Silicon with Seed Layer. *J. Electrochem. Soc.* 160 (11), D565–D569. doi:10.1149/2.099311jes

Catrangiu, A.-S., Sin, I., Prioteasa, P., Cotarta, A., Cojocaru, A., Anicai, L., et al. (2016). Studies of Antimony telluride and Copper telluride Films Electrodeposition from Choline Chloride Containing Ionic Liquids. *Thin Solid Films* 611, 88–100. doi:10.1016/j.tsf.2016.04.030

Chang, C. H., Rheem, Y., Choa, Y.-H., Shin, D. H., Park, D.-Y., and Myung, N. V. (2010). Bi and Te Thin Films Synthesized by Galvanic Displacement from Acidic Nitric Baths. *Electrochimica Acta* 55 (3), 743–752. doi:10.1016/j.electacta.2009.09.038

Chang, T., Cho, S., Kim, J., Schoenleber, J., Frantz, C., Stein, N., et al. (2015). Individual Thermoelectric Properties of Electrodeposited Bismuth telluride Nanowires in Polycarbonate Membranes. *Electrochimica Acta* 161, 403–407. doi:10.1016/j.electacta.2015.02.105

Chen, C.-L., Chen, Y.-Y., Lin, S.-J., Ho, J. C., Lee, P.-C., Chen, C.-D., et al. (2010). Fabrication and Characterization of Electrodeposited Bismuth telluride Films and Nanowires. *J. Phys. Chem. C* 114 (8), 3385–3389. doi:10.1021/jp909926z

Diliberto, S., Richoux, V., Stein, N., and Boulanger, C. (2008). Influence of Pulsed Electrodeposition on Stoichiometry and Thermoelectric Properties of Bismuth telluride Films. *Phys. Stat. Sol. (A)* 205 (10), 2340–2344. doi:10.1002/pssa.200779416

Dou, X., Li, G., Lei, H., Huang, X., Li, L., and Boyd, I. W. (2009). Template Epitaxial Growth of Thermoelectric Bi/BiSb Superlattice Nanowires by Charge-Controlled Pulse Electrodeposition. *J. Electrochem. Soc.* 156 (9), K149–K154. doi:10.1149/1.3156639

Dou, X., Li, G., and Lei, H. (2008). Kinetic versus Thermodynamic Control over Growth Process of Electrodeposited Bi/BiSb Superlattice Nanowires. *Nano Lett.* 8 (5), 1286–1290. doi:10.1021/nl073039b

Dughaish, Z. H. (2002). Lead telluride as a Thermoelectric Material for Thermoelectric Power Generation. *Physica B: Condensed Matter* 322 (1–2), 205–223. doi:10.1016/s0921-4526(02)01187-0

Elazem, D., Jung, H., Wu, T., Lim, J.-H., Lee, K.-H., and Myung, N. V. (2013). Morphology Change of Galvanically Displaced One-Dimensional Tellurium Nanostructures via Controlling the Microstructure of Sacrificial Ni Thin Films. *Electrochimica Acta* 106, 447–452. doi:10.1016/j.electacta.2013.05.117

Erdoan, B. Y., and Demir, Ü. (2011). Orientation-controlled Synthesis and Characterization of Bi 2Te3 Nanofilms, and Nanowires via Electrochemical Co-deposition. *Electrochimica Acta* 56 (5), 2385–2393.

Erdoğan, İ. Y., Ozar, T. O., and Demir, U. (2009). PbTe Alkaline _ Co-deposition. *Thin Solid Films* 517 (18), 5419–5424.

Faleev, S. V., and Léonard, F. (2008). Theory of Enhancement of Thermoelectric Properties of Materials with Nanoinclusions. *Phys. Rev. B* 77 (21), 214304. doi:10.1103/physrevb.77.214304

Frantz, C., Stein, N., Gravier, L., Granville, S., and Boulanger, C. (2010). Electrodeposition and Characterization of Bismuth telluride Nanowires. *J. Elec Materi* 39 (9), 2043–2048. doi:10.1007/s11664-009-1001-2

Frantz, C., Stein, N., Zhang, Y., Bouzy, E., Picht, O., Toimil-Molares, M. E., et al. (2012). Electrodeposition of Bismuth telluride Nanowires with Controlled Composition in Polycarbonate Membranes. *Electrochimica Acta* 69, 30–37. doi:10.1016/j.electacta.2012.01.040

Frantz, C., Vichery, C., Michler, J., and Philippe, L. (2015). Electrodeposition of PbTe Thin Films: Electrochemical Behavior and Effect of Reverse Pulse Potential. *Electrochimica Acta* 173, 490–496. doi:10.1016/j.electacta.2015.05.045

Frantz, C., Zhang, Y., Michler, J., and Philippe, L. (2016). On the Growth Mechanism of Electrodeposited PbTe Dendrites. *CrystEngComm* 18 (13), 2319–2326. doi:10.1039/c6ce00107f

Fu, J., Shi, J., Zhu, M., Liang, Y., Zhang, G., Shi, H., et al. (2013). Large-scale Synthesis and Characterisation of Ag/Bi 2 Te 3 Superlattice Nanowires via Pulse Electrodeposition. *Micro Nano Lett.* 8 (4), 188–190. doi:10.1049/mnl.2012.0850

Gan, Y. X., Sweetman, J., and Lawrence, J. G. (2010). Electrodeposition and Morphology Analysis of Bi-te Thermoelectric alloy Nanoparticles on Copper Substrate. *Mater. Lett.* 64 (3), 449–452. doi:10.1016/j.matlet.2009.11.045

Glatz, W., Durrer, L., Schwyter, E., and Hierold, C. (2008). Novel Mixed Method for the Electrochemical Deposition of Thick Layers of Bi2+xTe3−x with Controlled Stoichiometry. *Electrochimica Acta* 54 (2), 755–762. doi:10.1016/j.electacta.2008.06.065

Golgovici, F., Cojocaru, A., Anicai, L., and Visan, T. (2011). Surface Characterization of BiSbTe Thermoelectric Films Electrodeposited from Chlorides Aqueous Solutions and Choline Chloride Based Ionic Liquids. *Mater. Chem. Phys.* 126 (3), 700–706. doi:10.1016/j.matchemphys.2010.12.058

Golgovici, F., Cojocaru, A., Nedelcu, M., and Visan, T. (2010). Cathodic Deposition of Components in BiSbTe Ternary Compounds as Thermoelectric Films Using Choline-Chloride-Based Ionic Liquids. *J. Elec Materi* 39 (9), 2079–2084. doi:10.1007/s11664-009-1006-x

Ha, Y. C., Sohn, H. J., Jeong, G., Lee, C., and Rhee, K. I. (2000). Electrowinning of Tellurium From Alkaline Leach Liquor of Cemented Te. *J. Appl. Electrochem.* 30 (3), 315–322.

Hangarter, C. M., Lee, Y.-I., Hernandez, S. C., Choa, Y.-h., and Myung, N. V. (2010). Nanopeapods by Galvanic Displacement Reaction. *Angew. Chem. Int. Edition* 49 (39), 7081–7085. doi:10.1002/anie.201001559

Hasan, M., Gautam, D., and Enright, R. (2016). Electrodeposition of Textured Bi27Sb28Te45 Nanowires with Enhanced Electrical Conductivity. *Mater. Chem. Phys.* 173, 438–445. doi:10.1016/j.matchemphys.2016.02.035

Hatsuta, N., Takemori, D., and Takashiri, M. (2016). Effect of thermal Annealing on the Structural and Thermoelectric Properties of Electrodeposited Antimony telluride Thin Films. *J. Alloys Comp.* 685, 147–152. doi:10.1016/j.jallcom.2016.05.268

Hsu, K. F., Loo, S., Guo, F., Chen, W., Dyck, J. S., Uher, C., et al. (2004). Cubic AgPb M SbTe 2+ M : Bulk Thermoelectric Materials with High Figure of Merit. *Science* 303 (5659), 818–821. doi:10.1126/science.1092963

Ikemiya, N., Iwai, D., Yamada, K., Vidu, R., and Hara, S. (1996). Atomic Structures and Growth Morphologies of Electrodeposited Te Film on Au(100) and Au(111) Observed by *In Situ* Atomic Force Microscopy. *Surf. Sci.* 369 (1–3), 199–208. doi:10.1016/s0039-6028(96)00881-3

Jagadish, P. R., Li, L. P., Chan, A., and Khalid, M. (2016). Effect of Annealing on Virgin and Recycled Carbon Fiber Electrochemically Deposited with N-type Bismuth Telluride and Bismuth Sulfide. *Mater. Manufacturing Process.* 31 (9), 1223–1231. doi:10.1080/10426914.2015.1090590

Jagadish, R., Lau, P., and Chan, A. (2015). Effect of Annealing on Virgin and Recycled Carbon Fibre Electrochemically-Deposited with N-type Bismuth Telluride. *Chem. Eng. Trans.* 45, 1435–1440.

Jiang, C. H., Wei, W., Yang, Z. M., Tian, C., and Zhang, J. S. (2011). Electrodeposition of Tellurium Film on Polyaniline-Coated Macroporous Phenolic Foam and its Thermopower. *J. Porous Mater.* 19 (5), 819–823. doi:10.1007/s10934-011-9536-z

Jiang, C. H., Wei, W., Yang, Z. M., Tian, C., and Zhang, J. S. (2012). Electrodeposition of Tellurium Film on Polyaniline-Coated Macroporous Phenolic Foam and its Thermopower. *J. Porous Mater.* 19 (5), 819–823. doi:10.1007/s10934-011-9536-z

Jiang, Q., Liu, C., Song, H., Xu, J., Mo, D., Shi, H., et al. (2014). Free-standing PEDOT: PSS Film as Electrode for the Electrodeposition of Bismuth telluride and its Thermoelectric Performance. *Int. J. Electrochem. Sci.* 9 (12), 7540–7551.

Jin, Y., and Wang, W. (2010). Effect of Substrate on the Structure and Thermoelectric Properties of N-type Bi2Te3−y Se Y Thin Films Prepared by Electrodeposition. *J. Elec Materi* 39 (9), 1469–1475. doi:10.1007/s11664-010-1306-1

Jung, H., Park, D.-Y., Xiao, F., Lee, K. H., Choa, Y.-H., Yoo, B., et al. (2011). Electrodeposited Single Crystalline PbTe Nanowires and Their Transport Properties. *J. Phys. Chem. C* 115 (7), 2993–2998. doi:10.1021/jp110739v

Jung, H., Suh, H., Hangarter, C., and Lim, J. H. (2012). Programmable Synthesis of Shape-, Structure-, and Composition-Modulated One-Dimensional Heterostructures by Galvanic Displacement Reaction. *Appl. Phys. Lett.* 100 (22), 1. doi:10.1063/1.4722919

Kang, W.-S., Li, W.-J., Chou, W.-C., Tseng, M.-F., and Lin, C.-S. (2017). Microstructure and Thermoelectric Properties of Bi 2 Te 3 Electrodeposits Plated in Nitric and Hydrochloric Acid Baths. *Thin Solid Films* 623, 90–97. doi:10.1016/j.tsf.2016.12.047

Kim, J., Lee, J.-Y., Lim, J.-H., and Myung, N. V. (2016). Optimization of Thermoelectric Properties of P-type AgSbTe2 Thin Films via Electrochemical Synthesis. *Electrochimica Acta* 196, 579–586. doi:10.1016/j.electacta.2016.02.206

Kim, J., Lee, K. H., Kim, S.-D., Lim, J.-H., and Myung, N. V. (2018). Simple and Effective Fabrication of Sb2Te3 Films Embedded with Ag2Te Nanoprecipitates for Enhanced Thermoelectric Performance. *J. Mater. Chem. A.* 6, 349–356. doi:10.1039/c7ta09013g

Kim, J., Lim, J.-H., and Myung, N. V. (2018). Composition- and Crystallinity-dependent Thermoelectric Properties of Ternary BixSb2-xTey Films. *Appl. Surf. Sci.* 429, 158–163. doi:10.1016/j.apsusc.2017.06.260

Kim, J., Zhang, M., Bosze, W., Park, S.-D., Lim, J.-H., and Myung, N. V. (2015). Maximizing Thermoelectric Properties by Nanoinclusion of γ-SbTe in Sb2Te3 Film via Solid-State Phase Transition from Amorphous Sb-Te Electrodeposits. *Nano Energy* 13, 727–734. doi:10.1016/j.nanoen.2015.03.020

Kim, M.-Y., and Oh, T.-S. (2010b). Crystallization Behavior and Thermoelectric Characteristics of the Electrodeposited Sb2Te3 Thin Films. *Thin Solid Films* 518 (22), 6550–6553. doi:10.1016/j.tsf.2010.03.052

Kim, M.-Y., and Oh, T.-S. (2009). Electrodeposition and Thermoelectric Characteristics of Bi2Te3 and Sb2Te3 Films for Thermopile Sensor Applications. *J. Elec Materi* 38 (7), 1176–1181. doi:10.1007/s11664-008-0653-7

Kim, M.-Y., and Oh, T.-S. (2010a). Thermoelectric Characteristics of the Thermopile Sensors Processed with the Electrodeposited Bi-te and Sb-Te Thin Films. *Surf. Rev. Lett.* 17 (03), 311–316. doi:10.1142/s0218625x10013813

Kim, M.-Y., and Oh, T.-S. (2013). Thermoelectric Power Generation Characteristics of a Thin-Film Device Consisting of Electrodeposited N-Bi2Te3 and P-Sb2Te3 Thin-Film Legs. *J. Elec Materi* 42 (9), 2752–2757. doi:10.1007/s11664-013-2671-3

Ko, D.-K., Kang, Y., and Murray, C. B. (2011). Enhanced Thermopower via Carrier Energy Filtering in Solution-Processable Pt-Sb2Te3 Nanocomposites. *Nano Lett.* 11 (7), 2841–2844. doi:10.1021/nl2012246

Köse, H., Bicer, M., Tutunoglu, C., Aydin, A. O., and Sisman, I. (2009). The Underpotential Deposition of Bi2Te3-ySey Thin Films by an Electrochemical Co-deposition Method. *Electrochimica Acta* 54 (6), 1680–1686.

Kuleshova, J., Koukharenko, E., Li, X., Frety, N., Nandhakumar, I. S., Tudor, J., et al. (2010). Optimization of the Electrodeposition Process of High-Performance Bismuth Antimony telluride Compounds for Thermoelectric Applications. *Langmuir* 26 (22), 16980–16985. doi:10.1021/la101952y

Kulsi, C., Kargupta, K., and Banerjee, D. (2016). "Process Dependent Thermoelectric Properties of EDTA Assisted Bismuth telluride," in *AIP Conference Proceedings* (IEEE). doi:10.1063/1.4945148

Kulsi, C., Mitra, M., Kargupta, K., Ganguly, S., Banerjee, D., and Goswami, S. (2015). Effect of Different Surfactants and Thicknesses on Electrodeposited Films of Bismuth telluride and its Thermoelectric Performance. *Mater. Res. Express* 2 (10), 106403. doi:10.1088/2053-1591/2/10/106403

Lal, S., Gautam, D., and Razeeb, K. M. (2017). The Impact of Surfactant Sodium Dodecyl Sulfate on the Microstructure and Thermoelectric Properties of P-type (Sb1-xBix)2Te3Electrodeposited Films. *ECS J. Solid State. Sci. Technol.* 6 (3), N3017–N3021. doi:10.1149/2.0041703jss

Lee, J., Farhangfar, S., Lee, J., Cagnon, L., Scholz, R., Gösele, U., et al. (2008). Tuning the Crystallinity of Thermoelectric Bi2Te3nanowire Arrays Grown by Pulsed Electrodeposition. *Nanotechnology* 19 (36), 365701. doi:10.1088/0957-4484/19/36/365701

Lee, J., Kim, Y., Caglon, L., and Gosele, U. (2010). Power Factor Measurements of Bismuth telluride Nanowires Grown by Pulsed Electrodeposition. *physica status solidi (Rrl) - Rapid Res. Lett.* 4 (1-2), 43–45. doi:10.1002/pssr.200903368

Lee, K.-J., Song, H., Lee, Y.-I., Jung, H., Zhang, M., Choa, Y.-H., et al. (2011). Synthesis of Ultra-long Hollow Chalcogenide Nanofibers. *Chem. Commun.* 47 (32), 9107–9109. doi:10.1039/c1cc12312b

Lei, C., Burton, M., and Nandhakumar, I. S. (2017). Electrochemical Formation of P-type Bi0.5Sb1.5Te3Thick Films onto Nickel. *J. Electrochem. Soc.* 164 (4), D192–D195. doi:10.1149/2.1151704jes

Lei, C., Burton, M. R., and Nandhakumar, I. S. (2016). Facile Production of Thermoelectric Bismuth telluride Thick Films in the Presence of Polyvinyl Alcohol. *Phys. Chem. Chem. Phys.* 18 (21), 14164–14167. doi:10.1039/c6cp02360f

Lei, C., Ryder, K. S., Koukharenko, E., Burton, M., and Nandhakumar, I. S. (2016). Electrochemical Deposition of Bismuth telluride Thick Layers onto Nickel. *Electrochemistry Commun.* 66, 1–4. doi:10.1016/j.elecom.2016.02.005

Lensch-Falk, J. L., Banga, D., Hopkins, P. E., Robinson, D. B., Stavila, V., Sharma, P. A., et al. (2012). Electrodeposition and Characterization of Nano-Crystalline Antimony telluride Thin Films. *Thin Solid Films* 520 (19), 6109–6117. doi:10.1016/j.tsf.2012.05.078

Li, F.-H., and Wang, W. (2010). Electrodeposition of P-type BixSb2−xTey Thermoelectric Film from Dimethyl Sulfoxide Solution. *Electrochimica Acta* 55 (17), 5000–5005. doi:10.1016/j.electacta.2010.04.005

Li, F.-H., Wang, W., and Gao, J.-p. (2010). Electrodeposition of Bi X Sb2−x Te Y Thermoelectric Films from DMSO Solution. *J. Elec Materi* 39 (9), 1562–1565. doi:10.1007/s11664-010-1284-3

Li, F.-H., Wang, W., Gong, Y.-L., and Li, J.-Y. (2012). Electrodeposition of Sb X Te Y Thermoelectric Films from Dimethyl Sulfoxide Solution. *J. Elec Materi* 41 (11), 3039–3043. doi:10.1007/s11664-012-2202-7

Li, F., and Wang, W. (2009). Electrodeposition of BixSb2−xTey Thermoelectric Thin Films from Nitric Acid and Hydrochloric Acid Systems. *Appl. Surf. Sci.* 255 (7), 4225–4231. doi:10.1016/j.apsusc.2008.11.013

Li, G.-R., Yao, C.-Z., Lu, X.-H., Zheng, F.-L., Feng, Z.-P., Yu, X.-L., et al. (2008). Facile and Efficient Electrochemical Synthesis of PbTe Dendritic Structures. *Chem. Mater.* 20 (10), 3306–3314. doi:10.1021/cm8001942

Li, G.-r., Zheng, F.-l., and Tong, Y.-x. (2008). Controllable Synthesis of Bi2Te3 Intermetallic Compounds with Hierarchical Nanostructures via Electrochemical Deposition Route. *Cryst. Growth Des.* 8 (4), 1226–1232. doi:10.1021/cg700790h

Li, L., Xu, S., and Li, G. (2015). Enhancement of Thermoelectric Properties in Bi-sb-te Alloy Nanowires by Pulsed Electrodeposition. *Energ. Tech.* 3 (8), 825–829. doi:10.1002/ente.201500071

Li, W.-J. (2009). Electrodeposition of Bismuth telluride Films from a Nonaqueous Solvent. *Electrochimica Acta* 54 (27), 7167–7172. doi:10.1016/j.electacta.2009.07.008

Li, W.-J., Yu, W.-L., and Yen, C.-Y. (2011). Pulsed Electrodeposition of Bi2Te3 and Bi2Te3/Te Nanowire Arrays from a DMSO Solution. *Electrochimica Acta* 58 (1), 510–515. doi:10.1016/j.electacta.2011.09.075

Li, X.-H., Zhou, B., Pu, L., and Zhu, J.-J. (2008). Electrodeposition of Bi2Te3 and Bi2Te3 Derived Alloy Nanotube Arrays. *Cryst. Growth Des.* 8 (3), 771–775. doi:10.1021/cg7006759

Li, X.-l., Cai, K.-f., Li, H., Wang, L., and Zhou, C.-w. (2010). Electrodeposition and Characterization of Thermoelectric Bi2Se3 Thin Films. *Int. J. Miner Metall. Mater.* 17 (1), 104–107. doi:10.1007/s12613-010-0118-x

Li, X. L., Cai, K. F., Li, H., Yu, D. H., Wang, X., and Wang, H. F. (2010). Alumina Template-Assisted Electrodeposition of Bi2Te2.7Se0.3 Nanowire Arrays. *Superlattices and Microstructures* 47 (6), 710–713. doi:10.1016/j.spmi.2010.03.009

Li, X. L., Cai, K. F., Yu, D. H., and Wang, Y. Y. (2011). Electrodeposition and Characterization of Thermoelectric Bi2Te2Se/Te Multilayer Nanowire Arrays. *Superlattices and Microstructures* 50 (5), 557–562. doi:10.1016/j.spmi.2011.09.001

Lim, J.-H., Park, M., Lim, D.-C., Myung, N. V., Lee, J.-H., Jeong, Y.-K., et al. (2012). Synthesis and Thermoelectric/electrical Characterization of Electrodeposited SbxTey Thin Films. *Mater. Res. Bull.* 47 (10), 2748–2751. doi:10.1016/j.materresbull.2012.04.140

Lim, J.-H., Park, M. Y., Lim, D. C., Yoo, B., Lee, J.-H., Myung, N. V., et al. (2011). Electrodeposition of P-type Sb X Te Y Thermoelectric Films. *J. Elec Materi* 40 (5), 1321–1325. doi:10.1007/s11664-011-1629-6

Lim, J. H., Park, M., Lim, D.-C., and Myung, N. V. (2012). Electrical/Themoelectric Characterization of Electrodeposited Bi xSb2-xTe3 Thin Films. *AIP Conf. Proc.* 1449, 91–94. doi:10.1063/1.4731504

Lim, S.-K., Kim, M.-Y., and Oh, T.-S. (2009). Thermoelectric Properties of the Bismuth-Antimony-telluride and the Antimony-telluride Films Processed by Electrodeposition for Micro-device Applications. *Thin Solid Films* 517 (14), 4199–4203. doi:10.1016/j.tsf.2009.02.005

Limmer, S. J., Medlin, D. L., Siegal, M. P., Hekmaty, M., Lensch-Falk, J. L., Erickson, K., et al. (2015). Using Galvanostatic Electroforming of Bi1−xSbx Nanowires to Control Composition, Crystallinity, and Orientation. *J. Mater. Res.* 30 (02), 164–169. doi:10.1557/jmr.2014.354

Limmer, S. J., Yelton, W. G., Siegal, M. P., Lensch-Falk, J. L., Pillars, J., and Medlin, D. L. (2012). Electrochemical Deposition of Bi2(Te,Se)3Nanowire Arrays on Si. *J. Electrochem. Soc.* 159 (4), D235–D239. doi:10.1149/2.084204jes

Liu, D.-W., and Li, J.-F. (2008). Electrocrystallization Process during Deposition of Bi-te Films. *J. Electrochem. Soc.* 155 (7), D493. doi:10.1149/1.2907398

Liu, D.-W., and Li, J.-F. (2011). Microfabrication of Thermoelectric Modules by Patterned Electrodeposition Using a Multi-Channel Glass Template. *J. Solid State. Electrochem.* 15 (3), 479–484. doi:10.1007/s10008-010-1104-y

Ma, Y., Johansson, A., Ahlberg, E. P., and Anders, E. C. (2010). A Mechanistic Study of Electrodeposition of Bismuth Telluride on Stainless Steel Substrates. *Electrochimica Acta* 55 (15), 4610–4617. doi:10.1016/j.electacta.2010.03.018

Ma, Y., Ahlberg, E., Sun, Y., Iversen, B. B., and Palmqvist, A. E. C. (2011). Thermoelectric Properties of Thin Films of Bismuth telluride Electrochemically Deposited on Stainless Steel Substrates. *Electrochimica Acta* 56 (11), 4216–4223. doi:10.1016/j.electacta.2011.01.093

Ma, Y., Wijesekara, W., and Palmqvist, A. E. C. (2012). Thermoelectric Characteristics of Electrochemically Deposited Bi2Te3 and Sb2Te3 Thin Films of Relevance to Multilayer Preparation. *J. Electrochem. Soc.* 159 (2), D50.

Ma, Y., Wijesekara, W., and Palmqvist, A. E. C. (2012). Electrochemical Deposition and Characterization of Thermoelectric Ternary (Bi X Sb1−x)2Te3 and Bi2(Te1−y Se Y)3 Thin Films. *J. Elec Materi* 41 (6), 1138–1146. doi:10.1007/s11664-011-1790-y

Maas, M., Diliberto, S., de Vaulx, C., Azzouz, K., and Boulanger, C. (2014). Use of a Soluble Anode in Electrodeposition of Thick Bismuth Telluride Layers. *J. Elec Materi* 43 (10), 3857–3862. doi:10.1007/s11664-014-3292-1

Mannam, R., Agarwal, M., Roy, A., Singh, V., Varahramyan, K., and Davis, D. (2009). Electrodeposition and Thermoelectric Characterization of Bismuth Telluride Nanowires. *J. Electrochem. Soc.* 156 (8), B871. doi:10.1149/1.3139011

Manzano, C. V., Abad, B., Muñoz Rojo, M., Koh, Y. R., Hodson, S. L., Lopez Martinez, A. M., et al. (2016). Anisotropic Effects on the Thermoelectric Properties of Highly Oriented Electrodeposited Bi2Te3 Films. *Sci. Rep.* 6 (1), 19129. doi:10.1038/srep19129

Manzano, C. V., Rojas, A. A., Decepida, M., Abad, B., Feliz, Y., Caballero-Calero, O., et al. (2013). Thermoelectric Properties of Bi2Te3 Films by Constant and Pulsed Electrodeposition. *J. Solid State. Electrochem.* 17 (7), 2071–2078. doi:10.1007/s10008-013-2066-7

Martin, J., Wang, L., Chen, L., and Nolas, G. S. (2009). Enhanced Seebeck Coefficient through Energy-Barrier Scattering in PbTe Nanocomposites. *Phys. Rev. B* 79 (11), 115311. doi:10.1103/physrevb.79.115311

Matsuoka, K., Okuhata, M., and Takashiri, M. (2015). Dual-bath Electrodeposition of N-type Bi-Te/Bi-se Multilayer Thin Films. *J. Alloys Comp.* 649, 721–725. doi:10.1016/j.jallcom.2015.07.166

Mavrokefalos, A., Moore, A. L., Pettes, M. T., Shi, L., Wang, W., and Li, X. (2009). Thermoelectric and Structural Characterizations of Individual Electrodeposited Bismuth telluride Nanowires. *J. Appl. Phys.* 105 (10), 104318. doi:10.1063/1.3133145

Müller, S., Schötz, C., Picht, O., Sigle, W., Kopold, P., Rauber, M., et al. (2012). Electrochemical Synthesis of Bi 1− X Sb X Nanowires with Simultaneous Control on Size, Composition, and Surface Roughness. *Cryst. Growth Des.* 12 (2), 615–621.

Na, J., Kim, Y., Park, T., Park, C., and Kim, E. (2016). Preparation of Bismuth Telluride Films with High Thermoelectric Power Factor. *ACS Appl. Mater. Inter.* 8 (47), 32392–32400. doi:10.1021/acsami.6b10188

Narducci, D., Selezneva, E., Cerofolini, G., Frabboni, S., and Ottaviani, G. (2012). Impact of Energy Filtering and Carrier Localization on the Thermoelectric Properties of Granular Semiconductors. *J. Solid State. Chem.* 193 (0), 19–25. doi:10.1016/j.jssc.2012.03.032

Naylor, A. J., Koukharenko, E., Nandhakumar, I. S., and White, N. M. (2012). Surfactant-Mediated Electrodeposition of Bismuth Telluride Films and its Effect on Microstructural Properties. *Langmuir* 28 (22), 8296–8299. doi:10.1021/la301367m

Ng, I. K., Kok, K.-Y., Rahman, C. Z., Saidin, N. U., Ilias, S. H., Choo, T.-F., et al. (2014). Electrochemically Deposited BiTe-Based Nanowires for Thermoelectric Applications. *AIP Conf. Proc.* 1584, 125–128. doi:10.1063/1.4866117

Nguyen, H. P., Peng, X., Murugan, G., Vullers, R. J. M., Vereecken, P. M., and Fransaer, J. (2013). Electrodeposition of Antimony, Tellurium and Their Alloys from Molten Acetamide Mixtures. *J. Electrochem. Soc.* 160 (2), D75–D79. doi:10.1149/2.003303jes

Nguyen, H. P., Wu, M., Su, J., Vullers, R. J. M., Vereecken, P. M., and Fransaer, J. (2012). Electrodeposition of Bismuth telluride Thermoelectric Films from a Nonaqueous Electrolyte Using Ethylene Glycol. *Electrochimica Acta* 68, 9–17. doi:10.1016/j.electacta.2012.01.091

Ni, Y., Zhang, Y., and Hong, J. (2011). Potentiostatic Electrodeposition Route for Quick Synthesis of Featherlike PbTe Dendrites: Influencing Factors and Shape Evolution. *Cryst. Growth Des.* 11 (6), 2142–2148. doi:10.1021/cg101400w

Nolas, G. S., Sharp, J., and Goldsmid, H. J. (2001). *Thermoelectrics : Basic Principles and New Materials Developments*. New York: Springer.

Park, H., Jung, H., Zhang, M., Chang, C. H., Ndifor-Angwafor, N. G., Choa, Y., et al. (2013). Branched Tellurium Hollow Nanofibers by Galvanic Displacement Reaction and Their Sensing Performance toward Nitrogen Dioxide. *Nanoscale* 5 (7), 3058–3062. doi:10.1039/c3nr00060e

Park, K., Xiao, F., Yoo, B. Y., Rheem, Y., and Myung, N. V. (2009). Electrochemical Deposition of Thermoelectric SbxTey Thin Films and Nanowires. *J. Alloys Comp.* 485 (1-2), 362–366. doi:10.1016/j.jallcom.2009.05.106

Patil, P. B., Mali, S. S., Khot, K. V., Kondalkar, V. V., Ghanwat, V. B., Mane, R. M., et al. (2016). Synthesis of Bismuth Telluride Thin Film for Thermoelectric Application via Electrodeposition Technique. *Macromol. Symp.* 361 (1), 152–155. doi:10.1002/masy.201400234

Patil, P. B., Mali, S. S., Kondalkar, V. V., Mane, R. M., Patil, P. S., Hong, C. K., et al. (2015). Morphologically Controlled Electrodeposition of Fern Shaped Bi2Te3 Thin Films for Photoelectrochemical Performance. *J. Electroanalytical Chem.* 758, 178–190. doi:10.1016/j.jelechem.2015.09.019

Pelz, U., Jaklin, J., Rostek, R., Thoma, F., Kröner, M., and Woias, P. (2016). Fabrication Process for Micro Thermoelectric Generators (μTEGs). *J. Elec Materi* 45 (3), 1502–1507. doi:10.1007/s11664-015-4088-7

Peranio, N., Leister, E., Töllner, W., Eibl, O., and Nielsch, K. (2012). Stoichiometry Controlled, Single-Crystalline Bi2Te3 Nanowires for Transport in the Basal Plane. *Adv. Funct. Mater.* 22 (1), 151–156. doi:10.1002/adfm.201101273

Pinisetty, D., Davis, D., Podlaha-Murphy, E. J., Murphy, M. C., Karki, A. B., Young, D. P., et al. (2011). Characterization of Electrodeposited Bismuth-Tellurium Nanowires and Nanotubes. *Acta Materialia* 59 (6), 2455–2461. doi:10.1016/j.actamat.2010.12.047

Pinisetty, D., Gupta, M., Karki, A. B., Young, D. P., and Devireddy, R. V. (2011). Fabrication and Characterization of Electrodeposited Antimony telluride Crystalline Nanowires and Nanotubes. *J. Mater. Chem.* 21 (12), 4098–4107. doi:10.1039/c0jm01969k

Poudel, B., Hao, Q., Ma, Y., Lan, Y., Minnich, A., Yu, B., et al. (2008). High-Thermoelectric Performance of Nanostructured Bismuth Antimony Telluride Bulk Alloys. *Science* 320 (5876), 634–638. doi:10.1126/science.1156446

Qiu, C. X., and Shih, I. (1989). Epitaxial Growth of Tellurium by Electrodeposition. *Mater. Lett.* 8 (8), 309–312. doi:10.1016/0167-577x(89)90173-0

Qiu, W. J., Yang, S. H., Zhu, T. J., Xie, J., and Zhao, X. B. (2011). Antimony telluride Thin Films Electrodeposited in an Alkaline Electrolyte. *J. Elec Materi* 40 (7), 1506–1511. doi:10.1007/s11664-011-1647-4

Qiu, X., Lou, Y., Samia, A. C. S., Devadoss, A., Burgess, J. D., Dayal, S., et al. (2005). PbTe Nanorods by Sonoelectrochemistry. *Angew. Chem. Int. Ed.* 44 (36), 5855–5857. doi:10.1002/anie.200501282

Rashid, M. M., Cho, K. H., and Chung, G.-S. (2013). Rapid thermal Annealing Effects on the Microstructure and the Thermoelectric Properties of Electrodeposited Bi2Te3 Film. *Appl. Surf. Sci.* 279, 23–30. doi:10.1016/j.apsusc.2013.03.112

Rashid, M. M., and Chung, G.-S. (2013). Effect of Deposition Conditions on the Microstructure and the Thermoelectric Properties of Galvanostatically Electrodeposited Bi_2Te_3 Film. *Surf. Rev. Lett.* 20 (05), 1350044. doi:10.1142/s0218625x13500443

Mirandaa, C. R. B., Abramof, P. G., Melo, F. C. L., and Ferreira, N. G. (2004). Morphology and Stress Study of Nanostructured Porous Silicon as a Substrate for PbTe Thin Films Growth by Electrochemical Process. *Mater. Res.* 7, 619–623.

Richoux, V., Diliberto, S., and Boulanger, C. (2010). Pulsed Electroplating: a Derivate Form of Electrodeposition for Improvement of (Bi1−x Sb X)2Te3 Thin Films. *J. Elec Materi* 39 (9), 1914–1919. doi:10.1007/s11664-009-1054-2

Rostek, R., Sklyarenko, V., and Woias, P. (2011). Influence of Vapor Annealing on the Thermoelectric Properties of Electrodeposited Bi2Te3. *J. Mater. Res.* 26 (15), 1785–1790. doi:10.1557/jmr.2011.141

Rostek, R., Stein, N., and Boulanger, C. (2015). A Review of Electroplating for V-VI Thermoelectric Films: from Synthesis to Device Integration. *J. Mater. Res.* 30 (17), 2518–2543. doi:10.1557/jmr.2015.203

Roth, R., Rostek, R., Cobry, K., Kohler, C., Groh, M., and Woias, P. (2014). Design and Characterization of Micro Thermoelectric Cross-Plane Generators with Electroplated ${\rm Bi}_{2}{\rm Te}_{3}$, ${\rm Sb}_{x}{\rm Te}_{y}$, and Reflow Soldering. *J. Microelectromech. Syst.* 23 (4), 961–971. doi:10.1109/jmems.2014.2303198

Sadeghi, M., Dastan, M., Ensaf, M. R., Tehrani, A. A., Tenreiro, C., and Avila, M. (2008). Thick Tellurium Electrodeposition on Nickel-Coated Copper Substrate for 124I Production. *Appl. Radiat. Isot.* 66 (10), 1281–1286. doi:10.1016/j.apradiso.2008.02.082

Saloniemi, H., Kanniainen, T., Ritala, M., and Leskela, M. (1998). PbTe Alkaline _ Underpotential Deposition _ Potential & Composition. *Thin Solid Films* 326 (1–2), 78–82. doi:10.1016/s0040-6090(98)00524-0

Saloniemi, H., Kemell, M., Ritala, M., and Leskelä, M. (2000). PbTe Electrodeposition Studied by Combined Electrochemical Quartz crystal Microbalance and Cyclic Voltammetry. *J. Electroanalytical Chem.* 482 (2), 139–148. doi:10.1016/s0022-0728(00)00038-3

Schumacher, C., Reinsberg, K. G., Akinsinde, L., Zastrow, S., Heiderich, S., Toellner, W., et al. (2012). Optimization of Electrodeposited P-Doped Sb2Te3 Thermoelectric Films by Millisecond Potentiostatic Pulses. *Adv. Energ. Mater.* 2 (3), 345–352. doi:10.1002/aenm.201100585

Shin, K.-J., and Oh, T.-S. (2015). Micro-Power Generation Characteristics of Thermoelectric Thin Film Devices Processed by Electrodeposition and Flip-Chip Bonding. *J. Elec Materi* 44 (6), 2026–2033. doi:10.1007/s11664-015-3647-2

Şişman, İ., and Başoğlu, A. (2016). Effect of Se Content on the Structural, Morphological and Optical Properties of Bi2Te3−ySey Thin Films Electrodeposited by under Potential Deposition Technique. *Mater. Sci. Semiconductor Process.* 54, 57–64.

Snyder, G. J., Lim, J. R., Huang, C.-K., and Fleurial, J.-P. (2003). Thermoelectric Microdevice Fabricated by a MEMS-like Electrochemical Process. *Nat. Mater* 2 (8), 528–531. doi:10.1038/nmat943

Snyder, G. J., and Toberer, E. S. (2008). Complex Thermoelectric Materials. *Nat. Mater* 7 (2), 105–114. doi:10.1038/nmat2090

Snyder, G. J., and Ursell, T. S. (2003). Thermoelectric Efficiency and Compatibility. *Phys. Rev. Lett.* 91 (14), 148301. doi:10.1103/physrevlett.91.148301

Song, Y., Yoo, I.-J., Heo, N.-R., Lim, D. C., Lee, D., Lee, J. Y., et al. (2015). Electrodeposition of Thermoelectric Bi2Te3 Thin Films with Added Surfactant. *Curr. Appl. Phys.* 15 (3), 261–264. doi:10.1016/j.cap.2014.12.004

Sootsman, J. R., Chung, D. Y., and Kanatzidis, M. G. (2009). New and Old Concepts in Thermoelectric Materials. *Angew. Chem. Int. Ed.* 48 (46), 8616–8639. doi:10.1002/anie.200900598

Sorenson, T. A., Suggs, D. W., Nandhakumar, I. S., and Stickney, J. L. (1999). Phase Transitions in the Electrodeposition of Tellurium Atomic Layers on Au(100).

J. Electroanalytical Chem. 467 (1–2), 270–281. doi:10.1016/s0022-0728(99)00053-4

Sorenson, T. A., Varazo, K., Suggs, D. W., and Stickney, J. L. (2001). Formation of and Phase Transitions in Electrodeposited Tellurium Atomic Layers on Au(111). *Surf. Sci.* 470 (3), 197–214. doi:10.1016/s0039-6028(00)00861-x

Souza, P. B., Tumelero, M. A., Zangari, G., and Pasa, A. A. (2017). Tuning Electrodeposition Conditions towards the Formation of Smooth Bi2Se3Thin Films. *J. Electrochem. Soc.* 164 (7), D401–D405. doi:10.1149/2.0531707jes

Suggs, D. W., and Stickney, J. L. (1991). Characterization of Atomic Layers of Tellurium Electrodeposited on the Low-index Planes of Gold. *J. Phys. Chem.* 95 (24), 10056–10064. doi:10.1021/j100177a081

Suh, H., Jung, H. S., Myung, N. V., and Hong, K. (2014). Bamboo-like Te Nanotubes with Tailored Dimensions Synthesized from Segmental NiFe Nanowires as Sacrificial Templates. *Bull. Korean Chem. Soc.* 35 (11), 3227–3231. doi:10.5012/bkcs.2014.35.11.3227

Suh, H., Noh, J., Lee, J.-H., Lee, S.-H., Myung, N. V., Hong, K., et al. (2017). Morphological Evolution of Te and Bi2Te3 Microstructures during Galvanic Displacement of Electrodeposited Co Thin Films. *Electrochimica Acta* 255, 1–8. doi:10.1016/j.electacta.2017.09.049

Sumithra, S., Takas, N. J., Misra, D. K., Nolting, W. M., Poudeu, P. F. P., and Stokes, K. L. (2011). Enhancement in Thermoelectric Figure of Merit in Nanostructured Bi2Te3 with Semimetal Nanoinclusions. *Adv. Energ. Mater.* 1 (6), 1141–1147. doi:10.1002/aenm.201100338

Suresh, A., Chatterjee, K., Sharma, V. K., Ganguly, S., Kargupta, K., and Banerjee, D. (2009). Effect of pH on Structural and Electrical Properties of Electrodeposited Bi2Te3 Thin Films. *J. Elec Materi* 38 (3), 449–452. doi:10.1007/s11664-008-0635-9

Szczech, J. R., Higgins, J. M., and Jin, S. (2011). Enhancement of the Thermoelectric Properties in Nanoscale and Nanostructured Materials. *J. Mater. Chem.* 21 (12), 4037–4055. doi:10.1039/c0jm02755c

Szymczak, J., Legeai, S., Michel, S., Diliberto, S., Stein, N., and Boulanger, C. (2014). Electrodeposition of Stoichiometric Bismuth telluride Bi2Te3 Using a Piperidinium Ionic Liquid Binary Mixture. *Electrochimica Acta* 137, 586–594. doi:10.1016/j.electacta.2014.06.036

Tumelero, M. A., Benetti, L. C., Isoppo, E., Faccio, R., Zangari, G., and Pasa, A. A. (2016). Electrodeposition and Ab Initio Studies of Metastable Orthorhombic Bi2Se3: A Novel Semiconductor with Bandgap for Photovoltaic Applications. *J. Phys. Chem. C* 120 (22), 11797–11806. doi:10.1021/acs.jpcc.6b02559

Uda, K., Seki, Y., Saito, M., Sonobe, Y., Hsieh, Y.-C., Takahashi, H., et al. (2015). Fabrication of Π-structured Bi-te Thermoelectric Micro-device by Electrodeposition. *Electrochimica Acta* 153, 515–522. doi:10.1016/j.electacta.2014.12.019

Ueda, M., Mito, Y., and Ohtsuka, T. (2008). Electrodeposition of Sb-Te Alloy in AlCl3-NaCl-KCl Molten Salt. *Mater. Trans.* 49 (8), 1720–1722. doi:10.2320/matertrans.e-mra2008811

Wang, W., Ji, Y., Xu, H., Li, H., Visan, T., and Golgovici, F. (2013). A High Packing Density Micro-thermoelectric Power Generator Based on Film Thermoelectric Materials Fabricated by Electrodeposition Technology. *Surf. Coat. Tech.* 231, 583–589. doi:10.1016/j.surfcoat.2012.04.048

Wang, W., Zhang, G., and Li, X. (2008). Manipulating Growth of Thermoelectric Bi2Te3/Sb Multilayered Nanowire Arrays. *J. Phys. Chem. C* 112 (39), 15190–15194. doi:10.1021/jp803207r

Weber, J. E., Yelton, W. G., and Kumar, A. (2008). “Electrodeposition of Bi1-xSbx Nanowires as an Advanced Material for Thermoelectric Applications,” in *Functionalized Nanoscale Materials, 2008* (Springer, Dordrecht: Devices and Systems), 425–429.

Wu, M., Binnemans, K., and Fransaer, J. (2014). Electrodeposition of Antimony from Chloride-free Ethylene Glycol Solutions and Fabrication of Thermoelectric Bi2Te3/(Bi1−xSbx)2Te3 Multilayers Using Pulsed Potential Electrodeposition. *Electrochimica Acta* 147, 451–459. doi:10.1016/j.electacta.2014.08.111

Wu, M., Nguyen, H. P., Vullers, R. J. M., Vereecken, P. M., Binnemans, K., and Fransaer, J. (2013). Electrodeposition of Bismuth Telluride Thermoelectric Films from Chloride-free Ethylene Glycol Solutions. *J. Electrochem. Soc.* 160 (4), D196–D201. doi:10.1149/2.089304jes

Wu, M., Ramírez, S. A., Shafahian, E., Guo, L., Glorieux, C., Binnemans, K., et al. (2017). Electrodeposition of Bismuth telluride Thin Films Containing Silica Nanoparticles for Thermoelectric Applications. *Electrochimica Acta* 253, 554–562. doi:10.1016/j.electacta.2017.09.012

Wu, T., Lee, H.-K., and Myung, N. V. (2016). Electrodeposition of Dense Lead Telluride Thick Films in Alkaline Solutions. *J. Electrochem. Soc.* 163 (14), D801–D808. doi:10.1149/2.0631614jes

Wu, T., Zhang, M., Lee, K.-H., Lee, C.-M., Lee, H.-K., Choa, Y., et al. (2017). Electrodeposition of Compact Tellurium Thick Films from Alkaline Baths. *J. Electrochem. Soc.* 164 (2), D82–D87. doi:10.1149/2.1191702jes

Wu, Y., Lin, Z., Tian, Z., Han, C., Liu, J., Zhang, H., et al. (2016). Fabrication of Microstructured Thermoelectric Bi2Te3 Thin Films by Seed Layer Assisted Electrodeposition. *Mater. Sci. Semiconductor Process.* 46, 17–22. doi:10.1016/j.mssp.2016.01.014

Xiao, C., Yang, J., Zhu, W., Peng, J., and Zhang, J. (2009). Electrodeposition and Characterization of Bi2Se3 Thin Films by Electrochemical Atomic Layer Epitaxy (ECALE). *Electrochimica Acta* 54 (27), 6821–6826. doi:10.1016/j.electacta.2009.06.089

Xiao, F., Hangarter, C., Yoo, B., Rheem, Y., Lee, K.-H., and Myung, N. V. (2008). Recent Progress in Electrodeposition of Thermoelectric Thin Films and Nanostructures. *Electrochimica Acta* 53 (28), 8103–8117. doi:10.1016/j.electacta.2008.06.015

Xiaolong, L., and Zhen, X. (2014). The Effect of Electrochemical Conditions on Morphology and Properties of Bi2Se3 Thick Films by Electrodeposition. *Mater. Lett.* 129, 1–4. doi:10.1016/j.matlet.2014.05.009

Xue, Z., Li, X.-L., and Yu, D.-m. (2014). Bi2Se3/Bi Multiple Heterostructure Nanowire Arrays Formed by Pulsed Electrodeposition. *Superlattices and Microstructures* 74, 273–278. doi:10.1016/j.spmi.2014.06.012

Yagi, I., Lantz, J. M., Nakabayashi, S., Corn, R. M., and Uosaki, K. (1996). *In Situ* optical Second Harmonic Generation Studies of Electrochemical Deposition of Tellurium on Polycrystalline Gold Electrodes. *J. Electroanalytical Chem.* 401 (1–2), 95–101. doi:10.1016/0022-0728(95)04285-7

Yang, C.-K., Cheng, T.-C., Chen, T.-H., and Chu, S.-H. (2016). The Thermoelectric Properties of Electrochemically Deposited Te-Sb-Bi Films on Ito Glass Substrate. *Int. J. Electrochem. Sci.* 11 (5), 3767–3775. doi:10.20964/110371

Yang, Y., Kung, S. C., Taggart, D. K., Xiang, C., Yang, F., Brown, M. A., et al. (2008). Synthesis of PbTe Nanowire Arrays Using Lithographically Patterned Nanowire Electrodeposition. *Nano Lett.* 8 (8), 2447–2451. doi:10.1021/nl801442c

Yoo, I.-J., Lim, D. C., Myung, N. V., Jeong, Y.-K., Kim, Y. D., Lee, K. H., et al. (2013). Electrical/thermoelectric Characterization of Electrodeposited Bi X Sb2−x Te3 Thin Films. *Electron. Mater. Lett.* 9 (5), 687–691. doi:10.1007/s13391-013-2246-8

Yoo, I.-J., Myung, N. V., Lim, D. C., Song, Y., Jeong, Y.-K., Kim, Y. D., et al. (2013). Electrodeposition of BixTey Thin Films for Thermoelectric Application. *Thin Solid Films* 546 (3), 48–52. doi:10.1016/j.tsf.2013.05.036

Yoo, I.-J., Song, Y., Chan Lim, D., Myung, N. V., Lee, K. H., Oh, M., et al. (2013). Thermoelectric Characteristics of Sb2Te3 Thin Films Formed via Surfactant-Assisted Electrodeposition. *J. Mater. Chem. A.* 1 (17), 5430. doi:10.1039/c3ta01631e

Zebarjadi, M., Esfarjani, K., Dresselhaus, M. S., Ren, Z. F., and Chen, G. (2012). Perspectives on Thermoelectrics: from Fundamentals to Device Applications. *Energy Environ. Sci.* 5 (1), 5147–5162. doi:10.1039/c1ee02497c

Zeng, G., Zide, J. M. O., Kim, W., Bowers, J. E., Gossard, A. C., Bian, Z., et al. (2007). Cross-plane Seebeck Coefficient of ErAs:InGaAs⁄InGaAlAs Superlattices. *J. Appl. Phys.* 101 (3), 034502. doi:10.1063/1.2433751

Zhang, Y., Snedaker, M. L., Birkel, C. S., Mubeen, S., Ji, X., Shi, Y., et al. (2012). Silver-Based Intermetallic Heterostructures in Sb2Te3 Thick Films with Enhanced Thermoelectric Power Factors. *Nano Lett.* 12 (2), 1075–1080. doi:10.1021/nl204346g

Zhou, A., Fu, Q., Zhang, W., Yang, B., Li, J., Ziolkowski, P., et al. (2015). Enhancing the Thermoelectric Properties of the Electroplated Bi 2 Te 3 Films by Tuning the Pulse Off-To-On Ratio. *Electrochimica Acta* 178, 217–224. doi:10.1016/j.electacta.2015.07.164

Zhou, J., Lin, Q., Li, H., and Cheng, X. (2013). Phosphorus-doped Bismuth telluride Films by Electrodeposition. *Mater. Chem. Phys.* 141 (1), 401–405. doi:10.1016/j.matchemphys.2013.05.033

Zhu, W., Yang, Y., Zhou, D., and Xiao, C. (2008). Electrochemical Atom-By-Atom Growth of Highly Uniform Thin Sheets of Thermoelectric Bismuth telluride via the Route of ECALE. *J. Electroanalytical Chem.* 614 (1-2), 41–48. doi:10.1016/j.jelechem.2007.11.014

Zhu, Y.-B., and Wang, W. (2012). Microstructure and Thermoelectric Properties of P-type Bi-sb-te-se Thin Films Prepared by Electrodeposition Method. *Thin Solid Films* 520 (7), 2474–2478. doi:10.1016/j.tsf.2011.10.020

Zide, J. M. O., Vashaee, D., and Gossard, A. (2006). Demonstration of Electron Filtering to Increase the Seebeck Coefficient in In0.53Ga0.47As/In0.53Ga0.28Al0.19As Superlattices. *Phys. Rev. B* 74, 205335. doi:10.1103/PHYSREVB.74.205335

Zou, Z., Chen, S., and Cai, K. (2014). Preparation and Characterization of Electrodeposited $Cu_xBi_2Te_3$ Thermoelectric Films. *Mater. Sci. Forum* 787, 205–209.

Zou, Z. G., Cai, K. F., Chen, S., and Qin, Z. (2012). Pulsed Electrodeposition and Characterization of Bi2Te3−ySey Films. *Mater. Res. Bull.* 47 (11), 3292–3295. doi:10.1016/j.materresbull.2012.07.036

Conflict of Interest: The authors declare that the research was conducted in the absence of any commercial or financial relationships that could be construed as a potential conflict of interest.

The handling Editor declared a past co-authorship with the authors JK and JL.

frontiers in Chemistry

ORIGINAL RESEARCH
published: 21 January 2022
doi: 10.3389/fchem.2022.799305

Synthesis of Copper Telluride Thin Films by Electrodeposition and Their Electrical and Thermoelectric Properties

Jungjoon Park[1], Jinmyeong Seo[1], Jae-Hong Lim[2]* and Bongyoung Yoo[1]*

[1]Department of Materials Science and Chemical Engineering, Hanyang University, Ansan, South Korea, [2]Department of Materials Science and Engineering, Gachon University, Seongnam, South Korea

Intermetallic copper telluride thin films, which are important in a number of electronics fields, were electrodeposited using a potentiostatic method in low-pH aqueous electrolyte baths with various ion-source concentrations, and the electrical properties of the formed films were investigated after exfoliation from the substrate. The films were electrochemically analyzed by cyclic voltammetry, while surface and cross-sectional morphologies, compositional ratios, and electrical properties were analyzed by scanning electron microscopy, X-ray diffractometry, X-ray photoelectron spectroscopy, ultraviolet photoelectron spectroscopy, and Hall-effect experiments. The copper telluride thin films, which were synthesized at various potentials in each bath, exhibit different composition ratios and structures; consequently, they show a variety of electrical and thermoelectric properties, including different electrical conductivities, carrier concentrations, mobilities, and Seebeck coefficients. Among them, the thin film with a 1:1 Cu:Te ratio delivered the highest power factor due to carrier filtering at the interface between the two phases.

Keywords: copper telluride, electrodeposition, thermoelectric, compositional control, carrier filtering effect

Edited by:
Xifei Li,
Xi'an University of Technology, China

Reviewed by:
Changdong Gu,
Zhejiang University, China
Yaohui Zhang,
Harbin Institute of Technology, China

***Correspondence:**
Jae-Hong Lim
Authorslimjh@gachon.ac.kr
Bongyoung Yoo
byyoo@hanyang.ac.kr

Specialty section:
This article was submitted to Electrochemistry,
a section of the journal
Frontiers in Chemistry

Received: *21 October 2021*
Accepted: *03 January 2022*
Published: *21 January 2022*

Citation:
Park J, Seo J, Lim J-H and Yoo B (2022) Synthesis of Copper Telluride Thin Films by Electrodeposition and Their Electrical and Thermoelectric Properties.
Front. Chem. 10:799305.
doi: 10.3389/fchem.2022.799305

INTRODUCTION

Copper telluride has attracted increasing attention in recent years for potential thermoelectrics, quantum dot, battery, and plasmonics applications because of its p-type semiconductor properties (Kriegel et al., 2013; Nethravathi et al., 2014; Han et al., 2014; Zhang et al., 2016). However, synthesizing intermetallic semiconductors with exact CuTe and Cu_2Te stoichiometries is difficult, which is mainly due to copper vacancies; hence, copper telluride exists in a wide range of nonstoichiometric $Cu_{2-x}Te$ phases, including $Cu_{1.5}Te$, Cu_7Te_5, and Cu_7Te_4. Hence, the characteristics of a material can potentially be controlled by adjusting the copper telluride composition and structure.

Various methods have been developed for the synthesis of copper telluride, including hydrothermal, solvothermal, ion-exchange, vacuum-deposition, and electrodeposition techniques (Zhang et al., 2006; Dhasade et al., 2012; Kriegel et al., 2013; Nethravathi et al., 2014; Bhuvaneswari et al., 2017). Hydrothermal synthesis involves the decomposition of reactants or chemical reactions between them at high temperature and high pressure in an aqueous solution, while solvothermal synthesis is similar but involves a non-aqueous solvent (Nethravathi et al., 2014). These two synthesis methods are advantageous because they lead to nanostructures with uniform crystalline phases that are not stable at their melting points; however, they require expensive autoclaves, are associated with safety issues during reaction, and observing reaction process is impossible as the reaction proceeds in a “black box.” Ion-exchange synthesis involves the exchange of ionic components (Kriegel et al., 2013) and is widely used to prepare nanostructured metal chalcogenides because their properties can be controlled through cation or anion exchange. However, it has some drawbacks, including long production times and large pH changes during reaction (Chen and Wang, 2017; Cho et al., 2019). While these methods are outstanding for the synthesis of nanostructured materials, they require the use of additional processes, such as sintering, for thermoelectric applications (Zhang et al., 2020).

Vacuum-deposition processes, which include sputtering, e-beam evaporation, and chemical vapor deposition, are used to deposit thin films at pressures below atmospheric pressure (Bhuvaneswari et al., 2017) and are advantageous because they deposit good-quality thin films. However, some processes require expensive equipment while others require long production times. In contrast, electrodeposition involves the electrochemical reduction of metal ions in solution and has benefits that include high throughput, the formation of highly pure deposited films, wide deposition areas, low operating temperatures, and relative cost effectiveness. Electrodeposition can be used to tailor the composition of the deposited material by adjusting its wide range of controllable parameters, such as the concentration of the ion source, application potential, applied current density, solution pH, additives, and the electrical wave form, which provide outstanding advantages. These electrodeposition characteristics can be used to control the composition and stoichiometry of copper telluride, which has numerous metastable states.

In this study, low-pH electrolytes were used to synthesize copper telluride thin films by electrodeposition, with the composition of the electrodeposited thin films controlled by adjusting the concentration of the ion source and the applied potential. The electrical properties of the electrodeposited intermetallic copper telluride thin films, including carrier concentration, conductivity, mobility, and thermoelectric properties, were investigated by mechanically transferring the films from the original substrate to epoxy resin.

MATERIALS AND METHODS

Electrochemical Cell for Copper Telluride Electrodeposition

The electrolyte for copper telluride electrodeposition was prepared by dissolving $Cu(NO_3)_2{\cdot}3H_2O$ (Daejung) and TeO_2 (Sigma–Aldrich) in a mixture of deionized water and nitric acid. Copper nitrate was selected as the copper salt based on a previous study on $Cu_{2\text{-}x}Te$-film electrodeposition using various copper metal salts with various anions, such as sulfate, chloride, and nitrate (Zhang et al., 2011). First, 60% nitric acid (20 ml) was added to deionized water (80 ml) to form a pH 1.0 solution because TeO_2 has limited solubility in highly alkaline aqueous solutions, after which $Cu(NO_3)_2$ was dissolved in the solution to a concentration of 10, 7.5, or 5 mM. Finally, TeO_2 was dissolved in the solution to a concentration of 5, 7.5, or 10 mM) as the Te-ion source. The total ion concentration (Cu + Te) was 15 mM in each case.

A three-electrode system consisting of a Ag/AgCl reference electrode (Fisher Scientific, 13-620-53), a Pt plate (20 mm × 130 mm) counter electrode, and a $Si/SiO_2/Ti/Au$ wafer working electrode was used to electrodeposit CuTe. Each wafer sample was cleaved to be 12 mm × 10 mm in size. Prior to electrodeposition, cyclic voltammetry (CV) was used to understand the electrochemical reaction of Cu and Te on the Au substrate surface. A VersaSTAT MC potentiostat/galvanostat (Princeton Applied Research) was used for all electrochemical syntheses and analyses. Electrodeposition was performed at room temperature.

Characterizing the Electrodeposited Thin Films

The surface morphologies, film thicknesses, and compositions of the deposited thin films were investigated by scanning electron microscopy (SEM; TESCAN, MIRA3) augmented with energy-dispersive X-ray spectroscopy (EDS). The phase-formation behavior and crystal orientations of the films were investigated by conventional X-ray diffractometry (XRD; Rigaku D Max-2500) using Cu Kα radiation. The microstructure was elucidated by transmission electron microscopy (TEM, JEOL JEM-2010). The TEM samples were prepared with a focused ion beam (FIB, FEI, Nova Nanolab). Te binding energies were determined using X-ray photoelectron spectroscopy (XPS; Kratos AXIS-NOVA) with Monochromatic Al-Ka (1486.6 eV) photon source and ultraviolet photoelectron spectroscopy (UPS, Kratos AXIS-NOVA) with a He-I photon source (21.2 eV). The C 1s peak at 286.5 eV was used for calibration purposes. Samples were sputtered with Ar gas to remove contamination and the native oxide on the thin film prior to analysis. Films were detached from the substrate using Torr Seal epoxy (Struers, ProntoFix) to examine their electronic transport properties; therefore, the rear surface of the film was examined. The room-temperature electrical conductivity (σ), Hall mobility (μ_{Hall}), and carrier concentration (n_c) of each as-deposited and annealed thin film were determined using a Hall-effect measurement unit (ECOPIA, HMS-5300) in the van der Pauw configuration. Seebeck coefficients (S) were determined from plots of measured Seebeck voltages as functions of temperature difference (<3 °C) across the specimen ($S = \Delta V/\Delta T$) at 27°C using an a self-made S measurement system.

Mechanical Exfoliation of Cu-Te Thin Film

The electrodeposited copper telluride thin films were mechanically exfoliated from the conducting substrate for investigating the electrical and thermoelectric properties **Figures 1A–F** is a scheme of the exfoliation process. Cu foil was purchased from ILJIN MATERIALS. Each Cu foil was sliced into pieces of dimensions $15 \times 15\ \mathrm{mm}^2$ (**Figure 1A**). A Ti adhesive layer (20 nm) and Au seed layer (200 nm) were deposited using the E-beam evaporator after cleaning the Cu foil in 10%vol. H_2SO_4 to remove the native oxide

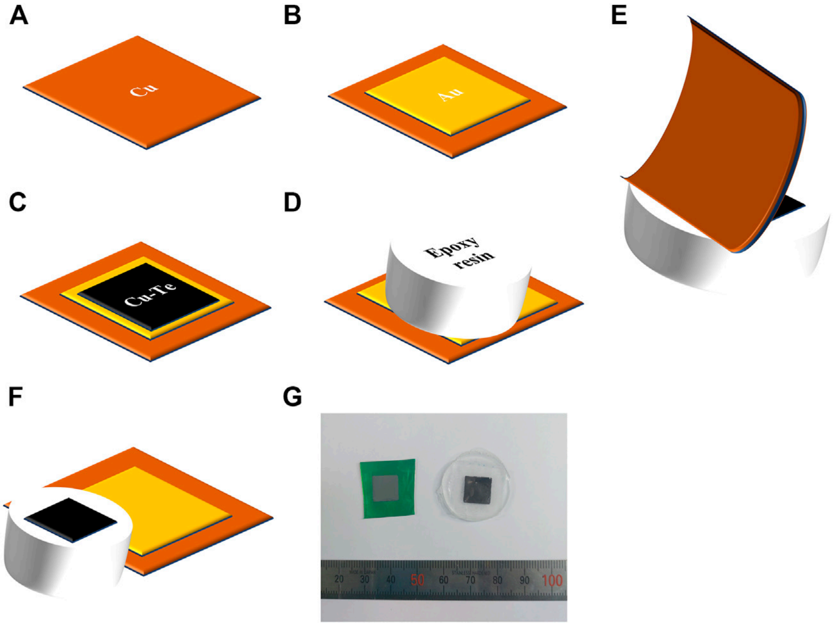

FIGURE 1 | Schematic depicting mechanical exfoliation: **(A)** Cu foil, **(B)** Au seed layer obtained by e-beam evaporation, **(C)** Cu-Te electrodeposition, **(D)** pasting and drying of epoxy resin, **(E)** mechanical exfoliation, **(F)** after mechanical exfoliation, **(G)** photograph of electrodeposited Cu-Te thin film (left) and mechanically exfoliated film on epoxy resin (right).

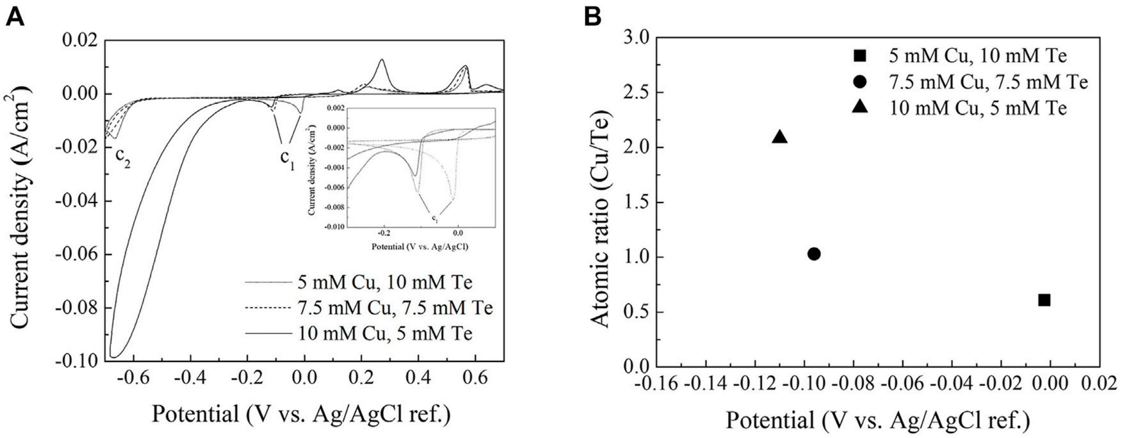

FIGURE 2 | **(A)** Cyclic voltammograms of a Au/Ti/Si substrate in $Cu(NO_3)_2{\cdot}3H_2O/TeO_2/HNO_3$ between −0.7 and 0.7 V. The inset shows the same cyclic voltammograms between −0.3 and 0.05 V **(B)** EDS data for thin films deposited in each bath at various potentials (−2.5, −96, and −110 mV).

layer of the Cu film (**Figure 1B**). Following the preparation of the substrate, Cu-Te thin films were deposited on it (**Figure 1C**). After rinsing and drying the sample, epoxy resin was pasted on the electrodeposited Cu-Te thin film, followed by hardening in air for 24 h (**Figure 1D**). Finally, the flexible Cu/Ti/Au foil substrate was exfoliated from the hardened epoxy resin on which the electrodeposited thin film was transferred (**Figures 1E,F**). This method enabled the exfoliation of the electrodeposited thin film from the conducting substrate without cracks on the surface, thereby allowing measurements of the electrical properties of the electrodeposited thin films. **Figure 1G** shows a photograph of the electrodeposited copper telluride thin film (left) and the transferred thin film on epoxy resin (right).

RESULTS AND DISCUSSION

Copper Telluride Electrodeposition

Figure 2A shows cyclic voltammograms of the copper telluride baths used in the electrodeposition experiments. The potential was swept in

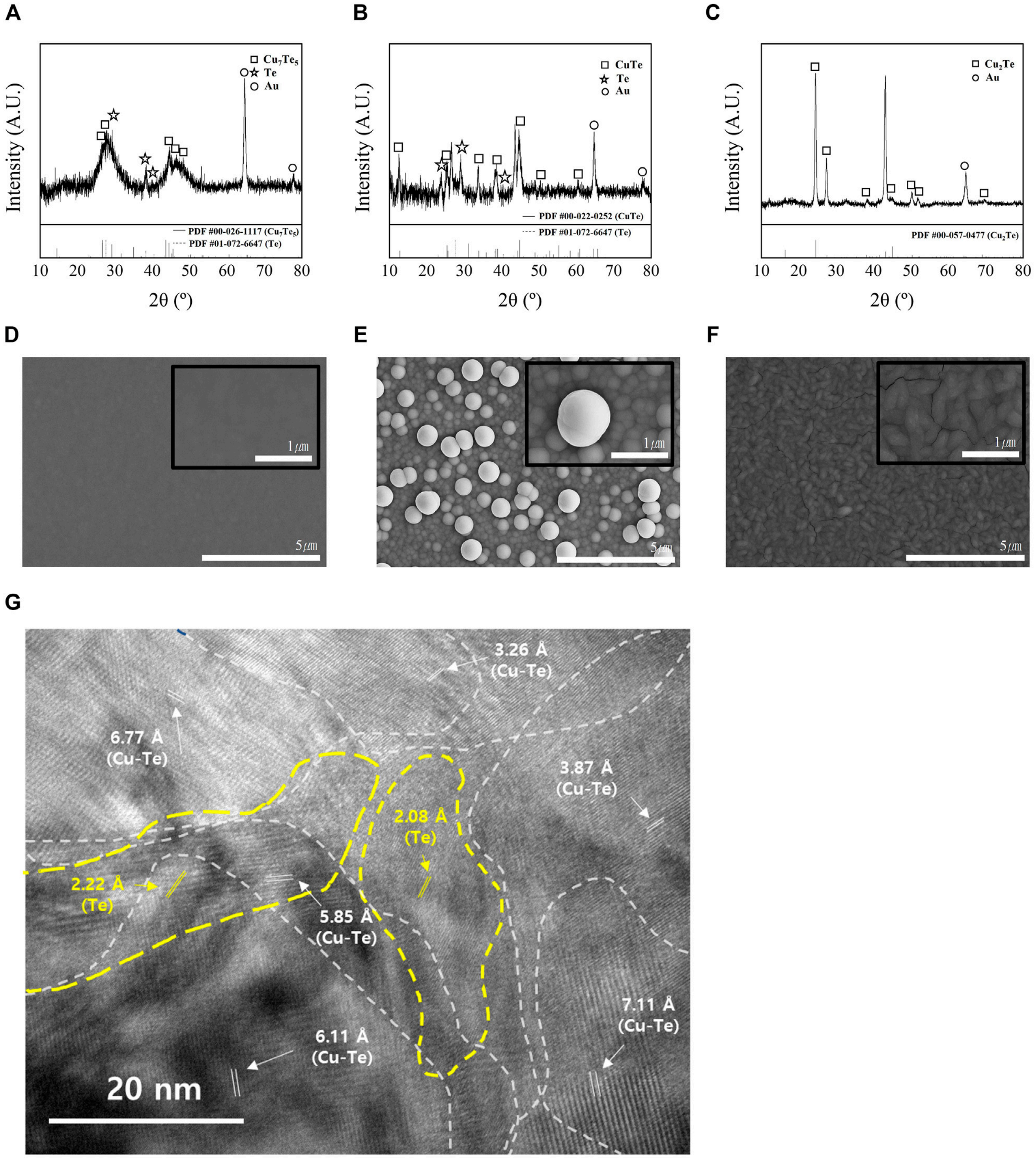

FIGURE 3 | XRD patterns thin films formed at Cu/Te compositional ratios of **(A)** 0.5 (PDF #00-026-1117: Cu_7Te_5, PDF #01-072-6647: Te), **(B)** 1 (PDF #00-022-0252: CuTe), **(C)** 2 (PDF #00-057-0477: Cu_2Te), and SEM images [10000x, 50000x (insets)] of thin films (1 mm) at Cu/Te compositional ratios of **(D)** 0.5 (Cu_7Te_5+Te), **(E)** 1 (CuTe), **(F)** 2 (Cu_2Te). **(G)** HR-TEM (250kx) image of thin films formed at a Cu/Te compositional ratio of 0.5.

the cathodic direction from the open-circuit potential (OCP) at a scan rate of 10 mV/s between −700 and 700 mV (vs. Ag/AgCl sat.) in steps of 10 mV/s and then back to the OCP. CV revealed that the copper telluride (C1) reduction peak at around −0.1 V varies with concentration. Copper has a more noble reduction potential (E_0 = 117 mV vs. Ag/AgCl sat.) than that of the Te ion (E_0 = – 200 mV vs. Ag/AgCl sat.) (Rudnik and Kozłowski, 2013). However, the reduction peak shifted in the positive direction with decreasing Cu/Te bath salt ratio, which suggests that the Te underpotential deposition (UPD) reaction occurs on the Au substrate surface, as previously observed by Sorenson et al. (2001), which accelerates copper telluride deposition at a more noble potential. This result also suggests that any increase or decrease in the limiting current of the reduction peak (C1) during CV is mainly due to the concentration of Te ions near the working electrode surface.

Secondary peaks (C2) began to appear at approximately −600 mV when the potential was moved in the negative direction (vs. Ag/AgCl sat.), which corresponds to the formation of H_2Te as given by (Kim et al., 2016)

$$\mathrm{Te} + 2\mathrm{H}^{+} + 2\mathrm{e}^{-} \rightarrow \mathrm{H_2Te} \tag{1}$$

Copper reduction appears to dominate after the copper telluride reduction peak (C1) in the 10 mM Cu + 5 mM Te bath, and the reduction peak corresponding to the formation of H_2Te (C2) is no longer clearly observed.

Figure 2B displays the atomic ratios of copper to tellurium of deposits formed in each bath as determined by EDS. Cu_2Te and CuTe stoichiometries were observed for thin films deposited in baths containing 10 mM Cu + 5 mM Te and 7.5 mM Cu + 7.5 mM Te, respectively. In contrast, the thin films deposited in the bath containing 5 mM Cu + 10 mM Te exhibited a 1:2 compositional ratio, which does not fit the stoichiometry of any intermetallic copper telluride compound; metallic Te and an intermetallic copper telluride compound possibly coexist based on this compositional ratio.

Figure 3 shows XRD patterns and SEM images of the electrodeposits formed in each bath. The reference powder diffraction files (PDFs) for copper tellurides and Te are: #00-026-1117 (Cu_7Te_5), #01-072-6647 (Te), #00-022-0252 (CuTe), and #00-057-0477 (Cu_2Te). The XRD pattern of the thin film with Cu/Te = 0.5 is shown in **Figure 3A**, which reveals the presence of both Cu_7Te_5 and Te, and the broad diffuse peaks in the XRD spectrum suggest that the film has a nanocrystalline phase. The HR-TEM image of the thin film with Cu/Te = 0.5 (**Figure 3G**) is consistent with the XRD pattern of the sample. The HR-TEM image at 250kx magnification does not show clear grain boundaries, but shows various orientations of 100 nm-sized grains with different d spacings that overlap each other. **Figure 3D** shows the SEM image of the $Cu_{0.5}Te$ thin film, which exhibits a smooth and dense surface morphology, while **Figure 3B** shows the XRD pattern of the thin film with Cu/Te = 1, which reveals the presence of crystalline intermetallic CuTe, and small amounts of Te. Unlike the surface morphology of the $Cu_{0.5}Te$ thin film, which exhibits a smooth and dense surface, the surface morphology of the CuTe thin film (**Figure 2E**) can be described as a cluster of small nanoparticles forming the thin film with spherical micrometer-sized particles on the top, akin to the formation of other chalcogenides under low-pH conditions (Saha et al., 2020). The thin film with Cu/Te = 2 (**Figure 3C**) shows obvious crystallinity that corresponds to intermetallic Cu_2Te; this thin film exhibits an ellipsoidal particle morphology with cracks that may result from internal tensile stresses (**Figure 3F**) (Eliaz et al., 2005). Materials with high carrier concentrations are generally less resistive than those with low carrier concentrations; hence, the observed cracks may adversely affect thin-film resistivity, resulting in poor thermoelectric properties.

The Te 3d XPS spectra of the thin films (**Figure 4**) show Te binding energies that correspond to Te^{4+} (576.1 eV, $3d_{5/2}$), Te^{0} (573.0 eV, $3d_{5/2}$), Te^{2-} (572.6 eV, $3d_{5/2}$), consistent with TeO_2, Te metal, and Te bound to Cu, respectively. The Te 3d XPS spectrum of the $Cu_{0.5}Te$ thin film (**Figure 4A**) shows high intensity Te^{2-} 3d peaks (87.3%) and less intense Te^{0} 3d peaks (12.7%) that corresponds to the left shoulders of the major peaks, with Te^{4+} 3d peaks noticeably absent. These data confirm that intermetallic Cu_7Te_5 and a small amount of Te metal coexist without TeO_2 in the thin film. The XPS pattern of the CuTe thin film is shown in **Figure 4B**, in which high intensity Te^{2-} 3d peaks (76.64%) and smaller Te^{0} 3d (16.84%) and Te^{4+} 3d (6.52%) peaks are observed, which implies that the CuTe thin film contains intermetallic CuTe, Te metal, and a small amount of TeO_2. Compared to the $Cu_{0.5}Te$ thin film, the CuTe thin film exhibits a somewhat larger Te^{0} peak, with a small amount of TeO_2 also observed. The Te 3d XPS spectrum of the Cu_2Te thin film is shown in **Figure 4C**. This film exhibits the largest Te^{4+} 3d peaks (46.76%) and the smallest Te^{2-} 3d (41.70%) and Te^{0} 3d (11.54%) peaks among the three thin film samples; it also shows a Cu LMM peak near 570 eV, consistent with the presence of Cu metal.

Electrical and Thermoelectrical Properties of Electrodeposited Copper Telluride Thin Films

Hall-effect measurements using the van der Pauw method were used to examine the electrical properties of the electrodeposited thin films after exfoliation. All films were deposited with the same applied charge at 5C to produce films with the same 2.5-μm thickness. However, we were unable to form a 2.5-μm-thick Cu_2Te film without delaminating it from the substrate prior to exfoliation due to internal stress. Consequently, a 1-μm-thick Cu_2Te sample was exfoliated from the substrate in this case. **Figure 5** displays the electrical characteristics of the copper telluride thin films, including carrier concentration, conductivity, and carrier mobility. All electrodeposited copper telluride thin films exhibited relatively high carrier concentrations (10^{21}–10^{23} cm^{-3}) as p-type semiconductors, which is consistent with the carrier concentrations of other copper chalcogenides and is ascribable to copper vacancies (Dorfs et al., 2011; Luther et al., 2011; Kriegel et al., 2012). The $Cu_{0.5}Te$ thin film is the least conductive (20 S cm^{-1}), which is due to electron scattering induced by the interface between the two phases and the large proportion of grain boundaries. The CuTe thin film deposited in this work exhibits the highest electrical conductivity (4,632 S cm^{-1}) among previously reported CuTe thin films. Bhuvaneswari et al. (2017) reported electrical conductivities of 384–714 S cm^{-1} for 1-μm-thick CuTe thin films deposited by vacuum evaporation. The conductivity of the CuTe thin film prepared in the current work is similar to that reported previously for bulk copper telluride (4200 S cm^{-1}) (He et al., 2015). Cu_2Te thin films are poorly conductive and have low carrier mobilities compared to their carrier concentrations.As discussed above (*vide supra*), the low conductivity and carrier mobility is possibly attributable to

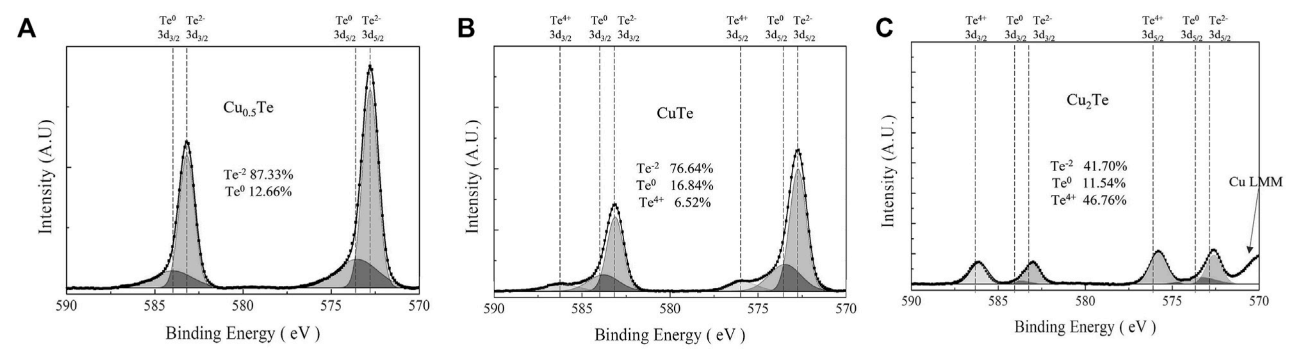

FIGURE 4 | Te 3d XPS spectra acquired from thin films at each Cu/Te compositional ratios of **(A)** 0.5, **(B)** 1, **(C)** 2.

cracks induced by stresses inside the thin film, as observed in the corresponding SEM image (**Figure 3F**).

Table 1 lists the thermoelectric properties of the electrodeposited thin films and others reported in the literature (Mansour et al., 1986; Nethravathi et al., 2014; Ghosh et al., 2016; Mukherjee et al., 2019; Mukherjee et al., 2020), including Seebeck coefficients, conductivities, and calculated power factors. The electrodeposited thin films have somewhat larger Seebeck coefficient than their bulk counterparts. Previously reported copper telluride bulk and thin film samples (Mansour et al., 1986; Nethravathi et al., 2014; Ghosh et al., 2016; Mukherjee et al., 2019; Mukherjee et al., 2020) exhibited relatively low Seebeck coefficients of between 4 and 40 μV K^{-1}. While electrodeposited Cu$_{0.5}$Te showed a particularly high Seebeck coefficient (346 μV K^{-1}), the Cu$_{0.5}$Te thin film is extremely poorly electrically conductive, which results in a low power factor (2.48 μW cm^{-1} K^{-1}). On the contrary, CuTe exhibited the highest power factor (7.71 μW cm^{-1} K^{-1}) despite its low Seebeck coefficient, which is ascribable to its high conductivity. The CuTe thin film has a high power factor because its conductivity is of similar order to that of the bulk sample but its Seebeck coefficient is considerably higher. In contrast, the Cu$_2$Te sample shows the lowest power factor owing to its low Seebeck coefficient and conductivity. While Seebeck coefficient and conductivity exist in a trade-off relationship, the Cu$_2$Te sample has low values owing to its cracked surface.

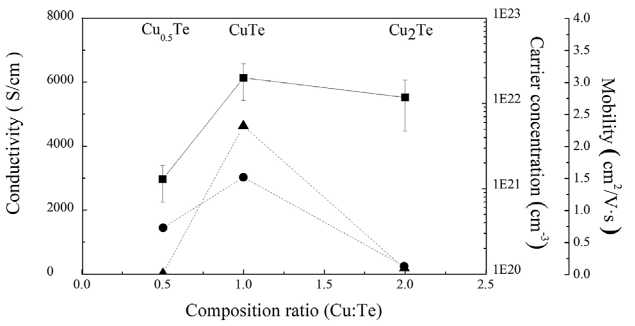

FIGURE 5 | Electrical properties of thin films deposited by electrodeposition as functions of the Cu/Te compositional ratio [▲ = Conductivity (S/cm), ■: Carrier concentration (cm^{-3}), ● = mobility (cm^2/V s)].

Pisarenko plots, which show relationships between Seebeck coefficients and carrier concentrations determined through Hall-effect measurements, are shown in **Figure 6**. The carrier effective masses of the electrodeposited thin films were calculated assuming a simple band structure using the following electron transport relationship:

$$S = \frac{8\pi^2 k_b^2}{3eh^2}\left(\frac{\pi}{3n}\right)^{2/3} m^* T \tag{2}$$

TABLE 1 | Thermoelectric properties of copper tellurides determined by Hall-effect measurement (this work) and the *S* measurement system at room temperature.

Compositional ratio (Cu/Te	Seebeck coefficient (μV K^{-1}	Conductivity (S cm^{-1}	Power factor (μW·cm^{-1}K^{-1}	Shape/Synthesis method	
0.5	346	20.74	2.48	Thin film/Electrodeposition	This work
1	40.8	4632	7.71	Thin film/Electrodeposition	This work
2	53.8	178.71	0.52	Thin film/Electrodeposition	This work
2	25	4,000	2.5	Bulk/Hot pressing	Nethravathi et al. (2014)
2	15	8,000	1.8	Bulk/Solid state reaction	Mukherjee et al. (2020)
2	15	6,427	1.6	Bulk/Solid state reaction	Mansour et al. (1986)
2	4	1,000	0.0016	Bulk/Melting	Ghosh et al. (2016)
1.75	40	2,550	4.1	Thin film/Electrodeposition	Mukherjee et al. (2019)

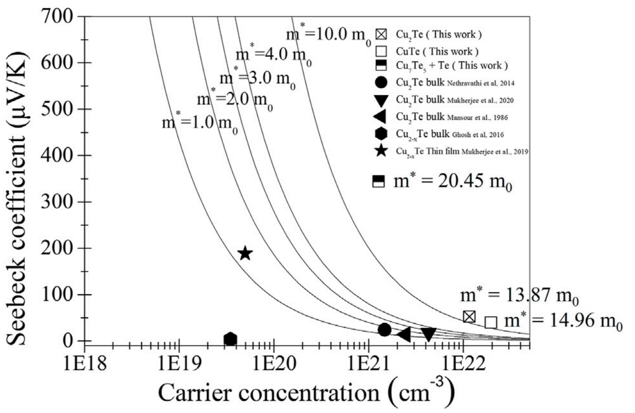

FIGURE 6 | Seebeck coefficients of copper telluride thin films deposited by electrodeposition and other methods as functions of carrier concentration (Pisarenko plots). Square symbols correspond to thin films prepared in this work. The solid lines are curves calculated for m* = 1, 2, 3, 4, and 10 m_0.

where S is the Seebeck coefficient, k_b is Boltzmann's constant, h is Planck's constant, n is carrier concentration, m* is the carrier effective mass, and T is temperature.

The solid curves shown in **Figure 6** correspond to m* = 1.0, 2.0, 3.0, 4.0, and 10.0 m_0, and are provided for guidance. The carrier concentrations and Seebeck coefficients of literature samples provided in **Table 1** are also plotted in the figure for comparison. All electrodeposited thin films show significantly high carrier effective masses compared to literature values, which is mainly due to the formation of potential wells at the interfaces between the two different phases, namely intermetallic copper telluride and tellurium metal. The potential wells of the two phases are responsible for the high Seebeck coefficients compared to those reported in the literature, despite their high carrier concentrations. This effect provides high power factors because high Seebeck coefficients are not traded off against thin film conductivity.

Figure 7A shows the potential well scheme resulting from the difference in the work function of intermetallic CuTe and that of Te metal at the interface between the two phases. As the two phases have different work functions, the potential difference creates a potential well that affects the thermoelectric properties of the thin film due to carrier filtering. There is a close relationship between the high thermoelectric performance and carrier effective mass. The carrier effective mass is proportional to the Seebeck coefficient. However, typically, a higher carrier effective mass

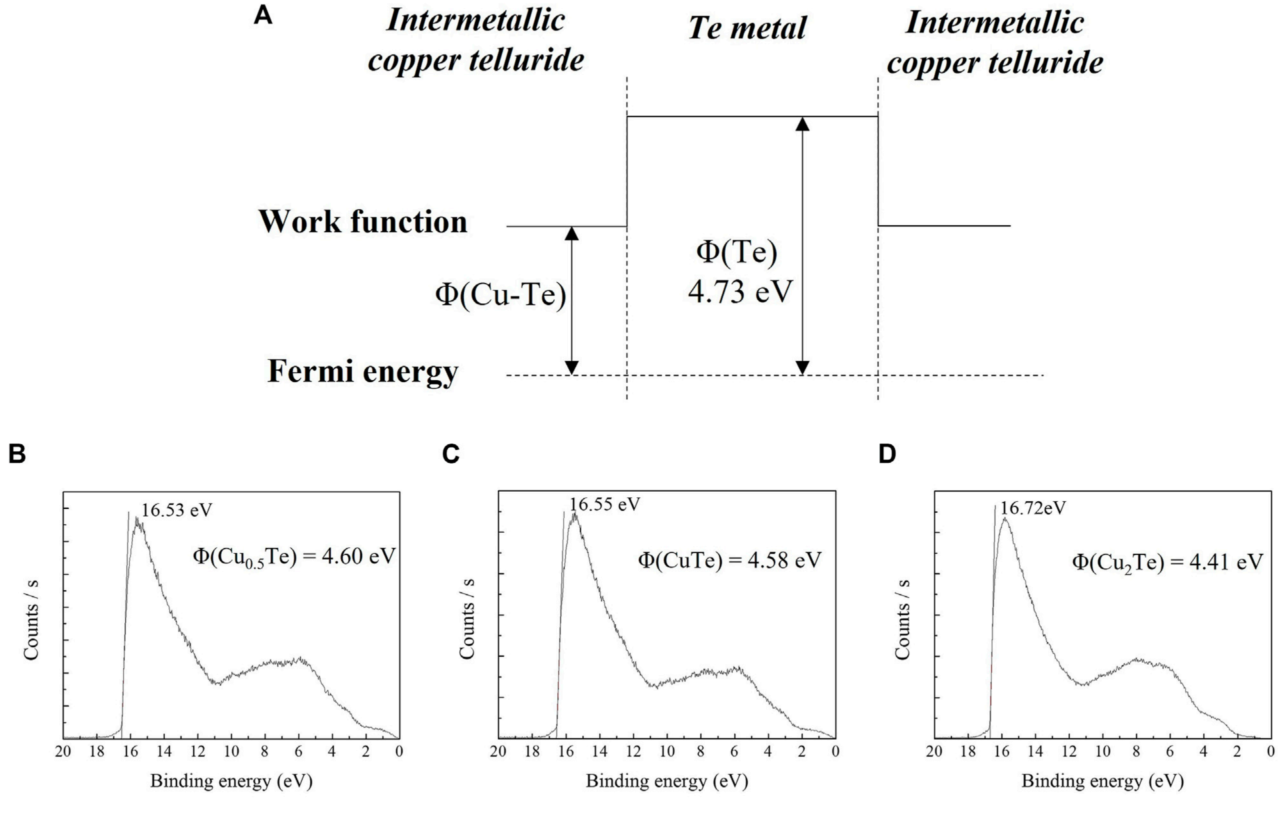

FIGURE 7 | (A) Potential well scheme at the interface between the intermetallic copper telluride and Te metal phases. UPS spectra acquired for calculating the work functions of: **(B)** $Cu_{0.5}Te$, **(C)** CuTe, and **(D)** Cu_2Te.

implies a lower conductivity of the material. To achieve high-performance thermoelectrics, increasing the carrier effective mass without degrading the conductivity of the material is essential. The carrier effective mass is expressed as $m^* = N_v^{2/3} m_b^*$, where N_v includes the orbital degeneracy and m_b^* is the average carrier effective mass for single-band valley degeneration. Thus, the carrier effective mass can be increased by introducing a band offset in the material without lowering the conductivity of the material (Pei et al., 2011). The potential difference between the Te metal and intermetallic CuTe was determined by UPS. **Figures 7B–D** show UPS spectra for intermetallic $Cu_{0.5}Te$, CuTe, and Cu_2Te, respectively, with the work functions of the various copper tellurides calculated using the equation:

$$\Phi = h\nu - E_{cutoff} \tag{3}$$

where Φ is the work function of the material, ν is the frequency of the He beam, and E_{cutoff} is the secondary electron cut-off energy of the material. The work functions of the copper tellurides were determined to be 4.60 eV ($Cu_{0.5}Te$), 4.58 eV (CuTe), and 4.41 eV (Cu_2Te). As the work function of Te metal is 4.73 eV (Michaelson, 1950), the potential differences between the two phases are 0.13, 0.15, and 0.32 eV, respectively. The band offset between the copper telluride and Te metal increases the Seebeck coefficient without sacrificing the conductivity of the thin film owing to carrier filtering. The CuTe thin film sample exhibits a particularly high-power factor due to Te precipitation inside the thin film, which results carrier-energy filtering.

CONCLUSION

In this study, stoichiometric intermetallic copper telluride thin films were successfully electrodeposited in aqueous solutions prepared using $Cu(NO_3)_2{\cdot}3H_2O$, TeO_2, and HNO_3. CV was used to determine appropriate electrodeposition potentials in a three-electrode system, while the thin film deposited in each bath was analyzed by SEM, EDS, and XRD. The electrodeposited thin films were exfoliated from the substrate and mounted on epoxy resin, and their electrical and thermoelectrical properties were examined using Hall-effect and thermoelectric measurements. Thin films deposited in baths at different potentials showed compositions and structures that affect their electrical and thermoelectric properties. The thin film with Cu/Te = 2 contains crystalline intermetallic Cu_2Te, while that with Cu/Te = 1 contains crystalline intermetallic CuTe and Te. In contrast, the thin film with Cu/Te = 0.5 exhibited a broad XRD pattern that corresponds to intermetallic Cu_7Te_5 and Te metal, suggestive of a nanocrystalline structure and the coexistence of Te metal. XPS also revealed the coexistence of Te metal in the film, with Te^0 peaks observed for thin films with Cu/Te ratios of 1 and 0.5. In other words, the coexistence of these two phases creates a band offset that improves thermoelectric properties by increasing the Seebeck coefficient of the thin film without sacrificing its conductivity. The band offset resulted in CuTe exhibiting the highest power factor of 7.71 $\mu W\, cm^{-1}\, K^{-1}$, with the potential difference between intermetallic CuTe and Te metal determined to be 0.15 eV by UPS.

DATA AVAILABILITY STATEMENT

The original contributions presented in the study are included in the article/supplementary material, further inquiries can be directed to the corresponding authors.

AUTHOR CONTRIBUTIONS

The concept for this study was designed by all authors. J-HL, BY and JP designed the experiment. JP performed all experiments. JP and JL analyzed and interpreted the data. All authors helped to write and revise the manuscript.

FUNDING

This research was supported by the Technology Innovation Program (20005011, Development of materials and process technology for highly luminance micro display with 2000 PPI resolution) funded By the Ministry of Trade, Industry and Energy (MOTIE, Korea) and the Basic Science Research Program through the National Research Foundation of Korea (NRF) funded by the Ministry of Science, ICT and Future Planning (No. 2015R1A5A1037548). This work was also supported by the Global Frontier Program through the Global Frontier Hybrid Interface Materials (GFHIM) project (grant number 2013M3A6B1078870).

REFERENCES

Bhuvaneswari, P. V., Ramamurthi, K., and Ramesh Babu, R. (2017). Influence of Substrate Temperature on the Structural, Morphological, Optical and Electrical Properties of Copper Telluride Thin Films Prepared by Electron Beam Evaporation Method. *Thin Solid Films* 632, 44–49. doi:10.1016/j.tsf.2017.04.035

Chen, H., and Wang, L. (Editors)(2017). “Posttreatment Strategies for Biomass Conversion,” in *Technologies for Biochemical Conversion of Biomass, Academic Press*, 197–217. doi:10.1016/b978-0-12-802417-1.00008-9

Cho, G., Park, Y., Hong, Y.-K., and Ha, D.-H. (2019). Ion Exchange: An Advanced Synthetic Method for Complex Nanoparticles. *Nano Convergence* 6, 1–17. doi:10.1186/s40580-019-0187-0

Dhasade, S. S., Han, S. H., and Fulari, V. J. (2012). A Nanostructured Copper Telluride Thin Film Grown at Room Temperature by an Electrodeposition Method. *J. Semicond.* 33, 093002. doi:10.1088/1674-4926/33/9/093002

Dorfs, D., Härtling, T., Miszta, K., Bigall, N. C., Kim, M. R., Genovese, A., et al. (2011). Reversible Tunability of the Near-Infrared Valence Band Plasmon Resonance in Cu2-xSe Nanocrystals. *J. Am. Chem. Soc.* 133, 11175–11180. doi:10.1021/ja2016284

Eliaz, N., Sridhar, T. M., and Gileadi, E. (2005). Synthesis and Characterization of Nickel Tungsten Alloys by Electrodeposition. *Electrochimica Acta* 50, 2893–2904. doi:10.1016/j.electacta.2004.11.038

Ghosh, A., Mitra, M., Banerjee, D., and Mondal, A. (2016). Facile Electrochemical Deposition of Cu7Te4 Thin Films with Visible-Light Driven Photocatalytic

Activity and Thermoelectric Performance. *RSC Adv.* 6, 22803–22811. doi:10.1039/C6RA00345A

Han, C., Li, Z., Li, W.-j., Chou, S.-l., and Dou, S.-x. (2014). Controlled Synthesis of Copper Telluride Nanostructures for Long-Cycling Anodes in Lithium Ion Batteries. *J. Mater. Chem. A.* 2, 11683–11690. doi:10.1039/C4TA01579G

He, Y., Zhang, T., Shi, X., Wei, S.-H., and Chen, L. (2015). High Thermoelectric Performance in Copper Telluride. *NPG Asia Mater.* 7, e210. doi:10.1038/am.2015.91

Kim, D., Park, K., Lee, S., and Yoo, B. (2016). Electrochemical Synthesis of ZnTe Thin Films from Citrate Bath and Their Electrical Properties with Incorporation of Cu. *Mater. Chem. Phys.* 179, 10–16. doi:10.1016/j.matchemphys.2016.04.046

Kriegel, I., Jiang, C., Rodríguez-Fernández, J., Schaller, R. D., Talapin, D. V., da Como, E., et al. (2012). Tuning the Excitonic and Plasmonic Properties of Copper Chalcogenide Nanocrystals. *J. Am. Chem. Soc.* 134, 1583–1590. doi:10.1021/ja207798q

Kriegel, I., Rodríguez-Fernández, J., Wisnet, A., Zhang, H., Waurisch, C., Eychmüller, A., et al. (2013). Shedding Light on Vacancy-Doped Copper Chalcogenides: Shape-Controlled Synthesis, Optical Properties, and Modeling of Copper Telluride Nanocrystals with Near-Infrared Plasmon Resonances. *ACS Nano* 7, 4367–4377. doi:10.1021/nn400894d

Luther, J. M., Jain, P. K., Ewers, T., and Alivisatos, A. P. (2011). Localized Surface Plasmon Resonances Arising from Free Carriers in Doped Quantum Dots. *Nat. Mater* 10, 361–366. doi:10.1038/nmat3004

Mansour, B., Mukhtar, F., and Barakati, G. G. (1986). Electrical and Thermoelectric Properties of Copper Tellurides. *Phys. Stat. Sol. (A)* 95 (2), 703–707. doi:10.1002/pssa.2210950240

Michaelson, H. B. (1950). Work Functions of the Elements. *J. Appl. Phys.* 21, 536–540. doi:10.1063/1.1699702

Mukherjee, S., Chetty, R., Madduri, P. V. P., Nayak, A. K., Wojciechowski, K., Ghosh, T., et al. (2019). Investigation on the Structure and Thermoelectric Properties of CuxTe Binary Compounds. *Dalton Trans.* 48, 1040–1050. doi:10.1039/C8DT04351E

Mukherjee, S., Parasuraman, R., Umarji, A. M., Rogl, G., Rogl, P., and Chattopadhyay, K. (2020). Effect of Fe Alloying on the Thermoelectric Performance of Cu2Te. *J. Alloys Comp.* 817, 152729. doi:10.1016/j.jallcom.2019.152729

Nethravathi, C., Rajamathi, C. R., Rajamathi, M., Maki, R., Mori, T., Golberg, D., et al. (2014). Synthesis and Thermoelectric Behaviour of Copper Telluride Nanosheets. *J. Mater. Chem. A.* 2, 985–990. doi:10.1039/C3TA12877F

Pei, Y., Shi, X., LaLonde, A., Wang, H., Chen, L., and Snyder, G. J. (2011). Convergence of Electronic Bands for High Performance Bulk Thermoelectrics. *Nature* 473, 66–69. doi:10.1038/nature09996

Rudnik, E., and Kozłowski, J. (2013). Electrochemical Studies on the Codeposition of Copper and Tellurium from Acidic Nitrate Solution. *Electrochimica Acta* 107, 103–110. doi:10.1016/j.electacta.2013.05.131

Saha, S., Johnson, M., Altayaran, F., Wang, Y., Wang, D., and Zhang, Q. (2020). Electrodeposition Fabrication of Chalcogenide Thin Films for Photovoltaic Applications. *Electrochem* 1, 286–321. doi:10.3390/electrochem1030019

Sorenson, T. A., Varazo, K., Suggs, D. W., and Stickney, J. L. (2001). Formation of and Phase Transitions in Electrodeposited Tellurium Atomic Layers on Au(111). *Surf. Sci.* 470, 197–214. doi:10.1016/S0039-6028(00)00861-X

Zhang, L., Ai, Z., Jia, F., Liu, L., Hu, X., and Yu, J. C. (2006). Controlled Hydrothermal Synthesis and Growth Mechanism of Various Nanostructured Films of Copper and Silver Tellurides. *Chem. Eur. J.* 12, 4185–4190. doi:10.1002/chem.200501404

Zhang, Y., Liu, Y., Calcabrini, M., Xing, C., Han, X., Arbiol, J., et al. (2020). Bismuth telluride-copper telluride Nanocomposites from Heterostructured Building Blocks. *J. Mater. Chem. C* 8, 14092–14099. doi:10.1039/D0TC02182B

Zhang, Y., Ni, Y., Wang, X., Xia, J., and Hong, J. (2011). Polycrystalline Cu7Te4 Dendritic Microstructures Constructed by Spherical Nanoparticles: Fast Electrodeposition, Influencing Factors, and the Shape Evolution. *Cryst. Growth Des.* 11, 4368–4377. doi:10.1021/cg200391d

Zhang, Y., Wang, Y., Zhang, J., Xi, L., Zhang, P., and Zhang, W. (2016). Pinning Down High-Performance Cu-Chalcogenides as Thin-Film Solar Cell Absorbers: A Successive Screening Approach. *J. Chem. Phys.* 144, 194706. doi:10.1063/1.4950818

Conflict of Interest: The authors declare that the research was conducted in the absence of any commercial or financial relationships that could be construed as a potential conflict of interest.

frontiers in Chemistry

ORIGINAL RESEARCH
published: 26 January 2022
doi: 10.3389/fchem.2021.791155

Enhanced Thermoelectric Properties of Composites Prepared With Poly(3,4-Ethylenedioxythiophene) Poly(Styrenesulfonate) and Vertically Aligned Se Wire

In Yea Kim[1], *Dong Won Chun*[2], *Sang-Il Kim*[3] *and Jae-Hong Lim*[1]*

[1]*Department of Materials Science and Engineering, Gachon University, Seongnam, South Korea,* [2]*Center for Energy Materials Research, Korea Institute of Science and Technology, Seoul, South Korea,* [3]*Department of Materials Science and Engineering, University of Seoul, Seoul, South Korea*

Controlling the electronic transport behavior in thermoelectric composites is one of the most promising approaches to enhance their power factor because this enables decoupling of the correlation between the electrical conductivity and Seebeck coefficient. Herein, we show that the unexpected high power factor of the Se nanowire array embedded in poly(3,4-ethylenedioxythiophene)-poly(styrenesulfonate) (PEDOT:PSS) can be achieved by controlling the interfacial band structure engineering. The electrical conductivity and Seebeck coefficient simultaneously increased, confirming that the synthesis of organic/inorganic hybrid thermoelectric materials with improved performance was possible. Our exploration can be helpful for the rational design of high-performance thermoelectric composites through interface engineering.

Keywords: thermoelectric, Se wires array, PEDOT:PSS, galvanic displacement, carrier scattering

Edited by:
Elizabeth J. Podlaha,
Clarkson University, United States

Reviewed by:
Hong Wang,
Xi'an Jiaotong University, China
Mohammadsadegh Beheshti,
Louisiana State University,
United States

Correspondence:
Jae-Hong Lim
limjh@gachon.ac.kr

Specialty section:
This article was submitted to
Electrochemistry,
a section of the journal
Frontiers in Chemistry

Received: *08 October 2021*
Accepted: *15 December 2021*
Published: *26 January 2022*

Citation:
Kim IY, Chun DW,
Kim S-I and Lim J-H (2022) Enhanced
Thermoelectric Properties of
Composites Prepared With Poly(3,4-
Ethylenedioxythiophene)
Poly(Styrenesulfonate) and Vertically
Aligned Se Wire.
Front. Chem. 9:791155.
doi: 10.3389/fchem.2021.791155

INTRODUCTION

Considering the expansion of thermoelectric (TE) materials to future energy and electronic devices, functional aspects (e.g., flexibility, transparency, and lightweight) need to be improved to widen their applicability (William and Wong, 2009; Reuss et al., 2015; Oh et al., 2016; Varghese et al., 2016; Ou et al., 2018). Organic TE materials have the potential for application in low-temperature energy harvesting systems and wearable (or flexible) heating and cooling devices (Yue and Xu, 2012; Wang and Yu, 2019). Recently, desirable results regarding the electronic transport properties of poly(3,4-ethylenedioxythiophene) (PEDOT)-based materials (Park et al., 2012; Kang et al., 2016; Kang and Snyder, 2017), such as the high TE performance of PEDOT:poly(styrenesulfonate) (PSS) and PEDOT:poly(3,4-ethylenedioxythiophene)-tosylate), have been demonstrated by engineering the degree of conformation at the molecular level (Bubnova et al., 2011; Kim et al., 2013; Noriega et al., 2013; Cho et al., 2014). An enhanced TE figure of merit ($zT = S^2\sigma T/\kappa$, where S, σ, and κ, are the Seebeck coefficient, electrical conductivity, and total thermal conductivity at a given absolute temperature T, respectively) of 0.42 was achieved at 300 K by mixing dimethyl sulfoxide with commercial PEDOT:PSS (Kim et al., 2013)[13]; however, it remains unsatisfactory for commercial applications. The limited zT values in PEDOT-based organic TE materials are mainly due to their poor electronic transport properties, which results in a low power factor (σS^2) despite their highly desirable low κ values (e.g., κ ~0.2 $Wm^{-1} K^{-1}$ for PEDOT:PSS).

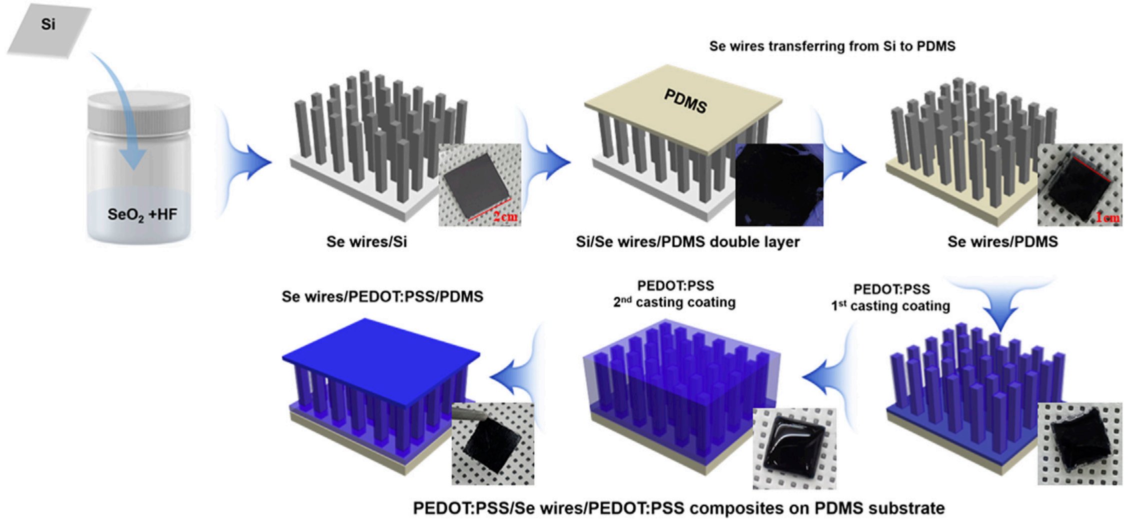

FIGURE 1 | Scheme of the synthesis of the Se wire and poly(3,4-ethylenedioxythiophene)-poly(styrenesulfonate) (PEDOT:PSS) composite.

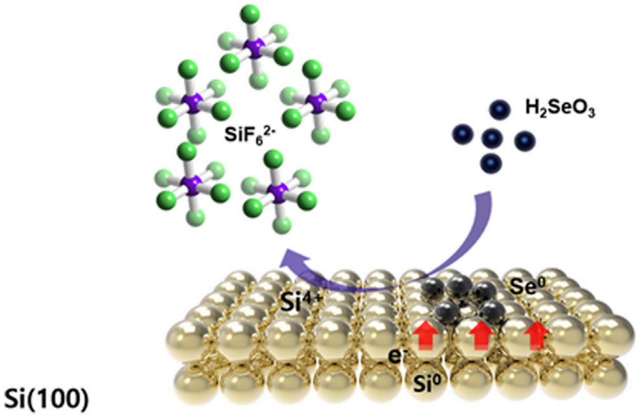

FIGURE 2 | Schematic representation of the synthesis of the Se nanowires by the galvanic displacement reaction of the Si wafer.

A nanocomposite approach by embedding nanoscale conductive fillers into the PEDOT-based matrix has been carried out to increase the σ (Du et al., 2012; Wang et al., 2012; Coates et al., 2013; Ju and Kim, 2016); however, improving the power factor is still challenging owing to the strong correlation between σ and S. For example, graphene was introduced and a high σ was obtained because of the aligned PEDOT:PSS chains along the graphene; however, S remained at the intrinsic level (Kim et al., 2012). A hybrid of inorganic compounds with a large S and highly conductive organic materials is a potential approach for achieving the theoretical maximum power factor because the independent control of σ and S becomes possible based on the parallel and series models in the composites. Additionally, the generation of a phase boundary between the organic TE matrix and inorganic compounds can trigger the improvement in S benefitting from a carrier filtering effect. This is because S is related to the energy derivative of the electronic density-of-states (DOS) and the carrier relaxation time through the Mott relationship (See et al., 2010; Yee et al., 2013; Du et al., 2014; Peng et al., 2016). However, there has been no experimental evidence for decoupling the correlation between σ and S, even in organic TE composites with well-controlled inorganic nanophases.

In the study by Roh et al. (2017), the inorganic $Ge_2Sb_2Te_5$ (GST) was arranged into a nanowire, and its performance was evaluated by fabricating a composite with PEDOT:PSS. Since this study produced aligned GST through the nanopattern printing method, the height of the GST nanowire was at the nanoscale. Nevertheless, it was confirmed that the decoupling phenomenon of this material increases the S, even though σ increases. This establishes that a well-arrayed structure can obtain an improved zT. However, its nanoscale length of the wire limits its performance improvement.

Various methods have been used to synthesize nanophase inorganic TEs, for example, methods using microwaves (Wang et al., 2017), the hydrothermal synthesis method (Li et al., 2019), and the electrochemical method (Recatala-Gomez et al., 2020). Among these methods, the galvanic displacement reaction (GDR) offers several advantages, including low synthesis cost and easy reaction conditions (Xin et al., 2021). This method is an electrochemical process driven by the redox potential difference between the sacrificial material and solution reacting ions.

In this study, a wire of length at the microscale was formed through the GDR. It is easier to control the length of the wire to increase the height of the inorganic materials *via* this method as compared to the nanoprinting method. In addition, a high S of $\geq$1,000 μV/K at room temperature is desired; therefore, the most attractive material, Se, is used (Kim et al., 2019). However, to use Se as a high-performance TE material, it is necessary to improve its σ, which can be achieved by forming a composite structure with the organic PEDOT:PSS.

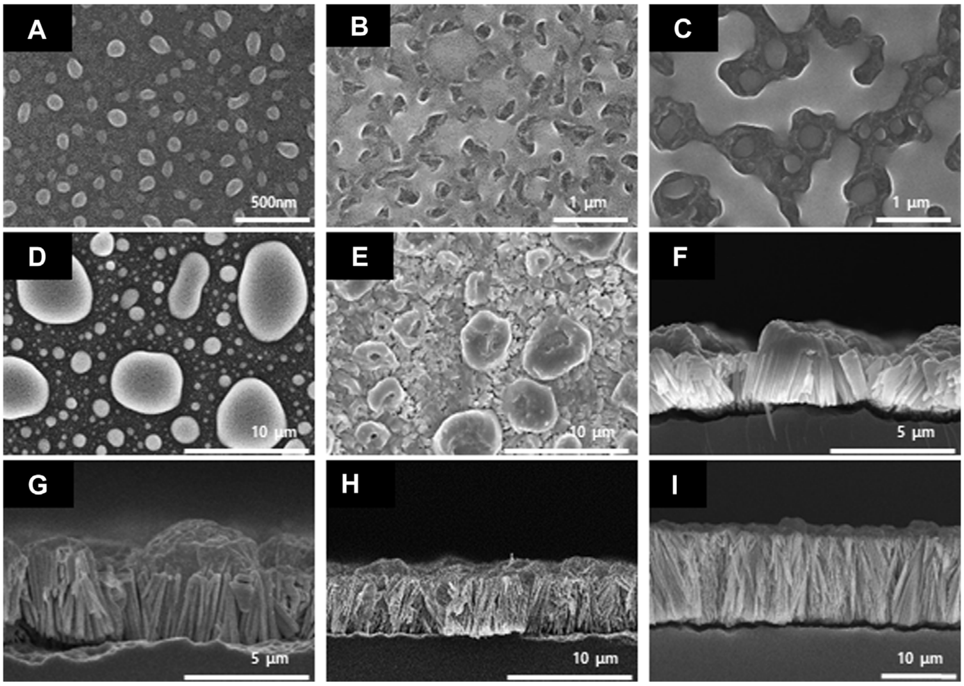

FIGURE 3 | Scanning electron microscopy images of the Se nanowires synthesized by the galvanic displacement reaction at different reaction times. Top-view **(A)** 5 min, **(B)** 30 min, **(C)** 1 h, **(D)** 3 h, and **(E)** 6 h; cross-section **(F)** 6 h, **(G)** 9 h, **(H)** 12 h, and **(I)** 24 h.

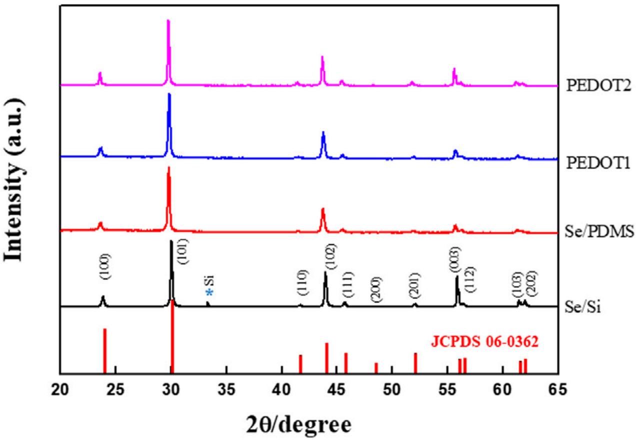

FIGURE 4 | X-ray diffraction pattern of the Se nanowire structure and Se nanowire:PEDOT. The structure change according to the PSS complex process is confirmed.

MATERIALS AND METHODS

Formation of Se Wire Array

The Se wires were formed on a silicon wafer (2 × 2 cm) using GDR. The wafer used in this work was *p*-type, boron-doped, (100)-oriented silicon. The silicon wafer was cleaned with acetone and ethanol. The solution used for the Se deposition is a combination of two chemicals: hydrofluoric acid (HF, J.T Baker, United States) and a saturated solution of selenium oxide (SeO_2, Sigma Aldrich, United States). The Se nanowire growth was processed in a Teflon vessel for 24 h at 70°C. After completion of the GDR, the synthesized Se wires were carefully rinsed several times with deionized water and ethanol. The Se wire was then dried in a desiccator for 1 day. The prepared wires were transferred to polydimethylsiloxane (PDMS, Sylgard® 184). The PDMS was prepared as a film and hardened at 25°C for 18 h. The silicon wafer on which the Se wires are grown was then placed on top of the prepared PDMS film and pressed with weak pressure. Throughout this process, Se wires were transferred to the PDMS film surface.

Formation of Se Wire and PEDOT:PSS Composition

The effect of doping ethylene glycol (EG, Samchun, Korea) on the TE properties of PEDOT:PSS was determined. According to the volume ratio, 2%, 4%, 6%, 8%, and 10% of EG was added to the PEDOT:PSS solution (Clevios™ PH1000) contained in each vial bottle. Then, the mixed solution of PEDOT:PSS/EG was applied to the Se wire array on the PDMS surface by drop-casting. The Se wire array applied with the PEDOT:PSS/EG mixed solution was dried in a vacuum oven at 40°C for 16 h. In addition, PEDOT:PSS was applied twice to increase the contact between the Se wire and PEDOT:PSS. The process of synthesizing the Se wire and the PEDOT:PSS composite is schematically illustrated in **Figure 1**.

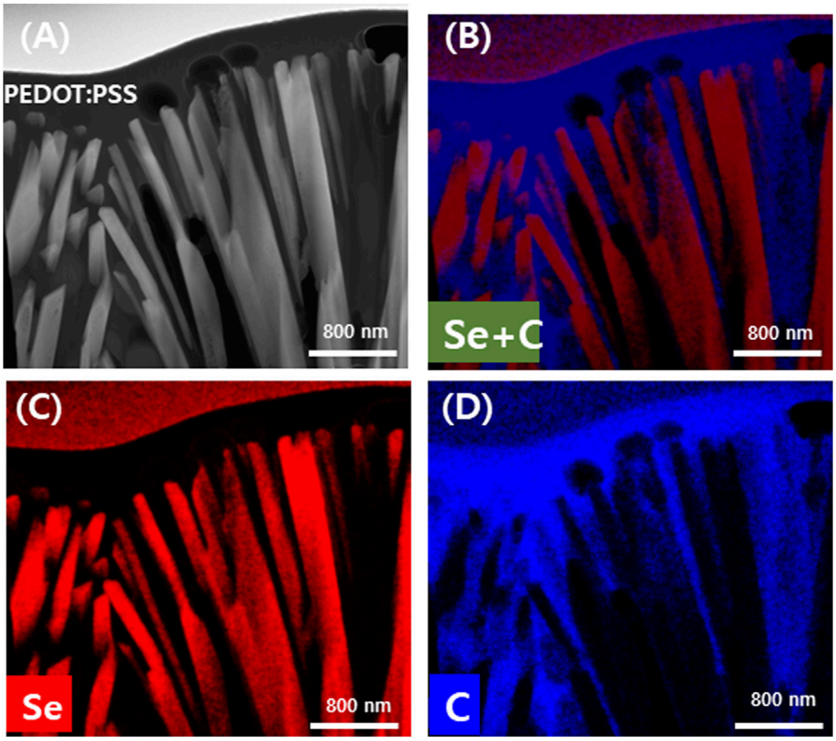

FIGURE 5 | Transmission electron microscopy energy dispersive spectroscopy analysis of the Se nanowires:PEDOT:PSS composite coated twice with PEDOT: PSS. TEM image **(A)** and mapping image according to element **(B)** Se and C **(C)** Se and **(D)** C.

Characterization of Prepared Se Wire and PEDOT:PSS

The Se wire array grown *via* the GDR was observed using scanning electron microscopy (SEM, Hitachi S-4200) and scanning transmission electron microscopy energy dispersive spectroscopy (STEM-EDS, Talos F200X, FE, US) at an accelerating voltage of 200 kV (Schottky X-FEG gun) equipped with a Super-X EDS system comprising four windowless silicon drift detectors (SDDs) in the STEM mode with a probe current of ~0.7 nA. The Se wire and composite structure were measured at 20°–65° (2θ) by X-ray diffraction (XRD, Ultima IV). The chemical state of the synthesized Se wire and the compound according to the PEDOT: PSS application was confirmed using X-ray photoelectron spectrometry (XPS, AXIS-NOVA, Kratos Inc.). To measure the work function, ultraviolet photoelectron spectroscopy (UPS, Thermo Fisher Scientific, NEXSA) was used. Conductivity of the synthesized Se wire/PEDOT:PSS composite was measured on a Keithley 2400 Electrometer using the four-point probe technique. The Seebeck coefficient was measured using Seebeck apparatus built in-house. Three samples were analyzed under each condition, and each measurement was repeated five times.

RESULTS AND DISCUSSION

Se wires were synthesized on a silicon substrate by immersing the Si substrate in a mixed solution consisting of 2 mM SeO_2 and 4.5 M HF at 70°C. The mobility of GDR is caused by the difference in the redox potential between the solid material and the ionic solution used. This technology uses primitive electrochemical phenomena that form the basis of a battery (Kakati et al., 2017)[30]. When a silicon substrate is immersed in an acidic fluoride solution containing only SeO_3^{2-}, the silicon atoms on the substrate are galvanically substituted by SeO_3^{2-} because of the difference in the redox potential of $SiF_6{}^{2-}/Si^0$ ($E^0 = -1.24$ V vs. NHE) and $HSeO_3/Se$ ($E^0 = 0.74$ V vs. NHE), described in the following equations (Jeong et al., 2013; Majidzade et al., 2018; Saha et al., 2020; Tran et al., 2020):

$$Si^0\,(S) + 6F^- \rightarrow SiF_6^{2-}\,(aq) + 4e^-\; E^0 = -1.24 \text{ vs. NHE} \qquad (1)$$

$$H_2SeO_3\,(aq) + 4H^+\,(aq) + 4e^- \rightarrow Se^0\,(s) + 3H_2O\, E^0 = 0.74 \text{ vs.NHE} \qquad (2)$$

During the GDR of Si, positive and negative reactions simultaneously occur on the Si surface as charges are exchanged through the substrate. The fluorine ions in the solution corrode and dissolve the Si substrate in the form of silicon hexafluoride, preventing the formation of passive silicon oxide and helping to maintain the reaction by constantly exposing the new Si surface (**Figure 2**).

As shown in **Figure 3**, it was confirmed that the nanowires formed by the nucleation and growth mechanisms (Hwang et al., 2019). Furthermore, we were able to determine the optimum reaction time required for the growth of the Se wire through the GDR method on the Si wafer surface. **Figure 3A–E** demonstrates

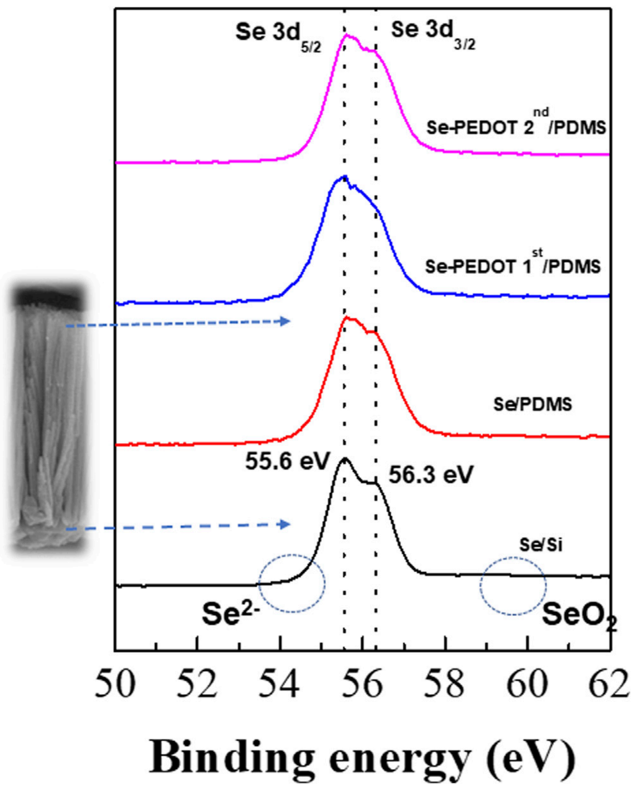

FIGURE 6 | X-ray photoelectron spectra of Se $3d_{5/2}$ BE and Se $3d_{3/2}$ of the Se wire:PEDOT:PSS composite.

the initial process of the Se wire formation; the SEM image is shown in the top view. At the initial stage, the 3D Se nuclei were formed on the Si wafer surface (**Figure 3A**). The mechanism by which this nucleus grows can be described as the Volmer–Weber nucleation and growth mechanism (Choi and Choi, 2013). Initially, the size of the nucleus was 100 nm; as the GDR reaction time increased, the nuclei formed on the surface grew, transforming into an island shape. Then, the grown island-shaped Se coalesced with the adjacent island-shaped Se and completely covered the Si wafer surface in the form of a film (**Figure 3E**). When the Si surface was completely covered, the reaction was completed on the upper surface. Thus, the reaction between the Si wafer and $HSeO_3^-$ and the growth of the Se wire required more than 6 h. To analyze the length of the Se wire grown *via* the GDR, a cross-section of the sample was obtained after 6 h (**Figure 3F**); it is apparent that the growth of the wire starts under the Se island. The Se wire grows vertically in the downward direction because a redox potential reaction occurs through Si etching by HF contained in the synthesis solution; however, the upper part of the Si wafer, where the Se thin film is formed, is not etched by HF. Nevertheless, Si is present under the Se thin film, the galvanic reaction occurs because of the etching, and the Se wire starts to grow in a vertical direction (Gadea et al., 2015). The Se wire produced by the 6-h reaction grew to a length of 2.11 μm randomly. However, after 9 h, the Se wire constantly grew in a vertical direction at a growth rate of 390 nm/h.

A composite with PEDOT:PSS with high σ and low κ was fabricated to improve the TE performance of the Se wire grown by the GDR method. The structure and elemental state of the Se wire and Se wire/PEDOT:PSS were analyzed using XRD and XPS. First, the Se wires were prepared on the Si wafer surface using the GDR method. All reflections of the prepared selenium nanowires are consistent with those of selenium (JCPDS card number 06-0362) (curve a in **Figure 4**). In addition, the structure of the Se wire, which was transferred to the PDMS, was maintained, and the structural characteristics of the Se wire/PEDOT:PSS composite were confirmed to have similar diffraction patterns to the Se wire. This implies that the composite did not undergo phase separation or change in its crystal structure. However, the reason for the high intensity of (003) in Se/Si is that the Se/Si XRD (003) peak intensity is stronger than other results because of the Se grain size (Lu et al., 1997; Cheng and Samulski, 2003). The reason for the change in the size of the grains is outlined in **Figure 3**, as the Se nano wire growth direction proceeds downward. Therefore, as the initial Se growth starts from the

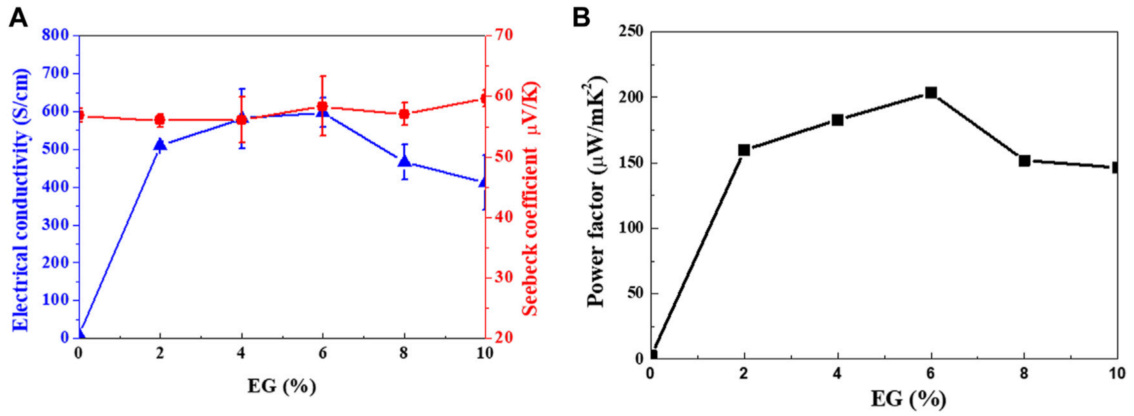

FIGURE 7 | (A) Seebeck coefficient and electrical conductivity, and **(B)** power factor of the Se wire/PEDOT:PSS composite as functions of ethylene glycol (EG) doping concentrations.

TABLE 1 | Comparison of the characteristics properties of organic/inorganic composite thermoelectric.

Materials	Methods	σ (S/cm)	S (μV/K)	PF (μW/mK^2)	Ref
SiC/PEDOT:PSS	Dilution–filtration and post-treatment	3,113	20.3	128.3	Wang et al. (2018)
Cu_2Se/PEDOT:PSS	Wet chemical process	1,047	50.8	270.3	Lu et al. (2019)
Bi_2Te_3/PEDOT:PSS	Hydrothermal and physical mixing methods	1,295	15.8	32.3	Cu et al. (2014)
Te nanowire/PEDOT:PSS	Wet chemical process	11	170	35	Coates et al. (2013)
Se nanowire/PEDOT:PSS	Galvanic displacement	596.76	58.3	203.29	This work

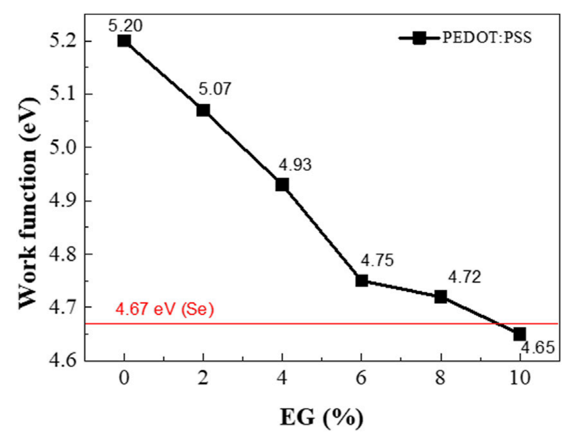

FIGURE 8 | Work function of the Se wire:PEDOT:PSS composite as a function of the EG doping concentration.

surface, the grain size is large, hence we were able to obtain this result. In addition, X-ray penetration is difficult owing to the PEDOT:PSS applied to the Se wire surface and transferred to the PDMS.

The location of the Se wire and PEDOT:PSS of the manufactured Se wire/composite was confirmed using STEM-EDS. **Figure 5A–D** shows the STEM and STEM-EDS mapping images of Si wire/PEDOT:PSS. It was revealed that the vertically aligned Se wires were covered by PEDOT:PSS. **Figure 5A** is a STEM image of a Se wire/PEDOT:PSS composite in which the Se wire and PEDOT:PSS are clearly distinguished. The obtained TEM image was confirmed to be consistent with the images shown in **Figure 3I**. To clearly distinguish the area identified in the TEM image, specific elements were identified *via* EDS mapping. **Figure 5C** coincides with the nanowire area composed of Se, and Figure 5D shows the element constituting PEDOT:PSS, which coincides with PEDOT:PSS in **Figure 5A**. **Figure 5B** corresponds with the identified Se and C *via* EDS mapping. Additionally, this result can be calculated as the area ratio of the Se wire and PEDOT:PSS. This confirmed that the Se wire and PEDOT:PSS area ratio was 54.57% and 45.43%, respectively. It was clarified that the Se wire surface was sufficiently coated and filled with PEDOT:PSS.

The interfacial reaction between the Se wires and PEDOT:PSS can be discussed using the XPS spectra of the Se wire/PEDOT:PSS composite according to the first and second applications of PEDOT:PSS (**Figure 6**). The $3d_{3/2}$ and $3d_{5/2}$ binding energies of pure Se appear at 56.3 and 55.4 eV, respectively, and the oxidized Se, Se^{2-} (54.6 eV) or SeO_2 (59.2 eV), are also observed (Jang et al., 2018). The binding energies of the synthesized Se wire are in the Se_0 state because $3d_{3/2}$ and $3d_{5/2}$ are identified at 55.6 and 56.3 eV, respectively. In addition, no other binding energy was identified as PEDOT:PSS. These results confirm that no oxidation occurred upon applying PEDOT:PSS; therefore, Se remained pure.

The above results also confirmed the viability of synthesizing Se nanowires and Se wire/PEDOT:PSS composites. However, the chain structure of PEDOT:PSS is released as the EG doping content increases (Lee et al., 2016; Roh et al., 2017). This change in the PEDOT:PSS chain structure shows a difference in filling between the Se wires upon application. Therefore, the electrical properties of PEDOT:PSS can be tuned using EG.

Figure 7 shows the TE properties (S, σ, and power factor) of the Se wire/PEDOT:PSS composite with different EG doping concentrations measured at 22°C–25°C. At 0% EG, the σ was as low as 8.03 S/cm and significantly increased to 509, 581, and 597 S/cm at 2%, 4%, and 6%, respectively. Further increasing the amount of EG gradually decreased the σ to 466 S/cm (8%) and 411 S/cm (10%). The increase in σ with increasing EG content in PEDOT:PSS (Lim, 2013) has been previously reported. On the other hand, the S of the Se wire/PEDOT:PSS composite remains relatively stable between 54 and 60 μV/K. However, a slight increase is observed at higher EG content; a maximum value of 59.61 μV/K at 10% EG and a minimum of 53.86 μV/K at 4% EG is observed. Furthermore, the power factor increased with EG doping (**Figure 7B**). At 2% EG, it increased by 61 times compared to that at 0% EG. A maximum power factor value (203.29 μW/mK^2) was observed at 6% EG for the PEDOT:PSS and Se wire because of the corresponding maximum electrical conductivity and unchanged S. **Table 1** contains a summary of the properties of representative organic/inorganic composite thermoelectric. As indicated in **Table 1**, the prepared thermoelectric material achieves an enhancive thermoelectrical performance compared to the other samples, which is only lower than Cu_2Se/PEDOT:PSS. However, the Cu_2Se/PEDOT:PSS composite was synthesized through complex processes, including long chemical reaction time, hard washing, filtration process, and cold-press process sequentially.

The effect of EG doping on the TE transport properties of the Se wire/PEDOT:PSS composite can be summarized as the following: 1) Compared to the undoped composite, at 2% EG, the σ significantly increased by more than 60 times, while the S remained the same. 2) As the amount of doped EG increased to

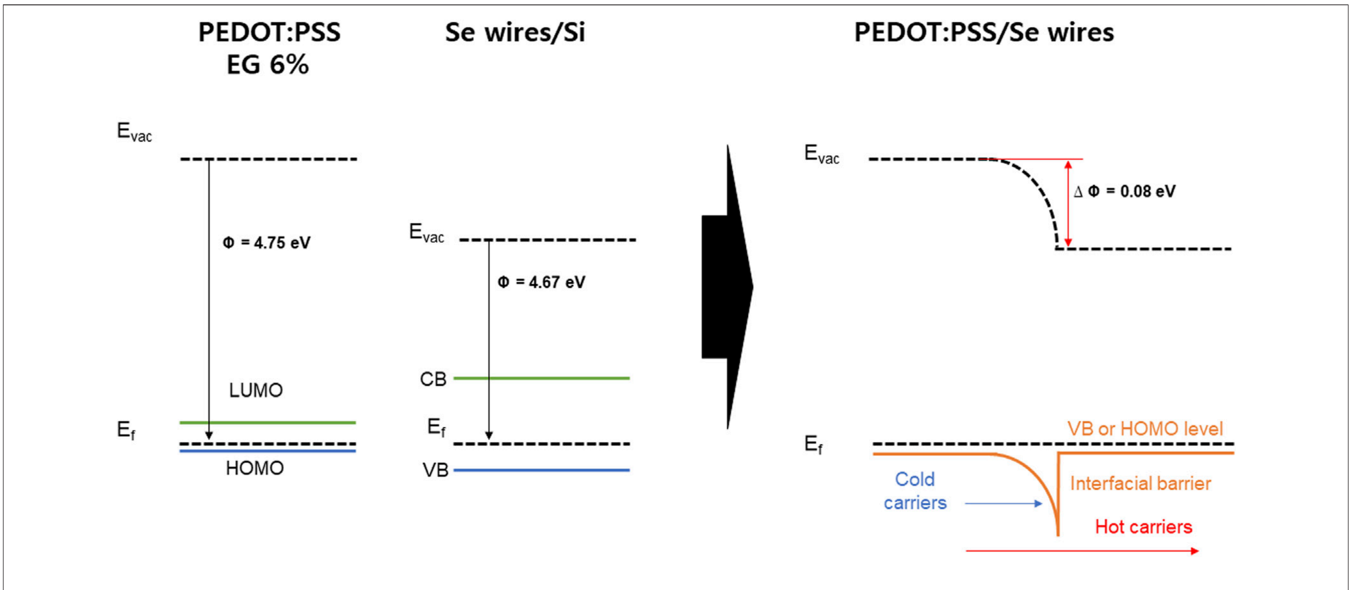

FIGURE 9 | Energy diagram of the PEDOT:PSS and Se wires/Si and energy filtering effects at PEDOT:PSS/Se wires junctions.

6%, σ and S simultaneously increased. 3) Above 6% EG, the S increased, while σ decreased.

In general, when S increases, σ tends to decrease; these characteristics can be correlated with the following equation:

$$S = \frac{8\pi^2 k_B^2}{3eh^2} m^* T \left(\frac{\pi}{3n}\right)^{\frac{2}{3}} \tag{3}$$

In addition, the σ is expressed as follows:

$$\sigma = ne\mu \tag{4}$$

where k_B is the Boltzmann constant, h is the Planck constant, m^* is the effective mass, and n and μ are the concentration and mobility of electrons, respectively. It can be seen that S is inversely proportional to n in **Eq. 3**. However, for 2%–6% EG (**Figure 7A**), a simultaneous increase in σ and S was observed. This may be due to the carrier energy filtering effect between the organic and inorganic TE materials. Carrier energy filtering restricts unnecessary carrier movement by removing cold carriers with low carrier energy because of the difference in work function between the organic and inorganic materials; thus, even if σ increases, S cannot decrease. To confirm the optimal EG concentration, the work function of PEDOT:PSS was analyzed using UPS.

It was confirmed that the work function of PEDOT:PSS decreased as a result of EG doping (**Figure 8**). Furthermore, the increase in the σ of PEDOT:PSS with increased EG doping affects the decrease in the work function.

As an example, **Figure 9** shows the band bending induced at the interface between PEDOT:PSS with 6% EG (work function ~4.75 eV) and the Se wires, which generates a possible carrier filtering effect. The work function difference between PEDOT:PSS with 6% EG and the Se wire yields a barrier height of 0.08 eV (4.75–4.67 eV). Therefore, the barrier height of the interface with the Se wires is expected to be 0.4, 0.26, and 0.08 eV for PEDOT:PSS with 2%, 4%, and 6% EG, respectively. As a result, S can be improved despite the increase in σ because of the possible carrier energy filtering effect (Song and Cai, 2017; Hu et al., 2018; Choi et al., 2016). For higher EG doping samples, the barrier height becomes very small (~0.05 eV) and negative (−0.02 eV), which might not successfully induce a carrier filtering effect.

CONCLUSION

In this study, the electrical and TE properties were measured for a GDR-grown Se wire coated with EG-doped PEDOT:PSS. For the undoped wire, the S and σ of the Se wire/PEDOT:PSS composite were 56.81 μV/K and 8.082 S/cm, respectively. Increasing the EG doping concentration increased the S and σ of the prepared composites, with maximum values (58.36 μV/K and 596.76 S/cm, respectively) observed at 6% EG. In addition, at 6% EG, the maximum value of the power factor (203.29 μW/mK^2) was obtained. Increasing the EG concentration improved the electrical conductivity because the charge path of PEDOT:PSS was controlled; as a result, an organic/inorganic composite with improved TE properties was obtained by adding a Se wire array with a high S. These results suggest a source technology that can enhance the properties of composite TE materials by controlling the structure and direction.

DATA AVAILABILITY STATEMENT

The original contributions presented in the study are included in the article/Supplementary material; further inquiries can be directed to the corresponding author.

AUTHOR CONTRIBUTIONS

IK carried out the experiments and wrote the manuscript. J-HL conceptualized and designed the study. DC supported the TEM analyses. S-IK and J-HL reviewed the manuscript. All authors contributed to the article and approved the submitted version.

FUNDING

This work was supported by the Global Frontier Program through the Global Frontier Hybrid Interface Materials (GFHIM) project (grant number 2013M3A6B1078870) and Noiseless Hyper-Speed Electric Power Systems Based on Interface- ontrolled Low-Dimensional Material Structures (2020R1A4A407983712).

REFERENCES

Bubnova, O., Khan, Z. U., Malti, A., Braun, S., Fahlman, M., Berggren, M., et al. (2011). Optimization of the Thermoelectric Figure of Merit in the Conducting Polymer Poly(3,4-Ethylenedioxythiophene). *Nat. Mater* 10 (6), 429–433. doi:10.1038/nmat3012

Cheng, B., and Samulski, E. T. (2003). Rapid, High Yield, Solution-Mediated Transformation of Polycrystalline Selenium Powder into Single-crystal nanowires Electronic Supplementary Information (ESI) Available: Histogram of Diameter Distribution of As-Prepared Single-Crystalline Trigonal Selenium Nanowires. See http://www.rsc.Org/suppdata/cc/b3/b303755j/. *Chem. Commun.* (16), 2024–2025. doi:10.1039/b303755j

Cho, B., Park, K. S., Baek, J., Oh, H. S., Koo Lee, Y.-E., and Sung, M. M. (2014). Single-Crystal Poly(3,4-Ethylenedioxythiophene) Nanowires with Ultrahigh Conductivity. *Nano Lett.* 14 (6), 3321–3327. doi:10.1021/nl500748y

Choi, Y. Y., and Choi, D. J. (2013). Investigating and Understanding the Initial Growth Mechanisms of Catalyst-free Growth of 1D SiC Nanostructures. *CrystEngComm.* 15(35) 6963–6970. doi:10.1039/C3CE40745D

Choi, J., Lee, J. Y., Lee, S.-S., Park, C. R., and Kim, H. (2016). High-Performance Thermoelectric Paper Based on Double Carrier-Filtering Processes at Nanowire Heterojunctions. *Adv. Energ. Mater.* 6 (9), 1502181. doi:10.1002/aenm.201502181

Coates, N. E., Yee, S. K., McCulloch, B., See, K. C., Majumdar, A., Segalman, R. A., et al. (2013). Effect of Interfacial Properties on Polymer-Nanocrystal Thermoelectric Transport. *Adv. Mater.* 25 (11), 1629–1633. doi:10.1002/adma.201203915

Du, Y., Shen, S. Z., Cai, K., and Casey, P. S. (2012). Research Progress on Polymer-Inorganic Thermoelectric Nanocomposite Materials. *Prog. Polym. Sci.* 37 (6), 820–841. doi:10.1016/j.progpolymsci.2011.11.003

Du, Y., Cai, K. F., Chen, S., Cizek, P., and Lin, T. (2014). Facile Preparation and Thermoelectric Properties of Bi2Te3 Based Alloy Nanosheet/PEDOT:PSS Composite Films. *ACS Appl. Mater. Inter.* 6 (8), 5735–5743. doi:10.1021/am5002772

Gadea, G., Morata, A., Santos, J. D., Dávila, D., Calaza, C., Salleras, M., et al. (2015). Towards a Full Integration of Vertically Aligned Silicon Nanowires in MEMS Using Silane as a Precursor. *Nanotechnology*. 26(19), 195302. doi:10.1088/0957-4484/26/19/195302

Hu, X., Zhang, K., Zhang, J., Wang, S., and Qiu, Y. (2018). Thermoelectric Properties of Conducting Polymer Nanowire-Tellurium Nanowire Composites. *ACS Appl. Energ. Mater.* 1(9) 4883–4890. doi:10.1021/acsaem.8b00909

Hwang, T.-Y., Song, Y., Kim, S., Lee, J., Eom, N. S. A., Kwon, Y.-T., et al. (2019). Rice-like Tellurium Thin Films Deposited by a Galvanic Displacement Reaction and Ultra-high Sensing Response to Hydrogen Sulfide (H2S) Gas at Room Temperature. *Sensors Actuators B: Chem.* 282, 756–764. doi:10.1016/j.snb.2018.11.075

Jang, J. H., Lee, E., Xiao, P., Park, K., Kim, I. Y., Henkelman, G., et al. (2018). Superior Oxygen Electrocatalysis on RuSe X Nanoparticles for Rechargeable Air Cathodes. *Adv. Energ. Mater.* 8 (8), 1702037. doi:10.1002/aenm.201702037

Jeong, D.-B., Lim, J.-H., Lee, J., Park, H., Zhang, M., Lee, Y.-I., et al. (2013). Template-Free Synthesis of Vertically Oriented Tellurium Nanowires *via* a Galvanic Displacement Reaction. *Electrochimica Acta* 111, 200–205. doi:10.1016/j.electacta.2013.07.228

Ju, H., and Kim, J. (2016). Fabrication of Conductive Polymer/Inorganic Nanoparticles Composite Films: PEDOT:PSS with Exfoliated Tin Selenide Nanosheets for Polymer-Based Thermoelectric Devices. *Chem. Eng. J.* 297, 66–73. doi:10.1016/j.cej.2016.03.137

Kakati, N., Lee, K., and Yoon, Y. S. (2017). Synthesis of ZnNiSnO 4 Nanorods by a Simple Hydrothermal Method as a New Anode Material for Li Ion Battery. *J. Alloys Comp.* 711, 387–394. doi:10.1016/j.jallcom.2017.04.011

Kang, S. D., and Snyder, G. J. (2017). Charge-Transport Model for Conducting Polymers. *Nat. Mater* 16 (2), 252–257. doi:10.1038/nmat4784

Kang, K., Watanabe, S., Broch, K., Sepe, A., Brown, A., Nasrallah, I., et al. (2016). 2D Coherent Charge Transport in Highly Ordered Conducting Polymers Doped by Solid State Diffusion. *Nat. Mater* 15 (8), 896–902. doi:10.1038/nmat4634

Kim, G. H., Hwang, D. H., and Woo, S. I. (2012). Thermoelectric Properties of Nanocomposite Thin Films Prepared with Poly(3,4-Ethylenedioxythiophene) Poly(Styrenesulfonate) and Graphene. *Phys. Chem. Chem. Phys.* 14 (10), 3530–3536. doi:10.1039/C2CP23517J

Kim, G.-H., Shao, L., Zhang, K., and Pipe, K. P. (2013). Engineered Doping of Organic Semiconductors for Enhanced Thermoelectric Efficiency. *Nat. Mater* 12 (8), 719–723. doi:10.1038/nmat3635

Kim, C., Hong, J., and Park, J.-W. (2019). Synthesis and Thermoelectric Properties of Selenium Nanoparticles Coated with PEDOT:PSS. *Polymers* 11 (6), 1052. doi:10.3390/polym11061052

Lee, W., Kang, Y. H., Lee, J. Y., Jang, K.-S., and Cho, S. Y. (2016). Improving the Thermoelectric Power Factor of CNT/PEDOT:PSS Nanocomposite Films by Ethylene Glycol Treatment. *RSC Adv.* 6 (58), 53339–53344. doi:10.1039/C6RA08599G

Li, Y., Li, C., Wang, B., Li, W., and Che, P. (2019). A Comparative Study on the Thermoelectric Properties of $CoSb_3$ Prepared by Hydrothermal and Solvothermal Route. *J. Alloys Comp.* 772, 770–774. doi:10.1016/j.jallcom.2018.09.114

Lim, E. (2013). Enhanced Photovoltaic Performance of P3HT:PCBM Cells by Modification of PEDOT:PSS Layer. *Mol. Crystals Liquid Crystals*, 585, 53–59. doi:10.1021/acsaem.8b00909 doi:10.1080/15421406.2013.849494

Lu, K., Zhang, H. Y., Zhong, Y., and Fecht, H. J. (1997). Grain Size Dependence of Mechanical Properties in Nanocrystalline Selenium. *J. Mater. Res.*, 12(4), 923–930. doi:10.1557/JMR.1997.0132

Lu, Y., Ding, Y., Qiu, Y., Cai, K., Yao, Q., Song, H., et al. (2019). Good Performance and Flexible PEDOT:PSS/Cu_2Se Nanowire Thermoelectric Composite Films. *ACS Appl. Mater. Inter.* 11 (13), 12819–12829. doi:10.1021/acsami.9b01718

Majidzade, V. A., Aliyev, A. S., Guliyev, P. H., Babayev, Y. N., Elrouby, M., and Tagiyev, D. B. (2018). Electrochemical Behaviour of Selenite Ions in Tartaric Electrolytes. *J. Electrochem. Sci. Eng.* 8 (3), 197–204. doi:10.5599/jese.490

Noriega, R., Rivnay, J., Vandewal, K., Koch, F. P. V., Stingelin, N., Smith, P., et al. (2013). A General Relationship between Disorder, Aggregation and Charge Transport in Conjugated Polymers. *Nat. Mater* 12 (11), 1038–1044. doi:10.1038/nmat3722

Oh, J. Y., Lee, J. H., Han, S. W., Chae, S. S., Bae, E. J., Kang, Y. H., et al. (2016). Chemically Exfoliated Transition Metal Dichalcogenide Nanosheet-Based Wearable Thermoelectric Generators. *Energy Environ. Sci.* 9 (5), 1696–1705. doi:10.1039/C5EE03813H

Ou, C., Sangle, A. L., Datta, A., Jing, Q., Busolo, T., Chalklen, T., et al. (2018). Fully Printed Organic-Inorganic Nanocomposites for Flexible Thermoelectric Applications. *ACS Appl. Mater. Inter.* 10 (23), 19580–19587. doi:10.1021/acsami.8b01456

Park, E., Kwon, O. s., Park, S. J., Lee, J. S., You, S., and Jang, J. (2012). One-pot Synthesis of Silver Nanoparticles Decorated Poly(3,4-Ethylenedioxythiophene) Nanotubes for Chemical Sensor Application. *J. Mater. Chem.* 22 (4), 1521–1526. doi:10.1039/C1JM13237G

Peng, S., Wang, D., Lu, J., He, M., Xu, C., Li, Y., et al. (2016). A Review on Organic Polymer-Based Thermoelectric Materials. *J. Polym. Environ.* 25 (4), 1208–1218. doi:10.1016/j.jmat.2021.03.013

Recatala-Gomez, J., Kumar, P., Suwardi, A., Abutaha, A., Nandhakumar, I., and Hippalgaonkar, K. (2020). Direct Measurement of the Thermoelectric Properties of Electrochemically Deposited Bi_2Te_3 Thin Films. *Sci. Rep.* 10 (1), 1–10. doi:10.1038/s41598-020-74887-z

Reuss, R. H., Raupp, G. B., and Gnade, B. E. (2015). Special Issue on Advanced Flexible Electronics for Sensing Applications [Scanning the Issue]. *Proc. IEEE* 103 (4), 491–496. doi:10.1109/JPROC.2015.2414486

Roh, S.-H., Kim, J., Park, W.-I., Kim, Y.-D., and Lim, J.-H. (2017). Fabrication and Characterization of $Ge_2Sb_2Te_5$ Nanowire Arrays and PEDOT: PSS Hybrid Thermoelectric Composites. *Korean J. Met. Mater.* 55 (6), 432–439. doi:10.3365/KJMM.2017.55.6.432

Saha, S., Johnson, M., Altayaran, F., Wang, Y., Wang, D., and Zhang, Q. (2020). Electrodeposition Fabrication of Chalcogenide Thin Films for Photovoltaic Applications. *Electrochem* 1 (3), 286–321. doi:10.3390/electrochem1030019

See, K. C., See, J. P., Chen, C. E., Majumdar, A., Urban, J. J., and Segalman, R. A. (2010). Water-Processable Polymer-Nanocrystal Hybrids for Thermoelectrics. *Nano Lett.* 10 (11), 4664–4667. doi:10.1021/nl102880k

Song, H., and Cai, K. (2017). Preparation and Properties of PEDOT:PSS/Te Nanorod Composite Films for Flexible Thermoelectric Power Generator. *Energy*. 125, 519–525. doi:10.1002/aelm.201800822

Tran, M., Roy, S., Kmiec, S., Whale, A., Martin, S., Sundararajan, S., et al. (2020). Formation of Size and Density Controlled Nanostructures by Galvanic Displacement. *Nanomaterials* 10 (4), 644. doi:10.3390/nano10040644

Varghese, T., Hollar, C., Richardson, J., Kempf, N., Han, C., Gamarachchi, P., et al. (2016). High-Performance and Flexible Thermoelectric Films by Screen Printing Solution-Processed Nanoplate Crystals. *Sci. Rep.* 6, 33135. doi:10.1038/srep33135

Wang, Q., Yao, Q., Chang, J., and Chen, L. (2012). Enhanced Thermoelectric Properties of CNT/PANI Composite Nanofibers by Highly Orienting the Arrangement of Polymer Chains. *J. Mater. Chem.* 22 (34), 17612. doi:10.1039/C2JM32750C

Wang, L., Chang, S., Zheng, S., Fang, T., Cui, W., Bai, P.-p., et al. (2017). Thermoelectric Performance of Se/Cd Codoped SnTe *via* Microwave Solvothermal Method. *ACS Appl. Mater. Inter.* 9(27), 22612–22619. doi:10.1021/acsami.7b06083

Wang, X., Meng, F., Wang, T., Li, C., Tang, H., Gao, Z., et al. (2018). High Performance of PEDOT:PSS/SiC-NWs Hybrid Thermoelectric Thin Film for Energy Harvesting. *J. Alloys Comp.* 734, 121–129. doi:10.1016/j.jallcom.2017.11.013

Wang., H., and Yu, C. (2019). Organic Thermoelectrics: Materials Preparation, Performance Optimization, and Device Integration. *Joule*. 3(1), 53–80. doi:10.1016/j.joule.2018.10.012

William, S., and Wong, A. S. (2009). *Flexible Electronics: Materials and Applications*. Stanford, CA: Springer.

Xin, J., Basit, A., Li, S., Danto, S., Tjin, S. C., and Wei, L. (2021). Inorganic Thermoelectric Fibers: A Review of Materials, Fabrication Methods, and Applications. *Sensors* 21 (10), 3437. doi:10.3390/s21103437

Yee, S. K., Coates, N. E., Majumdar, A., Urban, J. J., and Segalman, R. A. (2013). Thermoelectric Power Factor Optimization in PEDOT:PSS Tellurium Nanowire Hybrid Composites. *Phys. Chem. Chem. Phys.* 15 (11), 4024–4032. doi:10.1039/C3CP44558E

Yue, R., and Xu, J. (2012). Poly(3,4-ethylenedioxythiophene) as Promising Organic Thermoelectric Materials: A Mini-Review. *Synth. Met.* 162 (11–12), 912–917. doi:10.1016/j.synthmet.2012.04.005

Conflict of Interest: The authors declare that the research was conducted in the absence of any commercial or financial relationships that could be construed as a potential conflict of interest.

frontiers in Chemistry

ORIGINAL RESEARCH
published: 17 February 2022
doi: 10.3389/fchem.2022.815805

Edited by:
Jose Solla-Gullon,
University of Alicante, Spain

Reviewed by:
Daniel Martin-Yerga,
University of Warwick,
United Kingdom
Annamalai Senthil Kumar,
VIT University, India
Juliano Alves Bonacin,
State University of Campinas, Brazil

***Correspondence:**
Ashok Mulchandani
adani@engr.ucr.edu

†Present address:
Thien-Toan Tran,
Department of Chemical and
Biomolecular Engineering, University of
Notre Dame, Notre Dame, IN,
United States
Nosang V. Myung,
Department of Chemical and
Biomolecular Engineering, University of
Notre Dame, Notre Dame, IN,
United States

Specialty section:
This article was submitted to
Electrochemistry,
a section of the journal
Frontiers in Chemistry

Received: 15 November 2021
Accepted: 13 January 2022
Published: 17 February 2022

Citation:
Zhao G, Tran T-T, Modha S, Sedki M,
Myung NV, Jassby D and
Mulchandani A (2022) Multiplexed
Anodic Stripping Voltammetry
Detection of Heavy Metals in Water
Using Nanocomposites Modified
Screen-Printed Electrodes Integrated
With a 3D-Printed Flow Cell.
Front. Chem. 10:815805.
doi: 10.3389/fchem.2022.815805

Multiplexed Anodic Stripping Voltammetry Detection of Heavy Metals in Water Using Nanocomposites Modified Screen-Printed Electrodes Integrated With a 3D-Printed Flow Cell

Guo Zhao[1,2], *Thien-Toan Tran*[3†], *Sidharth Modha*[3], *Mohammed Sedki*[4], *Nosang V. Myung*[1†], *David Jassby*[5] *and Ashok Mulchandani*[1,6]*

[1]Department of Chemical and Environmental Engineering, University of California, Riverside, Riverside, CA, United States, [2]College of Artificial Intelligence, Nanjing Agricultural University, Nanjing, China, [3]Department of Bioengineering, University of California, Riverside, Riverside, CA, United States, [4]Materials Science and Engineering Program, University of California, Riverside, Riverside, CA, United States, [5]Department of Civil and Environmental Engineering, University of California, Los Angeles, Los Angeles, CA, United States, [6]Center for Environmental Research and Technology (CE-CERT), University of California, Riverside, Riverside, CA, United States

In this study, we present multiplexed anodic stripping voltammetry (ASV) detection of heavy metal ions (HMIs)—As(III), Cd(II), and Pb(II)—using a homemade electrochemical cell consisting of dual working, reference and counter screen-printed electrodes (SPE) on polyimide substrate integrated with a 3D-printed flow cell. Working and counter electrodes were fabricated by the screen-printing of graphite paste while the Ag/AgCl paste was screen-printed as a reference electrode (Ag/AgCl quasi-reference electrode). The working electrodes were modified with $(BiO)_2CO_3$-reduced graphene oxide (rGO)-Nafion [$(BiO)_2CO_3$-rGO-Nafion] and Fe_3O_4 magnetic nanoparticles (Fe_3O_4MNPs) decorated Au nanoparticles (AuNPs)-ionic liquid (IL) (Fe_3O_4-Au-IL) nanocomposites separately to enhance HMIs sensing. Electrochemical detection was achieved using square wave ASV technique. The desired structure of the flow electrochemical cell was optimized by the computational fluid dynamic (CFD). Different experimental parameters for stripping analysis of HMIs were optimized including deposition time, deposition potential and flow rate. The linear range of calibration curves with the sensing nanocomposites modified SPE for the three metal ions was from 0–50 µg/L. The limits of detection (S/N = 3) were estimated to be 2.4 µg/L for As(III), 1.2 µg/L for Pb(II) and 0.8 µg/L for Cd(II). Furthermore, the homemade flow anodic stripping sensor platform was used to detect HMIs in simulated river water with a 95–101% recovery, indicating high selectivity and accuracy and great potential for applicability even in complex matrices.

Keywords: 3D printing, screen printed electrode, heavy metals detection, anodic stripping voltammetry, flow injection

INTRODUCTION

With the development of global industrialization, especially, in the electronic and electrical industry, increasing amounts of heavy metal ions (HMIs) are inadvertently discharged into the environment. HMIs pose a great threat to ecological and human health because of their potential for bioaccumulation and toxicity (Verma and Singh, 2005; Wuana and Okieimen, 2011; Wu et al., 2018). Among different heavy metals, Cd(II), Pb(II), and As(III) are widely distributed in various environments (e.g., soil and water) with particularly high toxicity, which highlights the urgency for effective and rapid detection methods (Panov et al., 2008). Traditionally used analytical methods for the detection of HMIs include, atomic absorption spectroscopy (AAS) (Kenawy et al., 2000), atomic fluorescence spectrometry (AFS) (Wan et al., 2006), X-ray fluorescence spectrometry (XRF) (Galani-Nikolakaki et al., 2002) and inductively coupled plasma mass spectroscopy (ICP-MS) (Davis et al., 2007; Silva et al., 2009). These techniques have advantages of high sensitivity and selectivity; however, they have to be performed in a laboratory, which requires transportation of the samples to the laboratory, and use of expensive benchtop instrumentation by trained personnel. These increase the analysis costs and delay the results thereby limiting their widespread application, especially for portable and on-site detection. Additionally, these conventional instruments and techniques require time consuming intricate operating procedures and sample preconcentration steps (Bi et al., 2010).

Anodic stripping voltammetry (ASV)—an electrochemical analysis technique—is a promising method that can be used for HMIs detection with high sensitivity, selectivity and accuracy, while amenable for on-site detection and quantification when coupled to a portable potentiostat (Pandey et al., 2016). Furthermore, integrating the traditional batch mode ASV with a flow cell/system presents an attractive analytical platform for the continuous monitoring of HMIs (Becker and Locascio, 2002; Reyes et al., 2002; West et al., 2008). C. Henríquez et al. proposed an automatic multisyringe flow injection system coupled to a flow-through screen printed electrode (SPE) for the detection of Cd(II) (Henríquez et al., 2012). Z. M. Redha et al. developed a microfluidic sensor fabricated by screen printing and injection molding for electrochemical detection of Cu(II) and Pb(II) (Redha et al., 2009). Sun et al. described a flow electrochemical system for the detection of Pb(II) with a detection limit of 0.2 μg/L, showing a better sensitivity and reproducibility compared to the traditional batch mode ASV (Sun et al., 2017). However, the flow systems integrated with multiple SPEs, which can simultaneously detect Cu(II), Pb(II), and As(III), need to be further developed. The combination of ASV and flow system would enable automated, on-site and near-/real-time monitoring of HMIs in water samples at low cost, which can further mitigate the spread of environmental pollution (Alpízar et al., 1997; Economou, 2010). A three-electrode system, consisting of a reference electrode (RE), a counter electrode (CE) and a working electrode (WE), is generally used for the ASV analysis, in which the WE is the most important component due to its significant influence on the detection performance as a site for electrochemical reactions. The conventional electrodes such as glassy carbon electrode and carbon paste electrode are not suitable for small-volume analysis due to their relatively large size. Thus, the development of a planar sensor device compatible with a flow cell enables ease-of-integration of the sensor into the flow injection system.

The technique of screen-printing has been considered an effective method for the fabrication of whole electrode system in a small footprint/form factor, including the counter electrodes, reference electrodes and working electrodes, with a variety of printing patterns, either consisting of individual electrodes or electrode arrays. In addition, the screen-printed electrodes (SPEs) can be fabricated at low costs with high precision, and can be easily replaced during operation. The SPEs can be fabricated on different kinds of substrate, such as glass, ceramic and flexible polymer polyimide, based on the characteristics of printing. The SPEs printed on polyimide substrates are capable of integration in a flow cell with a small volume attributed to the thin and mechanically flexible property of the substrate material. However, there are still some problems that need to be resolved when SPEs are applied in flow system (Erlenkötter et al., 2000; Leca and Blum, 2000). First, SPEs should be incorporated in a flow cell with a good adaptability and mechanical stability. Second, the sensing area on SPE should be placed strategically in the flow channel to ensure efficient electrodeposition of HMIs in the flow channel on the working electrode surface. Third, the dead volume formed in the flow cell must be eliminated by the optimization of the flow cell geometry. Fourth, reliable sealing method is required to prevent leakage between the SPE and flow cell assembly. Furthermore, the sensitivity, selectivity, and specificity of the bare SPE-based sensors need to be improved. Thus, the modification of sensing materials has been widely investigated to enhance the performance of SPE-based stripping voltammetry detection of HMIs (Chen et al., 2013; Puy-Llovera et al., 2017; Tu et al., 2018). Lately, three-dimensional (3D) printing has received a great deal of attention as one kind of rapid prototyping technology, which has been widely applied in various microscale production fields (Andrew Clayton et al., 2006; Gross et al., 2014; Kolesky et al., 2014; Murphy and Atala, 2014; Johnson et al., 2015; Ambrosi et al., 2016; Au et al., 2016). With the decreased cost of printing systems, the flow cell can be fabricated with desired shape with extraordinary freedom (Whitesides, 2006; Ge et al., 2012).

Nano-materials/composites modified electrodes for detection of heavy metals Pb(II), Cd(II), and As(III) in water by ASV in batch electrochemical cells has received a great deal of attention (Bi et al., 2010; Pandey et al., 2016; Zhao et al., 2020; Sedki et al., 2021). While highly sensitive and selective, batch cells have limitations. In this paper, we achieved multiplexed ASV detection of As(III), Cd(II), and Pb(II) using planar SPEs on polyimide substrate integrated in a 3D-printed flow cell. The employment of the disposable SPEs avoided the traditional pretreatment process frequently-used to prepare glassy carbon or carbon paste WE, but obtained a comparable sensitivity based on the modification of the nanocomposites. Compared to the batch electrochemical cells in previously published papers, including ours (Zhao et al., 2020; Sedki et al., 2021), the flow electrochemical stripping analysis reported in this study has the advantages of: automation potential, high throughput analysis of large quantities of samples, high reliability due to reduced human intervention, miniaturization potential on the size of analytical cell/device, near-/real-time detection, integration with other analytical systems and capability for the simultaneous detection of As(III), Cd(II), and Pb(II). Additionally, the flow cell geometry was optimized and finally confirmed by COMSOL Multiphysics to resolve the problems existing in the application of SPEs in flow system based on a finite element method (FEM), which is a reliable and effective approach for the computational fluid dynamic (CFD) analysis. Furthermore, the polymer ASV flow cell with desired geometry and materials was fabricated by 3D-printing. Moreover, highly flexible SPEs were prepared by screen-printing a commercial graphite ink and an Ag/AgCl ink onto polyimide substrate. The SPEs were composed of two WEs, a CE and a Ag/AgCl quasi-RE. As well, two sensing nanocomposites, i.e., $(BiO)_2CO_3$-reduced graphene oxide (rGO)-Nafion ($(BiO)_2CO_3$-rGO-Nafion) and Fe_3O_4 magnetic nanoparticles (Fe_3O_4MNPs) @Au nanoparticles (AuNPs)-ionic liquid (IL) (Fe_3O_4-Au-IL), with different catalytic properties were used to modify the two WEs integrated in SPE separately based on our previous works (Zhao et al., 2020; Sedki et al., 2021) with small changes to obtain a good sensitivity and selectivity, as compared with the bare SPEs. On this basis, a homemade flow system for the stripping voltammetry analysis of HMIs was developed, comprising a nanocomposites-modified SPE integrated with an 3D-printed flow cell. The proposed flow injection system exhibited satisfactory results for the detection and quantification of Pb(Ⅱ), As(Ⅲ), and Cd(Ⅱ) in simulated river water samples.

EXPERIMENTAL

Reagents and Instruments

Cd(II) and Pb(II) standard solutions were obtained from Sigma-Aldrich (USA) and diluted as required before using. Arsenic trioxide (As_2O_3) was purchased from Strem Chemicals, INC. (USA). An As(III) stock solution (1 mg/ml) was prepared by dissolving As_2O_3 in the 1.0 M aqueous NaOH. Carbon Graphite Paste (C2030519P4) was purchased from Gwent Group (UK) and Silver Silver/Chloride Ink (Electrodag 7019) was purchased from Tekra (USA). Polyimide film (5 mil) was purchased from Amazon.com (USA). Sodium acetate trihydrate was obtained from Fisher Scientific (USA) and prepared as acetate buffer solution (0.2 M) with acetic acid for the electroanalysis of As(III), Pb(II), and Cd(II). All the above chemicals and reagents were analytically pure.

Scanning electron microscopy (SEM) (NovaNanoSEM 450) was used for surface characterization of the sensing nanocomposite modified SPE. A peristaltic pump was used to construct the sequential injection system that was obtained from Rainin Instrument Co., Inc. (CA, USA). Squeegee and screen mesh were obtained from Rheeliable Screen Print Supply (CA, USA). Square wave stripping voltammetry (SWASV) was performed on a CH Instrument 760C electrochemical work station using the proposed SPEs. Electrochemical impedance spectroscopy (EIS) and cyclic voltammetry (CV) were performed on the above electrochemical work station with a three-electrode system consisting of an Ag/AgCl reference electrode, a Pt wire counter electrode and a working electrode, i.e., GCE or the working electrode of SPE. The diameter of both the working electrodes was 3 mm. An optical microscope (KH-7700, Hirox, Japan) was used to characterize the thickness of the ink layers and a 3D printer Form2 (FormLabs, Somerville, MA, United States) was used to fabricate the flow cell.

Design and Preparation of SPE

To meet the requirements of simultaneous detection of Pb(II), Cd(II), and As(III), a flexible SPE configured with two WEs, one CE, and one RE was designed and fabricated. Additionally, the polyimide film was used as the substrate of the SPE. The WE and CE were made of graphite ink while Ag/AgCl ink was used for the preparation of the Ag/AgCl quasi-RE, as shown in **Figure 1A**. Moreover, two kind of sensing nanocomposites, i.e., $(BiO)_2CO_3$-rGO-Nafion and Fe_3O_4-Au-IL were drop casted on the two working electrodes, where $(BiO)_2CO_3$-rGO-Nafion was used for the detection of Pb(II) and Cd(II) and Fe_3O_4-Au-IL was used for the detection As(III). As shown in **Figure 1B**, the proposed SPE with a flexible polyimide substrate is flexible and amenable to incorporation in flow cell.

The procedure of SPE fabrication based on screen-printing is shown in **Supplementary Figure S1**, which illustrates the printing process of graphite ink and Ag/AgCl ink. The Ag/AgCl ink and graphite ink were printed separately on the polyimide substrate by the sweeping of a rubber squeegee across the screen surface. The desirable electrodes were obtained while the squeegee swept over an area on polyimide substrate, depositing the ink onto the substrate surface. After that, the obtained SPEs were dried in the oven at 60°C for 1 h. The patterning of the desirable electrode printed on the polyimide substrate was achieved by controlling the area with holes on the screen template, i.e., electrode pattern.

Fabrication of Flow Cell

The flow cell was first designed using Autodesk Inventor (Autodesk, San Rafael, CA, United States), and 3D-printed using a Form2 printer (FormLabs, Somerville, MA, United States), as shown in **Figure 5**. The flow cell was fabricated *via* stereolithography using standard clear resin from FormLabs. After that, the prepared flow device was washed in an isopropanol sonication bath for 20 min. The device was blown dry with pressurized air and photocured for 1.5 h at 60°C under ultraviolet light. The flow cell consists of two parts, i.e., bottom part and top part, which were assembled together using screws and nuts, as shown in **Supplementary Figure S2**. A sealed flow channel was formed by a gasket between top part and bottom part. The inlet and outlet were installed on the top of the flow cell, and a support was designed and used as an upholder for SPE.

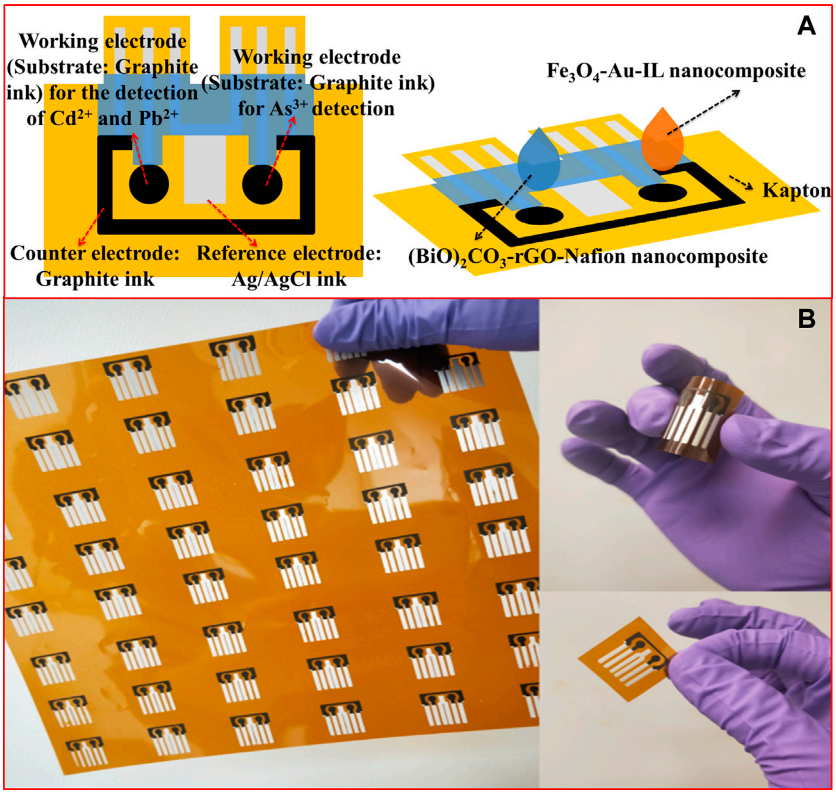

FIGURE 1 | (A) Schematic diagram of the SPE. **(B)** Optical images of the SPE.

Synthesis and Modification of Sensing Nanocomposites

The $(BiO)_2CO_3$-rGO-Nafion and Fe_3O_4-Au-IL sensing nanocomposites were synthesized based on previously reported protocols (Zhao et al., 2020; Sedki et al., 2021) using the following steps.

$(BiO)_2CO_3$-rGO-Nafion sensing nanocomposite: Briefly, a 60 ml mixture of 5 mg/ml $Bi(NO_3)_3.5H_2O$ and 0.5 mg/ml graphene oxide (GO) was prepared to obtain the GO-Bi^{3+} mixed solution. Then the mixed solution was chemically reduced by adding 0.51 g $NaBH_4$ at 60°C with continuous stirring for 2 h. The $(BiO)_2CO_3$-rGO deposit was obtained by the centrifuging of the above solution. Subsequently, the obtained deposit was washed for three times to remove the solvent residues, and then the deposit was placed in the oven at 50°C overnight to totally dry. 1 mg of obtained solid composite was added into 4 ml DMF and sonicated for 20 min. After that, 0.5 wt% Nafion solution with a volume of 800 μL was mixed with the above 4 ml $(BiO)_2CO_3$-rGO solution to get the $(BiO)_2CO_3$-rGO-Nafion suspension.

Fe_3O_4-Au-IL sensing nanocomposite: A 40 ml mixed solution of 0.8 mg/L $FeCl_3{\cdot}6H_2O$ and 0.5 mg/L $FeCl_2{\cdot}4H_2O$ was prepared using ethylene glycol (EG) as solvent. Next, the above solution was heated to 80°C and 0.15 ml PVA (1%) was added to the mixture. Then the pH of the solution was adjusted to 10.0 by dropwise addition of ammonium hydroxide (5% v/v). The liquid-solid separation of the obtained mixture was achieved by applying an external magnetic field, and then the separated solid composite was washed several times with DI water to remove the solvent. The resulting black product was dried at 60°C under vacuum for 24 h. The decoration of Fe_3O_4MNPs on AuNPs was accomplished by adding 5 mg Fe_3O_4 to 10 ml of 2 mg/ml $HAuCl_4{\cdot}3H_2O$ aqueous solution with a sonication. Then 10 ml sodium citrate (1.0%) was added to the solution of Fe_3O_4-Au^{3+} at 80°C under vigorous stirring for an hour to obtain the AuNPs-Fe_3O_4. After that, 100 μL 0.5% ionic liquid was mixed with the above solution to obtain the Fe_3O_4-Au-IL suspension.

Then 6 μL of a $(BiO)_2CO_3$-rGO-Nafion suspension and 6 μL of a Fe_3O_4-Au-IL suspension were modified on the two working electrodes integrated in SPE, separately, and solidified in oven at a temperature of 60°C.

Preparation of the Simulated River Water Samples

Water samples simulating the composition of river water spiked with varying concentrations of HMIs were prepared to evaluate the analytical performance of the proposed detection system. The simulated river water consisted magnesium nitrate (150 ppm), ammonium chloride (60 ppm), potassium chloride (500 ppm), sodium citrate (50 ppm) and calcium chloride (500 ppm). The concentration of total dissolved solids (TDS) was 1,260 ppm. The analyte solution consisting of simulated water and acetate buffer

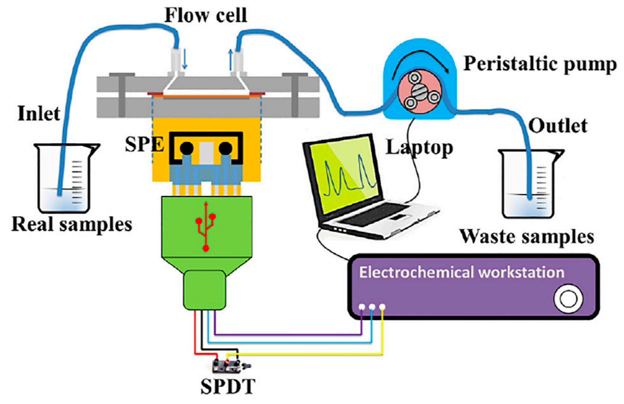

FIGURE 2 | Schematic illustration of the flow injection system for the analysis of HMIs.

(2.0 M, pH 5.0) with a volume ratio of 9:1 was used for each measurement to guarantee the pH 5.0 buffer condition with 0.2 M acetate.

Analysis Procedure of the Flow Injection System

The setup of the flow injection system is illustrated in **Figure 2**. A peristaltic pump was used to deliver the samples mixed with acetate buffer (pH 5.0, 0.2 M) through the tube and flow cell at a flow rate of 120 μL/s. The deposition and stripping steps were carried out using an electrochemical workstation that was connected to the SPE. The injected standards used to establish calibration plots were composed of acetate buffer (0.2 M, pH 5.0) with different concentrations of Cd(II), Pb(II), and As(III). The SWASV detection was carried out after the baseline signal of WEs in fluid channel has stabilized.

The flow injection analysis procedure should be consistent with the detection procedure of SWASV, which can be divided into three steps. In the first step, the water sample in the beaker was delivered to the flow cell through the channel by the pumping while applying the deposition (metal ions were electrochemically reduced to metal) potential of −1.2 V for 200 s on the Cd(II) and Pb(II) WE and −0.9 V for 250 s on the As(III) WE. During step 2, the pumping was manually paused first for 10 s, and a potential scanning (frequency, 25 Hz; increment potential, 5 mV; amplitude, 25 mV) was performed on WEs in a quiescent sample solution over a range of −0.55 to 0.05 V for As(III) and −1.25 to −0.65 V for Pb(II) and Cd(II). Finally, the surfaces of WEs were activated/regenerated by applying a potential of −0.4 V for Cd(II) and Pb(II) and +0.6 V for As(III) to remove the residual metals (step 3), which prepared the electrodes for a new cycle of stripping voltammetry analysis. The duration of each measurement was around 334.8 s for Cd(II) and Pb(II) and ~384.8 s for As(III). All the measurements were carried out in 0.1 M acetate buffer (pH = 5.0). A single-pole double-throw switch was used to electrically isolate the specific working electrode's electrochemical detection and quantification of the corresponding target analyte by switching the electrochemical workstation to connect with different working electrodes of SPE to achieve the detection of target HMIs serially.

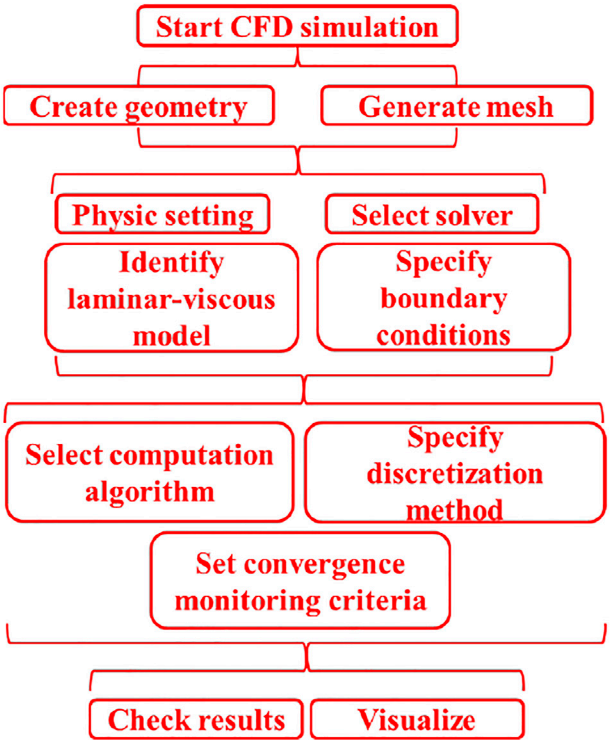

FIGURE 3 | Flow chart of CFD numerical methodology.

CFD Simulation Based on FEM

CFD simulation based on FEM was completed based on the steps illustrated on flowchart in **Figure 3** for the optimization of the desired structure of the flow electrochemical cell. In presented simulations non-compressible model of fluid was used, the fluid parameters, i.e., dynamic viscosity and density, were 0.89 cP and 1,000 kg/m^3, respectively. Additionally, the boundary conditions were as follows: fluid inlet velocity equal to 0.012 m/s, fluid mass-flow equal to 400 μL/min, fluid velocity equal to 0 m/s on channel walls.

RESULTS AND DISCUSSION

Optical Microscope Analysis of the Proposed SPE

The morphology of graphite layer and Ag/AgCl printed on polyimide was investigated by optical microscopy (**Supplementary Figure S3**). The images show the graphite ink formed a homogeneous and dense printing layer on the substrate (**Supplementary Figure S3A**) and Ag/AgCl layer had the grains in different sizes, which should be the AgCl and Ag, respectively, distributed uniformly on the substrate (**Supplementary Figure S3B**). It can be seen from the **Supplementary Figures S3C,D**, respectively, that the graphite layer and Ag/AgCl layer were printed stably on the polyimide substrate, and the boundary between carbon graphite layer and polyimide and the boundary between the Ag/AgCl layer and polyimide was clear and regular as well, demonstrating that the inks printed on the substrate were well distributed and controllable.

Supplementary Figure S4 shows the thickness of carbon graphite and Ag/AgCl layers printed on the polyimide substrate. The thickness of Ag/AgCl layer, used as RE, was 7.3 μm (**Supplementary Figure S4A**) and the thickness of carbon graphite layer, used as WE and CE, was 7.4 μm (**Supplementary Figure S4B**). Additionally, the carbon graphite layer printed on the Ag/AgCl layer can be seen in **Supplementary Figure S4C**, where Ag/AgCl layer was used as a conducting layer in this case. The results from the **Supplementary Figure S4C** indicated that the thickness of carbon graphite layer and Ag/AgCl layer were 7.2 and 7.3 μm, respectively, that were consistent with the results shown in **Supplementary Figures S4A,B**. This validated that the printing strategy used for the preparation of SPE in this study is reliable. Moreover, we investigated the thickness of graphite layer using simulation (**Supplementary Figures S4D,E**). The simulation of the graphite layer's thickness was carried out using the built-in software of the optical microscope (KH-7700, 156 Hirox, Japan). As illustrated in **Supplementary Figure S4E**, the simulated thickness of the graphite layer was 8.473 μm, which was almost the same to the thickness determined from **Supplementary Figure S4B**. Additionally, the simulated results also indicated that the printing layer thickness is relatively uniform.

Characterization of Sensing Nanocomposites Modified SPE

Electron microscopy, X-Ray Diffraction and Fourier transform infra-red spectroscopy were used to ensure the synthesized $(BiO)_2CO_3$-rGO and Fe_3O_4-Au nanocomposites had desired morphologies/structures and chemical compositions as reported in our previously published papers (Zhao et al., 2020; Sedki et al., 2021).

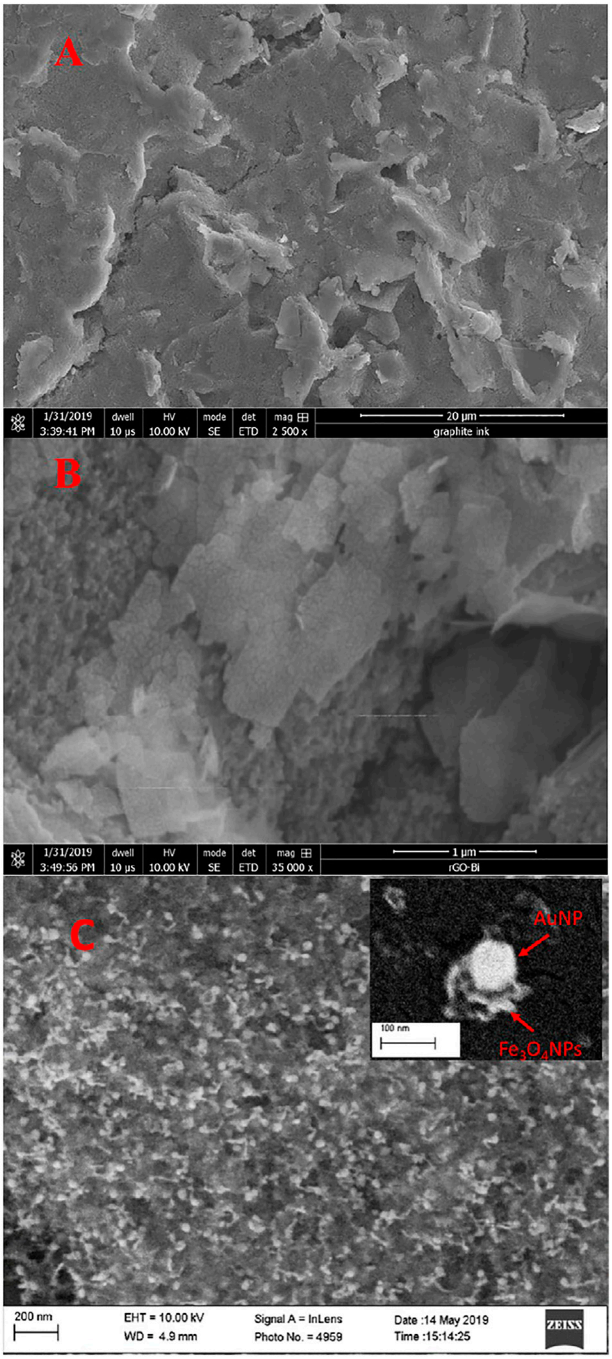

FIGURE 4 | SEM images of **(A)** bare SPE, **(B)** $(BiO)_2CO_3$-rGO-Nafion/SPE and **(C)** Fe_3O_4-Au-IL/SPE.

The surface morphologies of bare SPE, $(BiO)_2CO_3$-rGO-Nafion-modified SPE ($(BiO)_2CO_3$-rGO-Nafion/SPE) and Fe_3O_4-Au-IL-modified SPE (Fe_3O_4-Au-IL/SPE) were further examined in this paper. To investigate the morphology of sensing nanocomposites on the WEs of SPE, SEM was performed to observe the morphological changes resulting from the modification process, as shown in **Figure 4**. The bare/unmodified WE of SPE displayed a sheet-like structure, where the sheets can be ascribed to the graphite layers according to the composition of carbon ink (**Figure 4A**). After modification of the WE with the $(BiO)_2CO_3$-rGO-Nafion nanocomposite, the electrode morphology changed drastically, as evident by the abundance of nanoparticles observed on the graphite sheets, indicating the formation and uniform distribution of bismuth nanoparticles on the electrode (**Figure 4B**). The graphite sheet as a substrate on the WE of SPE supply a large specific area (Zhao et al., 2017) for the modification of $(BiO)_2CO_3$-rGO-Nafion film. Similarly, the altered morphology of Fe_3O_4-Au-IL-modified WE of SPE can be observed in **Figure 4C**. Many nanoparticles were distributed on the electrode surface, which are attributed to AuNPs and Fe_3O_4MNPs. In addition, it can be seen from **Figure 4C**, inset, that the AuNP is covered with Fe_3O_4MNPs, which can be expected to obtain a high catalytic performance for As(III)

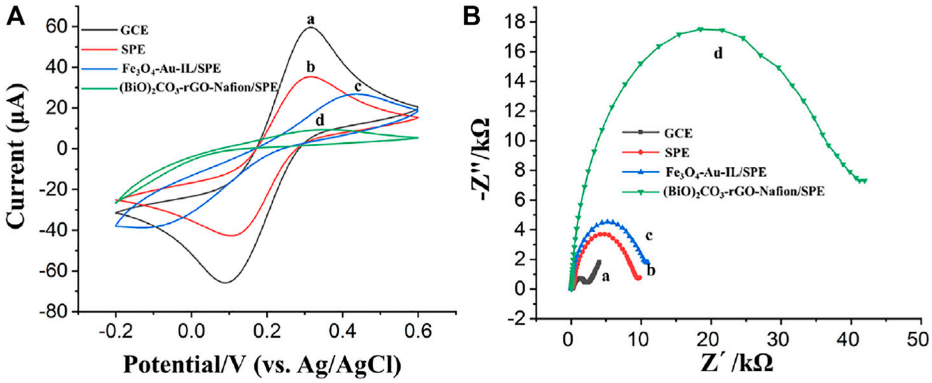

FIGURE 5 | (A) Cyclic voltammograms of (a) GCE, (b) SPE, (c) Fe_3O_4-Au-IL/SPE, and (d) $(BiO)_2CO_3$-rGO-Nafion/SPE. **(B)** Electrochemical impedance spectroscopy (EIS) of (a) GCE, (b) SPE, (c) Fe_3O_4-Au-IL/SPE, and (d) $(BiO)_2CO_3$-rGO-Nafion/SPE. CV and EIS were performed with a three-electrode system consists of an Ag/AgCl reference electrode, a Pt wire counter electrode and a working electrode, i.e., GCE or the working electrode of SPE. The diameter of both the working electrodes was 3 mm.

detection. Au and Fe_3O_4 NPs were identified from SEM and EDS, and EDS mapping results are shown in **Supplementary Figure S5**, where the color distribution of the elements elucidates their homogeneous distribution on the electrode surface. The catalytic activity of Fe_3O_4-Au-IL nanocomposite on the enhancement of SWASV response for As(III) detection was investigated by our previous works (Zhao and Liu, 2019; Sedki et al., 2021).

The electrochemical behavior of bare WE of SPE, different nanocomposites modified WE of SPE and bare GCE was investigated and compared by cyclic voltammetry (CV) using a platinum wire and a Ag/AgCl electrode as CE and RE, respectively (Zhao et al., 2016). **Figures 5Aa,Ab** show the comparison of cyclic voltammograms obtained at a SPE and at a glassy carbon electrode (GCE) in an electrolyte with 0.1 M KCl and 5 mM $[Fe(CN)_6]^{3-/4-}$. As illustrated, well-defined anodic and cathodic peaks corresponding to the oxidation and reduction of the $[Fe(CN)_6]^{3-/4-}$ redox probe were obtained at bare GCE, which was larger compared with the peak currents obtained at bare SPE WE. This maybe because the multilayer graphite nanosheets hinder the electron transfer from one graphite sheet to another one and/or the binder, dispersant, and solvent used for the preparation of SPE could block the electron transfer. After the modification of Fe_3O_4-Au-IL nanocomposite and $(BiO)_2CO_3$-rGO-Nafion nanocomposite on the SPEs, respectively, both of the peak currents at the electrode surface decreased due to the significant negative effect of poor conductivity of Fe_3O_4 and Nafion on the electron transfer on the surface of SPE, which was consistent with our previous reported results (Zhao et al., 2020; Sedki et al., 2021).

Electrochemical impedance spectroscopy (EIS) was also used to further characterize the properties of the bare SPE, Fe_3O_4-Au-IL/SPE and $(BiO)_2CO_3$-rGO-Nafion/SPE, in which the charge transfer resistance (Rct) at the interface of electrode/electrolyte can be qualitatively evaluated by the semicircle of Nyquist plot (Jiang et al., 2013). The EIS was carried out on the electrochemical work station with a potential and amplitude of 0.25 and 0.01 V, respectively, over a frequency range of 0.1 Hz–10^5 Hz. As shown in **Figures 5Ba,5Bb**, the semicircle diameter of bare SPE is larger than bare GCE, which indicated a large charge transfer resistance at the interface between electrode and electrolyte composed of 0.1 M KCl and 5 mM $[Fe(CN)_6]^{3-/4-}$. The EIS analysis of Fe_3O_4-Au-IL/SPE and $(BiO)_2CO_3$-rGO-Nafion/SPE can be seen in **Figures 5Bc,Bd**, respectively, which pointing out an increasing trend compared with bare SPE. A possible reason for this phenomenon can be ascribed to the poor electrical conductivity of Fe_3O_4 and Nafion. The analysis results of EIS were consistent with those of CV and our previous investigation results as well (Zhao et al., 2020; Sedki et al., 2021).

CFD Simulation of Flow Device Fabrication

The computational fluid dynamic (CFD) simulation (Malecha and Golonka, 2006; Malecha et al., 2011) was carried out to optimize the structure of the flow cell using COMSOL Multiphysics, and consequently obtain the optimum efficiency of deposition and stripping for the stripping voltammetry detection of HMIs. An incompressible 2D Navier–Stokes (NS) flow model was applied in the simulation of the flow characteristics in the flow cell. The flow along the inside wall of the flow cell was considered as a no-slip condition. Additionally, the water was used as an example of fluid for the CFD simulation with a density of 1,000 kg/m^3 and a dynamic viscosity of 0.89 cP (Vasudev et al., 2013). **Figure 6** shows the picture of real flow cell with specific dimension. The actual size of the desirable 3D printed flow cell was ~1 mm high, ~1 cm wide and ~2.5 cm long. According to the **Eqs 1, 2**, the calculated value of Reynolds number (Re) of the flow cell for a velocity of 0.012 m/s was around 24.27, which indicates that flow is laminar (Re < 2200).

$$Re = \frac{\rho u L}{\mu} \tag{1}$$

$$Dh = \frac{4A}{P} \tag{2}$$

where μ, u and ρ were the dynamic viscosity, velocity and density of the fluid, respectively. In addition, L is the characteristic linear

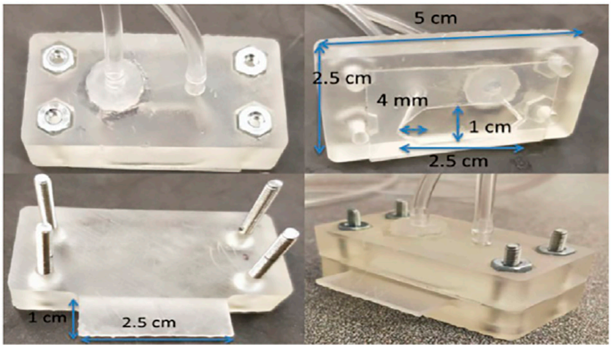

FIGURE 6 | Optical images of the flow cell.

dimension; *Dh* is the hydraulic diameter of the pipe; *A* is the cross-sectional area; and *P* is the wetted perimeter.

Taking the processes of electrodeposition and stripping of the HMIs and the characteristics of the fluid into account, the equations of convection-diffusion (3) and NS (4) were used here.

$$\frac{\partial c}{\partial t} = D\nabla^2 c - u \cdot \nabla c \tag{3}$$

$$\rho\left(\frac{\partial u}{\partial t} + u \cdot \nabla u\right) = -\nabla p + \mu\nabla^2 u + f \tag{4}$$

where u, μ and ρ are velocity, dynamic viscosity and density of the fluid, respectively. Moreover, c and D are the concentration and diffusion coefficient of the species, respectively. Additionally, p is the pressure and f is the external force.

To begin, we investigated and optimized the effect of positioning the inlet and outlet on the top (same side) of the rectangular flow cell by the simulation of flow field at different fluid velocity, i.e. 1 μm/s, 100 μm/s and 4 mm/s, at the inlet with a no-slip boundary condition (**Figure 7A**). According the results of flow field simulation, small vortices were formed along with "dead zones," i.e., regions without the distribution of flow, which can result in a negative effect on the deposition of HMs on the electrode. Moreover, when the fluid velocity increases to a high value, the samples solution will directly pass through the flow cell from inlet to outlet with a short residence time.

We next simulated the flow field trajectory in the flow cell with the inlet and outlet on opposite side of rectangle cell, as shown in **Figure 7B**. The results show that the flow field trajectories were uniformly distributed across the flow cell, but there were still some "dead zones." Based on this simulation results, a modification for the previous design was carried out with a goal of enabling the shape of the flow cell match the observed elliptical flow field. The simulated flow field trajectories in the optimized flow cell with ellipse shape is shown in **Figure 7C**, which indicated that the "dead zones" was efficiently eliminated. Furthermore, a uniformly distributed flow field can be also found in the elliptic cell.

Optimization of Detection Parameters

To obtain a low detection limit and a high sensitivity, the effect of deposition potential and time on the stripping voltammetry

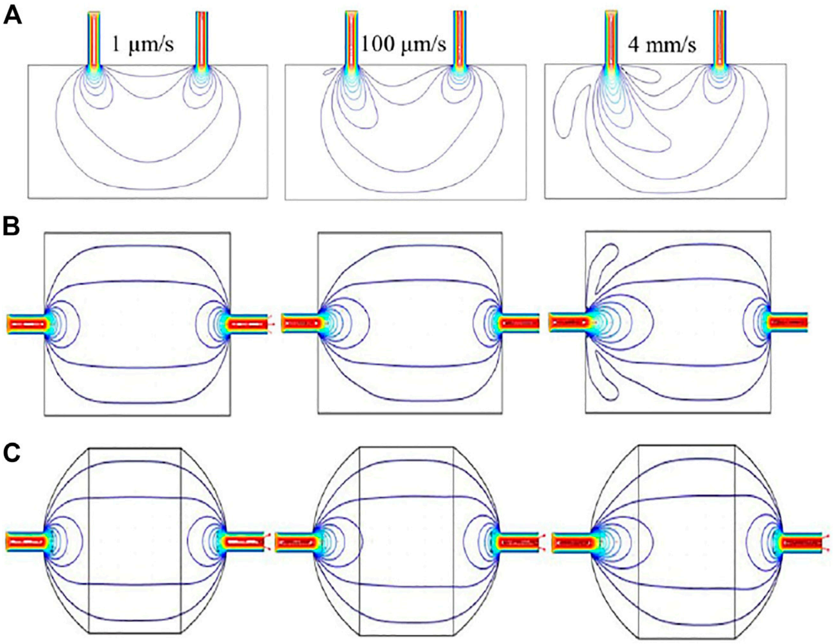

FIGURE 7 | Results of CFD simulation in **(A)** square chamber (inlet and outlet are on the same side), **(B)** square chamber (inlet and outlet are on each side), and **(C)** elliptical chamber (inlet and outlet are on each side).

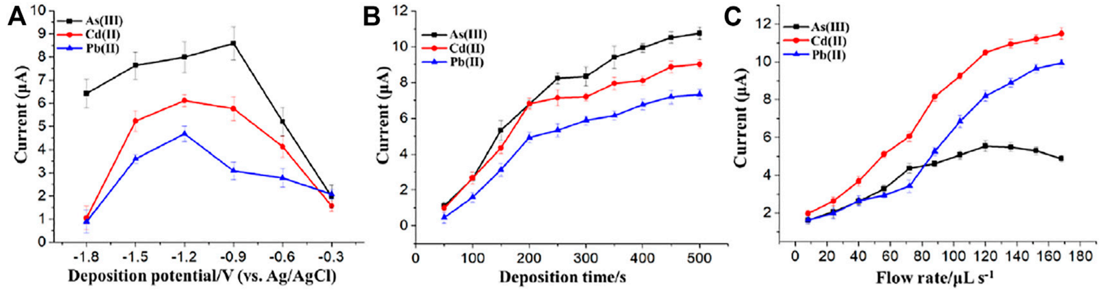

FIGURE 8 | (A) Effects of the **(A)** deposition potential, **(B)** deposition time and **(C)** flow rate on the stripping response of As(III), Cd(II), and Pb(II). Each data point is an average of 3 measurements from 3 electrodes and error bars represent ±1 standard deviation.

response were examined using the flow system containing 50 μg/L As(III) and 20 μg/L each of Pb(II) and Cd(II) in a wide range of parameter values. Deposition potential over a range of −0.3 V to −1.8 V was investigated, as shown in **Figure 8A**, where a highest stripping current can be found at the potential of −1.2 V for Pb(II) and Cd(II) and −0.9 V for As(III). Therefore, deposition potentials of −0.9 V for As(III) and −1.2 V for Cd(II) and Pb(II) were chosen for the following experiments.

The influence of deposition time on stripping voltammetry response of different modified electrodes is presented in **Figure 8B**. The stripping voltammetry responses of Pb(II) and Cd(II) and As(III) were slightly changed after the deposition time reached a specific value from the range of 50–500 s. Taking both the efficiency and sensitivity into account, 200 and 250 s were selected as the deposition time and used for the stripping voltammetry detection of Pb(II)/Cd(II) and As(III), respectively, in subsequent experiments.

As shown in **Figure 8C**, the optimal value of the delivery flow rate was investigated. For the flow injection analysis of 30 μg/L each of Pb(II) and Cd(II), the stripping peak currents rapidly increased when the flow rate increased from 8 to 120 μL/s and increased slightly from 120 to 168 μL/s. However, the stripping peak currents of 20 μg/L As(III) began to decrease when the flow rate was above 120 μL/s. In order to reduce the consumption of the reagents and the samples and increase the preconcentration efficiency, 120 μL/s was selected as the flow rate for the flow injection analysis of the three HMIs. The reasons for the decrease of the stripping current of As(III) as the flow rate increased above 120 μL/s can be explained as follows. The effect of flow rate on the stripping currents of HMIs was determined by the compromise between the thickness of diffusion layer and the time of residence. The time of residence at a lower flow rate was longer while the diffusion layer was thicker, which lead to a decrease of the As(III) stripping voltammetry response. However, the time of residence was too short at a higher flow rate (Kokkinos et al., 2016), although the thickness of the diffusion layer decreased.

Investigation of Electrode Precision

In order to verify the detection performance of the proposed electrodes, i.e., Fe_3O_4-Au-IL/SPE and $(BiO)_2CO_3$-rGO-Nafion/SPE, inter-electrode precision was investigated by the repetitive SWASV measurements of 20 μg/L Pb(II), Cd(II), and As(III) using five different electrodes, and reproducible results can be observed with relative standard deviations (RSDs) of 4.53% for Cd(II), 5.54% for Pb(II), and 3.36% for As(III). Additionally, intra-electrode precision of the proposed electrodes was further investigated by the five repeated SWASV measurements of 30 μg/L Pb(II), Cd(II), and As(III) using one electrode, which the RSDs were 2.68%, 2.95%, and 2.28% for Cd(II), Pb(II), and As(III), respectively. The proposed electrodes exhibited excellent inter-

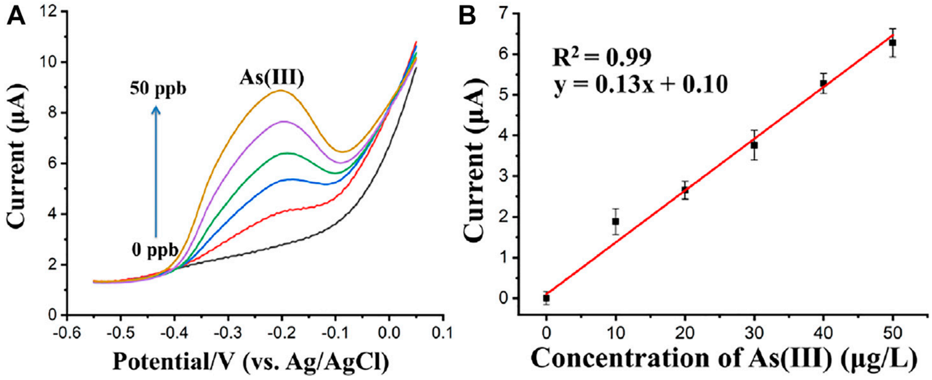

FIGURE 9 | (A) Square wave anodic stripping voltammograms of As(III) (0, 10, 20, 30, 40, and 50 μg/L). **(B)** The calibration curves for As(III). Each data point is an average of 3 measurements from 3 electrodes and error bars represent ±1 standard deviation.

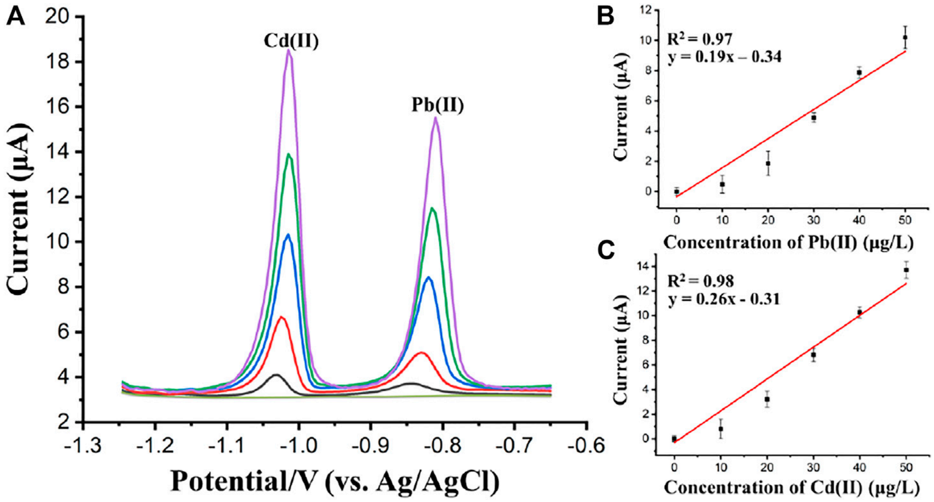

FIGURE 10 | (A) Square wave anodic stripping voltammograms of Cd(II) and Pb(II) (0, 10, 20, 30, 40, and 50 μg/L). The calibration curves for Pb(II) **(B)**, and Cd(II) **(C)**. Each data point is an average of 3 measurements from 3 electrodes and error bars represent ±1 standard deviation.

TABLE 1 | Comparison of different flow devices used in the detection of HMs.

Flow device	Deposition time	HMs	LOD
Redha et al. (2009)	500 s/300 s	Cu(II)/Pb(II)	4.4 ppb/5.9 ppb
Hong et al. (2016)	180 s/180 s	Cd(II)/Pb(II)	0.5 ppb/0.2 ppb
Kokkinos et al. (2016)	114 s	Pb(II)	0.5 ppb
Sun et al. (2017)	240 s	Pb(II)	0.2 ppb
Henríquez et al. (2012)	200 s	Cd(II)	0.79 ppb
This paper	200 s/250 s	Cd(II) and Pb(II)/As(III)	0.8 and 1.2 ppb/2.4 ppb

TABLE 2 | Results of multiplexed detection of Cd(II), Pb(II), and As(III) in simulated water samples.

Sample no	The concentrations of water samples before spiking (μg/L)			Added (μg/L)	The concentrations of water samples after spiking (μg/L)			Recovery (%)		
	Cd(II)	Pb(II)	As(III)		Cd(II)	Pb(II)	As(III)	Cd(II)	Pb(II)	As(III)
1	4.75	9.62	15.86	5	9.53	14.32	20.63	95.37	96.88	98.55
2	9.79	14.54	4.39	10	19.46	24.38	14.26	96.63	98.90	97.04
3	14.62	4.8	10.34	15	29.82	19.65	25.17	101.37	96.88	98.36

electrode and intra-electrode precision in repeated SWASV measurements of target metal ions under the optimal conditions. Moreover, the stability of the proposed electrodes was satisfying, as the stripping response of the proposed electrodes for Cd(II), Pb(II), and As (III) hardly changed after keeping in air for 1 week, which meet the detection requirement of wastewater.

Quantitative Detection of HMIs Using the Flow System

After the optimization of the SWASV parameters and flow rate, the flow system was applied in the detection of Cd(II), Pb(II), and As(III) in acetate buffer solution. In the case of As(III) detection, as shown in **Figure 9A**, Fe_3O_4-Au-IL modified electrode was used as WE with a deposition potential of –0.9 V for 250 s. The concentration of As(III) was proportional to its corresponding stripping peak current over a concentration range from 0 μg/L to 50 μg/L based on the optimal parameters obtained above, in which the correlation coefficient and equation of the linear regression were $R^2 = 0.99$ and Peak current = 0.13*Concentration of As(III) + 0.1, respectively, as shown in **Figure 9B**. The standard deviations of the slope and intercept of the linear regression equation were 0.005 and 0.133, respectively. Additionally, the limit of detection (LOD) of the Fe_3O_4-Au-IL modified electrode integrated in the proposed flow injection system for the stripping voltammetry analysis was 2.4 μg/L (S/N = 3). The LOD was calculated based on the equation of LOD = 3 × SD/S, in which SD is the standard deviation of blank response and S is the slope of calibration plot.

The detection performance of the proposed flow system was also verified by the analysis of Cd(II) and Pb(II) using SWASV. **Figure 10A** presents SWASV curves for different concentrations of Pb(II) and Cd(II) obtained at $(BiO)_2CO_3$-rGO-Nafion/SPE in acetate buffer (pH 5.0). The measurements of the SWASV were carried out using a deposition potential of −1.2 V for 200 s with a potential scanning from −1.25 V to −0.65 V in the stripping step. The stripping voltammetry responses for Pb(II) and Cd(II) showed monotonic linear relationship with increasing concentrations over a range of 0–50 μg/L, which can be seen in the calibration plots with linear regression analyses, as shown in **Figures 10B,C**, respectively. The regression equations were obtained as, Peak current = 0.19*Concentration of Pb(II)–0.34 (R^2 = 0.97) for Pb(II); and Peak current = 0.26*Concentration of Cd(II)–0.31 for Cd(II). The standard deviations of the slope and intercept of the linear regression equations for Pb(II) and Cd(II) were 0.018 and 0.469, 0.020, and 0.473 respectively. The LODs were estimated to be 1.2 μg/L for Pb(II) and 0.8 μg/L for Cd(II), respectively. The interference of non-target ions, such as Mg^{2+}, K^+, Na^+, Fe^{2+}, Mn^{2+}, Zn^{2+}, Ca^{2+}, Cu^{2+}, Cl^-, F^-, NO_3^-, CO_3^{2-}, PO_4^{2-} and SO_4^{2-} at 10^2-fold higher concentrations than As(III) and 10^4-fold higher concentrations than Pb(II) and Cd(II) on the stripping responses of target HMIs was investigated. The results showed that, amongst the non-target ions, there was a small interference from Zn(II) on Pb(II) and Cd(II) detection at the $(BiO)_2CO_3$-rGO-Nafion/SPE. However, the concentration of Zn(II) in most waters is at trace level, which would not make a significant influence on the stripping current of Cd and Pb (Zhao et al., 2020; Sedki et al., 2021). Additionally, the results also showed peak current decrease of ~28.56 and ~24.92%, respectively, for Cd(II) and Pb(II) at the $(BiO)_2CO_3$-rGO-Nafion/SPE in presence of 10^4 fold higher Cu(II) concentration and ~18.95% for As(III) at the Fe_3O_4-Au-IL/SPE in presence of 10^2 fold higher concentration of Cu(II). However, this would not make a significant influence on the stripping currents of target HMIs as the concentration of Cu(II) in most waters is at trace level. Furthermore, masking agent, such as hexacyanoferrate (II), that mask copper effectively without having a detrimental effect on the responses of target HMIs can be used to block Cu(II) interference (Crowley and Cassidy, 2002; Zhao et al., 2016). Furthermore, the detection performance comparison of several different reported flow devices are shown in **Table 1**. According to the results presented in **Table 1**, the proposed 3D-printed flow cell integrated with a nanocomposites modified SPE exhibited a comparable and even lower detection limit and less deposition time. Moreover, the proposed flow system was easy to fabricate with a low cost, and finally achieved the detection of Pb(II), Cd(II), and As(III) serially.

Application to Simulated River Water Samples

The stripping voltammetry analysis of Pb(II), Cd(II), and As(Ⅲ) in simulated/synthetic water samples was performed using the proposed flow system to estimate the applicability of the proposed platform composed of a 3D printed flow cell device coupled to a flexible SPE comprising two sensing nanocomposite modified working electrodes. The procedure of simulated river water experiment can be described as follows: First, the measurement was carried out for the initial water sample, and the corresponding results were obtained, i.e., the concentrations of water samples before spiking, which are listed in the second column of **Table 2**. After that, the standard solutions of specific HMIs were added into the water samples, consequently, the concentrations of water samples after spiking were obtained, i.e., the concentrations of water samples after spiking, which are listed in the fourth column of **Table 2**. As shown in **Table 2**, the average recoveries of Pb(II), Cd(II), and As(Ⅲ) were calculated to be 97.55%, 97.79%, and 97.98%, respectively, demonstrating excellent accuracy and selectivity of the sensor system for the targets even in presence of very high concentration of ions such as Mg^{2+}, K^+, Na^+, NH_4^+ Ca^{2+}, Cl^-, NO_3^- and citrate, and the feasibility/potential of the proposed system for environmental monitoring of Pb(II), Cd(II), and As(Ⅲ) in complex water samples.

CONCLUSION

In this paper, a flexible and disposable SPE for the stripping voltammetry measurement of Cd(II), Pb(II), and As(Ⅲ) coupled to a 3D-printed flow cell has been developed. The SPE integrated two different working electrodes modified by $(BiO)_2CO_3$-rGO-Nafion nanocomposite and Fe_3O_4-Au-IL nanocomposite for the SWASV determination of Cd(II)/Pb(II) and As(Ⅲ), respectively, which efficiently enhanced the sensitivity of the sensor. The design of the 3D printed flow cell was optimized by the CFD simulation to ensure efficient deposition of HMIs. The morphology and electrochemical property of different modified electrodes were also investigated. Additionally, experimental parameters for electrochemical detection of HMIs coupled with flow cell (e.g., flow rate, deposition period, and deposition potential) were optimized. The flow cell coupled with nanocomposite-modified multiplexed SPE provided effective and rapid detection of HMIs with low LODs and excellent recovery, which suggests a potential for future application in automated in-line detection of HMIs in the field.

DATA AVAILABILITY STATEMENT

The original contributions presented in the study are included in the article/**Supplementary Material**, further inquiries can be directed to the corresponding author.

AUTHOR CONTRIBUTIONS

GZ was responsible for the modification of sensors, electrochemical measurements and original draft preparation. T-TT was responsible for the design and fabrication of the microfluidic device and the revision of the manuscript. SM was responsible for the fabrication of SPE. MS was responsible for the synthesis and characterization of the materials. AM, NM, and DJ were responsible for conceptualization, supervision, project administration, funding acquisition and preparation of the manuscript.

FUNDING

This research was supported by the Department of Energy under award number FE0030456. AM acknowledges the financial support of W. Ruel Johnson Chair.

SUPPLEMENTARY MATERIAL

The Supplementary Material for this article can be found online at: https://www.frontiersin.org/articles/10.3389/fchem.2022.815805/full#supplementary-material

REFERENCES

Alpízar, J., Cladera, A., Cerdà, V., Lastres, E., García, L., and Catasús, M. (1997). Simultaneous Flow Injection Analysis of Cadmium and lead with Differential Pulse Voltammetric Detection. *Anal. Chim. Acta* 340, 149–158. doi:10.1016/S0003-2670(96)00547-8

Ambrosi, A., Moo, J. G. S., and Pumera, M. (2016). Helical 3D-Printed Metal Electrodes as Custom-Shaped 3D Platform for Electrochemical Devices. *Adv. Funct. Mater.* 26, 698–703. doi:10.1002/adfm.201503902

Andrew Clayton, T., Lindon, J. C., Cloarec, O., Antti, H., Charuel, C., Hanton, G., et al. (2006). Pharmaco-metabonomic Phenotyping and Personalized Drug Treatment. *Nature* 440, 1073–1077. doi:10.1038/nature04648

Au, A. K., Huynh, W., Horowitz, L. F., and Folch, A. (2016). 3D-printed Microfluidics. *Angew. Chem. Int. Ed.* 55, 3862–3881. doi:10.1002/anie.201504382

Becker, H., and Locascio, L. E. (2002). Polymer Microfluidic Devices. *Talanta* 56, 267–287. doi:10.1016/S0039-9140(01)00594-X

Bi, Z., Chapman, C. S., Salaün, P., and van den Berg, C. M. G. (2010). Determination of Lead and Cadmium in Sea- and Freshwater by Anodic Stripping Voltammetry with a Vibrating Bismuth Electrode. *Electroanalysis* 22, 2897–2907. doi:10.1002/elan.201000429

Chen, C., Niu, X., Chai, Y., Zhao, H., and Lan, M. (2013). Bismuth-based Porous Screen-Printed Carbon Electrode with Enhanced Sensitivity for Trace Heavy Metal Detection by Stripping Voltammetry. *Sensors Actuators B Chem.* 178, 339–342. doi:10.1016/j.snb.2012.12.109

Crowley, K., and Cassidy, J. (2002). Trace Analysis of Lead at a Nafion-Modified Electrode Using Square-Wave Anodic Stripping Voltammetry. *Electroanalysis* 14, 15–16. doi:10.1002/1521-4109(200208)14:15/16<1077:aid-elan1077>3.0.co;2-3

Davis, A. C., Calloway, C. P., Jr, and Jones, B. T. (2007). Direct Determination of Cadmium in Urine by Tungsten-Coil Inductively Coupled Plasma Atomic Emission Spectrometry Using Palladium as a Permanent Modifier. *Talanta* 71, 1144–1149. doi:10.1016/j.talanta.2006.06.005

Economou, A. (2010). Recent Developments in On-Line Electrochemical Stripping Analysis-An Overview of the Last 12 Years. *Anal. Chim. Acta* 683, 38–51. doi:10.1016/j.aca.2010.10.017

Erlenkötter, A., Kottbus, M., and Chemnitius, G. C. (2000). Flexible Amperometric Transducers for Biosensors Based on a Screen Printed Three Electrode System. *J. Electroanal. Chem.* 481, 82–94. doi:10.1016/s0022-0728(99)00491-x

Galani-Nikolakaki, S., Kallithrakas-Kontos, N., and Katsanos, A. A. (2002). Trace Element Analysis of Cretan Wines and Wine Products. *Sci. Total Environ.* 285, 155–163. doi:10.1016/S0048-9697(01)00912-3

Ge, L., Yan, J., Song, X., Yan, M., Ge, S., and Yu, J. (2012). Three-dimensional Paper-Based Electrochemiluminescence Immunodevice for Multiplexed Measurement of Biomarkers and point-of-care Testing. *Biomaterials* 33, 1024–1031. doi:10.1016/j.biomaterials.2011.10.065

Gross, B. C., Erkal, J. L., Lockwood, S. Y., Chen, C., and Spence, D. M. (2014). Evaluation of 3D Printing and its Potential Impact on Biotechnology and the Chemical Sciences. *Anal. Chem.* 86, 3240–3253. doi:10.1021/ac403397r

Henríquez, C., Laglera, L. M., Alpizar, M. J., Calvo, J., Arduini, F., and Cerdà, V. (2012). Cadmium Determination in Natural Water Samples with an Automatic Multisyringe Flow Injection System Coupled to a Flow-Through Screen Printed Electrode. *Talanta* 96, 140–146. doi:10.1016/j.talanta.2012.01.032

Hong, Y., Wu, M., Chen, G., Dai, Z., Zhang, Y., Chen, G., et al. (2016). 3D Printed Microfluidic Device with Microporous Mn2O3-Modified Screen Printed Electrode for Real-Time Determination of Heavy Metal Ions. *ACS Appl. Mater. Inter.* 8 (48), 32940–32947. doi:10.1021/acsami.6b10464

Jiang, Y.-Y., Wang, K., Xu, C.-Z., Yang, X.-D., and Li, H.-H. (2013). Application of Alizarin/graphene-Chitosan Modified Electrode on Detection of Human Telomere DNA. *Chin. J. Anal. Chem.* 41, 481–487. doi:10.1016/S1872-2040(13)60641-6

Johnson, B. N., Lancaster, K. Z., Zhen, G., He, J., Gupta, M. K., Kong, Y. L., et al. (2015). 3D Printed Anatomical Nerve Regeneration Pathways. *Adv. Funct. Mater.* 25, 6205–6217. doi:10.1002/adfm.201501760

Kenawy, I. M. M., Hafez, M. A. H., Akl, M. A., and Lashein, R. R. (2000). Determination by AAS of Some Trace Heavy Metal Lons in Some Natural and Biological Samples after Their Preconcentration Using Newly Chemically Modified Chloromethylated Polystyrene-PAN Ion-Exchanger. *Anal. Sci.* 16, 493–500. doi:10.2116/analsci.16.493

Kokkinos, C., Economou, A., Goddard, N. G., Fielden, P. R., and Baldock, S. J. (2016). Determination of Pb(II) by Sequential Injection/stripping Analysis at All-Plastic Electrochemical Fluidic Cells with Integrated Composite Electrodes. *Talanta* 153, 170–176. doi:10.1016/j.talanta.2016.03.025

Kolesky, D. B., Truby, R. L., Gladman, A. S., Busbee, T. A., Homan, K. A., and Lewis, J. A. (2014). 3D Bioprinting of Vascularized, Heterogeneous Cell-Laden Tissue Constructs. *Adv. Mater.* 26, 3124–3130. doi:10.1002/adma.201305506

Leca, B., and Blum, L. J. (2000). Luminol Electrochemiluminescence with Screen-Printed Electrodes for Low-Cost Disposable Oxidase-Based Optical Sensors. *Analyst* 125, 789–791. doi:10.1039/b002284p

Malecha, K., and Golonka, L. J. (2006). "CFD Simulations of LTCC Based Microsystems," in 2006 29th International Spring Seminar on Electronics Technology, St. Marienthal, Germany, 10–14 May, 2006 (IEEE), 156–160. doi:10.1109/ISSE.2006.365377

Malecha, K., Pijanowska, D. G., Golonka, L. J., and Kurek, P. (2011). Low Temperature Co-fired Ceramic (LTCC)-based Biosensor for Continuous Glucose Monitoring. *Sensors Actuators B Chem.* 155, 923–929. doi:10.1016/j.snb.2011.01.002

Murphy, S. V., and Atala, A. (2014). 3D Bioprinting of Tissues and Organs. *Nat. Biotechnol.* 32, 773–785. doi:10.1038/nbt.2958

Pandey, S. K., Singh, P., Singh, J., Sachan, S., Srivastava, S., and Singh, S. K. (2016). Nanocarbon-based Electrochemical Detection of Heavy Metals. *Electroanalysis* 28, 2472–2488. doi:10.1002/elan.201600173

Panov, V. P., Zykova, I. V., and Chekrenev, S. A. (2008). Heavy Metals: The Industry and Environmental protection. *Fibre Chem.* 40, 241–245. doi:10.1007/s10692-008-9045-2

Puy-Llovera, J., Pérez-Ràfols, C., Serrano, N., Díaz-Cruz, J. M., Ariño, C., and Esteban, M. (2017). Selenocystine Modified Screen-Printed Electrode as an Alternative Sensor for the Voltammetric Determination of Metal Ions. *Talanta* 175, 501–506. doi:10.1016/j.talanta.2017.07.089

Redha, Z. M., Baldock, S. J., Fielden, P. R., Goddard, N. J., Brown, B. J. T., Haggett, B. G., et al. (2009). Hybrid Microfluidic Sensors Fabricated by Screen Printing and Injection Molding for Electrochemical and Electrochemiluminescence Detection. *Electroanalysis* 21 (3-5), 422–430. doi:10.1002/elan.200804415

Reyes, D. R., Iossifidis, D., Auroux, P.-A., and Manz, A. (2002). Micro Total Analysis Systems. 1. Introduction, Theory, and Technology. *Anal. Chem.* 74, 2623–2636. doi:10.1021/ac0202435

Sedki, M., Zhao, G., Ma, S., Jassby, D., and Mulchandani, A. (2021). Linker-Free Magnetite-Decorated Gold Nanoparticles (Fe3O4-Au): Synthesis, Characterization, and Application for Electrochemical Detection of Arsenic (III). *Sensors* 21, 883. doi:10.3390/s21030883

Silva, E. L., Roldan, P. d. S., and Giné, M. F. (2009). Simultaneous Preconcentration of Copper, Zinc, Cadmium, and Nickel in Water Samples by Cloud point Extraction Using 4-(2-Pyridylazo)-Resorcinol and Their Determination by Inductively Coupled Plasma Optic Emission Spectrometry. *J. Hazard. Mater.* 171, 1133–1138. doi:10.1016/j.jhazmat.2009.06.127

Sun, Q., Wang, J., Tang, M., Huang, L., Zhang, Z., Liu, C., et al. (2017). A New Electrochemical System Based on a Flow-Field Shaped Solid Electrode and 3D-Printed Thin-Layer Flow Cell: Detection of Pb2+ Ions by Continuous Flow Accumulation Square-Wave Anodic Stripping Voltammetry. *Anal. Chem.* 89, 5024–5029. doi:10.1021/acs.analchem.7b00383

Tu, J., Gan, Y., Liang, T., Wan, H., and Wang, P. (2018). A Miniaturized Electrochemical System for High Sensitive Determination of Chromium(VI) by Screen-Printed Carbon Electrode with Gold Nanoparticles Modification. *Sensors Actuators B Chem.* 272, 582–588. doi:10.1016/j.snb.2018.06.006

Vasudev, A., Kaushik, A., Tomizawa, Y., Norena, N., and Bhansali, S. (2013). An LTCC-Based Microfluidic System for Label-free, Electrochemical Detection of Cortisol. *Sensors Actuators B Chem.* 182, 139–146. doi:10.1016/j.snb.2013.02.096

Verma, N., and Singh, M. (2005). Biosensors for Heavy Metals. *Biometals* 18, 121–129. doi:10.1007/s10534-004-5787-3

Wan, Z., Xu, Z., and Wang, J. (2006). Flow Injection On-Line Solid Phase Extraction for Ultra-trace lead Screening with Hydride Generation Atomic Fluorescence Spectrometry. *Analyst* 131, 141–147. doi:10.1039/b511829h

West, J., Becker, M., Tombrink, S., and Manz, A. (2008). Micro Total Analysis Systems: Latest Achievements. *Anal. Chem.* 80, 4403–4419. doi:10.1021/ac800680j

Whitesides, G. M. (2006). The Origins and the Future of Microfluidics. *Nature* 442, 368–373. doi:10.1038/nature05058

Wu, W., Wu, P., Yang, F., Sun, D.-l., Zhang, D.-X., and Zhou, Y.-K. (2018). Assessment of Heavy Metal Pollution and Human Health Risks in Urban Soils Around an Electronics Manufacturing Facility. *Sci. Total Environ.* 630, 53–61. doi:10.1016/j.scitotenv.2018.02.183

Wuana, R. A., and Okieimen, F. E. (2011). Heavy Metals in Contaminated Soils: a Review of Sources, Chemistry, Risks and Best Available Strategies for Remediation. *ISRN Ecol.* 2011, 1–20. doi:10.5402/2011/402647

Zhao, G., and Liu, G. (2019). Electrochemical Deposition of Gold Nanoparticles on Reduced Graphene Oxide by Fast Scan Cyclic Voltammetry for the Sensitive Determination of As(III). *Nanomaterials* 9, 41. doi:10.3390/nano9010041

Zhao, G., Yin, Y., Wang, H., Liu, G., and Wang, Z. (2016). Sensitive Stripping Voltammetric Determination of Cd(II) and Pb(II) by a Bi/multi-Walled Carbon Nanotube-Emeraldine Base Polyaniline-Nafion Composite Modified Glassy Carbon Electrode. *Electrochim. Acta* 220, 267–275. doi:10.1016/j.electacta.2016.10.059

Zhao, G., Wang, H., Liu, G., and Wang, Z. (2017). Simultaneous and Sensitive Detection of Cd(II) and Pb(II) Using a Novel Bismuth Film/Ordered Mesoporous Carbon-Molecular Wire Modified Graphite Carbon Paste Electrode. *Electroanalysis* 29, 497–505. doi:10.1002/elan.201600430

Zhao, G., Sedki, M., Ma, S., Villarreal, C., Mulchandani, A., and Jassby, D. (2020). Bismuth Subcarbonate Decorated Reduced Graphene Oxide Nanocomposite for the Sensitive Stripping Voltammetry Analysis of Pb(II) and Cd(II) in Water. *Sensors* 20, 6085. doi:10.3390/s20216085

Conflict of Interest: The authors declare that the research was conducted in the absence of any commercial or financial relationships that could be construed as a potential conflict of interest.

frontiers
in Chemistry

ORIGINAL RESEARCH
published: 07 March 2022
doi: 10.3389/fchem.2022.820379

Stress-Affected Oxygen Reduction Reaction Rates on UNS S13800 Stainless Steel

Carlos M. Hangarter*, Rachel M. Anderson and Steven A. Policastro

Chemistry Division, U.S. Naval Research Laboratory, Washington, DC, United States

This work investigates the previously unexplored impact of tensile stress on oxygen reduction reaction (ORR) kinetics of a precipitation-hardened, stainless-steel fastener material, UNS S13800. ORR is known to drive localized and galvanic corrosion in aircraft assemblies and greater understanding of this reaction on structural alloys is important in forecasting component lifetime and service requirements. The mechano-electrochemical behavior of UNSS13800 was examined using amperometry to measure the reduction current response to tensile stress. Mechanical load cycles within the elastic regime demonstrated reversible electrochemical current shifts under chloride electrolyte droplets that exhibited a clear potential dependence. Strain ramping produced current peaks with a strain rate dependence, which was distinct from the chronoamperometric shifts during static tensile load conditions. Finally, mechanistic insight into the dynamic and static responses was obtained by deoxygenation, which demonstrated ORR contributions that were distinct from other reductive processes.

Keywords: galvanic corrosion, atmospheric corrosion, ORR, stress, strain, stainless-steel, mechano-electrochemistry

Edited by:
Syed Mubeen Jawahar Hussaini,
The University of Iowa, United States

Reviewed by:
Yao Yang,
Shanghai Jiao Tong University, China
Fan Yang,
Plug Power Inc., United States
Abhishek Lahiri,
Brunel University London,
United Kingdom

****Correspondence:***
Carlos M. Hangarter
carlos.hangarter@nrl.navy.mil

Specialty section:
This article was submitted to
Electrochemistry,
a section of the journal
Frontiers in Chemistry

Received: *23 November 2021*
Accepted: *31 January 2022*
Published: *07 March 2022*

Citation:
Hangarter CM, Anderson RM and Policastro SA (2022) Stress-Affected Oxygen Reduction Reaction Rates on UNS S13800 Stainless Steel.
Front. Chem. 10:820379.
doi: 10.3389/fchem.2022.820379

INTRODUCTION

Mechanical stress and strain effects on reaction kinetics are well recognized for noble metal electrocatalyst materials (Amakawa et al., 2013; Du et al., 2015; Yan et al., 2016). For Pt catalysts, elastic strain has been deconvoluted from ligand effects using a NiTi shape memory alloy substrate. Compressive strain resulted in a 52% enhancement of the oxygen reduction reaction (ORR) kinetic rate while tensile strain led to a 35% decrease of the rate constant. These effects were attributed to changes in the overlap of adsorbate bonding and anti-bonding states with the Pt d-band. The mechanism was argued to originate from increased (compression) or decreased (tension) adsorbate bonding strength when the surface coverage of reaction intermediates was decreased or increased, respectively. Similar work has also been shown for Pd monolayers, in which lattice mismatch with various substrates is employed to induce compressive and tensile strain, to produce a linear correlation with hydrogen desorption potentials, in agreement with d-band theory (Kibler et al., 2005). Additionally, a large area of nanoparticle ORR catalyst research is based on lattice strains that arise from size and alloying effects, providing a clear and significant correlation between reaction kinetics and strain on clean metal surfaces (Strasser et al., 2010).

In contrast to noble metals, structural alloys are microstructurally heterogeneous and covered with relatively thick surface oxides, on the order of nanometers, that consequently yield a more complex electrocatalytic response to stress. Surface oxides are essentially dielectric, or semiconducting, thin films that span a range of conductivities. They are also subject to several distinct charge transfer mechanisms that influence their response to stress (Paola, 1989; Costa et al., 2014). Further, the passive films on structural alloys are not isomorphous. They range from amorphous to polycrystalline; typically falling within a nanocrystalline regime over alloy grains and have less order over intergranular regions (Maurice and Marcus, 2018). As a result, stress has multiple mechanistic routes to impact corrosion reaction kinetics (Chen et al., 2008; Thébault et al., 2011; Wang et al., 2014; Van den Steen et al., 2016; Hangarter C. and Policastro S. A., 2017; Hangarter C. M. and Policastro S. A., 2017; Liu et al., 2017; Palani et al., 2017; Alexander et al., 2018). Strain on pristine semiconductors induces density of states shifts that have been shown to impact charge carrier mobility (Sun et al., 2007). In addition, applied strains can drive defect formation and migration within the oxide, which the point defect model (Macdonald, 2011), has suggested can affect charge transfer rates at the metal-oxide interface. The complexity of the response of the oxide to strain suggests that there are multiple mechanisms occurring within the oxide. These can be observed, not only beyond the transition between elastic and plastic deformation of the oxide, but even within the expected elastic deformation region of the stress-strain curve for the oxide.

Vignal et al. (2001) used electrochemical impedance spectroscopy (EIS) studies to demonstrate elastic stress induced increased passive film conductivity for UNS S31600. These differences were argued to arise from film micro-plasticity above 70% of the yield strength. A separate report used a redox couple, $Ru(NH_3)_6{}^{3+/2+}$, with a scanning electrochemical microscopy (SECM) feedback loop to quantify stress-affected charge transfer. That study examined UNS S31600 and found the heterogeneous kinetic constant decreased with applied tensile stress while the transfer coefficient remained unchanged (Sun et al., 2008). A similar SECM study on UNS S30400L yielded contradictory results with a different redox mediator, $Fe(CN)_6{}^{3-/4-}$. This discrepancy was attributed to adsorption differences in the supporting electrolyte (KNO_3 vs. KSO_4) as well as chemical and electronic structure differences of the passive film. Qualitative agreement with the latter was observed for acid treated UNS S30200 stainless steel springs under tensile stress, but the magnitude was greater, essentially doubling the kinetic constant. Taken as a whole, these reports indicate that the kinetic responses to elastic tensile stress for austenitic stainless steels is dependent on the material, pretreatment, and electrolyte due to passive film differences. In addition, there could also be opposing stress mechanisms at play in the elastic vs. plastic regimes (Sun et al., 2007; Sun et al., 2008; Svedruzic and Gregg, 2014; Maurice and Marcus, 2018).

The impact of stress and strain on the ORR kinetics is important from a galvanic corrosion perspective because aluminum alloys are commonly used for aircraft applications due to their high strength-to-weight ratio. However, because of the difficulty posed by the non-weldability of high-strength aluminum alloys, aircraft components are typically joined with fasteners (Boyer et al., 1984). These fasteners are usually made from stainless steel or titanium alloys that are more noble than the aluminum alloys used in airframe construction. Once electrical and ionic conductivity between the dissimilar metals is in place, galvanic corrosion can occur(Matzdorf et al., 2013; Feng et al., 2014; Feng and Frankel, 2014; Hangarter C. and Policastro S. A., 2017). This galvanic process consists of the ORR on the more noble material driving corrosion of the aluminum alloy, often at an accelerated rate. Prior work has shown that the galvanic corrosion in atmospheric environments can be more complex than what occurs under immersion conditions. Atmospheric environments are characterized by discontinuous electrolytes or droplets with unique physical and chemical constraints. These distinctions include an electrolyte that varies with temperature and humidity, with chloride concentrations from deliquescence to below seawater concentrations and oxygen diffusion lengths defined by electrolyte geometry (Schindelholz and Kelly, 2012; Liu et al., 2017; Marshall et al., 2019). The complexity of a galvanic atmospheric corrosion system is such that standard accelerated tests (e.g., ASTM B117) will often fail to produce the correct corrosion mechanisms and exhibit poor correlations with corrosion rates obtained from atmospheric exposures. Addressing the challenge of atmospheric corrosion requires targeted modeling and experimental approaches that can duplicate corrosion rates and reactions observed in relevant environments.

From an atmospheric perspective, the impact of chloride concentration on native oxide film charge transfer has yet to be examined. Recent work in dilute chloride electrolytes has demonstrated that chloride ions decreased passivity due to hindered enrichment of Cr^{3+}, Mo^{4+} and Mo^{6+} content, while increasing hydroxylation in the passive film outer layer (Wang et al., 2020). This suggests the range of chloride concentrations experienced during galvanic atmospheric corrosion likely has an impact on passive film structure and charge transport. Importantly, stress-affected charge transfer studies discussed above have been limited to austenitic stainless steels. No work to date has specifically examined stress-affected kinetics on precipitation hardened martensitic alloys, which are typically used for high strength application in the aerospace industry. Moreover, while studies with redox mediators provide insight into charge transfer behavior, their redox potential is typically more positive than that required for ORR.

This work examines the effect of stress on cathodic current rates, to include ORR, for precipitation hardened stainless steel UNS S13800 PH. Chronoamperometry was used to monitor the effect of stress profiles on ORR current in real time. A droplet electrolyte cell in an environmental chamber was utilized to attain atmospheric corrosion conditions in high chloride concentrations. Two different experimental cell configurations were used for complementary oxygenated and deoxygenated experiments that enabled further analysis of the amperometric results.

MATERIALS AND METHODS

Materials

The as-received UNS S13800 was precipitation hardened at 950°C with nominal composition indicated in **Table 1**. Sodium chloride (>99%), acetone (>99%) and isopropyl alcohol (>99%) (Fisher

TABLE 1 | Nominal composition of UNS S13800.

Cr	Ni	Mo	Al	Mn	Si	C	N	P	S	Fe
12.75	8	2.25	1.125	0.1	0.1	0.05	0.01	0.01	0.008	Balance

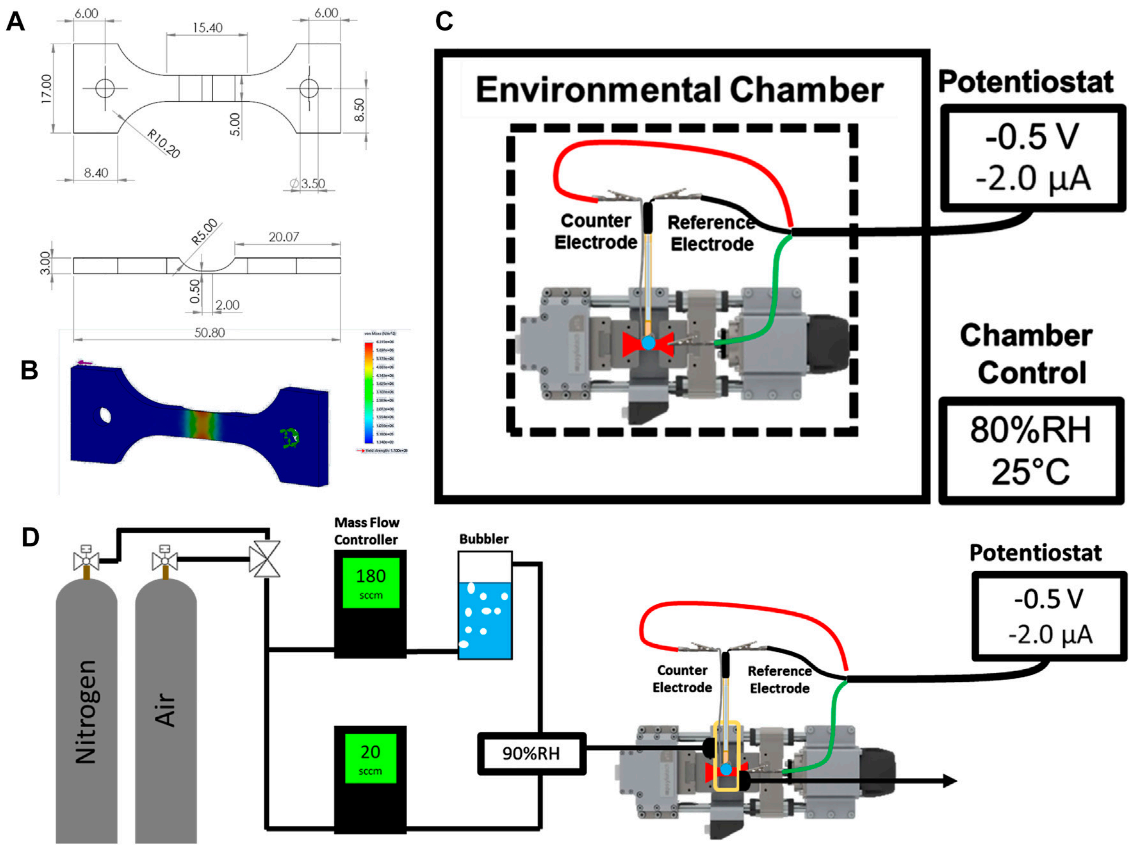

FIGURE 1 | Schematic of the machined sample (mm) **(A)** and the corresponding static stress analysis **(B)**. Schematics for the environmental chamber configuration **(C)** and gas flow cell **(D)** are shown with labeled components.

Scientific; Pittsburgh, PA, United States) were used without further purification.

Sample Preparation

UNS S13800 specimens were machined from bar stock into double-notch dogbone coupons. The dimensions and static stress analysis are shown in **Figures 1A,B**. A refining sequence of SiC paper (220P to 4000P) was used to grind the top surface down to a final notch thickness of 60–100 μm. Coupons were subsequently polished with 3 and 1 μm aqueous diamond slurries on a microfiber polishing pad. The polished coupons were washed with ultra-sonication in acetone, isopropyl alcohol, and 18 MΩ cm water for 5 min each. Cleaned coupons were dried under flowing nitrogen gas and masked to electrochemically constrain the active area above the notch region using polyester tape with a rubber-silicone adhesive blend.

Characterization

Two different configurations were used to characterize the mechano-electrochemical behavior of UNS S13800. The first configuration is shown in **Figure 1C** and consisted of a compact load frame (Psylotech, Evanston, IL, United States) fixed to an aluminum breadboard inside an environmental chamber. The chamber was used to establish the temperature and relative humidity around the system. The relative humidity for a given temperature determines the partial pressure of water at that temperature, which determines the equilibrium water activity for hygroscopic salts above the efflorescence point (Shinohara et al., 2004; Van den Steen et al., 2016; Policastro et al., 2019). Relative humidity values of 95% and 80% (at 25°C) were used to maintain concentrations of approximately 0.6 and 4.6 M NaCl, respectively (Tang et al., 1986; Tang et al., 1997; Policastro et al., 2019). The coupon was mounted to the load frame with clamp grips containing garolite spacers to prevent

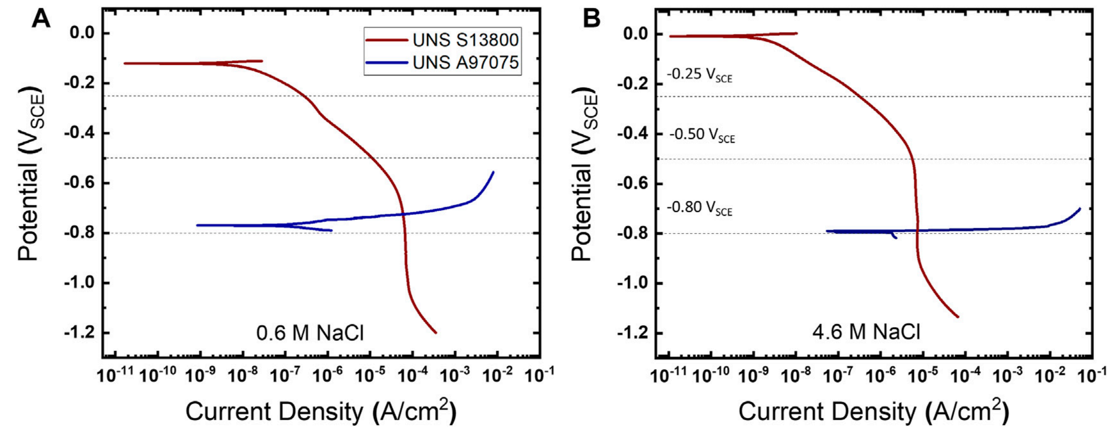

FIGURE 2 | The polarization curves for UNS S13800 and UNS A97075 in **(A)** 0.6 and **(B)** 4.6 M NaCl at 25°C.

ground loops between the load frame and the potentiostat controller. 0.6 or 4.6 M NaCl electrolyte (5–100 µl) was dispensed onto the active region of the specimen and a micromanipulator was used to position the reference and counter electrode in contact with the electrolyte. After positioning, the chamber was closed and allowed to stabilize for 30 min before initiation of the electrochemical experiments.

The second configuration (**Figure 1D**) was used to perform deoxygenated experiments with flowing gases without the use of a commercial environmental chamber. This setup, which employed a small plastic cell fixed to the specimen, enclosed the notch region of the specimen, but excluded the grip region. The cell was sealed to the specimen with marine epoxy (5200, 3M; St. Paul, MN, United States). Likewise, the reference and counter electrodes were fixed to the cell lid with marine epoxy. Threaded luer connectors were attached and sealed to the cell body for the gas inlet and outlet. The specimen was masked with polyester tape in the same way as the first setup. The relative humidity inside the small plastic cell was set by partitioning a fraction of the total gas flow through an aqueous bubbler to obtain both dry and saturated (100% RH) gas lines that were then recombined prior to entering the cell. The flow rate of each line was fixed with mass flow controllers to reach the specified relative humidity. Dry air and nitrogen were used as the flowing gas feed during oxygenated and deoxygenated experiments, respectively.

Both configurations used a Pt wire counter electrode and Ag/AgCl reference electrode. The reference electrode was checked against a saturated calomel electrode (SCE) prior to use and all potentials are reported against SCE (V_{SCE}). Chronoamperometric experiments were conducted at −0.25, −0.5 and −0.8 V_{SCE}. Mechanical load profiles conducted during chronoamperometric experiments were sequences performed with displacement control consisting of a tensile ramp, a static load, and a compressive ramp back to the pre-loaded state. Stress was measured with an inline load cell. A series of load sequences were utilized to examine strain rate effect and reproducibility.

Bulk polarization experiments were conducted in 0.6 and 4.6 M NaCl with a jacketed corrosion cell. A water circulator was used to maintain a steady temperature during experiments. Coupons were 1″ × 1″ × 1/8″ and masked to a 5/16″ diameter circle with polyester tape. A Pt mesh and SCE were used as counter and reference electrodes, respectively, with the reference electrode inside a fritted salt bridge containing saturated KCl to minimize ohmic drop. Potentiodynamic scans were performed cathodically (UNS S13800) from 0.02 V_{OCP} to −1.2 V_{SCE} and anodically (UNS A97075) −0.02 V_{OCP} to −0.6 V_{SCE} at a scan rate of 0.167 mV/s after an 18-h open circuit hold.

RESULTS

Polarization

The cathodic polarization response for UNS S13800 is overlaid with the anodic response for UNS A97075 (AA7075T6) in **Figure 2**. These polarization curves were performed in cylindrical-bodied corrosion test cells (BioLogic; Knoxville, TN, United States) containing 300 ml of either 0.6 or 4.6 M NaCl. These NaCl concentrations are of interest in atmospheric corrosion as they correspond to sea water and the equilibrium NaCl droplet concentrations at 25°C/80% RH, respectively (Tang et al., 1997). UNS S13800 has a well-defined OCP between 0.0 and −0.1 V_{SCE} which is followed by the ORR activation region until approximately −0.5 V_{SCE}, at which point the current transitions to diffusion limited ORR. In both cases onset of the hydrogen evolution reaction (HER) from water reduction occurs negative of the ORR limiting current, −1.0 V_{SCE} in 0.6 M NaCl and −0.9 V_{SCE} in the 4.6 M NaCl.

The potentials selected for the mechano-electrochemical experiments on the stainless-steel oxide were potentials at which ORR was under activation control (−0.25 V_{SCE}), mixed control (−0.5 V_{SCE}) and diffusion control (−0.8 V_{SCE}). The latter is in close proximity to galvanic corrosion potentials observed from polarization experiments in **Figure 2** (curve cross-over), which is the anticipated potential when UNS S13800 is coupled to UNS A97075. Anodic polarization of

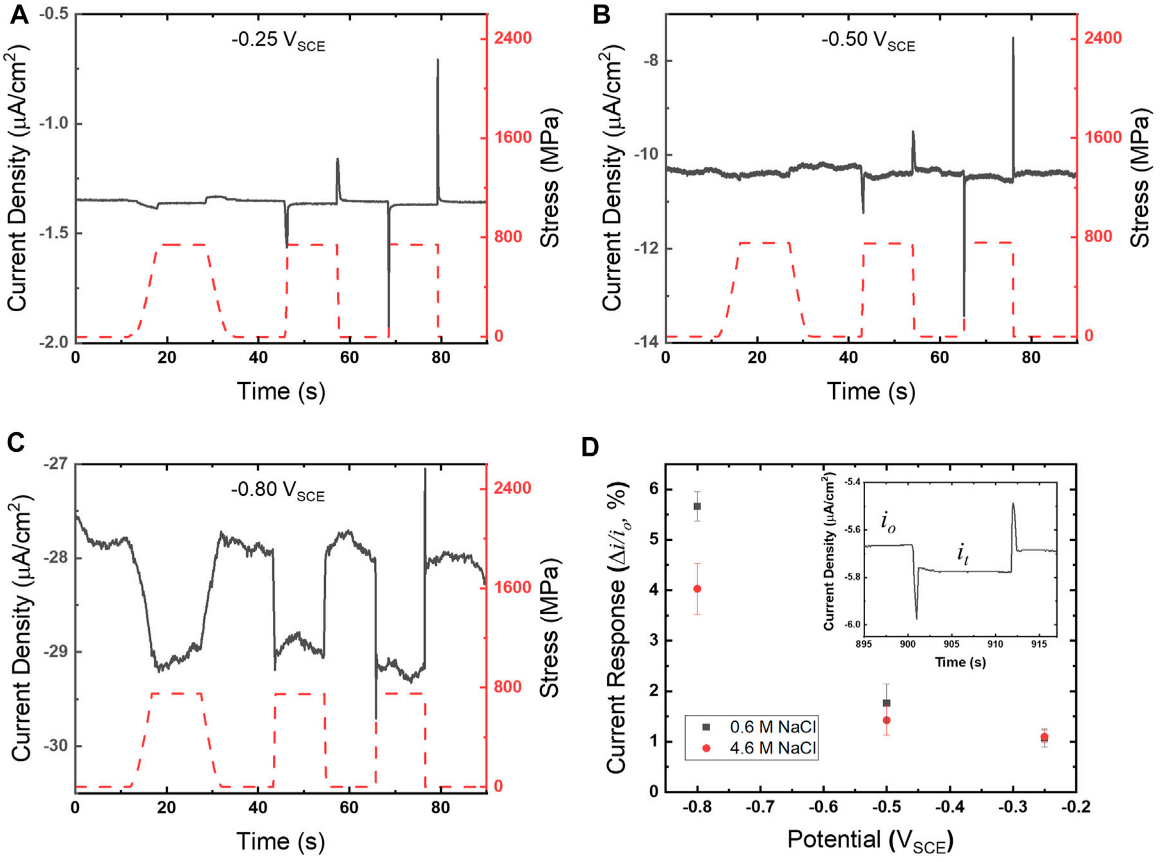

FIGURE 3 | Chronoamperograms (gray solid line, left ordinate) and corresponding stress profiles (red dashed line, right ordinate) for UNS S13800 with 25 μl of 4.6 M NaCl at 25°C and 80% RH for **(A)** −0.25 V$_{SCE}$, **(B)** −0.50 V$_{SCE}$ and **(C)** −0.80 V$_{SCE}$. Strain rates for **(A–C)** follow a sequence of 0.0002, 0.002 and 0.02/s. The current responses for 4.6 and 0.6 M NaCl determined from **Eq. 1** are shown in **(D)** as a function of potential.

UNS A97075 displays rapid activation spanning over five orders of magnitude in corrosion rate in 50 and 30 mV for the dilute and concentrated NaCl solutions, respectively. The intersection of polarization curves has been used to predict both the galvanic corrosion potential and current. In **Figures 2A,B** the galvanic current is measured at 60 μA/cm^2 and 7.4 μA/cm^2 in 0.6 and 4.6 M NaCl, respectively.

The polarization curves in **Figure 2** suggest UNS S13800-UNS A97075 galvanic couples in a 1:1 cathode to anode area ratio would be under cathodic control. This is due to the ORR diffusion limited behavior near the galvanic potential, which results in relative potential insensitivity of the ORR rate in contrast to the much smaller Tafel slope of UNS A97075. Additionally, the predicted galvanic corrosion rate from polarization curves in **Figure 1** is ~8.1 times larger in 0.6 M NaCl (60 μA/cm^2) than 4.6 M NaCl (7.4 μA/cm^2). This is in accord with the limiting diffusion current (i_l) equation:

$$i_l = \frac{nFD_{O_2}C_{O_2}}{\delta} \tag{1}$$

Equation 1 indicates the limiting current density is proportional to the Faraday constant (F), the reaction equivalent (n), oxygen diffusivity (D_{O_2}) and oxygen concentration (C_{O_2}) and inversely proportional to the diffusion thickness layer (δ). The oxygen saturation concentrations for the two NaCl concentrations reside at 214 and 68 μmol O$_2$/kg H$_2$O for 0.6 and 4.6 M NaCl, respectively(Millero et al., 2002). The oxygen diffusivities have been reported to be 1.97 × 10^{-5} and 1.40 × 10^{-5} cm^2/s for 0.6 and 4.6 M NaCl at 25°C, respectively(Mizuno and Kelly, 2013). These differences give a $D_{O_2}C_{O_2}$ ratio of 118:10, an 11 fold difference in driving force for oxygen diffusion, which is similar to the limiting current density ratio.

Chronoamperometry

Chronoamperograms for UNS S13800 were collected utilizing the experimental configuration shown in **Figure 1C**. Representative chronoamperograms, along with the overlaid concurrent stress profile (right ordinate), are shown in **Figures 3A–C**. The stress reaches values of 700–800 MPa, residing well within the elastic regime for UNS S13800 which is reported to be ~1,450 MPa (Tyler et al., 1991). Tensile holds were examined at varied strain rates that included some combination of 0.00002, 0.0002, 0.002 and 0.02/s. The measured current transients showed an increased cathodic current during the strain ramp. The cathodic current stabilized during the tensile hold and then returned to baseline values upon release to the pre-loaded state. Additionally, cathodic and anodic current peaks demarcated initiation and termination

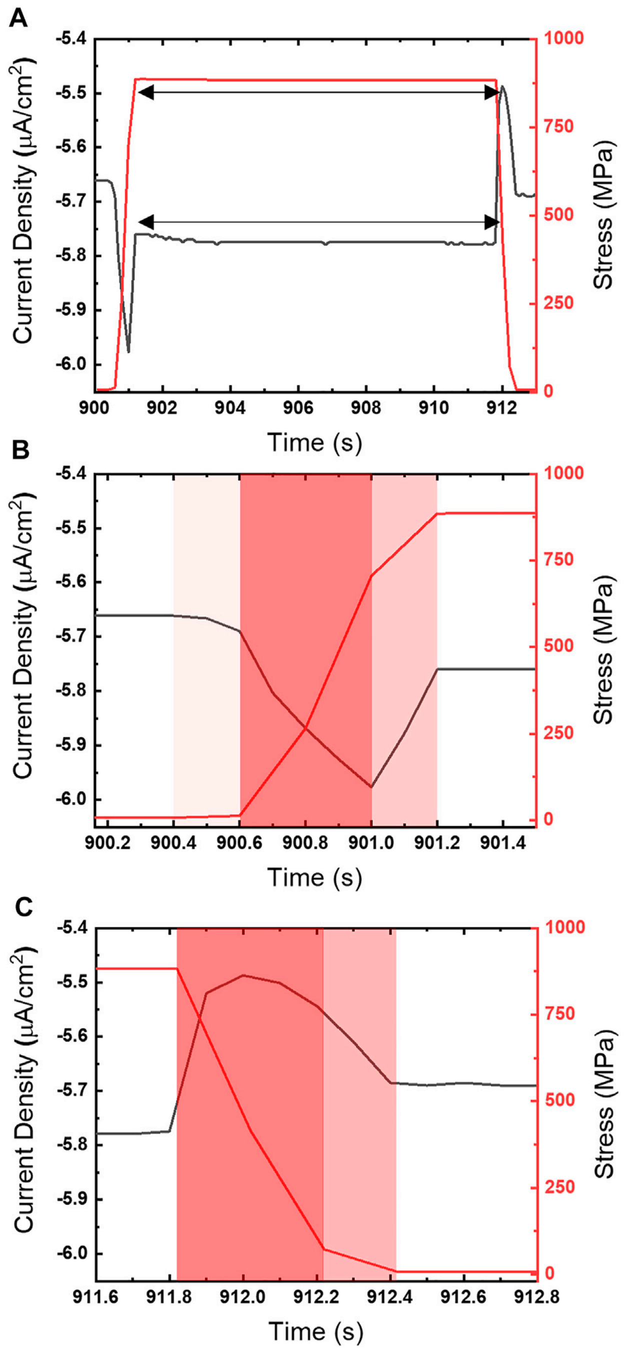

FIGURE 4 | (A) Chronoamperogram (left ordinate) overlaid with stress profile (right ordinate) for UNS S13800 under 25 µl of 4.6 M NaCl at 25°C and 80% RH at −0.50 V_{SCE}. The current response and stress profile to **(B)** tensile and **(C)** compressive ramping are also shown on a finer time scale. The nominal strain rate during ramping is 0.002/s.

of the response for the faster strain rates. Quantification of the current response to tension was determined by the difference in current under tension (i_t) and the baseline current (i_o) using the following equation:

$$R = \frac{i_t - i_o}{i_o} \times 100 \qquad (2)$$

The current response for UNS S13800 under 0.6 and 4.6 M NaCl is shown in **Figure 3B** with an inset displaying i_t and i_o regions of the current response. Values for i_t and i_o were determined from the average of current values over the 5 s just prior to tensile and compressive ramping, respectively. The current response increased monotonically with more negative potentials. Measurements performed in dilute NaCl solutions displayed a larger current response when the ORR was under diffusion limited control.

Close examination of the chronoamperometry in comparison with the stress profiles (**Figure 4**) reveal the current peaks observed during high strain rates closely follow tension ramping and relaxation steps. The cathodic peak (**Figure 4B**) can be split into a cathodic (ascending) and anodic (descending) region that correspond with the transition from the strain rate maximum (red) to a declining strain rate (pink) just prior to the static hold. The response during relaxation (**Figure 4C**) does not exhibit a distinct correlation between current direction and strain rate changes. In contrast, the anodic peak that occurs once the strain rate changes to relaxation, rapidly rises over the course of 0.2 s to a maximum value, but then turns cathodic while the strain ramp is still at 0.002/s.

DISCUSSION

Identifying the reaction processes affected by mechanical load profiles is important for interpretation of mechano-electrochemical responses on oxide covered structural alloys. From **Figure 3** the two primary amperometric responses include a shift in the reduction current during tensile holds and current peaks during strain ramps with electrochemical polarity (cathodic and anodic) that corresponds to strain direction (tensile and compressive). Although ORR is recognized as the primary reductive reaction in oxygenated environments for potentials this work examined, additional contributions could arise from oxide dynamics or even HER. Importantly, HER is also occurring at the most negative potential examined, albeit at rates 1–2 orders of magnitude smaller than ORR based on extrapolation of the HER Tafel slope in **Figure 2**.

A modified experimental configuration shown in **Figure 1D** was implemented to switch between oxygenated (air) and deoxygenated (N_2) atmospheres to better identify ORR contributions. This strategy allowed for direct comparison of amperometric baseline shifts and current peaks in oxygenated and deoxygenated environments, shown in **Figure 5** for −0.25 and −0.80 V_{SCE}, along with concurrent stress profiles (**Figure 5** bottom plots). A fine scale view of the chronoamperograms at −0.25 V_{SCE} is shown in the middle plot of **Figure 5A**. Comparison in these environments reveals the current response in N_2 (red line) is close to the baseline during the tensile hold, while a clear shift was observed in air (gray line). The N_2 ramp regions at −0.25 V_{SCE} display current peaks that are aligned and of the same approximate magnitude as the corresponding oxygenated experiments. However, an anodic oscillation is observed

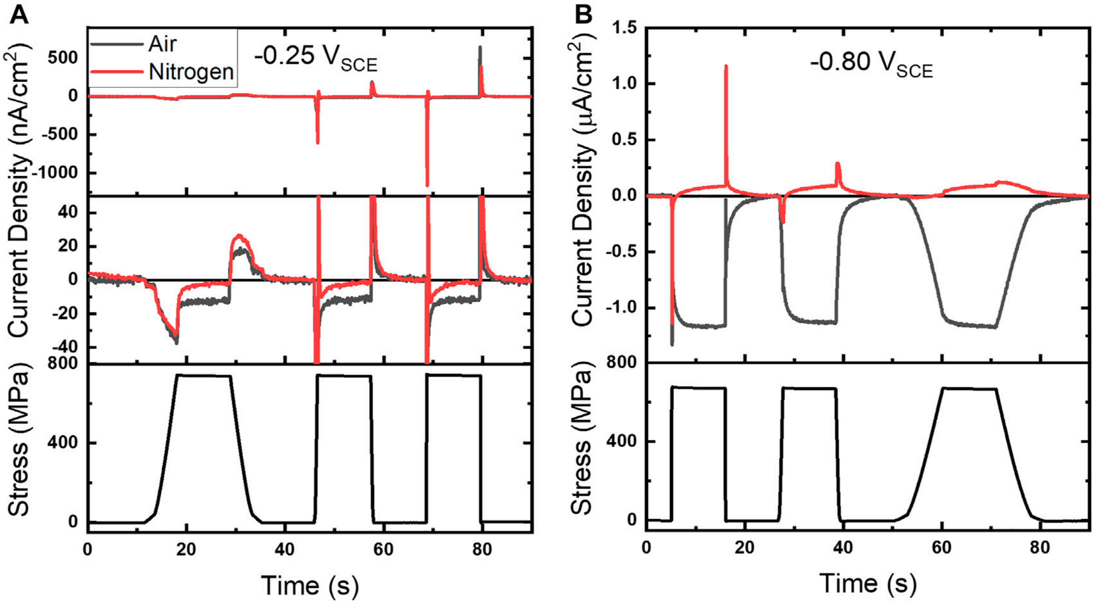

FIGURE 5 | (A) Baseline subtracted chronoamperograms under 25 µl of 4.6 M NaCl in air and nitrogen atmospheres along with corresponding stress profile at **(A)** −0.25 V_{SCE} and **(B)** −0.80 V_{SCE}. A finer scale chronoamperogram is shown in the middle plot of **(A)**.

following the cathodic peak at both 0.002 and 0.02/s. At the more negative potential, -0.80 V_{SCE}, the deoxygenated environment not only suppresses ORR but an anodic current, with respect to the baseline current, is observed for each strain rate. These results, as a whole, demonstrate the current shift during tensile holds (i_t) is primarily attributable to ORR while the current peaks are likely a conflated response to ORR and oxide dynamics.

Surface oxides play an important role in dictating charge transfer on corrosion resistant materials. Therefore, oxide dynamics under mechanical loads are important in understanding the amperometric behavior reported in this effort (Moffat et al., 1992). Specific oxide behavior is often quite difficult to definitively assign as this umbrella term may include changes in charge carrier concentration/mobility, oxide thickness, and electroactive adsorbed species, as shown in **Figure 6**. Even though these mechanisms are discussed and depicted separately in **Figure 6**, it is important to recognize they are not necessarily mutually exclusive.

The increased ORR current during tensile holds is consistent with a drop in oxide resistance. Moreover, this resistance change appears fully reversible with a return to the current baseline values after decay of the current peak. Although the reductive potentials examined in this study for galvanic relevance produce oxides with distinct behavior with respect to those typically observed in repassivation studies (Sidane et al., 2011; Nazarov et al., 2019), some efforts have looked at charge carrier density across anodic and cathodic potentials (Moffat et al., 1992; Vignal et al., 2001). Vignal et al. have considered the impact of mechanical stress on the conductivity of the oxide in the context of a bilayer oxide structure and aging. Their work showed that while acceptor density, i.e., inner p-type chromium oxide conductivity, of aged oxides is not impacted by mechanical stress, passive films formed in the presence of elastic stress exhibited a discernible increase in donor concentration with increase tensile stress. The amperometric results reported here correlate with the latter in both preparation and tension response. That is, our experiment examined polished samples without a passive film growth procedure, and their behavior correlates with higher conductance under tensile stress, manifesting as an increased ORR current.

Recent density functional theory calculation have also indicated that tensile strain on chromium oxide introduces both Cr and O vacancies (Mi et al., 2018). These vacancies were predicted to introduce energy states below the conduction band, with Cr vacancies causing a significant decrease in the band gap. These model predictions are consistent with our results that showed an increased charge transfer for ORR during applied tensile strain. Similar modeling work has also underscored the importance of vacancy formation during applied tension to reconcile theoretical and experimental fracture behavior of chromia (Li et al., 1999; Hirota et al., 2002; Pang et al., 2007; Islam et al., 2017). That being said, structural alloy surface oxides have been shown to span epitaxial crystallinity to amorphous regions as chromium content increases above 11% (Olsson and Landolt, 2003). Surface oxides have also been recently shown to demonstrate rapid surface diffusion with liquid-like behavior that brings into question passive film plasticity (Yang et al., 2018).

Additionally, a thinned oxide layer, proposed by the film rupture-repassivation model, is congruent with greater conductance during tensile stress (Song et al., 2006). In this model, thinning of the oxide is thought to occur while the oxide is undergoing elastic deformation, consistent with mechanisms of defect formation in response to strain, uptake of chloride ions and subsequent displacement of hydroxide that releases Fe^{3+} ions, prior to crack nucleation and growth (Marcus et al., 2008). Importantly, several efforts have shown chloride does not impact the inner passivation layers; only the iron rich outer layers

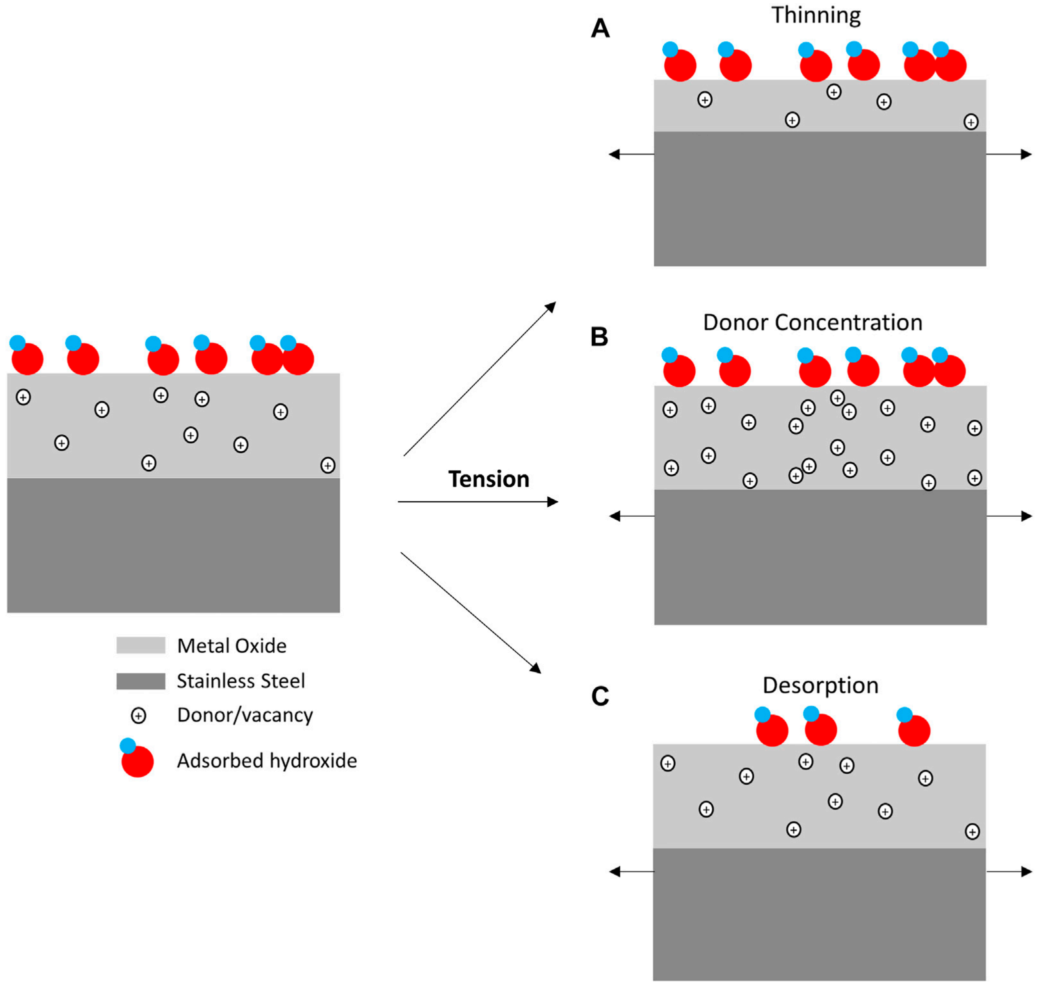

FIGURE 6 | Schematic of mechanisms that may impact reductive reaction rates going from an unstressed to tensile state include conductance changes from **(A)** oxide thinning and **(B)** donor concentration/mobility changes as well as rate changes from **(C)** ad/desorption phenomena.

produced in chloride environments (Natishan et al., 2012; Natishan, 2018; Wang et al., 2020). This view is consistent with other groups that have argued chloride adsorption occurs at defect sites, which lowers the energy barrier for oxidation producing lateral heterogeneity that manifest as morphological instabilities (Sato, 1971; Zhang et al., 2018; Ramanathan and Voorhees, 2019). While cracking has been associated with anodic repassivation current from electrolyte exposure of new metal surface area, more facile charge transfer should result from a thinner resistive inner layer. This reasoning implies a thinning mechanism would only apply to the current shift during tensile holds and excludes current peak behavior during tensile ramps.

One contention with either perspective of the resistive oxide response to tension (**Figure 6A**) would be the larger current response to tensile stress in the diffusion limited region ($-0.8\ V_{SCE}$). ORR in this potential window is considered to proceed at rates faster than transport occurs, which should not be influenced by sample stress. However, previous efforts have demonstrated hysteresis in cyclic polarization experiments with discernible current difference between -0.6 and $-0.8\ V_{SCE}$ that were attributed to oxide reduction during the tail end of the cathodic sweep (Alexander et al., 2018).

The amperometric response during strain ramping is unique in that a reductive current peak occurs during tensile ramping with the converse being true during relaxation, despite many oxide growth, dissolution and defect/donor reactions being oxidative in nature (Seyeux et al., 2013). The current polarity and time scale is not consistent with repassivation, which should produce anodic current peaks on the order of 1–10 ms upon applied tension (Kolman and Scully, 1999). While some of this current may be a consequence of increased ORR, these peaks are clearly observed in the absence of oxygen. Integration of the peaks from the deoxygenated chronoamperogram in **Figure 5A** produced a charge between 5 and 7 nC for each peak. This similarity in peak charge (Coulombs) across ramp rates appears to be a capacitance shift. This is not surprising considering the potential dependent capacitance values of passive films reported previously (Jovancicevic and Bockris, 1986; Santamaria et al., 2015). This capacitance includes changes in the oxide, such as ion release, phase changes and adsorption, all of which will impact the double layer, with the former displaying potential dependence from formal passive film formation potentials to those examined in this study. Redox reactions within the passive film include reduction of Fe^{3+} to Fe^{2+} during cathodic peaks, with the reverse reaction occurring during anodic peaks. Similarly an increase in specific desorption of anionic species (e.g., OH^-) from an oxide during tensile stress will give rise to a cathodic peak, with adsorption producing an anodic peak (McCafferty, 2010). The time scale for these reactions has been shown to be on the order of a minute for pH stepping experiments with iron (Jovancicevic and Bockris, 1986).

ORR on stainless steels and iron is generally recognized as proceeding with adsorption of molecular oxygen onto the surface followed by reduction steps and product dissociation (Jovancicevic and Bockris, 1986; Calvo and Schiffrin, 1988; Ng et al., 2020). ORR on oxide covered stainless steels in chloride electrolytes has been shown to follow the four electron pathway as well as a mix of two and four electron pathways (Le Bozec et al., 2001; Alexander et al., 2018). Pre-reduced stainless steels were shown to follow the four electron pathway, while polished and passivated surfaces include a mix of 2 and 4 electron pathways. Recent work has also shown that transport limitations can impact reaction pathway, shifting from the four-electron pathway to mixed response as the diffusion layer decreases (Alexander et al., 2018). These reaction pathways imply a shift in adsorbed species as well as their reactivity. The amperometric response to tension in **Figure 3** may therefore reside in reaction pathway valence shifts or adsorbate shifts that increase site availability, both of which may increase ORR current.

In the context of chloride concentration effects (**Figure 3D**), chloride has been previously shown to decrease iron content in stainless steel passive films (Kocijan et al., 2007). Experimental data and theoretical calculations have examined ORR at both Cr_2O_3 and Fe_2O_3 rich surfaces and found ORR proceeds preferentially at Fe_2O_3 (Le Bozec et al., 2001; Ng et al., 2020). Hematite essentially reduces the overpotential required for ORR, with respect to chromia. Density functional theory calculations predict hydroxide-terminated hematite surfaces to exhibit the lowest ORR overpotential (Ng et al., 2020). Results for several pretreated stainless steel surfaces (i.e., polished, pre-reduced, chemically treated and electrochemically passivated) have also found that Fe^{2+} enrichment, by evaluation of Fe^{2+}:Fe^{3+} content in the oxide, reduces the ORR overpotential (Le Bozec et al., 2001). While chloride adsorption and incorporation have not been shown to result in film thickness differences for typical marine corrosion chloride concentrations (<1 M NaCl), atmospheric studies have demonstrated thinning of the iron oxide outer layer under concentrated NaCl near the deliquescence point (Jung et al., 2012).

This suggests a possible explanation for the chloride-dependent differences plotted in **Figure 3D**, in which chloride tempers the amperometric response to tensile stress most significantly at $-0.8\ V_{SCE}$. At this potential, reduction of Fe^{3+} to Fe^{2+} is expected to be more significant and hence the effect of chloride-induced loss of reducible iron may be more pronounced. The polarization resistance values of the stabilized surface oxides in bulk solutions of 0.6 and 4.6 M NaCl were observed to be 1.6 and 5.2 MΩ, respectively. These values were determined from the linear region, OCP ±5 mV, of the polarization data plotted in **Figure 2**. The increase in polarization resistance with chloride concentration may arise from selective displacement of hydroxide groups and the dissolution of Fe^{3+} described above (Marcus et al., 2008). This conductance and overpotential relationship with chloride may be responsible for $[Cl^-]$ dependent behavior observed herein.

SUMMARY

In summary, this work has examined the role of tensile stress on oxygen reduction rates for UNS S13800 in chloride electrolytes. Deoxygenated amperometry was utilized to discern ORR contributions to current shifts during static tensile holds and dynamic current during strain ramping. The current response of the UNS S13800 to tensile stress is shown to increase at more negative potentials, with the strongest response occurring at $-0.8\ V_{SCE}$, a relevant potential for galvanic corrosion with aluminum alloys. This behavior was attributed to decreased oxide resistance from some combination of changes in donor concentration, oxide thinning, cracking and/or adsorption effects. The oxygen free current peaks during strain ramps were attributed to changes in specific adsorption and redox reactions with metal cations. These results highlight the importance of mechanical stress effects on corrosion reaction rates. Further distinction of the mechanism at play in this system will require examination of the surface oxide structure by spectroscopic or alternating current techniques.

DATA AVAILABILITY STATEMENT

The raw data supporting the conclusion of this article will be made available by the authors, without undue reservation.

AUTHOR CONTRIBUTIONS

This study was conceived by CH, RA, and SP. The electrochemical measurements and data analysis was performed by CH. The original draft was written by CH. The manuscript was revised by RA and SP. All authors contributed to the article and approved the submitted version.

FUNDING

This work was sponsored by the Office of Naval Research, ONR, under grant/contract no. N0001421WX00709. The views and conclusions contained herein are those of the authors and should not be interpreted as necessarily representing the official policies or endorsements, either expressed or implied, of the Office of Naval Research, the U.S. Navy, or the U.S. government.

REFERENCES

Alexander, C. L., Liu, C., Alshanoon, A., Katona, R. M., Kelly, R. G., Carpenter, J., et al. (2018). Oxygen Reduction on Stainless Steel in Concentrated Chloride Media. *J. Electrochem. Soc.* 165 (13), C869–C877. doi:10.1149/2.0181813jes

Amakawa, K., Sun, L., Guo, C., Hävecker, M., Kube, P., Wachs, I. E., et al. (2013). How Strain Affects the Reactivity of Surface Metal Oxide Catalysts. *Angew. Chem. Int. Ed.* 52 (51), 13553–13557. doi:10.1002/anie.201306620

Boyer, H. E., Gall, T. L., and American Society for Metals (1984). *Metals Handbook*. Metals Park, Ohio: American Society for Metals.

Calvo, E. J., and Schiffrin, D. J. (1988). The Electrochemical Reduction of Oxygen on Passive Iron in Alkaline Solutions. *J. Electroanalytical Chem. Interfacial Electrochemistry* 243 (1), 171–185. doi:10.1016/0022-0728(88)85037-x

Chen, Z. Y., Cui, F., and Kelly, R. G. (2008). Calculations of the Cathodic Current Delivery Capacity and Stability of Crevice Corrosion under Atmospheric Environments. *J. Electrochem. Soc.* 155 (7), C360–C368. doi:10.1149/1.2926557

Costa, D., Ribeiro, T., Mercuri, F., Pacchioni, G., and Marcus, P. (2014). Atomistic Modeling of Corrosion Resistance: A First Principles Study of O2Reduction on the Al(111) Surface Covered with a Thin Hydroxylated Alumina Film. *Adv. Mater. Inter.* 1 (3), 1300072. doi:10.1002/admi.201300072

Du, M., Cui, L., Cao, Y., and Bard, A. J. (2015). Mechanoelectrochemical Catalysis of the Effect of Elastic Strain on a Platinum Nanofilm for the ORR Exerted by a Shape Memory Alloy Substrate. *J. Am. Chem. Soc.* 137 (23), 7397–7403. doi:10.1021/jacs.5b03034

Feng, X., Lu, X., Zuo, Y., and Chen, D. (2014). The Passive Behaviour of 304 Stainless Steels in Saturated Calcium Hydroxide Solution under Different Deformation. *Corrosion Sci.* 82, 347–355. doi:10.1016/j.corsci.2014.01.039

Feng, Z., and Frankel, G. S. (2014). Galvanic Test Panels for Accelerated Corrosion Testing of Coated Al Alloys: Part 2-Measurement of Galvanic Interaction. *CORROSION* 70 (1), 95–106. doi:10.5006/0907

G. Kolman, J. R. Scully, D., and Scully, J. R. (1999). Continuum Mechanics Characterization of Plastic Deformation-Induced Oxide Film Rupture. *Philosophical Mag. A* 79 (10), 2313–2338. doi:10.1080/01418619908214287

Hangarter, C. M., and Policastro, S. A. (2017b). Electrochemical Characterization of Galvanic Couples under Saline Droplets in a Simulated Atmospheric Environment. *Corrosion* 73 (3), 268–280. doi:10.5006/2254

Hangarter, C., and Policastro, S. A. (2017a). Microelectrode Test Configurations for Measurement of Galvanic Current under Saline Drops in Simulated Atmospheric Conditions. *ECS Trans.* 75 (29), 11–22. doi:10.1149/07529.0011ecst

Hirota, K., Motono, H., Yoshinaka, M., and Yamaguchi, O. (2002). Fabrication and Mechanical Properties of Almost Fully-Densified Cr2O3 Ceramics. *J. Mater. Sci. Lett.* 21 (11), 853–854. doi:10.1023/A:1015766427172

Islam, M. M., Couvant, T., Marcus, P., and Diawara, B. (2017). Stress Concentration in the Bulk Cr2O3: Effects of Temperature and Point Defects. *J. Chem.* 2017, 1–8. doi:10.1155/2017/7039436

Jovancicevic, V., and Bockris, J. O. M. (1986). THE MECHANISM OF OXYGEN REDUCTION ON IRON IN NEUTRAL SOLUTIONS. *J. Electrochem. Soc.* 133 (9), 1797–1807. doi:10.1149/1.2109021

Jung, R.-H., Tsuchiya, H., and Fujimoto, S. (2012). XPS Characterization of Passive Films Formed on Type 304 Stainless Steel in Humid Atmosphere. *Corrosion Sci.* 58, 62–68. doi:10.1016/j.corsci.2012.01.006

Kibler, L. A., El-Aziz, A. M., Hoyer, R. d., and Kolb, D. M. (2005). Tuning Reaction Rates by Lateral Strain in a Palladium Monolayer. *Angew. Chem. Int. Ed.* 44 (14), 2080–2084. doi:10.1002/anie.200462127

Kocijan, A., Donik, Č., and Jenko, M. (2007). Electrochemical and XPS Studies of the Passive Film Formed on Stainless Steels in Borate Buffer and Chloride Solutions. *Corrosion Sci.* 49 (5), 2083–2098. doi:10.1016/j.corsci.2006.11.001

Le Bozec, N., Compère, C., L'Her, M., Laouenan, A., Costa, D., and Marcus, P. (2001). Influence of Stainless Steel Surface Treatment on the Oxygen Reduction Reaction in Seawater. *Corrosion Sci.* 43 (4), 765–786. doi:10.1016/s0010-938x(00)00113-x

Li, T., Brook, R. J., and Derby, B. (1999). Fabrication of Reaction-Bonded Cr2O3 Ceramics. *J. Eur. Ceram. Soc.* 19 (8), 1651–1664. doi:10.1016/S0955-2219(98)00261-1

Liu, C., Srinivasan, J., and Kelly, R. G. (2017). Editors' Choice-Electrolyte Film Thickness Effects on the Cathodic Current Availability in a Galvanic Couple. *J. Electrochem. Soc.* 164 (13), C845–C855. doi:10.1149/2.1641713jes

Macdonald, D. D. (2011). The History of the Point Defect Model for the Passive State: A Brief Review of Film Growth Aspects. *Electrochimica Acta* 56 (4), 1761–1772. doi:10.1016/j.electacta.2010.11.005

Marcus, P., Maurice, V., and Strehblow, H.-H. (2008). Localized Corrosion (Pitting): A Model of Passivity Breakdown Including the Role of the Oxide Layer Nanostructure. *Corrosion Sci.* 50 (9), 2698–2704. doi:10.1016/j.corsci.2008.06.047

Marshall, R. S., Kelly, R. G., Goff, A., and Sprinkle, C. (2019). Galvanic Corrosion between Coated Al Alloy Plate and Stainless Steel Fasteners, Part 1: FEM Model Development and Validation. *CORROSION* 75 (12), 1461–1473. doi:10.5006/3308

Matzdorf, C. A., Nickerson, W. C., Rincon Troconis, B. C., Frankel, G. S., Li, L., and Buchheit, R. G. (2013). Galvanic Test Panels for Accelerated Corrosion Testing of Coated Al Alloys: Part 1-Concept. *Corrosion* 69 (12), 1240–1246. doi:10.5006/0905

Maurice, V., and Marcus, P. (2018). Current Developments of Nanoscale Insight into Corrosion protection by Passive Oxide Films. *Curr. Opin. Solid State. Mater. Sci.* 22 (4), 156–167. doi:10.1016/j.cossms.2018.05.004

McCafferty, E. (2010). Relationship between the Isoelectric point (pHpzc) and the Potential of Zero Charge (Epzc) for Passive Metals. *Electrochimica Acta* 55 (5), 1630–1637. doi:10.1016/j.electacta.2009.10.040

Mi, Z., Chen, L., Shi, C., Ma, Y., Wang, D., Li, X., et al. (2018). The Effects of Strain and Vacancy Defects on the Electronic Structure of Cr2O3. *Comput. Mater. Sci.* 144, 64–69. doi:10.1016/j.commatsci.2017.12.012

Millero, F. J., Huang, F., and Laferiere, A. L. (2002). Solubility of Oxygen in the Major Sea Salts as a Function of Concentration and Temperature. *Mar. Chem.* 78 (4), 217–230. doi:10.1016/S0304-4203(02)00034-8

Mizuno, D., and Kelly, R. G. (2013). Galvanically Induced Intergranular Corrosion of AA5083-H131 under Atmospheric Exposure Conditions: Part 2-Modeling of the Damage Distribution. *Corrosion* 69 (7), 681–692. doi:10.5006/0813

Moffat, T. P., Yang, H., Fan, F. R. F., and Bard, A. J. (1992). Electron-Transfer Reactions on Passive Chromium. *J. Electrochem. Soc.* 139 (11), 3158–3167. doi:10.1149/1.2069049

Natishan, P. M. (2018). 2017 W.R. Whitney Award: Perspectives on Chloride Interactions with Passive Oxides and Oxide Film Breakdown. *Corrosion* 74 (3), 263–275. doi:10.5006/2511

Natishan, P. M., O'Grady, W. E., Martin, F. J., Rayne, R. J., Kahn, H., and Heuer, A. H. (2012). "The Effect of Chloride on Passive Oxide Film Breakdown on Stainless Steels and Aluminum," in *Critical Factors in Localized Corrosion 7*. Editors J. R. Kish, G. S. Frankel, A. J. Davenport, N. Birbilis, and K. Zavadil, 41, 49–57. doi:10.1149/1.3697577*ECS Trans.*

Nazarov, A., Vivier, V., Vucko, F., and Thierry, D. (2019). Effect of Tensile Stress on the Passivity Breakdown and Repassivation of AISI 304 Stainless Steel: A Scanning Kelvin Probe and Scanning Electrochemical Microscopy Study. *J. Electrochem. Soc.* 166 (11), C3207–C3219. doi:10.1149/2.0251911jes

Ng, M.-F., Blackwood, D. J., Jin, H., and Tan, T. L. (2020). DFT Study of Oxygen Reduction Reaction on Chromia and Hematite: Insights into Corrosion Inhibition. *J. Phys. Chem. C* 124 (25), 13799–13808. doi:10.1021/acs.jpcc.0c03559

Olsson, C.-O. A., and Landolt, D. (2003). Passive Films on Stainless Steels-Chemistry, Structure and Growth. *Electrochimica Acta* 48 (9), 1093–1104. doi:10.1016/S0013-4686(02)00841-1

Palani, S., Rose, A., and Legg, K. (2017). *Modeling Galvanic Corrosion Behavior Of Carbon Fiber Composite/Al 7050 Joints Under Extended Exposures*. Birmingham, AL: Department of Defense - Allied Nations Technical Corrosion Conference

Pang, X., Gao, K., and Volinsky, A. A. (2007). Microstructure and Mechanical Properties of Chromium Oxide Coatings. *J. Mater. Res.* 22 (12), 3531–3537. doi:10.1557/jmr.2007.0445

Paola, A. D. (1989). Semiconducting Properties of Passive Films on Stainless Steels. *Electrochimica Acta* 34 (2), 203–210. doi:10.1016/0013-4686(89)87086-0

Policastro, S. A., Hangarter, C. M., Anderson, R. M., and Friedersdorf, F. (2019). Effect of Confined Electrolyte Volumes on Galvanic Corrosion Kinetics in Statically Loaded Materials. *Corrosion Rev.* 37(5), 521–531. doi:10.1515/corrrev-2019-0016

Ramanathan, R., and Voorhees, P. W. (2019). Morphological Stability of Steady-State Passive Oxide Films. *Electrochimica Acta* 303, 299–315. doi:10.1016/j.electacta.2019.01.146

Santamaria, M., Di Franco, F., Di Quarto, F., Pisarek, M., Zanna, S., and Marcus, P. (2015). Photoelectrochemical and XPS Characterisation of Oxide Layers on 316L Stainless Steel Grown in High-Temperature Water. *J. Solid State. Electrochem.* 19 (12), 3511–3519. doi:10.1007/s10008-015-2849-0

Sato, N. (1971). A Theory for Breakdown of Anodic Oxide Films on Metals. *Electrochimica Acta* 16 (10), 1683–1692. doi:10.1016/0013-4686(71)85079-X

Schindelholz, E., and Kelly, R. G. (2012). Wetting Phenomena and Time of Wetness in Atmospheric Corrosion: a Review. *Corrosion Rev.* 30 (5-6), 135–170. doi:10.1515/corrrev-2012-0015

Seyeux, A., Maurice, V., and Marcus, P. (2013). Oxide Film Growth Kinetics on Metals and Alloys. *J. Electrochem. Soc.* 160 (6), C189–C196. doi:10.1149/2.036306jes

Shinohara, T., Hosoya, Y., and Oshikawa, W. (2004). "Effect of Thickness of Water Film on Atmospheric Corrosion Behavior of Carbon Steel," in *Meeting of the Electrochemical Society*. Editors D. A. Shifler, T. Tsuru, and P. M. Natishan, 121–132.

Sidane, D., Devos, O., Puiggali, M., Touzet, M., Tribollet, B., and Vivier, V. (2011). Electrochemical Characterization of a Mechanically Stressed Passive Layer. *Electrochemistry Commun.* 13 (12), 1361–1364. doi:10.1016/j.elecom.2011.08.010

Song, F. M., Raja, K. S., and Jones, D. A. (2006). A Film Repassivation Kinetic Model for Potential-Controlled Slower Electrode Straining. *Corrosion Sci.* 48 (2), 285–307. doi:10.1016/j.corsci.2005.02.001

Strasser, P., Koh, S., Anniyev, T., Greeley, J., More, K., Yu, C., et al. (2010). Lattice-strain Control of the Activity in Dealloyed Core-Shell Fuel Cell Catalysts. *Nat. Chem* 2 (6), 454–460. doi:10.1038/nchem.623

Sun, P., Liu, Z., Yu, H., and Mirkin, M. V. (2008). Effect of Mechanical Stress on the Kinetics of Heterogeneous Electron Transfer. *Langmuir* 24 (18), 9941–9944. doi:10.1021/la801009f

Sun, Y., Thompson, S. E., and Nishida, T. (2007). Physics of Strain Effects in Semiconductors and Metal-Oxide-Semiconductor Field-Effect Transistors. *J. Appl. Phys.* 101 (10), 104503. doi:10.1063/1.2730561

Svedruzic, D., and Gregg, B. A. (2014). Mechano-Electrochemistry and Fuel-Forming Mechano-Electrocatalysis on Spring Electrodes. *J. Phys. Chem. C* 118 (33), 19246–19251. doi:10.1021/jp506279q

Tang, I. N., Munkelwitz, H. R., and Wang, N. (1986). Water Activity Measurements with Single Suspended Droplets: The NaCl-H2o and KCl-H2o Systems. *J. Colloid Interf. Sci.* 114 (2), 409–415. doi:10.1016/0021-9797(86)90426-1

Tang, I. N., Tridico, A. C., and Fung, K. H. (1997). Thermodynamic and Optical Properties of Sea Salt Aerosols. *J. Geophys. Res.* 102 (D19), 23269–23275. doi:10.1029/97JD01806

Thébault, F., Vuillemin, B., Oltra, R., Allely, C., and Ogle, K. (2011). Modeling Bimetallic Corrosion under Thin Electrolyte Films. *Corrosion Sci.* 53 (1), 201–207. doi:10.1016/j.corsci.2010.09.010

Tyler, P. S., Levy, M., and Raymond, L. (1991). Investigation of the Conditions for Crack Propagation and Arrest under Cathodic Polarization by Rising Step Load Bend Testing. *Corrosion* 47 (2), 82–87. doi:10.5006/1.3585857

Van den Steen, N., Simillion, H., Dolgikh, O., Terryn, H., and Deconinck, J. (2016). An Integrated Modeling Approach for Atmospheric Corrosion in Presence of a Varying Electrolyte Film. *Electrochimica Acta* 187, 714–723. doi:10.1016/j.electacta.2015.11.010

Vignal, V., Oltra, R., Verneau, M., and Coudreuse, L. (2001). Influence of an Elastic Stress on the Conductivity of Passive Films. *Mater. Sci. Eng. A* 303 (1), 173–178. doi:10.1016/S0921-5093(00)01843-8

Wang, S.-S., Jiang, J.-T., Dai, S.-L., Seidman, D. N., Frankel, G. S., and Zhen, L. (2014). Effect of Surface Roughness on Breakdown Behavior of Al-Zn-Mg-Cu Alloy. *J. Electrochem. Soc.* 161 (9), C433–C440. doi:10.1149/2.1131409jes

Wang, Z., Seyeux, A., Zanna, S., Maurice, V., and Marcus, P. (2020). Chloride-induced Alterations of the Passive Film on 316L Stainless Steel and Blocking Effect of Pre-passivation. *Electrochimica Acta* 329, 135159. doi:10.1016/j.electacta.2019.135159

Yan, K., Maark, T. A., Khorshidi, A., Sethuraman, V. A., Peterson, A. A., and Guduru, P. R. (2016). The Influence of Elastic Strain on Catalytic Activity in the Hydrogen Evolution Reaction. *Angew. Chem. Int. Ed.* 55 (21), 6175–6181. doi:10.1002/anie.201508613

Yang, Y., Kushima, A., Han, W., Xin, H., and Li, J. (2018). Liquid-Like, Self-Healing Aluminum Oxide during Deformation at Room Temperature. *Nano Lett.* 18 (4), 2492–2497. doi:10.1021/acs.nanolett.8b00068

Zhang, B., Wang, J., Wu, B., Guo, X. W., Wang, Y. J., Chen, D., et al. (2018). Unmasking Chloride Attack on the Passive Film of Metals. *Nat. Commun.* 9 (1), 2559. doi:10.1038/s41467-018-04942-x

Author Disclaimer: The views and conclusions contained herein are those of the authors and should not be interpreted as necessarily representing the official policies or endorsements, either expressed or implied, of the Office of Naval Research, the U.S. Navy, or the US government.

Conflict of Interest: The authors declare that the research was conducted in the absence of any commercial or financial relationships that could be construed as a potential conflict of interest.

frontiers in Chemistry

ORIGINAL RESEARCH
published: 11 March 2022
doi: 10.3389/fchem.2022.806553

The Influence of Titania Nanoparticles on the Electrodeposition of Ni-Mo-W Composites in Aqueous Electrolytes at Different Electrolyte Temperatures

Usoa Izagirre-Etxeberria[1,2] *and Elizabeth J. Podlaha*[1,3]*

[1]*Department of Chemical Engineering, Northeastern University, Boston, MA, United States,* [2]*TECNALIA, Basque Research and Technology Alliance (BTRA), Parque Tecnológico de San Sebastián, San Sebastian, Spain,* [3]*Department Department of Chemical and Biomolecular Engineering Clarkson University, Potsdam, NY, United States*

The electrodeposition of Ni-Mo-W alloys and composites with TiO_2 are examined with a rotating Hull cell to better understand the influence of the particle on the deposition composition and morphology. The addition of the TiO_2 particle to the electrolyte and deposit, significantly affected the deposit composition when the electrolyte temperature was 65^0C. Both Ni and Mo composition in the deposit was enhanced, but not due to higher reaction rates. The enhancement was a result of an apparent inhibition by the hydrogen evolving side reaction. The W partial current density was most significantly inhibited. The deposit morphology changed with the addition of TiO_2 with a reduction of microcracks compared to the particle-free deposit. The results suggest that the adsorption of the hydrogen intermediate from the side reaction is influenced by the particle, hindering hydrogen desorption, and indirectly affects the partial current densities of the nickel, molybdate and tungstate ion reduction and the morphology.

Keywords: electrodeposition, Ni-Mo-W, composite, titania, Hull cell

Edited by:
Jae-Hong Lim,
Gachon University, South Korea

Reviewed by:
Ligang Feng,
Yangzhou University, China
Seunghoe Choe,
Korea Institute of Materials Science, South Korea

***Correspondence:**
Elizabeth J. Podlaha
epodlaha@clarkson.edu

Specialty section:
This article was submitted to Electrochemistry, a section of the journal Frontiers in Chemistry

Received: *31 October 2021*
Accepted: *24 January 2022*
Published: *11 March 2022*

Citation:
Izagirre-Etxeberria U and Podlaha EJ (2022) The Influence of Titania Nanoparticles on the Electrodeposition of Ni-Mo-W Composites in Aqueous Electrolytes at Different Electrolyte Temperatures. Front. Chem. 10:806553. doi: 10.3389/fchem.2022.806553

INTRODUCTION

A challenge in alloy electrodeposition containing Mo, and/or W, is that the deposition exhibits induced codeposition behavior (Brenner, 1963; Landolt, 1994; Schwartz et al., 2004). Induced codeposition is characterized by the inability of molybdenum and tungsten ions in water to be reduced to its zero valence state unlike most transition metal ions. Interestingly, both molybdate and tungstate ions can be coaxed into reduction when codeposited with another element to form an alloy. The elements, which have the best inducing capability, are the iron-group elements: Ni, Co, and Fe. In Brenner's review (Brenner, 1963) it was recognized that the composition of the solid state alloy was not reflective of the amount of ions in the electrolyte, suggesting a coupled reaction mechanism. Today there is not a general consensus on how these alloys codeposit and thus the control of the deposit composition and subsequent structure leading to the desired properties are still difficult to predict *a priori*. Combined with a second phase particle the deposit composition is even more difficult to predict and work that can contribute to this understanding is needed.

Several comprehensive reviews summarize the induced codeposition mechanism (Fukushima, et al., 1979; Eliaz and Gileadi, 2008; Landolt, 1994; Tsyntsaru et al., 2012; Allahyarzadeh, et al., 2016). In early work by Ernst et al. (1955); (Ernst and Holt, 1958), they suggested that the reduction of Mo or W ions was governed by hydrogen, on account of the observation that generally as more Mo or W is codeposited into an alloy the hydrogen side reaction tends to be higher, or in other words, the current efficiency is lower. Fukushima (Fukushima et al., 1979; Oue, et al., 2009) noted that hydrogen can be readily adsorbed onto the codeposited iron-group element and that the inducing element, such as Mo was reduced at these sites, thus, placing an emphasis on the iron-group solid state as the catalyst in reducing the inducing element (e.g., Mo) and effectively placing a theoretical upper limit for Mo (or W) codeposition in an alloy. Chassaign et al. (1989) reported that the iron-group ion was responsible for the formation of the intermediate, not the solid state. There is also a view that iron-group metal tungstate or molybdate complexes are precursors to tungsten or molybdenum alloys (Younes and Gileadi, 2002; Younes-Metzler et al., 2003) and a contrasting view that the iron-group metal induces adsorption of tungstate or molybdate intermediates at the solid state surface (Podlaha and Landolt, 1996b; Podlaha and Landolt, 1996b; Podlaha and Landolt 1997), and more recent experimental results supported the concept of the adsorbed ion-group element being the governing species to induce the reduction of Mo or W ions according to **Eq. 1** through **[4]** (Sun, et al., 2013), using Ni as one example iron-group element, and where "L" represents a ligand, common in many plating scenarios.

$$\mathrm{MoO_4^{2-} + NiL\,(I)_{ads} + 2H_2O + 2e^- \rightarrow [Ni\,(I)LMoO_2]^{2-}_{ads} + 4OH^-} \tag{1}$$

$$\mathrm{[Ni\,(I)LMoO_2]^{2-}_{ads} + 2H_2O + 4e^- \leftrightarrow Mo\,(s) + NiL\,(I)_{ads} + 4OH^-} \tag{2}$$

and in the same manner for tungstate reduction,

$$\mathrm{WO_4^{2-} + NiL\,(I)_{ads} + 2H_2O + 2e^- \rightarrow [Ni\,(I)LWO_2]^{2-}_{ads} + 4OH^-} \tag{3}$$

$$\mathrm{[Ni\,(I)LWO_2]^{2-}_{ads} + 2H_2O + 4e^- \leftrightarrow W\,(s) +} N\mathrm{iL\,(I)_{ads} + 4OH^-} \tag{4}$$

Since the current efficiency can be manipulated to be low or high, by changing the metal ion composition and pH it was thought that the side reaction was not a controlling feature of the induced codeposition mechanism.

Electrodeposited Ni-W and Ni-Mo alloys are of interest for use as corrosion resistant coatings (Quang, et al., 1971; Raman, et al., 2007; Alimadadi et al., 2009), as magnetic materials (Gomez, et al., 2006; Ohgai, et al., 2013), as electrocatalyst for the hydrogen evolution reaction in water splitting (Fan et al., 1994; Navarroi-Flores, et al., 2005; Jamesh, 2016) and as combined wear resistant and corrosion resistant coatings (Urlberger, 1999; Slavcheva et al., 2005; Haseeb et al., 2008). Electrodeposited alloys of Ni-Mo-W may offer combined properties, and has been used as corrosion resistant electrocataysts for the hydrogen evolution reaction (Raj, 1992; Raj and Vasu, 1992; Sun et al., 2013). Cesiulis, et al., 2001 reported enhanced corrosion resistance in amorphous Ni-Mo-W ternary alloy films combined with other interesting properties such as low thermal expansion coefficients and premium hardness. Ni-Mo-W alloys are also important as in creating transition metal sulfides as catalytic precursors on hydrodesulphurization reactions of organic molecules such as tiophene, benzotiophene and dibenzotiophene (Olivas et al., 2009). In this context, the addition of Mo to Ni-W is advantageous as it promotes an amorphous structure when treated at high temperature with H_2S/H_2 and results in a Ni-Mo-W-S active catalyst. Composites of Ni-W and Ni-Mo can permit further tailorability of properties. For example, electrodeposited Ni-Mo-ZrO_2 coatings have been reported to improve microhardness and corrosion properties of Ni-Mo alloy coatings (Laszczynska, et al., 2016) and electrodeposited Ni-W-SiC composites have been reported to enhance the corrosion resistance, hardness and wear resistance over that of Ni-W coatings (Yao et al., 2017; Singh, et al., 2016), as SiC it is known to improve properties in Ni films (Lee, et al., 2007). Titania particles have been codeposited with Ni-W coatings and both the hardness and corrosion resistance was improved by the presence of titania (Kumar, et al., 2013). Enhanced electrocatalysis of the hydrogen evolution reaction (HER) in water splitting application has been reported for Ni-W-TiO_2 composite in comparison to Ni-W due to a rougher surface that was created by the addition of the TiO_2 particle (Zou, et al., 2004), associated with a change in the morphology. Zhang et al. (2018) have reported an intrinsic enhancement of HER kinetics for Ni-W-TiO_2 nanocomposite coatings compared to the nanoparticle-free counterparts. Few studies address the influence of the particle on the alloy composition that can have a large impact of the deposit composition. Previous work with Ni-W-TiO_2 showed that the deposit tungsten content was slightly decreased with accompanying titania (Zhang and Podlaha-Murphy, 2017). Here, electrodeposited Ni-Mo-W and Ni-Mo-W-TiO_2 composites are examined with a focus on addressing the role of the particle on the metal reduction rates (*i.e.*, partial current densities) that dictate the composition.

A convenient way to assess deposit composition is with the trapezoidal Hull cell (Hull, 1939) that generates a current distribution along the working electrode surface created by cell geometric considerations, and when the current distribution is categorized as a primary current distribution, i.e., under conditions when kinetics are rapid and ohmic effects are dominate. Nobe adapted this technique to alloy electrodeposition (e.g., Wei, et al., 2008) to swiftly identify the composition and morphology of the deposit with variable current density. A rotating version of the Hull cell (RHC) provides better control of the hydrodynamic environment at the cathode surface via control of the rotation rate. Madore and Landolt, 1993 presented design conditions for obtaining a large variation in current distribution along the length of a cathode for the Ni-Cu system that mimics the distribution that is created in a conventional Hull cell. The current distribution is generated by placing the anode at either bottom or top of a rotating cylinder that is shield by a plastic tube, and open only at one end. If the anode is placed near the bottom of the cell and the insulating tube is open at the bottom then the current density is highest in this region and decreases along the cathode cylinder length. They demonstrated the deconvolution of partial current densities in a Ni-Cu alloy by mapping the current distribution to a polarization curve. The work presented here will follow this established approach and is the first demonstration of the use of the RCHC of the electrodeposition of Ni-W-Mo-TiO_2 composites.

EXPERIMENTAL

Two electrode experimental set-ups were used: *i.* a rotating cylinder electrode (RCE) with uniform current distribution. and *ii.* a rotating cylindrical Hull cell (RCHC), with non-uniform distribution, as the working electrode. In both cases copper was the substrate. In the RCE configuration, copper cylindrical electrodes with a diameter of 0.6 and 1.0 cm length were used. In the RCHC configuration, the copper cylindrical rods were longer, having a length of 8 cm length. The counter electrode was a platinum coated, titanium anode. The electrolyte contained 0.15 M nickel sulfate, 0.005 M sodium molybdate, 0.375 M sodium citrate, 0.1 M sodium tungstate and 0.1 M boric acid. Different electrolyte temperatures were examined: 25°C, 45°C and 65°C. The electrolyte pH was maintained at 7 with sodium hydroxide and sulfuric acid additions. The TiO_2 particle type added to the electrolyte were an anatase nanopowder, with purity of 99.7% supplied by Sigma Aldrich, with a reported diameter size lower than 25 nm. A low particle loading of 12.5 g L^{-1} was used so as not to significantly influence the hydrodynamics of the RCE and RCHC electrodes.

The RCHC experiments were obtained using an average current density of 66.3 mA cm^{-2} using a Solartron SI 1287 galvanostat for a period of 25 min at a constant rotation rate of 500 rpm. The rotation rate was controlled with a Pine Instruments modulated speed high precision rotator. The temperature was controlled using a thermostatic bath. An estimate of the local current density, *i* (z), along the dimensionless position, *z*, was determined from a primary current distribution correlation described by the following (Madore and Landolt, 1993),

$$\frac{i(z)}{i_{avg}} = \frac{0.535 - 0.458\,z}{\left[0.0233 + (z)^2\right]^{1/2}} + 8.52 \times 10^{-5} \exp\{7.17\,(z)\} \qquad [5]$$

where i_{avg} is the average applied current density. Hence the variation of the current density along the cathode length can be estimated to provide a rapid evaluation of the deposit composition and morphology as a function of current density.

A computer controlled potentiostat and impedance system (Solartron SI 1287 potentiostat coupled to Solartron Analytical 1252A frequency Response Analyzer) were used to conduct the potentiodynamic scans. Polarization curves were measured with and without titania nanoparticles on a RCE electrode at the three examined temperatures and at a constant rotation rate of 500 rpm. A saturated calomel electrode was used as the reference electrode. The polarization scans were performed by increasing the cell potential from the open circuit value until -3.0 V vs SCE and corrected for ohmic drop with impedance spectroscopy.

An X-Ray fluorescence (XRF) instrument, model Kevex Omicron, was used to analyze composition and thickness of the deposits. Thirty points were analyzed along each of the cylindrical cathodes. The TiO_2 amount of the deposits was confirmed using a scanning electron microscope, model Hitachi S4800 field emission coupled to an EDAX detecting unit, which provides an order of magnitude higher precision. The thickness was confirmed gravimetrically. The partial current densities of Ni, Mo and W were calculated from the thickness and composition analysis using Faraday´s law. Scanning electron microscopy was also used to examine the morphology of characteristic deposits.

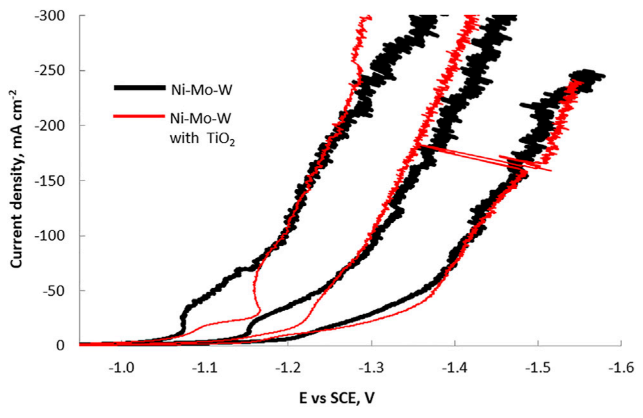

FIGURE 1 | RCE polarization curves from the electrodeposition of a Ni-Mo-W alloy for a particle free electrolyte and in the presence of titania particles at 25°C, 45°C and 65°C.

RESULTS

The polarization curves in **Figure 1** show the effect of the addition of TiO_2 particles on the total current density during Ni-Mo-W ternary electrodeposition at different electrolyte temperatures and at a rotation rate of 500 rpm. The total current density is inhibited when titania nanoparticles are present in the electrolyte at low current densities with the degree of change largest at 65°C and lowest at 25°C. The inhibition of the total current density increases notably with temperature. At more negative potential values than -1.3 V, -1.2 V and -1.0 V vs SCE, at 25°C, 45°C and 65°C, respectively, the total current density is not notably inhibited nor enhanced by the addition of the nanoparticles. In order to analyze which reaction causes the changes in the total current density observed in the different regions, the partial current densities were examined with the RCHC, with a forced variation in current distribution along the cathode length.

The thickness and the composition change of the composite along the RCHC electrode length, at 25°C, 45°C and 65°C, is shown in **Figure 2**. The deposit thickness (**Figure 2A**) at 25°C and 45°C, did not change appreciably with the addition of the TiO_2 particles. However, at the higher temperature, 65°C, the addition of titania particles significantly lowered the deposit thickness compared to the alloy without nanoparticles. Generally, at the high temperature of 65°C, there is a much thicker deposit compared to the lower temperatures, even with the addition of particles. The composition of nickel, (**Figure 2B**), molybdenum

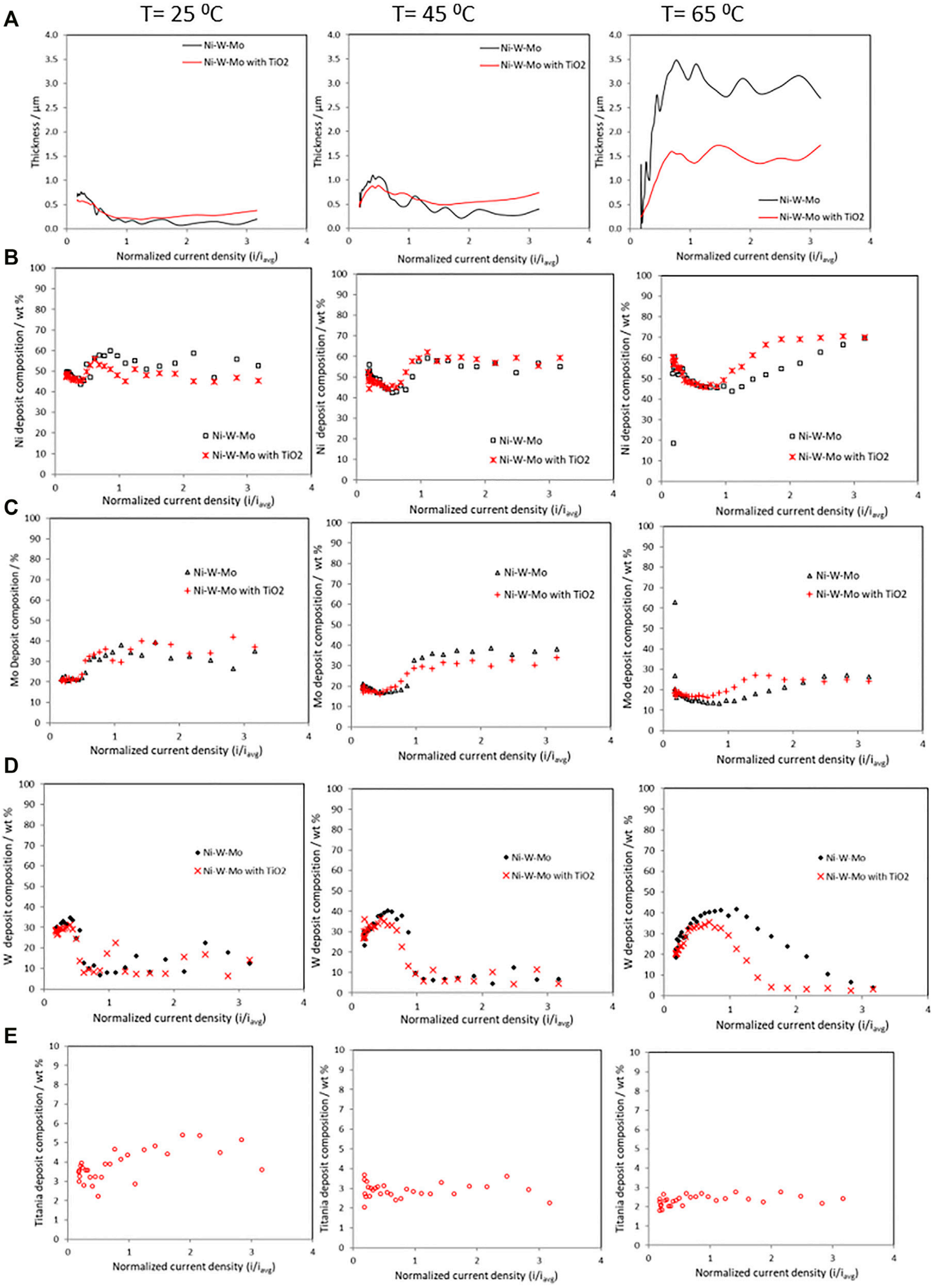

FIGURE 2 | Deposit composition measurements on a rotating Hull cell during the electrodeposition of Ni-Mo-W with and without TiO_2, at 25°C, 45°C and 65°C, **(A)** thickness variation **(B)** Ni wt%, **(C)** Mo wt%, **(D)** W wt% and **(E)** TiO_2 wt%.

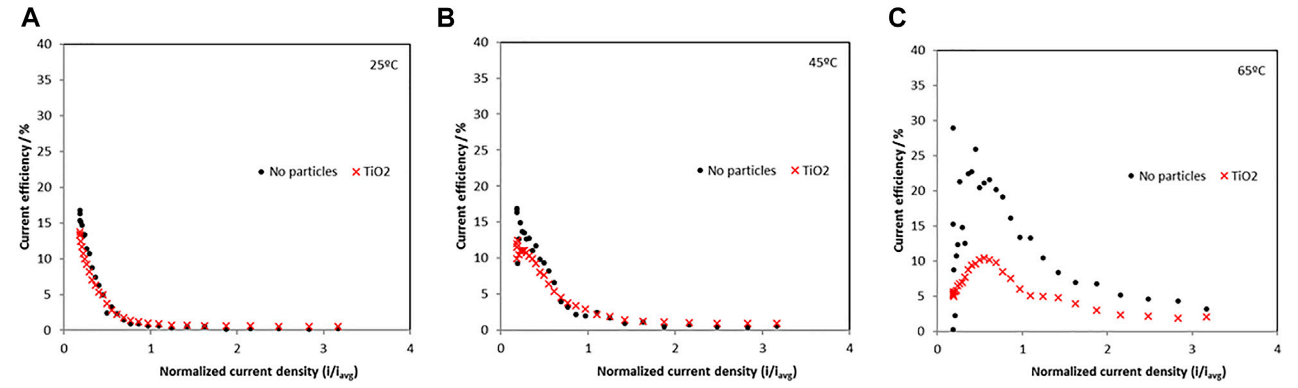

FIGURE 3 | Current efficiency of Ni-Mo-W electrodeposition with and without addition of titania nanoparticles at **(A)** 25°C, **(B)** 45°C and **(C)** 65°C.

(**Figure 2C**), and tungsten (**Figure 2D**) with and without the addition of 12.5 g L^{-1} of TiO_2 particles, show that there is a similar change in the Ni and Mo composition with current density, with a drop in composition as the current density increases and then a rise in its composition, with the tungsten exhibiting the opposite behavior. There is slightly more Ni in the deposit at the low and high current density regions at 65°C compared to 25°C and 45°C, when there is no TiO_2 present in the electrolyte, however when i/i_{avg} has a value of 1–2 (66.3–132.6 mA cm^{-2}), the amount of Ni in the deposit is larger at the lower temperatures. The addition of the TiO_2 particles only has a significant effect on the Ni deposit composition at the high temperature and at high current density. At the low current density region, there is a comparable amount of W and Mo despite having 20 times more tungstate in the electrolyte than molybdate. With a change of temperature, the composition does change when there are no particles present depending on the applied current density. In the low current density region, there is a drop in the Mo deposit content with an increase in temperature, but at 25°C, the composition reaches a peak at 38 wt% but then falls with an increase in the applied current density, while at 45°C, at high current density, the composition remains near the same 38 wt% so is higher than when the electrolyte temperature is at 25°C. A further increase in the temperature to 65°C leads to lower Mo content at all current densities. There is little difference in Mo composition when TiO_2 particles are present or not at the low current density region for all temperatures. In the medium range of current density the addition of particles does not significantly affect the Mo deposition composition at 25°C and at 45°C, but slightly increases it at 65°C. The behavior of the W composition with current density rises with the applied current density with or without particles, reaches a maximum, and then falls to nearly zero, with an associated rise in Mo and Ni. A similar drop in the tungsten amount with an increase of applied current density, has been previously reported (Sun et al., 2013) in a Ni-Mo-W electrodeposit when no TiO_2 particles are in the electrolyte; here the particles exaggerate this effect. The enhancement of the Ni composition with the particle addition was observed in the medium and high current density regions while the enhancement of molybdenum was observed in the low and medium current density regions. The TiO_2 particle concentration in the resulting Ni-W-Mo-TiO_2 composite thin films is shown in **Figure 2E**. The titania amount incorporated into the composite coatings (**Figure 2E**) decreased as temperature increased from 25°C to 65°C.

The current efficiency at 25°C, 45°C and 65°C is shown in **Figure 3** and are relatively low indicating a significant hydrogen evolution side reaction. When no particles are present, the maximum current efficiencies occurred in the low current density regions and dropped as current was increased. The maximum current efficiency increased as temperature increased from 25°C to 65°C. At 65°C the current efficiency had a maximum of 25% in the low-density region without particles and decreased to a maximum of around 10% with the addition of particles.

Figure 4 shows representative SEM micrographs at three regions on the RCHC electrodeposit at low, medium and high current densities at 65°C and from the electrolytes with and without the addition of TiO_2 nanoparticles. The Ni-W-Mo alloy deposit (**Figure 4A,C,D**) showed a smooth surface morphology with a progressive increase of micro-cracks as the current density increased. When particles were added, at the same current density regions, (**Figure 4B,E,F**) significantly fewer micro-scale cracks were observed but the deposit was more nodular.

DISCUSSION

The partial current densities of nickel, molybdenum, tungsten and the side reaction were determined to provide further insight on how the reaction rates were affected by temperature and the particle addition. The partial current densities of the metal ion reduction rates and the side reaction rate is shown in **Figures 5**, **6**, respectively, determined using Faraday's law from the composition and thickness along the RCHC length. Using the polarization curves in **Figure 1**, the *x*-axis scale was correlated with the applied working electrode potential.

An increase in the temperature shifts the metal reduction rates to less positive potentials (*i.e.*, depolarizes the deposition). The

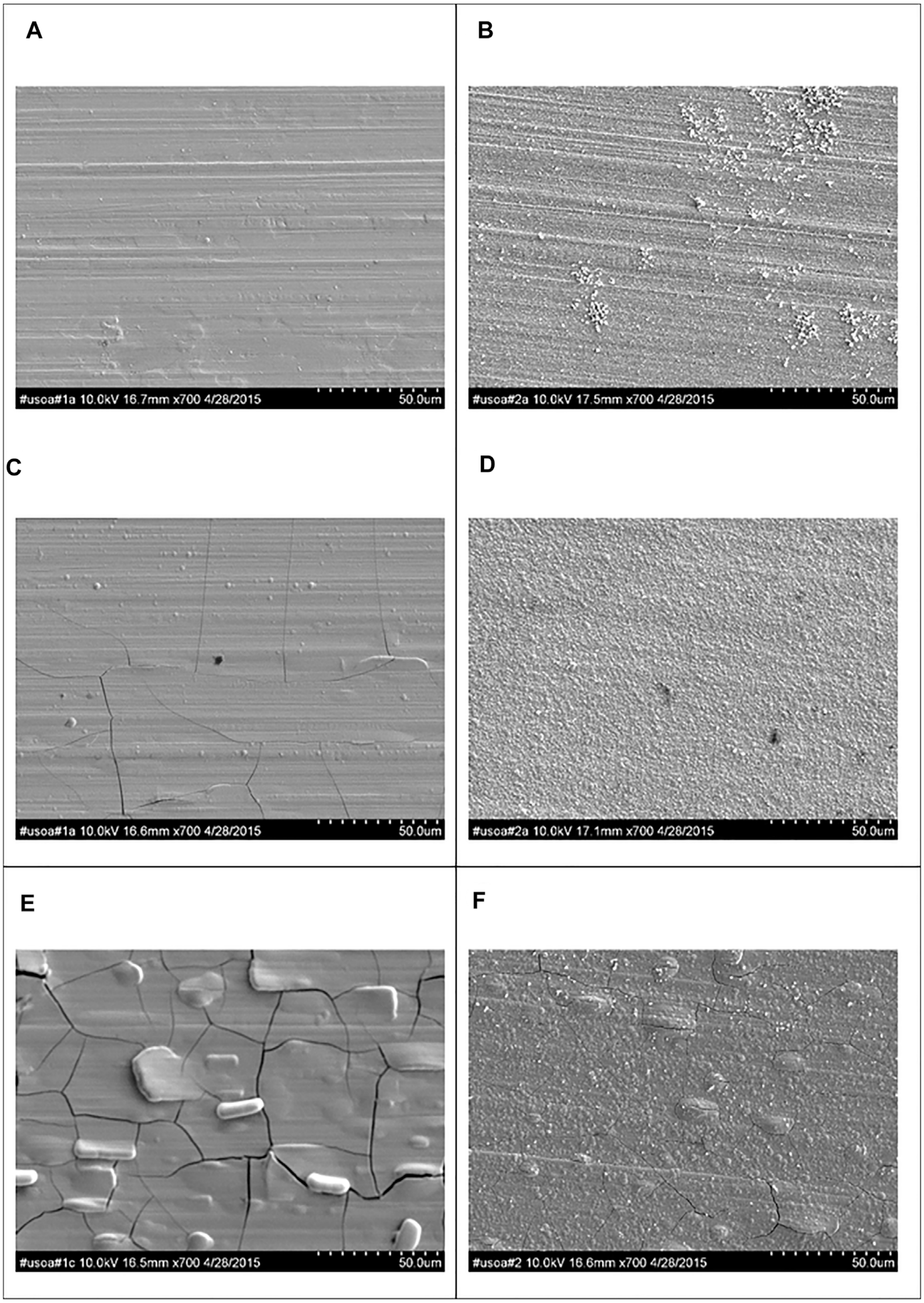

FIGURE 4 | SEM micrographs at the **(A,B)** low **(C,D)** medium and **(E,F)** high current density regions of RHC samples electrodeposited during 25 min at 65°C and 500 rpm (a,c,e) without and (b,d,f) with the addition of 12.5 g L^{-1} of titania nanoparticles.

side reaction is also depolarized with temperature. When no TiO_2 particles are present, all the partial current densities of the individual metals increase with potential, when the total current density is confined to the low region and the side reaction is small. This potential dependence indicates a kinetic reaction control. The Ni and Mo partial current densities exhibit a

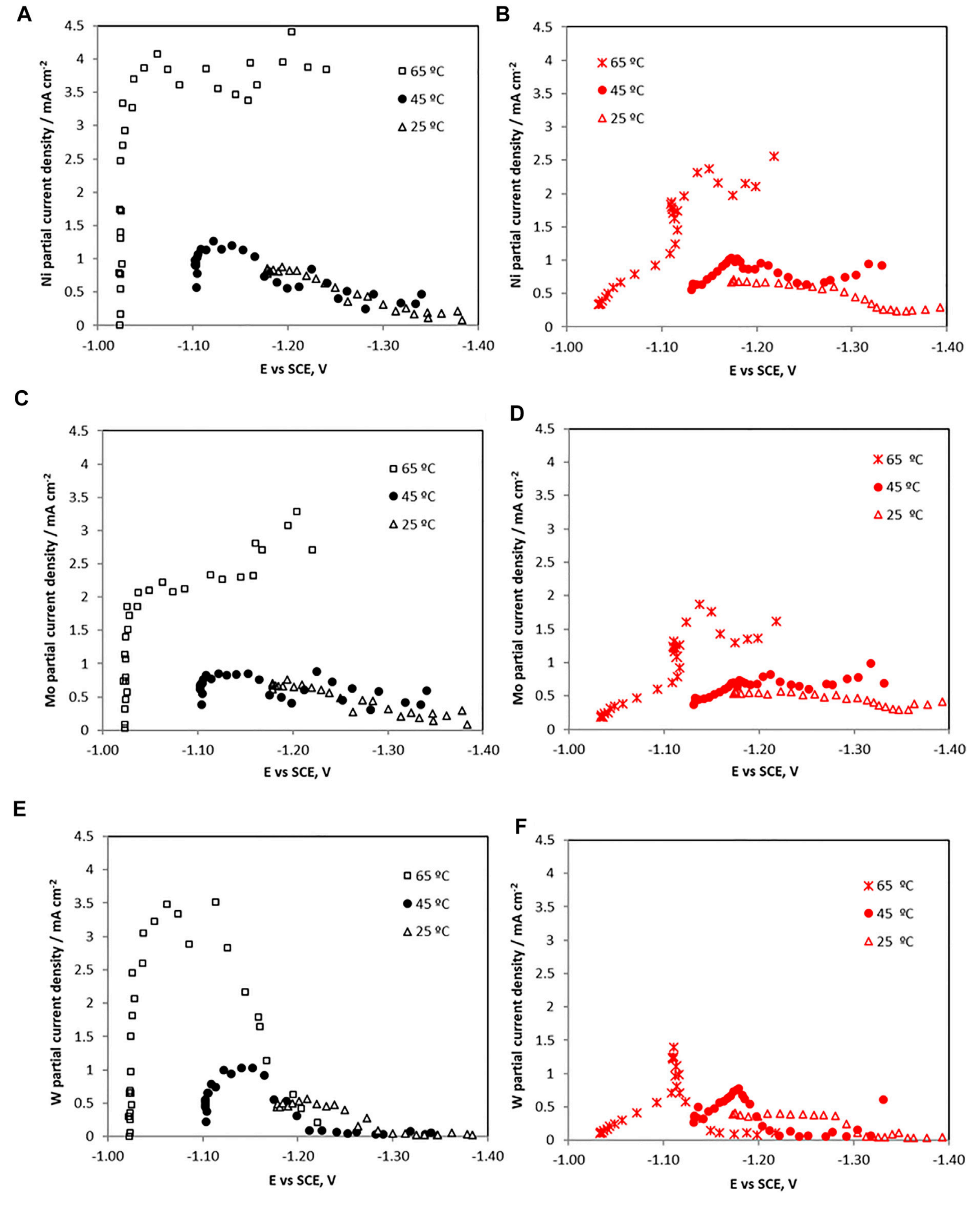

FIGURE 5 | The partial current densities with potential of each metal ion reduction without (left) and with (right) TiO_2 particles for **(A,B)** Ni **(C,D)** Mo, and **(E,F)** W during the electrodeposition of Ni-Mo-W at different electrolyte temperatures.

sharp change and then remain relatively constant at 65°C, between −1 and −1.2 V vs SCE. At lower temperatures the Ni and Mo partial current densities decrease in this potential range. Only the tungsten partial current density suffers a drop at higher overpotentials, occurring when the side reaction, associated with a large increase in the slope of the hydrogen evolution reaction.

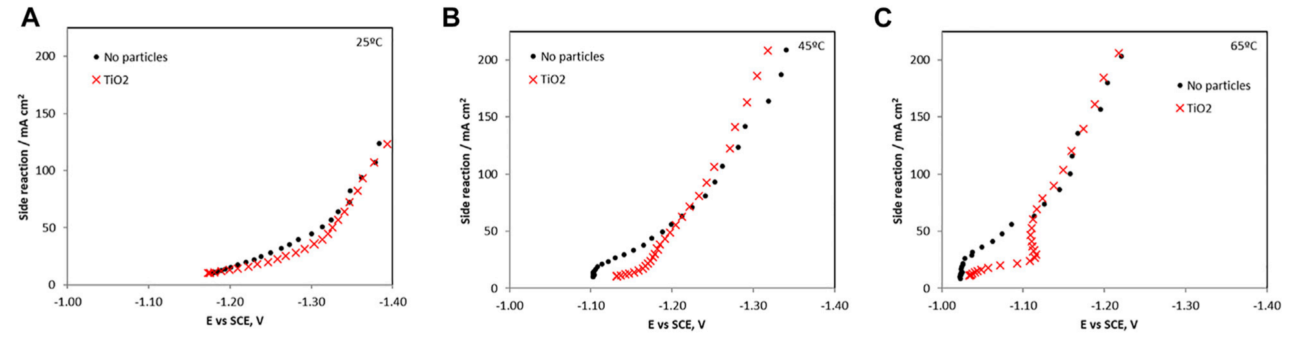

FIGURE 6 | The hydrogen evolution side reaction partial current densities with and without the addtion of TiO2 in the electrolyte **(A)** 25°C, **(B)** 45°C, and **(C)** 65°C.

To determine if the horizontal region of the Ni and Mo partial current densities at 65°C are reflective of a mass transport control region, the limiting current densities were calculated using the empirical Eisenberg equation (Eisenberg, et al., 1954).

$$\mathrm{i_L = 0.01nFC^bD^{0.644}v^{-0.344}S^{0.7}d_i^{0.4}} \qquad [6]$$

where n is the number of electrons transferred, F is Faraday´s constant, C^b is the metal bulk concentration, and D is the metal diffusion coefficient. Assuming diffusion coefficients of nickel, molybdenum and tungsten to be close to 5 x 10^{-6} cm^2 s^{-1}, electrons transferred of 2, 6 and 6 for nickel, molybdenum and tungsten, respectively, with an estimated kinematic viscosity, v, using that of water, 0.01 cm^2 s^{-1}, an electrode rotation rate, S, of 500 rpm and cathode diameter, d_i 0.6 cm, the resulting limiting current density values for the individual metal ions reduction reactions are 34, 3, and 69 mA cm^{-2} for Ni, Mo and W, respectively. The calculated limiting current density value for molybdenun presents the same order of magnitude than that observed in **Figure 5**, so the molybdenum electrodeposition may be under a mass transport control at the higher total current density region, attributable to the low concentration used. In the case of nickel and tungsten, the calculated limiting current densities were one order of magnitude higher than those observed. Hence, these metals did not reach their mass transport limited current densities so kinetic effects control their deposition, even when the Ni partial current density appears horizontal.

When TiO_2 particles were present, all the metal ion reduction reaction rates (*i.e.*, partial current densities) are shifted to more negative, less noble potentials, and inhibited at 65°C. At the lower temperatures the metal reduction rates were not significantly inhibited with the addition of the TiO_2. Interestingly, the side reaction rate (**Figure 6**) is progressively more inhibited with temperature at the low current density region. At 65°C, it is the most inhibited with added particles until −1.12 V vs SCE. At this point, the side reaction rate increases sharply with an associated inflection in the nickel and molybdenum partial current densities. The tungsten current density exhibited a maximum at -1.12 V vs SCE and dropped to zero at higher overpotentials. For the side reaction, its partial current density reached the values measured in the electrolyte without particles at potential values more negative than −1.12 V. Thus, the decrease in the composite efficiency (**Figure 3**) at high current density was attributed primarily with a decrease of the metal rates, not an increase in the side reaction. In the region between 1.1 V and −1.2 V vs SCE the total current density in **Figure 1** decreased when particles were present due to the lowering of all the reaction rates, both the metal and the side reaction.

Correlating these features with the composition of the Ni-Mo-W alloy material electrodeposited at 65°C, (**Figure 2**) the maximum tungsten composition (~40 wt%) was achieved at the lower overpotential values, i.e. when the tungsten partial current density was maximum. Then, at higher overpotentials, the deposit continued to be enriched in nickel and in molybdenum mainly due to the drop of the tungsten partial current density, since nickel and molybdenum partial current densities remained practically constant with potential. When the particles were present, interestingly, there is a current density region where the nickel and molybdenum composition in the deposit increases, with an associated decrease in tungsten wt%. This behavior is not attributed to an enhancement of the nickel and molybdenum partial current densities but in fact a decrease, with less of a relative decrease compare to tungsten partial current density.

According to the Sun-Bairchanya-Podlaha model (Sun, et al., 2013), the observed lowering of the partial current densities is consistent with a decrease of the adsorbed mixed-metal intermediates, shown in equations (1)–(4). Since there is a substantial inhibition of the tungsten at larger overpotentials, or larger applied cathodic current densities, there may be an associated decrease in the formation of the $[Ni(I)LWO_2]^{2-}_{ads}$ intermediate. The large inhibition occurs at a point when the side reaction increases (compare **Figure 5** and **Figure 6** (c)) and that may be due to the added adsorbed hydrogen species.

The hydrogen evolution reaction on Ni-W electrodeposits is known to follow a Volmer-Heyrovsky mechanism in alkaline electrolytes (Popczyk and Losiewicz, 2015),

$$H_2O + M + e^- \rightarrow M - H_{ads} + OH^- \qquad [7]$$

$$H_2O + M - H_{ads} + e^- \rightarrow H_2 + M + OH^- \qquad [8]$$

with expected adsorption of hydrogen, H_{ads}, at the electrode surface. Since the drop of the tungsten partial current density coincides with the large increase in the hydrogen evolution side reaction, it may be that this adsorbed intermediate is complicit in interfering with the tungsten reduction. However, the nickel and molybdenum are affected to a lesser extent by the adsorbed hydrogen. The adsorption of all species are limited by the available surface area. The impact of the H_{ads} has less an effect on Ni and Mo, suggesting that there is a smaller change of the adsorbed intermediates of $Ni(I)_{ads}$ and $[Ni(I)LMO_2]_{ads}^{2-}$. Adsorption energies are temperature dependent and thus changes in temperature are expected to alter the fractional coverage of the intermediates. Thus it is possible that there is a composition for surface sites where H_{ads}, $Ni(I)_{ads}$ and $[Ni(I)LMO_2]_{ads}^{2-}$ is favored over $[Ni(I)LWO_2]_{ads}^{2-}$.

The small amount of particles in the deposit and in the electrolyte has a substantial impact on the reaction rates, lowering them, including the side reaction, considerably. Since the current efficiency is reduced (**Figure 3**) when the particles are added, the relative amount of the total metal reduction rates is reduced more than the hydrogen evolution side reaction at the intermediate current densities. At high applied current densities, or larger overpotential, the side reaction occurring when the particles are present is not altered, but the metal rates are reduced leading to an even larger decrease in the current efficiency. Thus, the particles may be indirectly affecting the H_{ads}, which then impacts all the other adsorbed species.

The particle also lowers the extent of cracking of the deposit. Since cracks may be due to the absorbed hydrogen as noted in Co-Mo (Gómes et al., 2001) and Ni-W electrodeposits (Younes and Gileadi, 2000) the particle may be decreasing the absorbed hydrogen and hence enhancing the adsorbed H_{ads} intermediate on the surface. Thus, a model consistent with the partial current density observations and the changes in cracking is that the TiO_2 particles changes the surface environment to promote the hydrogen intermediate adsorption H_{ads}. This intermediate has a larger effect to poison the tungstate ion reduction compared to both nickel and molybdate ion reduction, suggesting that the adsorption intermediates of nickel and molybdate is considerably greater than that of tungsten.

From a practical point of view, the electrodeposition of Ni-W-Mo alloy coatings reinforced with TiO_2 nanoparticles can be a good strategy to combine corrosion resistant coatings with electrocatalysis, for applications such as water splitting, since it has been recently recognized that the addition of TiO_2 can also improve the hydrogen evolution reaction in basic electrolytes in Mo-alloys (Zhang, et al., 2018; Wang et al., 2019, Wang et al., 2020). The addition of TiO_2 also is beneficial to reduce the extent of cracks and to provide improved roughness to the surface, important to surface finishing applications. However, electrodeposition parameters such as current density must be very carefully controlled since TiO_2 incorporation can be detrimental to incorporate tungsten that contributes to the overall corrosion and wear resistance.

CONCLUSION

Ni-Mo-W and Ni-Mo-W-TiO_2 composites were electrodeposited from aqueous citrate electrolytes with an increase in the electrolyte temperature resulting in a positive potential shift of the deposition and higher current efficiency. It is the first report of Ni-Mo-W-TiO_2 electrodeposits. However, at a higher electrolyte temperature (65^0C), the deposit composition was largely influenced by the addition of TiO_2 particularly at high current densities that coincided with a large rise in the hydrogen evolution side reaction. The addition of TiO_2 did not promote any metal reduction reaction. Changes in the deposit composition were due to different extents of metal partial current density inhibition, thought to be due to an increase in adsorbed hydrogen from the side reaction.

DATA AVAILABILITY STATEMENT

The raw data supporting the conclusions of this article will be made available by the authors, without undue reservation.

AUTHOR CONTRIBUTIONS

EP writing, editing and directed the research, UI-E conducted all experiments.

FUNDING

The United States National Science Foundation, #0957448, and the American Electroplaters and Surface Finishing (AESF) in part supported this work.

ACKNOWLEDGMENTS

The authors acknowledge the US National Science Foundation, #0957448, help from W. Fowle for SEM set-up, and release time from Tecnalia.

REFERENCES

Alimadadi, H., AhmadiAliofkhazraei, M. M., Aliofkhazraei, M., and Younesi, S. R. (2009). Corrosion Properties of Electrodeposited Nanocrystalline and Amorphous Patterned Ni-W alloy. *Mater. Des.* 30, 1356–1361. doi:10.1016/j.matdes.2008.06.036

Allahyarzadeh, M. H., Aliofkhazraei, M., Rezvanian, A. R., Torabinejad, V., and Sabour Rouhaghdam, A. R. (2016). Ni-W Electrodeposited Coatings: Characterization, Properties and Applications. *Surf. Coat. Technol.* 307, 978–1010. doi:10.1016/j.surfcoat.2016.09.052

Arulraj, I. (1992). Nickel Based Composite Electrolytic Surface Coatings as Electrocatalysts for the Cathodes in the Energy Efficient Industrial Production of Hydrogen from Alkaline Water Electrolytic Cells. *Int. J. Hydrogen Energ.* 17, 413–421. doi:10.1016/0360-3199(92)90185-y

Arunsunai Kumar, K., Paruthimal Kalaignan, G., and Muralidharan, V. S. (2013). Direct and Pulse Current Electrodeposition of Ni-W-TiO2 Nanocomposite Coatings. *Ceramics Int.* 39, 2827–2834. doi:10.1016/j.ceramint.2012.09.054

Brenner, A. (1963). *Electrodeposition of Alloys: Principles and Practice*. New York: Academic Press, 399–450.

Cesiulis, H., Baltutiene, A., Donten, M., Donten, M., and Stojek, Z. (2001). Increase in Rate of Electrodeposition and in Ni(II) Concentration in the bath as a Way to Control Grain Size of Amorphous/nanocrystalline Ni-W Alloys. *J. Solid State. Electrochem.* 6, 237–244. doi:10.1007/s100080100225

Chassaing, E., Vu Quang, K., and Wiart, R. (1989). Mechanism of Nickel-Molybdenum alloy Electrodeposition in Citrate Electrolytes. *J. Appl. Electrochem.* 19, 839–844. doi:10.1007/bf01007931

Eisenberg, M., Tobias, C. W., and Wilke, C. R. (1954). Ionic Mass Transfer and Concentration Polarization at Rotating Electrodes. *J. Electrochem. Soc.* 101, 306–319. doi:10.1149/1.2781252

Eliaz, N., and Gileadi, E. (2008). "Induced Codeposition of Alloys of Tungsten, Molybdenum and Rhenium with Transition Metals, in Modern Aspects of Electrochemisry," in *Modern Aspects of Electrochemistry*. Editors C. G. Vayenas, R. E. White, and M. E. Gamboa-Aldeco (New York, NY: Springer), Vol. 42.

Ernst, D. W., Amlie, R. F., and Holt, M. L. J. (1995). Electrodeposition of Molydenum Alloys from Aqueous Solutions. *J. Electrochem. Soc.* 102, 461–469.

Ernst, D. W., and Holt, M. L. (1958). Cathode Potentials during the Electrodeposition of Molybdenum Alloys from Aqueous Solutions. *J. Electrochem. Soc.* 105, 686–692. doi:10.1149/1.2428691

Fan, C., Piron, D. L., Sleb, A., and Paradis, P. (1994). Study of Electrodeposited Nickel-Molybdenum, Nickel-Tungsten, Cobalt-Molybdenum, and Cobalt-Tungsten as Hydrogen Electrodes in Alkaline Water Electrolysis. *J. Electrochem. Soc.* 141, 382–387. doi:10.1149/1.2054736

Fukushima, H., Akiyama, T., Akagi, S., and Higashi, K. (1979). Role of Iron-Group Metals in the Induced Codeposition of Molybdenum from Aqueous Solution. *Trans. JIM* 20, 358–364. doi:10.2320/matertrans1960.20.358

Gómes, E., Pellicer, E., and Vallés, E. (2001). Electrodeposited Cobalt-Molybdenum Magnetic Materials. *J. Electroanalytical Chem.* 517, 109–116. doi:10.1016/S0022-0728(01)00682-9

Gómez, E., Pellicer, E., Duch, M., Esteve, J., and Valles, E. (2006). Molybdenum alloy Electrodeposits for Magnetic Actuation. *Electrochimica Acta* 51, 3214–3222. doi:10.1016/j.electacta.2005.09.010

Haseeb, A. S. M. A., Albers, U., and Bade, K. (2008). Friction and Wear Characteristics of Electrodeposited Nanocrystalline Nickel-Tungsten alloy Films. *Wear* 264, 106–112. doi:10.1016/j.wear.2007.02.004

Hull, R. O. (1939). *Apparatus and Process for the Study of Plating Solutions*. US patent No. 2,149,344.

Jamesh, M. I. (2016). Recent Progress on Earth Abundant Hydrogen Evolution Reaction and Oxygen Evolution Reaction Bifunctional Electrocatalyst for Overall Water Splitting in Alkaline media. *J. Power Sourc.* 333, 213–236. doi:10.1016/j.jpowsour.2016.09.161

Landolt, D. (1994). Electrochemical and Materials Science Aspects of alloy Deposition. *Electrochimica Acta* 39, 1075–1090. doi:10.1016/0013-4686(94)e0022-r

Laszczynska, A., Winiarski, J., Szczygiel, B., and Szczygiel, I. (2016). Electrodeposition and Characterization of Ni-Mo-ZrO_2 Composite Coatings. *Appl. Surf. Sci.* 369, 224–231. doi:10.1016/j.apsusc.2016.02.086

Lee, H.-K., Lee, H.-Y., and Jeon, J.-M. (2007). Codeposition of Micro- and Nano-Sized SiC Particles in the Nickel Matrix Composite Coatings Obtained by Electroplating. *Surf. Coat. Technol.* 201, 4711–4717. doi:10.1016/j.surfcoat.2006.10.004

Madore, C., and Landolt, D. (1993). The Rotating Cylinder Hull Cell - Design and Application. *Plating Surf. Finishing* 80, 73–78.

Navarro-Flores, E., Chong, Z., and Omanovic, S. (2005). Characterization of Ni, NiMo, NiW and NiFe Electroactive Coatings as Electrocatalysts for Hydrogen Evolution in an Acidic Medium. *J. Mol. Catal. A: Chem.* 226, 179–197. doi:10.1016/j.molcata.2004.10.029

Ohgai, T., Tanaka, Y., and Washio, R. (2013). Nanocrystalline Structure and Soft Magnetic Properties of Nickel-Molybdenum alloy Thin Films Electrodeposited from Acidic and Alkaline Aqueous Solutions. *J. Solid State. Electrochem.* 17, 743–750. doi:10.1007/s10008-012-1924-z

Olivas, A., Galván, D. H., Alonso, G., and Fuentes, S. (2009). Trimetallic NiMoW Unsupported Catalysts for HDS. *Appl. Catal. A: Gen.* 352, 10–16. doi:10.1016/j.apcata.2008.09.022

Oue, S., Nakano, H., Kobayashi, S., and Fukushima, H. (2009). Structure and Codeposition Behavior of Ni-W Alloys Electrodeposited from Ammoniacal Citrate Solutions. *J. Electrochem. Soc.* 156, D17–D22. doi:10.1149/1.3006389

Podlaha, E. J., and Landolt, D. (1996a). Induced Codeposition: I. An Experimental Investigation of Ni-Mo Alloys. *J. Electrochem. Soc.* 143, 885–892. doi:10.1149/1.1836553

Podlaha, E. J., and Landolt, D. (1996b). Induced Codeposition: II. A Mathematical Model Describing the Electrodeposition of Ni-Mo Alloys. *J. Electrochem. Soc.* 143 (3), 893–899. doi:10.1149/1.1836554

Podlaha, E. J., and Landolt, D. (1997). Induced Codeposition: III. Molybdenum Alloys with Nickel, Cobalt, and Iron. *J. Electrochem. Soc.* 144, 1672–1680. doi:10.1149/1.1837658

Popczyk, M., and Łosiewicz, B. (2015). Influence of Surface Development of Ni/W Coatings on the Kinetics of the Electrolytic Hydrogen Evolution. *Ssp* 228, 293–298. doi:10.4028/www.scientific.net/ssp.228.293

Quang, K. V., Chassaing, E., Bourelier, F., and Montuelle, J. (1971). Uncracked Electrolytic Nickel-Molybdenum alloy Platings and Heat Treatments for High Resistance to Acid. *Corrosion* 19, 237–248.

Raj, I. A., and Vasu, K. I. (1992). Transition Metal-Based Cathodes for Hydrogen Evolution in Alkaline Solution: Electrocatalysis on Nickel-Based Ternary Electrolytic Codeposits. *J. Appl. Electrochem.* 22, 471–477. doi:10.1007/bf01077551

Raman, K. R. S. G. S., Raman, S. G. S., and Seshadri, S. K. (2007). Corrosion Behaviour of Electrodeposited Nanocrystalline Ni-W and Ni-Fe-W Alloys. *Mater. Sci. Eng. A* 460-461, 39–45. doi:10.1016/j.msea.2007.02.055

Schwartz, M., Myung, N. V., and Nobe, K. (2004). Electrodeposition of Iron Group-Rare Earth Alloys from Aqueous Media. *J. Electrochem. Soc.* 151, C468–C477. doi:10.1149/1.1751196

Singh, S., Sribalaji, M., Wasekar, N. P., Joshi, S., Sundararajan, G., Singh, R., et al. (2016). Microstructural, Phase Evolution and Corrosion Properties of Silicon Carbide Reinforced Pulse Electrodeposited Nickel-Tungsten Composite Coatings. *Appl. Surf. Sci.* 364, 264–272. doi:10.1016/j.apsusc.2015.12.179

Slavcheva, E., Mokwa, W., and Schnakenberg, U. (2005). Electrodeposition and Properties of NiW Films for MEMS Application. *Electrochimica Acta* 50, 5573–5580. doi:10.1016/j.electacta.2005.03.059

Sun, S., Bairachna, T., and Podlaha, E. J. (2013). Induced Codeposition Behavior of Electrodeposited NiMoW Alloys. *J. Electrochem. Soc.* 160, D434–D440. doi:10.1149/2.014310jes

Tsyntsaru, N., Cesiulis, H., Donten, M., Sort, J., Pellicer, E., and Podlaha-Murphy, E. J. (2012). Modern Trends in Tungsten Alloys Electrodeposition with Iron Group Metals. *Surf. Engin. Appl.Electrochem.* 48, 491–520. doi:10.3103/s1068375512060038

Urlberger, H. H. (1999). Coatings with High Efficiency. Corrosion- and Wear -resistant Nickel Alloys. *Metalloberflaeche* 53, 15–18.

Wang, C., Bilan, H. K., and Podlaha, E. J. (2019). Electrodeposited Co-mo-TiO2 Electrocatalysts for the Hydrogen Evolution Reaction. *J. Electrochem. Soc.* 166, F661–F669. doi:10.1149/2.1091910jes

Wang, C., and Podlaha, E. J. (2020). Communication-Electrodeposited Co-mo-P-TiO2 Composites Electrocatalysts for the Hydrogen Evolution Reaction. *J. Electrochem. Soc.* 167, 132502–132506. doi:10.1149/1945-7111/abb7e7

Wei, J. C., Schwartz, M., and Nobe, K. (2008). Aqueous Electrodeposition of SmCo Alloys. *J. Electrochem. Soc.* 155, D660–D665. doi:10.1149/1.2961013

Yao, Y., Yao, S., Zhang, L., and Wang, H. (2007). Electrodeposition and Mechanical and Corrosion Resistance Properties of Ni-W/SiC Nanocomposite Coatings. *Mater. Lett.* 61, 67–70. doi:10.1016/j.matlet.2006.04.007

Younes, O., and Gileadi, E. (2000). Electroplating of High Tungsten Content Ni/W Alloys. *Electrochem. Solid-State Lett.* 3, 543–545.

Younes, O., and Gileadi, E. (2002). Electroplating of Ni/W Alloys. *J. Electrochem. Soc.* 149, C100–C111. doi:10.1149/1.1433750

Younes-Metzler, O., Zhu, L., and Gileadi, E. (2003). The Anomalous Codeposition of Tungsten in the Presence of Nickel. *Electrochimica Acta* 48, 2551–2562. doi:10.1016/s0013-4686(03)00297-4

Zhang, Y., Bilan, H. K., and Podlaha, E. (2018). Enhancing the Hydrogen Evolution Reaction with Ni-W-TiO2 Composites. *Electrochemistry Commun.* 96, 108–112. doi:10.1016/j.elecom.2018.10.015

Zhang, Y., and Podlaha-Murphy, E. J. (2017). Electrodeposition of Ni-Fe-Mo-W Alloys – Parts 15. *Prod. Finishing* 81, 9–16.

Zou, Y., Xiao, Z., Fei, X., and Ren, X. (2004). Preparation Technology and Properties of Nickel-Tungsten-Titanium Dioxide Composite Plating. *Mater. Prot.* 37, 24–26.

Conflict of Interest: The authors declare that the research was conducted in the absence of any commercial or financial relationships that could be construed as a potential conflict of interest.

Advantages of publishing in Frontiers

OPEN ACCESS
Articles are free to read
for greatest visibility
and readership

FAST PUBLICATION
Around 90 days
from submission
to decision

HIGH QUALITY PEER-REVIEW
Rigorous, collaborative,
and constructive
peer-review

TRANSPARENT PEER-REVIEW
Editors and reviewers
acknowledged by name
on published articles

Frontiers
Avenue du Tribunal-Fédéral 34
1005 Lausanne | Switzerland

Visit us: www.frontiersin.org
Contact us: frontiersin.org/about/contact

REPRODUCIBILITY OF RESEARCH
Support open data
and methods to enhance
research reproducibility

DIGITAL PUBLISHING
Articles designed
for optimal readership
across devices

FOLLOW US
@frontiersin

IMPACT METRICS
Advanced article metrics
track visibility across
digital media

EXTENSIVE PROMOTION
Marketing
and promotion
of impactful research

LOOP RESEARCH NETWORK
Our network
increases your
article's readership